2015

Neural Circuit Dependence of Acute and Subacute Nociception in C. Elegans

Yifan Xu

NEURAL CIRCUIT DEPENDENCE OF ACUTE AND SUBACUTE NOCICEPTION IN *C. ELEGANS*

A Thesis Presented to the Faculty of

The Rockefeller University

in Partial Fulfillment of the Requirements for

the degree of Doctor of Philosophy

by

Yifan Xu

June 2015

Neural circuit dependence of acute and subacute nociception in *C. elegans*

Yifan Xu, Ph.D.

The Rockefeller University 2015

Nociception, the detection and avoidance of harmful cues, is a crucial system in all organisms. Animals use nociceptive systems to escape from substances that decrease survival, and can also modulate the threshold for avoidance behaviors to weigh the attractive features of an environment against its harmful features. To allow regulation, the nociception system of mammals incorporates multiple feedback and feedforward loops in its central and peripheral pathways. The nociception system of the roundworm *Caenorhabditis elegans* shares many features of the mammalian circuit. Both neural circuits feature a direct path from sensory neurons to motor neurons that is connected by a single class of interneuron, bypassing the higher processing centers. Both neural circuits also feature higher processing pathways that receive information from sensory neurons and provide further input onto the direct pathway.

While the anatomical wiring of the *C. elegans* nervous system has been known for decades, how sensory neurons access different downstream paths in the circuit is less clear. One possible route of differential access of sensory input to downstream neurons is through different dynamics of activation. The temporal dimension of neural circuits cannot be deduced by anatomical wiring, but must be measured directly. In my thesis, I have characterized and manipulated the dynamic properties of a classical nociceptor in *C. elegans*, the polymodal sensory neuron ASH, and asked how these properties instruct downstream circuits and behavior.

I thus first elucidated ASH calcium activation dynamics using simple step responses and using a newly developed systems identification approach for *C. elegans*. Using both long pulses and rapidly fluctuating “white noise” sequences of different nociceptive stimuli, I deduced their ASH activation profiles and linear temporal filters describing how the neuron summates the history of stimulus encounter. This analysis demonstrated that ASH calcium responses to natural stimuli include both linear features and multiple nonlinear components. Mutations in G protein-coupled sensory signaling disrupt both fast linear filtering and sustained responses to nociceptive stimuli. Mutations in a voltage gated calcium channel alter the temporal qualities of the ASH response in a pattern suggesting a role of this channel in sensory adaptation. In the

course of these studies, I discovered several additional classes of sensory neurons that respond to nociceptive stimuli with robust calcium responses, even though past studies did not demonstrate a role for these neurons in nociceptive behavior.

To gain experimental control over the dynamic activity that initiates nociceptive signaling, I ectopically expressed the pheromone receptors SRG-34 and SRG-36 in ASH and activated this system with their endogenous ligand, the ascaroside C3. ASH does not normally detect C3, but when it expresses either of these receptors it generates robust calcium responses to C3. These calcium signals have distinct temporal dynamics: SRG-34 mediated calcium signals are fast rising and fast adapting, while SRG-36 mediated calcium signals increase slowly during stimulation with little adaptation. Expression of SRG-34 or SRG-36 in ASH caused animals to avoid C3. Remarkably, time-aligned histograms of C3-induced avoidance behavior during stimulus onset, presence, and removal closely followed the dynamics of ASH calcium activity at these same time points, with a fast onset and adaptation for SRG-34 and a slow, sustained avoidance of SRG-36.

ASH can directly activated the backward command motor neuron AVA or indirectly activate AVA through other neuronal pathways, including the intermediate interneuron AIB. Selectively silencing the AIB interneuron with the a chemical genetics system using the histamine-gated chloride channel resulted in complete loss of nociceptive avoidance behaviors induced by slow-ramping SRG-36 receptor in ASH, but had less of an effect on SRG-34 avoidance. Selectively silencing the AVA backward command interneuron reduced reversals, but spared or increased other avoidance behaviors for both SRG-34 and SRG-36. These results indicate that downstream interneurons are engaged in different ways, and to different degrees, depending on the mechanism of ASH activation.

I next monitored the activity of AIB and AVA neurons in freely-moving ASH:*srg-34* or ASH:*srg-36* animals responding to C3. In ASH:*srg-34* animals, AIB and AVA begin increasing activity upon C3 onset. In ASH:*srg-36* worms, AIB increased activity before AVA. Together with my AIB silencing results, these observations suggest that AIB accumulates signals from ASH over time to promote AVA activity. Using a coherent type-1 feed forward loop with a calcium slope-determined AND or OR logic, I modeled features of AIB contribution to nociceptive behaviors in response to different ASH temporal dynamics. These findings suggest that feedforward excitation loops, a motif seen in *C. elegans* and mammalian nervous systems, can result in behaviorally-salient consequences in response to different sensory neuron calcium dynamics.

ACKNOWLEDGEMENTS

First and foremost, thanks to Cori Bargmann for taking me on as a student, for her constant and dedicated mentorship, for giving me time to learn everything I want to learn, and for giving me the resources to do all the experiments I imagined doing. Her constant enthusiasm for each project in the lab, her vision for the direction neuroscience should head in, her professional leadership skills, and her lack of fear in pursuing important questions are awe-inspiring. Also, thanks to Cori for letting me invite animal friends into the lab and then taking responsibility for their well being in my absence.

Thanks to my committee, Gaby Maimon, Winrich Freiwald, and Jeremy Dittman for being the best scientific cheerleaders in the world. They always had my best interests in mind and offered great suggestions for how to keep projects on track -I couldn't be more lucky to assemble this crowd together once a year for their input. Thanks to my outside reader, Andres Villu Maricq, for taking the time to read my thesis and for flying to New York twice.

Thanks to my collaborators inside and outside of the Bargmann Lab –Rebecca Butcher for synthesizing ascarosides without delay. Navin for knowing the HisCl construct and for having an explanation for everything in politics. Patrick McGrath for letting me use his receptors to investigate my own questions, for being there to bounce ideas off of, and for letting me hang out with June. Saul Kato, for being patient with my MATLAB skills and for the countless Oslo lattes. Sagi Levy –for having the patience to figure out uncode-like code in order to help me analyze data, and for teaching me that for every experiment, there needs to be at least 30 control experiments conducted in parallel. For my labmates in the east bays: Andrew Gordus –for dressing sharply on the best occasions, for always having a great story handy, and for his willingness to listen to my hare-brained ideas before pointing me in a more logical direction. To Steve Flavell –for letting our pet dragon walk all over his bench right before he isolates RNA, and for never getting angry enough to throw a chair. To Christine, for all the late night conversations, for having extra plates every time I need them, for designing the calendar of lab memories, for all the chess games and all the macarons. To Johannes, who let me use his computer whenever it was acting smarter than mine, and for patiently teaching everyone how to use the Johannes-scope. To Tapan, for being great company during my early days in the lab. To Manuel for all the delicious food excursions. To Jennifer Garrison for always knowing exactly how to cheer me up when nothing was working, for sharing her passion for science with me, and for always showing up with the perfect cocktail. To Alejandro, May, Donovan, and Xin for

making the lab a wonderful place to work. To Hernan for freezing numerous strains for me and for showing off his salsa dancing skills. To Manoush, who made sure plates and S Basal was always in stock. To Priscilla for integrating strains, ordering items on short notice and for always having cute animal pictures handy. To Holly –for knowing exactly what office supplies I was craving.

For my past labs and labmates who were not afraid to try to teach me science. Thanks to Brigit Riley and the Orr lab members who didn't laugh me out of town when I referred to the ice bucket as a flower pot. For Dan Tracey for his excitement about every pain project and for always believing in my potential. For the Katz lab from 2004-2006 –Adi Mizrahi, Dayu Lin, Steve Shea, Ben Arenkiel, Wenqin Luo, Yoram Ben-Shaul, Ian Davison, Huimeng Lei, Bonnie Kissell and especially Larry, for the constant reminder that science should be creative above all, and that life is too short to be anything but happy.

Thanks to the MDPhD office (Ruthie, Olaf, Elaine, Kenneth, Renee) for being completely organized and supportive. Thanks to the Paul and Daisy Soros Fellowship for New Americans for not only giving me financial support, but for also giving me a global network of kind, talented, and brilliant friends in all disciplines. For my med school community who weren't quite sure what I was doing to worms but who made it their responsibility to keep me sane with cats, wine, and food –Jennifer Covert, Andre Schaffer, Jessica Yee, Krzysztof Glomski, Sha-Har Admoni, Xiao Peng, Nikki Goodsmith, Sandeep Kishore, Marina Stasenko. For the CSA crew and the gymnastics crew for making the upper east side more exciting. For Susan Patrick, Allison Schafer, Lisa Orthober and Fanny Matheis for their unconditional love and encouragement across many different time zones.

TABLE OF CONTENTS

LIST OF FIGURES

LIST OF FIGURES (Continued)

LIST OF TABLES

INTRODUCTION: The temporal dimension of neural circuits

Numerous coordinated efforts are underway to assemble complete brain connectomes in multiple organisms. The *C. elegans* connectome has been available for over 25 years, and has definitively demonstrated one thing: the anatomical wiring of cell bodies, gap junctions, and synapses, by themselves, is far from the complete scaffold through which genes give rise to behavior. Superimposed on anatomical wiring are many more dimensions of processing. Neuropeptides and neuromodulators can signal across diverse anatomical distances through connections invisible to the electron microscope. Synaptic strength between neurons can vary independent of the size or number of connections between them, both at baseline and after learning.

Another dimension superimposed on pure anatomical wiring is the temporal dimension of stimulus encoding and transmission. Many types of visual, somatosensory, and olfactory neurons can track encounters of the same stimulus over time to assess the changing quality of the environment. Some sensory neurons, such as olfactory neurons in flies, can encode different stimuli with different rates or patterns of activity. Thus, neurons can track changes over time (use time as a denominator) or use temporal dynamics to encode stimulus identity (use time as a numerator). My thesis will focus on how different temporal dynamics in a single sensory neuron draw on different circuit requirements to generate behavioral dynamics.

As an animal navigates its natural environment, it must make behavioral decisions on a variety of timescales. In some cases, it must make an immediate decision about whether it has encountered a dangerous stimulus. A suddenly looming stimulus must trigger immediate flight by a fly before its demise by the swatter. A hand encountering a hot stove must draw away from it immediately to escape injury. This decision and subsequent action must be rapid to avoid the stimulus in a timely manner. The speed of escape is crucial, so detailed information about the stimulus can be sacrificed. This “deterministic” circuit, in principle, requires only a sensory relay with a specific threshold to trigger a motor output. On the other hand, the same animal must also sample the ongoing statistics of its environment to integrate the presence of sub-threshold dangers with the presence of favorable cues and its own internal state. For instance, while gazelles will normally avoid the scent of their predators, the reward of food or water will entice them out of hiding, especially if they are thirsty or hungry. This second decision will typically be slower than the first response and will involve multiple layers of processing. At any point, the speed requirement of the deterministic state can override the fine calculations of the basal state

in favor of escape. Trading accuracy for speed has been demonstrated in many neural circuits, including rodent olfactory systems and primate visual-motor pathways (Rinberg et al., 2006; Heitz and Schall, 2012). However, other than studies showing that chronic pain patients complete tasks with increased speed but decreased accuracy, little work has been done on the tradeoff between speed and accuracy in the nociception system (Veldhuijzen et al., 2006). Does subthreshold information accumulate in the sensory neuron that triggers deterministic behaviors? If the stimulus remains after the initial response is triggered, does the organism treat the ongoing stimulus differently from an acute stimulus? How do neural circuits process both fast and slow signals simultaneously?

My thesis will address these questions in the context of *C. elegans* nociception. In this introduction, I will first describe what is known about the mammalian nociception system, from peripheral cell types and molecules to the downstream circuits. As examples of temporal encoding that provide useful precedent for my work, I will describe fly olfaction and mammalian vision. Finally, I will give a direct review of *C. elegans* nociception and touch responses.

1. Vertebrate nociception: peripheral neural circuits and molecules

Nociception in vertebrates has many of the same molecular receptors and signal transduction pathways as that of *C. elegans*. Moreover, circuit motifs are also maintained anatomically and molecularly from the peripheral to central nervous system.

Anatomy: Mammalian nociceptor classes and their projections

Nociceptors of the mammalian nervous system reside in the Dorsal Root Ganglion (DRG) along the vertebral column. They are characterized by their pseudo-unipolarity, with both the peripheral (dendrite) and central (axon) processes branching off a common axonal stalk from the cell body (Basbaum et al., 2009). Only the peripheral branch can detect and communicate the quality of the environment and local inflammation; only the central branch can release Ca^{2+}-dependent neurotransmitters onto spinal cord interneurons. The peripheral branch can, however, release molecules into the tissue that it innervates in response to tissue damage. The nociceptor can also receive information in the spinal cord, allowing an interplay of central and peripheral modulation of pain sensation that depends on mood, internal state, and external cues.

In mammals, there is spatial, anatomical, and molecular segregation of different somatosensory modalities. For instance, light, non-painful touch is conveyed through large

diameter myelinated Aβ fibers. Medium diameter myelinated Aδ fibers are the first class of nociceptors, communicating “fast”, well-localized, pain with their free nerve endings (Meyer et al., 2008). A third type of fiber in this system, the thin, unmyelinated C fibers, conveys poorly localized “slow” pain and comprises the second nociceptor class. The sensations communicated by the two nociceptor classes are “fast” and “slow” due to the ability of electrical cues to be conducted more rapidly in larger diameter, myelinated fibers compared to thin, unmyelinated ones –thus, signals from Aδ and C fibers are nicknamed “first” and “second” pain, respectively (Dubin and Patapoutian, 2010). There are two types of fast-conducting Aδ fibers: Type I has high thresholds of activation for mechanical (pin prick), heat, and chemical stimuli, all of which lower their thresholds in the settings of maintained stimulation or tissue injury. Type II mediates the “first pain” to noxious heat, with a low heat threshold and a high mechanical threshold. Among C-fiber nociceptors, one population is sensitive to heat and mechanical stimuli, and a second population responds physiologically to both heat and chemicals but only responds to mechanical stimulation in the setting of injury and inflammation (Schmidt et al., 1995).

Due to their anatomy, A-fibers have small receptive fields that transduce location-specific pain (Mense et al., 2008); C-fiber branches are broadly distributed and the pain associated with them is diffuse and difficult to localize.

Circuits, direct and indirect

The indirect and direct circuits of pain sensation begin at the same neurons, but differences in connectivity result in differences in the speed and nature of outcomes that they control. The direct circuit of the DRG is best exemplified by the “withdraw reflex,” a reflex arc that begins when the peripheral branch of a nociceptor is activated by an above-threshold heat or mechanical stimulus that is conducted to the axonal branch via action potentials. The nociceptor releases the neurotransmitter glutamate onto a spinal cord interneuron that immediately activates the motor neuron innervating the area where the sensation occurred. This one-relay circuit results in the sudden contraction of flexor muscles and the reciprocal relaxation of extensor muscles, drawing the affected body part away from the stimulus in less than a second, before the conscious perception of pain has occurred. For instance, humans will immediately withdraw a hand from a hot stove and register the pain only after the fact, minimizing burn damage.

Conscious recognition of the noxious stimulus sensed by DRG neurons does eventually occur, through the "indirect circuit" that involves multiple ascending pathways and descending feedback pathways between hindbrain, midbrain, and cortical structures. C-fibers of the DRG synapse onto interneurons in the superficial laminae I and II of the dorsal spinal cord, while Aδ fibers synapse onto interneurons in laminae I and V. These second-order lamina interneurons can modify pain signals before relaying them onward, either directly or through additional inhibitory and excitatory spinal cord neurons. Laminae I and V of the spinal cord are the major output layers, which send ascending information to the brain along two main pathways (Basbaum and Jessell, 2000). The spinothalamic tract reaches the thalamus and somatosensory cortex for precise sensory-discrimination of the pain experience (location and intensity of stimulus). The spinoreticulothalamic tract reaches the brainstem, anterior cingulate cortices, and insular cortex to process affective-cognitive aspects of poorly localized pains (Basbaum et al., 2009). Additional tertiary regions of processing include the parabrachial nuclei and dorsolateral pons, which send fast messages to the amygdala for the emotional aversive components of pain, and multiple descending inhibitory and facilitatory pathways from the periaqueductal gray and rostral ventral medulla that modulate pain perception according to behavior and homeostasis. Human fMRI imaging studies suggest that prefrontal cortex also processes pain (Heinricher et al., 2009; Basbaum et al., 2009).

Signal transduction and molecular signatures of nociception

In both vertebrates and invertebrates, specific signal transduction molecules are expressed in different nociceptive regions and mediate sensation of different painful stimuli. Among these are vertebrate channels that sense high temperatures (TRPV1), aversive cold (TRMP8), and irritating chemicals like wasabi (TRPA1). The TRPV1 channel plays a role in multiple nociceptive processes (Caterina et al., 2001). TRPV1 can be directly activated by high temperatures (>43 degrees Celsius), or by chemical irritants such as capsaicin. It can be also be indirectly activated downstream of a variety of G protein-coupled receptors through the PKC/DAG/PIP_2 pathways (Solinski et al., 2012). TRPV1 marks a set of neurons that are essential for sensation of noxious pain from chemical and heat, as well as other neurons. TRPV1 is expressed in all heat-sensitive C-fibers, heat-sensitive Aδ fibers and the "silent" C-fibers. Not all TRPV1-expressing neurons have equal properties: different C-fiber types show different activation dynamics to capsaicin, suggesting modulation of TRPV1 by other C-fiber

type-specific molecules. TRPV1 activation in Aδ fibers has different consequences than TRPV1 activation in C-fibers: Aδ that express TRPV1 respond more rapidly than C-fibers to mediate the "first pain" to heat; these fibers are eliminated by repeated capsaicin treatment while C-fibers are not (Treede et al., 1995; Campell and LaMotte, 1983; Ringkamp et al., 2001). Nevertheless, the sensory transduction events mediated by TRPV1 ultimately result in action potential firing of the relevant DRG neurons. Given the prevalence of TRPV1 expression in heat-sensitive, cold-sensitive, and mechanically sensitive nociceptors, it was initially surprising that a genetic deletion of TRPV1 in mice only partially reduced noxious heat sensitivity and did not affect C-fiber cold or mechanical-responsive at all (Caterina et al., 2000; Davis et al., 2000; Zimmermann et al., 2005). This suggests the existence of additional molecular sensors for noxious stimuli. Ongoing studies of other sensory transduction molecules are helping to clarify this observation.

Noxious heat is not the only temperature that activates nociceptor neurons in the DRG. Cooling the skin to 15° C activates a set of A and C-fibers with firing rates that increase in a graded manner with every decrease in temperature (Carr et al., 2009; Babes et al., 2004; Babes, 2009; Bautista et al., 2007). TRPM8, also called the menthol receptor, is activated by cooling below 20° C in vitro, and is necessary for behavioral avoidance of moderately unpleasant cool temperatures. TRPM8 is in 15% of all somatosensory neurons. While the majority of TRPM8 expressing neurons are small-diameter, unmyelinated C-fibers, a small subset are lightly-myelinated Aδ fibers with faster signal conductance (Julius, 2013). Less than 30% of TRPM8-expressing DRG neurons co-express TRPV1 (Julius, 2013). The rest are not co-labeled, suggesting that cold nociception is both anatomically and functionally distinct from other nociception modalities (Kobayashi et al., 2005). Mouse knockouts of TRPM8 have cold-modality specific defects (Bautista et al., 2007; Dhaka et al., 2007; Colburn et al., 2007).

TRPA1 is co-expressed with TRPV1, and is activated by irritating thiol agents such as wasabi (Bautista et al., 2005; Kobayashi et al., 2005). TRPA1 is expressed exclusively in peptidergic C-fibers that mediate neurogenic inflammation through the secretion of substance P, neurokinin A, and CGRP. Through TRPA1 activation, these secreted substances help induce pain and hyperalgesia to acute noxious heat and also mediate inflammatory pain syndromes from environmental irritants (Bautista et al., 2006). A completely different channel, Piezo2, appears to be the main sensor of noxious mechanical stimuli. It is expressed in many neurons that also express TRPV1, explaining why nociceptive neurons can be both mechanically-activated and heat-activated (Coste et al., 2010).

For all temperature and mechanical nociception, the constitutively-active potassium channel KCNK2 (TREK) and the mechanically-gated, inward rectifying KCNK4 (TRAAK) channels may set how easily neurons can be depolarized (Kung et al., 2010). Mice with mutations in these potassium channels show increased pain sensitivity (Dubin and Patapoutian, 2010). Signal transduction in the DRGs also depends upon voltage-gated Na+, Ca+, and K+ channels that regulate action potential dynamics. At least 59 such channels are expressed in the DRGs, many with alternative splice forms. The voltage-gated sodium channels Nav1.7 and 1.8 channels are probably the best studied of these channels. Mice with deletions in these channels have severe mechanosensory defects (Nassar et al., 2005; Akopian et al., 1999; Rush et al., 2007). Humans with loss-of-function mutations in NaV1.7 channels cannot feel pain, resulting in extreme tissue damage and eventually death; humans with gain-of-function mutations have severe congenital pain syndromes such as erythromelalgia and paroxysmal extreme pain disorder with associated extreme burning sensations (Cox et al., 2006; Dib-Hajj et al., 2008; Estacion et al., 2008; Fertleman et al., 2006; Yang et al., 2004).

Voltage-gated calcium channels are implicated in pain disorders as well, and have proved to be good drug targets. VGCCs are heteromeric proteins with one pore subunit (the α1 subunit) and multiple accessory subunits. The P/Q VGCCs are expressed in synaptic terminals of DRG neurons ending on laminae II-IV and are implicated in familial hemiplegic migraines (deVries et al., 2009). N and T type VGCCs are expressed in C-fibers in pathological settings such as diabetic neuropathy or nerve injuries, and the represented α1 subunits, Cav2.2 and Cav3.2, increase sensitivity to mechanical and thermal stimuli (Cao et al., 2006; Zamponi et al., 2009; Messinger et al., 2009). The N-type VGCC is selectively blocked by ω-conotoxin, which is administered intrathecally as the drug ziconotide to ameliorate intractable cancer pain (Rauck et al., 2009). The VGCC α2δ subunit modulates the activation and inactivation kinetics of VGCCs. The $\alpha 2_1$ and $\alpha 2_2$ clsses of α2δ subunits are targeted by gabapentin, another drug used to treat pain (Davies et al., 2007; Luo et al., 2001).

Modulation of nociception by injury

After injury from heat, mechanical stimuli, sunburn, or a chemical irritant, the affected area will exhibit enhanced pain to normally painful stimuli (hyperalgesia) as well as the sensation of pain to normally unpainful stimuli (allodynia). This sensitization is dependent on C-fibers that decrease their activation thresholds and begin to perceive pain in the immediate zone of flare and a secondary zone surrounding it (Sandkhuler, 2009). Part of this sensitization is cell-

intrinsic, and occurs via a mechanism of neurogenic inflammation called the dorsal root reflex, defined as antidromic impulses traveling towards the periphery along primary afferent fibers to invade peripheral arborizations. Peripheral or central stimulation of C-fibers thus produces plasma extravasation and vasodilation in the peripheral receptor field through release of peptides like substance P, CGRP, somatostatin and cytokines into interstitial tissue. The subsequent recruitment of immune cells to this area results in accumulation of blood cells, edema, and additional liberated enzymes (like kallikreins) that sensitize peripheral terminals and activate further second messenger cascades (McMahon et al., 2008; Lin et al., 2007; Richardson et al., 2002). This inflammatory reaction then lowers TRPV1 and TRPA1 activation threshold in C-fibers through allosteric modulation or a second-messenger signaling pathway so that the nerve fiber responds more strongly to all nociceptive stimuli (Julius, 2013).

One inflammatory molecule, bradykinin, binds bradykinin receptor 2 (BR2) on cell membranes to activate the G_s cascade. This cascade results in the phosphorylation of TRPA1 by protein kinase A to decrease the activation threshold of DRG neurons coexpressing BR2 and TRPA1 (Mizumura et al., 2002; Wang et al., 2008). Other mechanisms of pain modulation are mechanistically diverse. The accumulation of Na+ channels in injured nerves can increase sensitivity. NGF binds the Trk-A nuclear receptor to increase substance P expression, whose release enhances TRPV1 and Nav1.8 currents (Cang et al., 2009). TRPA1 is seen in all chemically-sensitive C-fibers, and is also activated by endogenous factors produced by inflammation; it sensitizes neurons under nitrative and oxidative stress when prostaglandin products, nitrooleic acid, hydrogen peroxidase, bradykinin, and hydrogen sulfide are plentiful. Mutation of TRPA1 results in decreased tissue injury-evoked sensitization to both thermal and mechanical stimuli and protection from asthma inflammation (Bautista et al., 2006; Kwan et al., 2006; Cazares et al., 2009).

Neurogenic sensitization can cross modalities. For example, in TRPV1-mediated hypersensitivity to mechanical stimuli, Piezo2-mediated mechanosensation may be potentiated since Piezo2 is localized in 20% of DRG neurons, most of which are nociceptors that express TRPV1 (Coste et al., 2010). TRPM8 can act as an analgesic as well, and counteract the effects of heat channels or formalin-induced inflammatory hyperalgesia (Dhaka et al., 2007).

Modulation by non-neuronal cell types

Modulation does not only occur through action of nerve terminals themselves. The “inflammatory soup” consists of many inflammation-promoting compounds and is made by both

neurons and non-neural cells in the context of injury or irritation. Peripheral nociceptive nerve terminals are surrounded by keratinocytes, mast cells, and Langerhan cells of the epidermis, allowing them to monitor a variety of factors secreted in the skin (Lumpkin and Caterina, 2007). Immune cells (such as mast cells, basophils, platelets, macrophages, and neutrophils) and skin tissue (such as endothelial cells, keratinocytes and fibroblasts) secrete inflammatory factors in response to external injury, tumor destruction of normal tissue, or noxious stimulation. These factors include TNFα, IL-1β, proteases, ATP, protons, neurotrophins, cytokines and chemokines, eicosinoids, lipids, prostaglandins, thromboxanes, keukotrienes, histamine, serotonin, and endocannabinoids, and they act on equally diverse receptors and channels expressed by nociceptors such as RTKs, K2Ps, GPCRs, TRPs, ASIC/P2X that decrease pain thresholds and result in further inflammatory signaling (Ritner et al., 2009). This inflammatory response results in hyperalgesia and allodynia and thus has been a significant target of painkillers, including the NSAID COX-1/COX-2 cyclooxygenase inhibitors aspirin and ibuprofen (Meyer et al., 2008). The temperature sensitive channels TRPV3 and TRPV4 are expressed on keratinocytes, so it's possible that nociceptor activation is amplified by signals that keratinocytes release in response to heat (Patapoutian et al., 2009; Lumpkin and Caterina, 2007; Mandadi et al., 2009).

Glial involvement is also widespread in pain modulation, with microglia physically accumulating at injured areas to induce edema and hypersensitivity through release of ATP, fractalkine, BDNF, and cytokines. Glial factors can activate receptors in the spinal cord lamina as well as the nerve terminals, such as P2-R, CX3CR1, trkB and toll-like receptors.

Pain modulation by circuit mechanisms

There is significant plasticity in synaptic strength, both homosynaptically and heterosynaptically, in the pain circuit. Plasticity can result either from decreased inhibition or from increased excitation, and can occur in primary afferents, second-order interneurons, or descending facilitory and inhibitory brain pathways. The two best-delineated mechanisms of circuit potentiation for pain responses are the loss of tonic inhibition from inhibitory interneurons and NMDA receptor-mediated increases in neural excitability.

GABAergic neurons are widely distributed throughout the dorsal spinal column. In the gate control theory of pain, hyperalgesia can result when loss of tonic inhibition by inhibitory interneurons, and thus loss of GABA and glycinergic tone, result in decreased dampening of pain signals and the recruitment of normally unresponsive fibers to pathologically sense pain.

For example, light-touch conducting Aβ fibers can be pathologically induced to engage the pain machinery, resulting in allodynia in the setting of disinhibition (Latremoliere and Woolf, 2009). Also, giving the glycine receptor antagonist strychnine to rodents results in nociceptive hypersensitivity, a circuit-level process that requires PKCγ neurons in lamina II and projection neurons in lamina I (Malan et al., 2002; Miraucourt et al., 2007). Conversely, increased excitability can occur when glutamate activates normally-silent postsynaptic lamina I NMDA receptors in injury. NMDA activation can strengthen the synapse between DRGs and spinal neurons, and will thereby result in hyperalgesia at the level of postsynaptic neurons.

Circuit modulations in pain can become quite complex, and can cross modalities. One example, described as “Thunberg’s illusion”, a hand held against a grill of alternating innocuous warm and cool bars will cause the subject to report an intense burning sensation that is absent if the same hand is held against the warm or cool bars separately (Craig and Bushnell, 1994). In other examples, while emotional qualities of pain are, by definition, not nociceptive, the subjective experience of patients on morphine, who can sense pain without feeling any aversion, is thought to be a feature of emotional pain modulation. Interestingly, despite the cross-modulation of heat and mechanical modalities, agonists of the peptidergic μ-opioid receptors result in loss of heat pain aversion while agonists of nonpeptidergic δ-opioid receptors result in loss of mechanical pain aversion. The “Reynolds Experiments” from 1969 showed that rats experiencing electrical stimulation of the midbrain medullary raphe magnus and periaqueductal grey regions did not attempt any escape from a surgical laparotomy (Reynolds, 1969). This lead to current work suggesting the anti-nociceptive effects of morphine may engage this brain region (Hellman and Mason, 2012).

Much of mammalian pain modulation depends on internal modulatory contexts that have yet to be localized. Attention to distractions will often decrease sensation of persistent pain; soldiers injured in the line of duty or athletes injured on the field report less pain than those who sustain the same injury in a less heroic context; the shock of being eaten by a lion apparently results in endogenous opioid secretion that results in euphoria rather than pain; chili-eating contests results in heart attacks for some and cause euphoria in others. Requirements for hunger and sleep can also greatly influence sensitivity to painful stimuli (Basbaum et al., 2009).

Temporal features of mammalian nociception

Temporal separation of nociceptive signals in mammals begins with the DRG sensory neurons. The “first” and “second” pains transduced by Aδ and C-fibers occur along

anatomically-separated tracts with different conduction speeds for the same stimulus, and both differ from the even faster conduction of light touch by Aβ fibers. Different types of Aδ fibers have intrinsically different coding of stimulation over time. While both respond to both mechanical and heat stimuli, class I fibers exhibit prolonged responses, a late peak, and sensitization to repeated stimulus exposure, while class II fibers peak quickly before adapting and do not respond to repeated stimuli (Table 1.1). This temporal and anatomical segregation of parallel stimuli is maintained across synaptic levels (Gasser and Erlanger, 1929). Fast, direct sensory-motor connections in the spinal cord (mediated by the fast adapting class II Aδ fibers) mediate behaviors that are temporally differentiated from cognitive and emotional aspects of pain processing mediated by the brain. Since the kinetics of voltage-gated channels can be modulated by their α2δ subunits, cell activation dynamics can be changed with inflammatory potentiation of this subunit or the drug inhibition of this process.

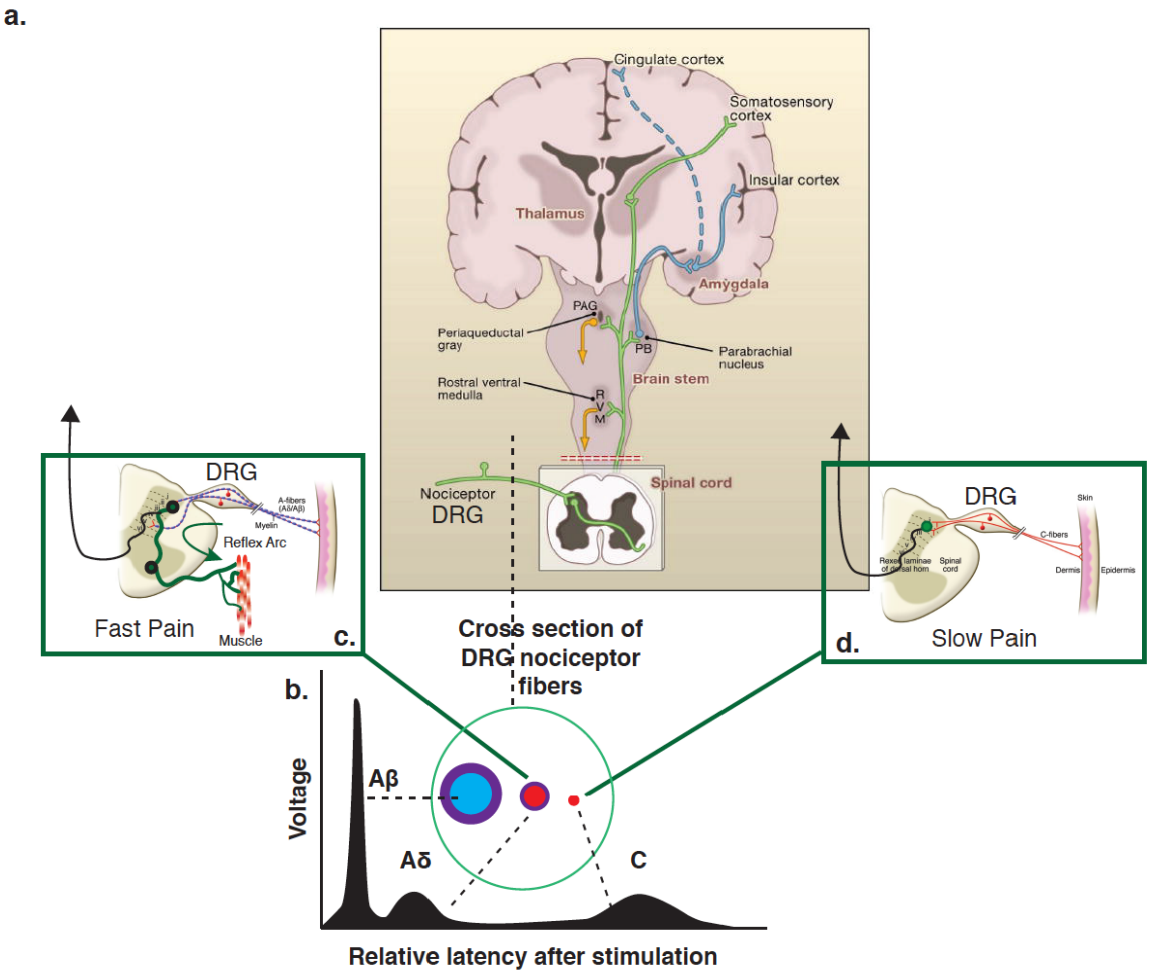

Figure 1.1. Pain sensation enters the mammalian central nervous system via Dorsal Root Ganglion Fibers
a) Peripheral pain enters the central nervous system via nociceptive in the DRG. A cross section of the DRG tract shows **b)** myelinated (purple), large diameter Aβ fibers (blue), myelinated, small diameter Aδ fibers (red with purple), and even smaller, unmyelinated C fibers (red). Aβ fibers are activated by innocuous touch and relay fast, sharp, adapting signals. Aδ fibers convey fast pain signals from mechanical and thermal stimulation. A subset of them are responsible for the triggering the withdraw reflex **(c)**. C fibers conduct mechanical, thermal, and chemical-induced pain signals slowly and do not contribute to the withdraw reflex **(d)**. Figures compiled and modified from Basbaum *et al.*, 2009 and Dubin and Patapoutian, 2010.

Table 1.1: Dorsal Root Ganglion fibers transmit information about diverse pain stimuli to the central nervous system with different conductance properties.

Type	Myelination	Diameter	Speed of Conduction	Sensation	Dynamics
Aβ	Yes	6-12 μM	35-90 m/s	Innocuous touch	Fastest
Aδ	Yes	1-5 μM	5-40 m/s	Fast/First/Acute Pain, mechanical and thermal	Fast
- Class I					-Prolonged response, late peak, -Sensitization with repeated exposure
- Class II					-Short response, fast peak, -Adapting to repeated exposure
C	No	0.2-1.5 μM	0.5-2 m/s	Slow/Second/Dull Pain, mechanical, thermal, chemical	Slow

Nociceptor activation requires depolarization of the peripheral terminals above a threshold duration and intensity. Nociceptors are considered to be electrically silent until all-or-none activity occurs upon adequate stimulation; this activity only translates to the sensation of pain in situations when the frequency of activity temporally summates with other pre and postsynaptic signals from central influences (Woolf and Ma, 2007). However, there is evidence of sub-threshold spiking and oscillations in DRGs (Liu et al., 2000; Amir et al., 2002). Increases in these events are thought to be a consequence of nerve injury and a possible mechanism of subsequent neuropathic pain. It is unclear, however, whatever post-synaptic neurons detect or summate such sub-threshold dynamics and allow their propagation to higher processing systems or subsequent behavior. While labeled-line stimulus transduction in the mammalian DRG system has been extensively studied, little has been done to examine parsing and feature extraction of painful stimuli before its conductance into the central nervous system.

2. Parallel Pathways in Parsing –Retinal ganglion cells in the visual system

After sensory inputs are detected, circuits can segregate information into parallel processing streams. This process has been examined most intensely in the mammalian visual system. The entire visual field is divided into the small receptive fields of rod and cone receptors, which effectively detect pixels whose higher features begin to be extracted within the retina. Six main cell types in the vertebrate retina are the photoreceptors, horizontal interneurons, bipolar interneurons, amacrine interneurons, retinal ganglion cell projection neurons (RGCs), and Muller glial cells. The photoreceptors, bipolar neurons, amacrine neurons, and retinal ganglion cells can each be be divided into multiple subtypes from structural, genetic, and electrophysiological characteristics, for a total of about 100 cell types (Maslund, 2012). These cells have cell bodies in three distinct layers and process in two plexiform layers. Each plexiform layer can be subdivided into different sublamina that have synaptic connections from different cell types.

Parallel processing in the retina begins with rod and cone photoreceptors specialized for dim light versus brighter light and colors, respectively. Rod photoreceptors synapse onto a single type of bipolar cell, whereas cones synapse onto around 15 classes of bipolar cells. Among cone bipolar neurons, some are activated and some are inhibited by glutamate released from photoreceptor terminals. ON and OFF bipolar cells differ in their glutamate receptor expression: the AMPA and kainite receptors in OFF cells allow cations into the cell, while the mGluR6 metabotropic receptor of ON cells closes the cation channel TRPM1 and hyperpolarizes the cell (Morgans et al., 2009; Shen et al., 2009). The G-protein mediated signal transduction pathway in ON bipolar cells is slower than the ligand-gated channels in OFF bipolar cells, as demonstrated by recordings in tiger salamander retina in response to light transients and white noise light patterns (Burkhardt et al., 2007). More diversity subdivides these general classes. Two other classic types of ON and OFF bipolar cells, the sustained and transient types, differentially express kainite and AMPA glutamate receptors that are slow and fast inactivating, respectively (Awatramani and Slaughter, 2000; DeVries, 2000). Within these major bipolar cell types are subtypes that exhibit complex mixtures of ON/OFF/sustained/transient properties, thought to be mediated by signal transduction molecules like RGS proteins, that can act as timers to turn off G-protein activation at specific rates (Cao et al., 2012). Bipolar cell activation is then transduced to about 25 retinal ganglion cell types. RGCs that receive information from ON bipolar cells have receptive fields that are ON-center, but OFF surround. RGCs that receive information from OFF bipolar cells have

receptive fields that are OFF-center, but ON surround. The two main types of RGCs, M and P types, best signal motion (with fast adapting responses) and presence (with slow sustained responses to color and duration), respectively. Using these pathways, feature extraction along the tiled spacing of RGCs in the two-dimensional retina result in faithful transmission about object colors, the velocity of stimuli, the orientation and size of shapes, and the permanence of objects. The diversity of retinal ganglion cell properties is enhanced by regulatory inputs from about 50 amacrine cell types. Ultimately, the different RGCs send their axons out of the retina to various retinorecipient structures in the brain. Thus, prior to cortical processing, the retina has converted light pixels from the visual field into compact features of the visual scene necessary for the beginning of perception.

3. Temporal coding as a proxy for stimulus identity

How is a time-varying signal encoded in the nervous system? In insect olfaction, recent system identification approaches have characterized temporal features of both sensory and second-order neurons. In these studies, odor plumes have been presented to locusts (Geffen et al., 2009) and flies (Nagel and Wilson, 2010; Kim et al, 2011; French et al, 2011; Su et al., 2011) with a “white-noise” m-sequence stimulus sequence. The m-sequence consists of pseudo-random ON/OFF pulses of stimuli that are agnostic to the properties of the neuron being recorded. Statistically, the stimulus sequence is spectrally unbiased since the finite length m-sequence presented during an experiment has the same sharply peaked autocorrelation as a theoretical infinite-length random sequence. The neuron’s response dynamics to this sequence is considered the “output” response while the m-sequence used is considered the “input” response. A series of linear algebra algorithms can then derive the temporal summation properties of the neuron that would generate the “output” from the “input” (Dayan and Abbott, 2001; Westwick and Kearney, 2003). Often, this model consists of a linear-nonlinear (L-N) cascade, in which the input is convolved by a linear temporal filter and followed by the application of a static nonlinearity in order to generate the output. These modeling parameters can therefore characterize the time-dependence of neural responses for different stimuli as a series of L-N filters.

In the *Drosophila* olfactory system, the systems identification approach showed that varying odor identity can provoke different temporal response properties in the same neuron, and that different neurons respond to the same stimulus with different temporal response properties (Nagel and Wilson, 2010). This diversity in temporal responses suggests that in

insect olfaction, time-varying processes encode stimulus identity. This property may be related to the underlying molecular biology of insect olfaction. *Drosophila* olfaction on fewer than 100 broadly-tuned ligand-gated channels that directly depolarize neurons. In olfactory systems where many hundreds of ligand-GPCR cascades can detect ligand on a receptor level before second messenger systems depolarize the neuron (as is the case in mammals and *C. elegans*), stimulus identity may be encoded by more selective GPCR activation and be less reliant on temporal encoding (Kato et al., 2014).

The use of temporal information for identity coding does not preclude temporal analysis of odor stimuli in insects. In locust projection neurons downstream of olfactory neurons, the derived L-N filters of response dynamics suggest that the neural population represents odor dynamics independent of stimulus identity at this next relay, with activity that reflects the temporal dynamics of odor encounter (Geffen et al., 2009). Individual olfactory sensory neurons may not present temporal information about odors well, but the complete population of sensory neurons conveys dynamic information to subsequent levels.

4. The *C. elegans* nociception circuit

As an animal navigates through its environment, it must sense and respond to a variety of cues that are critical for its survival. While it is crucial to find and evaluate the nutritional quality of food sources, it is even more crucial to be able to quickly detect dangerous stimuli and escape from these aversive cues. As in humans, a deterministic avoidance can allow the nematode worm *C. elegans* to escape above-threshold, high-level nociceptive cues, whereas subthreshold noxious stimuli can be integrated with favorable stimuli to allow the worm to evaluate its environmental quality. In addition, internal states such as satiety and starvation can change the relative weights of positive and negative cues.

Wild-type hermaphrodite *C. elegans* have exactly 302 neurons with stereotyped lineage and identities (White et al., 1986). They can sense a vast variety of mechanical stimuli, volatile odors, and soluble taste cues that signal the presence of nutrients, conspecifics, and physical features of the environment (Bargmann and Horvitz, 1993). These sensory neurons signal through classical neurotransmitters, neuropeptides, and electrical gap junctions to interneurons, and also receive feedback in the form of neuropeptide and neuromodulators. The terminal level of interneurons, termed command interneurons, synapse onto motor neurons that synapse on muscles to guide behaviors (de Bono and Maricq, 2005; Bargmann, 2006; Goodman, 2006).

C. elegans avoid harsh mechanical body touch, light and harsh nose touch, low and high temperatures, low and high oxygen levels, carbon dioxide, heavy metals, low and high pH, drastic osmolarity changes, heavy metals, and bitter compounds (Tobin and Bargmann, 2004; Bargmann, 2006; Hilliard et al., 2004, Hilliard et al., 2006). Many sensory neurons are dedicated to the detection of these stimuli. While some of these nociceptors, such as the temperature-sensitive AFD neurons or the oxygen sensitive URX neurons, appear to be dedicated to one modality, many of these nociceptors drive behavior to many sensory modalities. The polymodal multidendritic PVD neurons, for instance, tile the body wall and can sense both harsh touch and cold temperatures (Way and Chalfie, 1989). The polymodal FLP neurons are similarly multidendritic but head-specific, and can drive reversal behavior to gentle nose touch, harsh head touch, and heat. The classical *C. elegans* polymodal nociceptor is the amphid sensory neuron ASH, which directly senses both mechanical and chemical cues (Bargmann, 2006; Hilliard et al., 2004; Hilliard et al., 2005).

ASH has ciliated dendrites that are exposed to the external environment, and is capable of sensing high-osmolarity solutions, blue/UV light, bitter compounds, heavy metals, toxic volatile odorants, aversive nose touch, high and low pH, and detergents (Hilliard et al., 2004; Hilliard et al., 2005). Genetic mutations, cell-specific laser ablations, and a variety of behavioral assays have been used to demonstrate the requirement of ASH for avoidance of these cues (Kaplan and Horvitz, 1993; Bargmann, 2006; Goodman, 2006). Calcium imaging and electrophysiology have confirmed the activation of ASH by many of these stimuli (Hilliard et al., 2005; Schafer, 2006). A summary of known ASH stimuli, and the signal transduction molecules in ASH required to mediate escape behavior, are in Table 1.2 and Figure 2.8. Some molecules are required in a common ASH signal transduction pathway to detect many stimuli. For instance, *osm-9* and *ocr-2*, *C. elegans* homologs of TRPV1, are required for detection of all ASH stimuli except blue light (Colbert et al., 1997; Liu et al., 2010, Tobin et al., 2002). ASH-specific rescue of *osm-9* under ASH-selective promoters, such as *sra-6, osm-10*, or *gpa-13,* results in full behavioral rescue of these defects (Hart et al., 1999; Bargmann, 2006). Similarly, the G-protein alpha subunit encoded by *odr-3* is required for many ASH-mediated responses, and in some cases acts together with a second Gα subunit encoded by *gpa-3* (Roayaie et al., 1998; Jansen et al., 2007; Hilliard et al., 2004; Hilliard et al., 2005). Other G-protein regulatory molecules, such as the Regulator of G-protein Signaling molecule *rgs-3* and the G-protein Receptor Kinase *grk-2*, are also implicated in these pathways (Ferkey et al., 2007; Fukuto et al., 2004). *fat-3*, a lipid desaturase that is required for polyunsaturated fatty acid (PUFA) synthesis

in ASH, bridges the G-protein cascade of *odr-3* and *gpa-3* and the TRP activation signal of *osm-9* for a subset of stimuli (Kahn-Kirby et al., 2004).

Some sensory molecules are required only for modality-specific ASH responses. The WD-40 STAND-ATPase protein *qui-1*, for instance, is required only for sensation of quinine and other bitter compounds (Leipe et al., 2004; Hilliard et al., 2004). *osm-10*, a cytosolic molecule with no homology to other known proteins, is specifically required for osmolarity avoidance (Hart e al., 1999). *tmc-1* appears to be a sodium-activated channel that is specifically required for sodium ion sensation (Chatzigeorgiou et al., 2013). *dcar-1*, the only deorphaned G-protein coupled receptor expressed on ASH, detects Dihydrocaffeinic Acid (DHCA), a bitter alkaloid (Aoki et al., 2011).

Activation of ASH with a nociceptive stimulus results in depolarization of the neuron via these signal transduction cascades (Goodman et al., 1998; Geffeney et al., 2011). Beginning at the cilia, G-protein couple receptor activation is thought to drive the TRP channels *osm-9 ocr-2* open, allowing nonspecific cation entry at depolarization (Bargmann, 2006). Depolarization results in activation of the *egl-19* voltage gated calcium channels, and further calcium entry (Bargmann, 2006; Kato et al., 2014). Since *C. elegans* neurons have graded potentials rather than action potentials, calcium levels are usually correlated with the temporal dynamics of neuron activation (Goodman et al., 1998; Kato et al., 2014).

Table 1.2: Summary of known ASH stimuli, receptors, and signal transduction molecules that mediate escape behavior

Function in ASH	*Gene*	Known stimulus dependence
GPCRs	*dcar-1*	DHCA
	sra-6	No known ligand, most commonly used ASH promoter
Gα	*odr-3*	High osmolar glycerol, copper
	gpa-3	quinine
	egl-30, goa-1	
Gβ	*gpb-2/eat-11*	
Gγ	*gpc-1*	
RGS	*rgs-3, egl-10, eat-16*	

Other G protein signaling regulators	*grk-2, arr-1*	
Signal transduction	*mec-10, deg-1, trpa-1*	mechanical stimuli
	tmc-1	High osmolar NaCl,
	qui-1	Quinine, SDS
	osm-10	glycerol
	osm-9, ocr-2	All ASH activity (except light response)
	lite-1	Light response
	fat-3	Lipid-dependent signaling
	egl-19	Voltage-gated calcium channel
	dgk-1, dgk-3, odr-4, odr-8	
Neurotransmission	*eat-4*	Glutamate vesicle transporter
	egl-3, egl-21	Neuropeptide processing
	unc-13, unc-18	Neurotransmitter release

Perhaps surprisingly, activation of ASH by different stimuli appears to engage different synaptic mechanisms for avoidance behavior. ASH is required for initiation of reversals to nose touch (Kaplan and Horvitz, 1993) and osmolarity (Hilliard et al., 2002), requiring glutamate for both behaviors. However, glutamate receptors necessary for each modality appears to differ. For instance, while the GLR-1 AMPA-like ionotropic glutamate receptor is required for reversals to nose touch, a deletion of this gene has no effect on reversals generated by high-osmolarity stimulus (Maricq et al., 1995; Hart et al., 1995). Further, while osmotic avoidance is reduced in worms with defects in either NMDA or non-NMDA receptors, nose touch appears to only require non-NMDA glutamate receptor function (Mellem et al., 2002).

The shortest pathway from ASH to behavior is the “direct” pathway from ASH to the main backward command interneuron AVA, comprising about 10% of anatomically defined presynaptic junctions from ASH (White et al., 1986). AVA is highly presynaptic and postsynaptic to other command interneurons that dictate backward (AVE, AVD) and forward (AVB) movement, all of which have pre-synaptic inputs from ASH as well. While the ASH synapses

onto AVA have been demonstrated to be excitatory glutamatergic connections (de Bono and Maricq, 2005), it is presumed that the ASH synapses onto AVB are inhibitory. In all, command neurons comprise about 50% of ASH synaptic output, and coordinate a balance of backward and forward locomotion through gap junctions and synapses onto motor neurons (White et al., 1986). AVA has gap junctions and chemical synapses onto both backward (VA/DA) and forward (VB/DB) motor neurons, with a bias toward backward motor neurons. AVB, the forward command interneuron, inverts this pattern with predominant gap junctions to forward motor neurons. ASH activation results in backward motor neuron activation through AVA to elicit a reversal away from the stimulus (de Bono and Maricq, 2005). Wild type worms, upon acute encounter of high osmolarity stimuli, will begin to reverse in less than 1 second (Hilliard et al, 2004). This “direct” circuit motif of a sensory neuron activating motor neurons via one interneuron is reminiscent of the “reflexive” circuit mediated by the mammalian pseudounipolar dorsal root ganglia (DRG) neurons in the spinal cord (Basbaum and Julius, 2009).

Like the mammalian pain and nociception circuit, however, ASH also projects to and receives input from other neurons that can modulate nociceptive behavior (Hilliard et al., 2005; Hilliard et al., 2002; Sambongi et al., 1999). This allows 1) ASH to integrate attractive cues with nociceptive cues, 2) ASH to cooperate with neurons that promote non-avoidance behaviors, and 3) ASH to summate nociceptive inputs with other nociceptive neurons to enhance avoidance behavior.

1. ASH can compete with other neurons to promote avoidance behavior.

ASH-sensed stimuli are often also sensed by other neurons, especially neurons that promote the attractive properties of the stimulus. In a situation where ASH promotes stimulus avoidance and another neuron promotes stimulus attraction, the competition between the two neurons determines the direction of movement. For example, ASEL and ASH compete at high pH stimuli to attract and repel animals from the stimulus, respectively. Mutations that double the number of ASEL neurons or eliminate ASEL showed that the higher the “dosage” of ASEL activity in the worm, the more attracted the worm is to high pH, though ASH will dominate with repulsion when the pH is very high. This study shows that ASH responses, especially weak signals, can be competitive with cues from other neurons (Murayama and Maruyama, 2013).

2. ASH can cooperate with other neurons in non avoidance behavior.

ASH participates in the "hub-and-spoke" RMG-centered circuit implicated in social versus solitary behavior of *npr-1* mutants (Macosko et al., 2009; de Bono et al., 2002). Wild-type N2 *C. elegans* strains expresses the high-activity allele of *npr-1* in RMG, which acts to inhibit this "hub" interneuron/motor neuron and promote solitary behavior. The low-activity *npr-1(ad609lf)* allele does not inhibit RMG, promoting aggregation at borders of bacterial lawns. RMG is gap-junctioned to "spoke" sensory neurons that detect diverse attractive and aversive environmental cues such as attractive pheromones (ASK), aversive pheromones (ADL), environmental oxygen levels (URX), noxious cues (ASH and IL2), light (IL2), and volatile odorants (AWB, ASH). Eliminating "spoke" inputs from ASH and ADL (through cell ablation or loss of *osm-9*, *ocr-2*, *odr-4* or *odr-8* genes) in the *npr-1* social background results in loss of aggregation behavior, suggesting that ASH and ADL induce aggregation through their detection of aversive cues (de Bono et al., 2002). The effect of ASH on this behavior requires the intact RMG hub. ASH's role in *npr-1* induced aggregation behavior shows that it does not simply trigger a "labeled-line" between aversive cues and acute reversal behavior, but instead provides input into modulatable behaviors as well.

3. ASH can cooperate with other neurons in avoidance behavior.

A small jab to the point of the nose leads to a reversal behavior that requires two neurons, ASH and FLP (Kaplan and Hovitz, 1993). Ablation of either results in partial defects, with a more severe observed if both are ablated. Both are known polymodal nociceptors. The FLP neurons, with highly-branched multidendritic arbors surrounding the head, can respond to harsh touch and heat applied to the animal's head, while only detecting gentle touch when it is applied directly to the animal's nose. However, FLP's many talents do not all derive from different signal transduction cascades within the neuron itself. While FLP's ability to sense harsh head touch is cell-autonomous, Chatzigeorgiou and colleagues (2011) showed that its ability to detect other modalities requires a gap-junctioned network involving other two other head neurons. While cell ablation of these two neurons had little effect on nose-touch behavior, OLQ and CEP, whose "spoke" responses must be additively relayed to FLP through the "hub" interneuron RIH, were ultimately responsible for FLP's role in nose touch behavior. The "spokes" of this circuit can laterally facilitate and non-linearly amplify FLP activation when they are active. Inactivation of either OLQ or CEP activity by genetic mutation that leaves silent cells results in an electrical shunt wherein the entire circuit becomes inhibited, while laser inactivation

of OLQ or CEP by cell destruction allows the remaining cells to function (Rabinowitch et al., 2013). This peripheral integration component of nose-touch sensation is then added to the cell-autonomous nose-touch detection by ASH neurons in downstream command interneurons to generate a full behavioral response.

Two different modalities, nose touch and harsh touch, are both sensed and distributed through all hub and spoke neurons. This leads to the question of whether the two modalities can be distinguished. Piggott et al. presented evidence showing that these different modalities can access different downstream circuits (2011). In this work, the downstream circuit of ASH concentrated on the connections between the interneurons AIB, RIM, and AVA (Figure 1.2). AIB and RIM have reciprocal synapses and gap junctions, RIM synapses onto and has gap junctions with AVA, and AIB synapses onto AVA (White et al., 1986). Using a combination of ablation and light-activation/inhibition techniques, nose touch was shown to stimulate reversals via a disinhibitory circuit parallel to the ASH direct stimulatory circuit. This model suggested that AVA –ASH activation activates AIB, which inhibits RIM through the glutamate-gated chloride channel *avr-14* to disinhibit backward locomotion. This motif is similar to the dopamine-dependent disinhibition motor circuit in mammalian basal ganglia, which runs parallel to the stimulatory mammalian DRG circuit for motor control (Piggott et al., 2011). In the same study, even though it is sensed through the same ASH sensory neuron, an osmotic stimulus activated RIM rather than inhibiting it while also directly activating the AVA backward command interneuron. Thus, different ASH stimuli can access different components of downstream circuits to effect motor outcomes, in direct and indirect ways, suggesting a differential distribution of initial sensory information throughout a circuit. A reassembled, integrated decision then directs forward or backward movement. This model can allow different modalities to be differently modulated, while also allowing a mechanism for preserving stimulus identity.

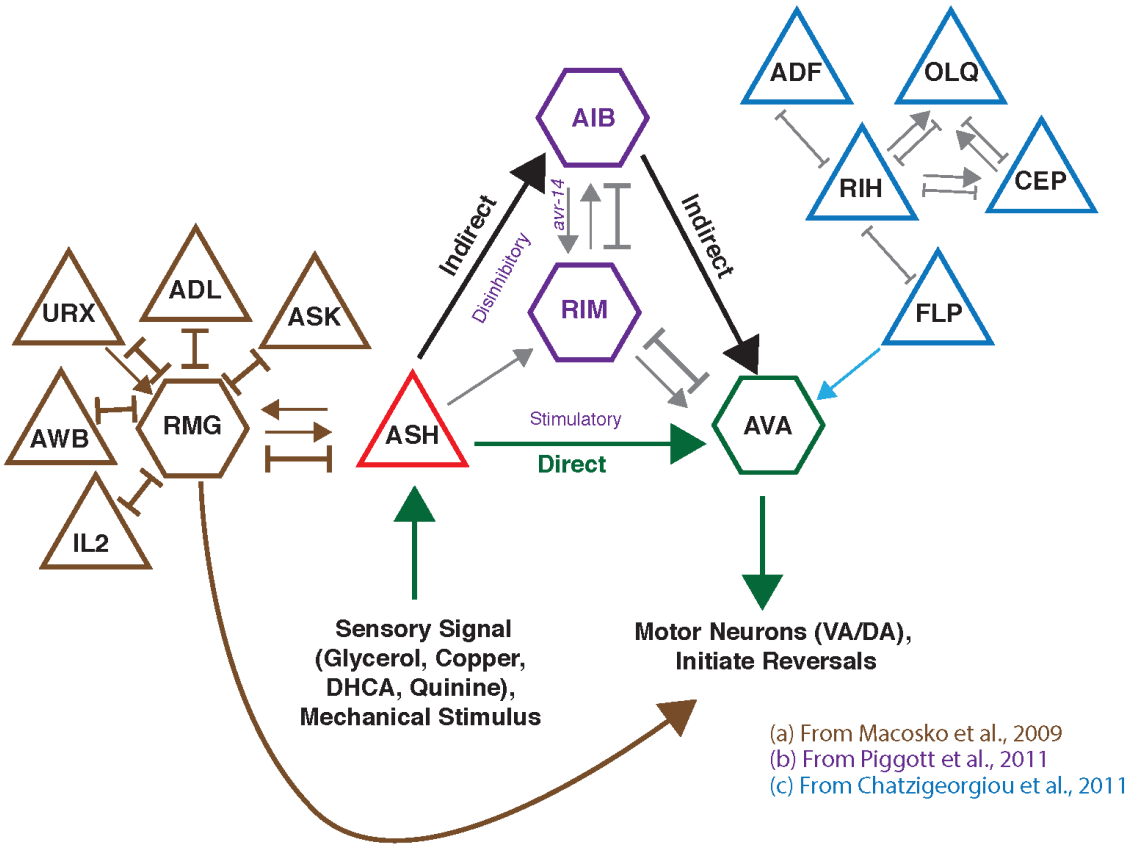

Figure 1.2. ASH participates in many nociception circuits.
a) ASH responses contribute to the non-avoidance social behaviors mediated by the RMG hub-and-spoke circuit described by Macosko et al., 2009 (brown). **b)** Piggott et al. showed in 2011 that ASH nose touch activates a disinhibitory circuit from AIB to RIM that is dependent on the inhibitory channel *avr-14* for behavior. ASH high osmolarity stimulation, on the other hand, directly activates the simulatory pathway from ASH to AVA (purple). This suggests that there are multiple pathways of instruction between ASH and command interneruons. **c)** ASH can cooperate with other neurons in avoidance behavior. The nose-touch pathway uses a hub-and-spoke circuit (blue) through RIH to stimulate AVA, but ASH activation of AVA is concurrently required to generate the full avoidance response (Chatzigeorgiou et al., 2011).

Weaker nociceptive stimuli are modulated by external and internal cues, as shown by work conducted on 1-octanol avoidance. Termed the “smell on a stick” assay (Chao et al., 2004; Troemel et al., 1995), the forward-moving worm is presented with an eyelash or pipette tip that has been dipped into the test solution and the delay time to reversal is scored. This assay can be conducted on or off food, and with the presence of exogenous compounds on the agar plate, in order to assess the modulation of aversive responses by external cues. When crawling without food, *C. elegans* reverses to 100% octanol (3-5s) with a shorter latency than it reverses to 30% octanol (8-10s) (Chao et al., 2004; Wragg et al, 2007). These responses are largely ASH-specific, since abolishing ASH responses using signal transduction mutants (*osm-9*) or laser ablation results in significantly lengthened response latencies of (>16s) (Troemel et al.,

1995; Ezak et al., 2010). Intriguingly, if the worm is presented with the same stimuli in the presence of food, both 100% and 30% octanol elicit reversals within 3-5s (Troemel et al., 1995; Chao et al., 2004; Fukuto et al., 2004; Wragg et al., 2007). This result began a series of studies on the how food modulates the latency of the dilute octanol response time, concentrating specifically on neuromodulators that could mimic food or starvation.

Neurotransmitters and neuromodulators regulate response latencies to 30% octanol both by acting directly on ASH and by acting indirectly on other cells (Table 1.3 is in no way exhaustive). Serotonin, dopamine, tyramine, and octopamine have all been implicated in this role. To highlight some key modulation effects of octanol avoidance assays, exogenous serotonin (5-HT) mimics the presence of food (Chao et al., 2004; Wragg et al., 2007; Harris et al., 2009; Harris et al., 2011), calibrating all latencies down to 3-5s. Octopamine and tyramine, biogenic amines structurally similar to mammalian norepinephrine and epinephrine, counteract 5-HT by increasing response latencies across all conditions to 8-10s (Mills et al., 2012; Wragg et al., 2007; Hapiak et al., 2013; Harris et al., 2010). This modulation can be countered if the animal is “pre-adapted” to a biogenic amine for 6 hours prior to the assay, but the adaptation to each amine diverges along different pathways (Wragg et al., 2007). Pre-adaptation to tyramine increases sensitivity to the presence of all exogenous amines. Pre-adaptation to octopamine abolishes the octopamine antagonism of serotonin in a manner that suggests dependence on dopamine (DA) (Wragg et al., 2007; Ezak and Ferkey, 2010). Members of the G-protein pathway, including receptors (*octr-1*), Gα proteins (*gpa-11*), G-protein receptor kinases (*grk-2*), and regulators of G-protein signaling (*rgs-3*) regulate these avoidance responses, both within ASH and in other neurons that modulate ASH (Chao et al., 2004; Mills et al., 2012; Hapiak et al., 2013; Ezak et al., 2010; Ferkey et al., 2007; Fukuto et al., 2004). Neuropeptides secreted by ASH can be reduced by *egl-3* neuropeptide processing enzyme mutations; glutamate release by ASH can be reduced by *eat-4* vesicular glutamate transporter mutations; both *eat-4* and *egl-3* affect ASH response latency (Chao et al., 2004; Hart et al., 1999; Kass et al., 2001; Mellem et al., 2002). Maintenance of insulin levels and serotonin levels within the organism are also crucial for appropriate responses as demonstrated through chemical processing and receptor mutants (Harris et al., 2011; Harris et al., 2009). Thus, a delicate balance of multiple signals converges on the octanol avoidance behavior to modulate response latencies.

Table 1.3: Response time to 100% and 30% 1-octanol by diverse humeral, environmental, and genetic cascades (from Chao et al., 2004; Harris et al., 2011; Harris et al., 2010; Harris et al., 2009; Wragg et al., 2007; Fukuto et al., 2004, Mills et al., 2012; Hapiak et al., 2013; Ezak et al., 2010)

Octanol %	Food Status	Time to Reverse	Modulators	Modulated Time	Depends on	Modulated Time	Counteracted By	Modulated Time
100%	ON or OFF	3 - 5 s	Octopamine (+)	8 - 10 s	*ser-6* (ASI, ADL)			
					nlp-6, 7, 9 (ASI)			
	OFF				Octopamine preadaptation	3 - 5 s		
					nlp-3	>10 s		
			Tyramine (+)	8 - 10 s	*tyra-3* (ASI)			
					nlp-1, nlp-14, nlp-18 (ASI)			
	OFF				Tyramine preadaptation	3 - 5 s		
	ON		*grk-2 (ASH), rgs-3, egl-3, cat-2*	> 12 s				
			eat-4	> 10 s				
			glr-1	> 5 s				
30%	OFF	8 - 10 s	5-HT (+)	3 - 5 s	*gpa-11* (ASH, ADL)			
					gsa-1, egl-30 (ASH)			
					nlp-3 (ASH)			
					ser-5 (ASH)			
					ser-1 (NSM)			
					ins-1 (ADF, RIC, NSM)			
					Octopamine (+)	8 - 10 s	*gsa-1,egl-30* (ASH)	

							ser-6 (AWB, ASI, ADL, AWC, ASER)	
							nlp-6, 7, 9 (ASI)	
							Tyramine preadaptation	3 - 5 s
							Octopamine preadaptation	3 - 5 s
					Tyramine (+)	8 - 10 s	*nlp1, 14, 18* (ASI)	
							Tyramine preadaptation	3 - 5 s
							Octopamine preadaptation	5 - 8 s
			Dopamine (-)	3- 5 s	*dop-1, 2, 3, cat-2, dat-1*			

The web of signal transduction cascades and neurocircuit components maintaining avoidance behavior is astounding, but the results can be distilled down to a few trends. Since endogenous levels of these neurotransmitters and neuromodulators are known to vary by past experience and nutritional state, the basal level of "nociceptive tone" can easily be measured by responses to less aversive cues (such as 30% octanol) while highly aversive cues (such as 100% octanol) may not depend on the endogenous nociceptive tone. Interestingly, modulations of responses either lengthen the latency of a 3-5s response to 8-10s or vice versa, suggesting that there are two main "aversion states" mediated by ASH. Since many more factors impact the response time of dilute octanol compared to concentrated octanol, the shorter, 3-5s aversion state appears to be a more "deterministic" state for stronger aversion while the longer 8-10s aversion state appears to be more "modulated," integrating cues throughout the neurocircuit. The correlation of a longer time before reversal, sensation of weaker stimuli, and differences in modulation between stronger and weaker stimuli hint at a temporal dimension of nociception.

The temporal dimension of behavior in *C. elegans* nociception has been studied mainly to assess the strength of the stimulus at invoking behavior. Little progress has been made on how (or where) the neurocircuit encodes time. This is partly due to the resolution of initial assays that measured the sensitivity of *C. elegans* to aversive cues. Historically, nociception was measured in binary assays. First, the ability to escape a toxic "ring" of stimuli was shown to be

an assay for ASH dysfunction (Culotti and Russell, 1978). Those who could not sense the stimulus simply ran outside the ring while those who were repelled by the substance stayed in the ring. Next, the drop test, generated by Hilliard and colleagues, scored the percentage of worms in different mutant backgrounds that reversed to a presentation of soluble repellent (2002). In some drop test experiments, the time spend in reversals was counted (Hilliard et al., 2002). In parallel, the first temporally sensitive assay by Troemel and colleagues (the “smell on the stick” assay) counted the exposure time to different repellents that were required before worms began to reverse (1999).

Do *C. elegans* use a temporal dimension to encode and decode nociceptive, ASH-encoded stimuli? Do they use time to track the features of the stimulus such as identity and strength, or can they code for exposure time itself? Previous studies have implicated a role of timing in the sequence of motor responses, and have attempted to look for molecular substrates of timing. For example, in the monoamine modulation of touch responses, tyramine was shown to orchestrate a sequence of behaviors characterized by a reversal followed by an omega turn, characterized by a deep bend of the head towards its own tail. Tyramine released by RIM first activates the *lgc-55* fast-acting ion channel to coordinate reversals through AVB forward command neurons, then effects a slower response through the GPCR *ser-2* on the VD motor neurons to initiate neck muscle contraction and subsequent turning (Donnelly et al., 2013). Executing a sequence of behaviors involves temporal coordination, and suggests that time is an essential factor in executing proper escape and can be encoded via different molecular pathways or different neurons.

Another example of temporal tracking investigates how ongoing responses and acute responses are differentially encoded. Busch et al. showed that the oxygen-sensing neurons URX, AQR and PQR can code both tonic and phasic responses to an oxygen shift using intracellular calcium levels to encode environmental oxygen levels (2012). High oxygen levels result in baseline maintenance of high intracellular calcium levels associated with high neuropeptide release and increased turning behavior. The opposite was found with low environmental oxygen. Superimposed on these “tonic” responses to a high or low oxygen environment are transient “phasic” spikes in intracellular calcium, neuropeptide, and behavior that occur upon sudden shifts in oxygen levels. The slope of the phasic upshift in intracellular calcium levels of URX was shown to elicit reversals through the AVA backward command interneuron (Busch et al., 2012). Therefore, while the worm can tonically respond to ongoing environmental cues with neuropeptides, sudden changes in external cues result in a rise in

calcium, with an associated phasic slope increase that superimposes an acute behavioral response on top of tonic behavior.

In another example where timing may be important, the role of ASH in modulating solitary and social behavior through the RMG hub-and-spoke circuit motif suggests that there is a coincidence detection component in sensory integration. Temporally accurate information would therefore be necessary for such summation to occur. Similarly, the octanol avoidance assays, with their two reversal initiation timescales, suggests that a "timer" in the worm receives information through ASH to keep track of stimulus exposure so that longer exposures to less harmful stimuli will still elicit aversion.

C. elegans neurons' graded potentials and stereotyped anatomical circuits are the ideal system with which to investigate the temporal dimension of nociceptive sensation and behavior. Recent advances in microfluidic technology allow precise stimulation of *C. elegans* so that neural activity and behaviors, time-aligned to encounters and exits of stimulus, can be measured on timescales as precisely as <1s (Kato et al., 2014; Larsch et al., 2013; Albrecht and Bargmann, 2010). Rather than a binary behavior score of whether a worm reversed or not within a given time, and rather than having to count the time to begin or complete a reversal, we can now elucidate, in a whole population of worms, what percentage of the population is executing each behavior at a precise time after initial stimulus encounter or removal. Moreover, in addition to reversal states, we can also define forward states, pause states, and omega states of sharp curvature (Ramot et al., 2008; Albrecht and Bargmann, 2010). Our resolution of calcium imaging has significantly increased as well with the advent of sensitive, fast fluorescent indicators like GCaMP3 and GCaMP5, married to the temporally precise presentation and removal of soluble stimuli in microfluidic devices (Chronis et al., 2007; Kato et al., 2014; Larsch et al., 2013). Presentation and removal of stimuli at faster than 200ms has been shown, along with the ability to present "white-noise" stimuli at speeds faster than the fusion rate of neural activity, which can be used to extract the intrinsic temporal filters of *C. elegans* neurons (Kato et al., 2014). Neuron silencing has achieved improvement as well –the creation of histamine-gated chloride channels allows hyperpolarization of specific neurons during behavior or imaging experiments without the confounding factor of developmental rewiring in laser ablation or genetic mutations (Pokala et al., 2014). This toolbox allows us to investigate the temporal dimension of *C. elegans* neurocircuits and ask how dynamic information from the sensory neuron is propagated and translated into behavior.

Perspective:

Extensive temporal analysis in neuroscience has concentrated on sensory neuron dynamics, interneuron dynamics, and behavioral dynamics. Very few studies, however, have tracked how different activation dynamics from the same sensory neuron differently engages interneuron types to generate behavior. In my thesis, I have specifically looked at the parsing and propagation of temporal information from sensory neuron to behavior. I investigated which aspects of ASH calcium dynamics were salient for different interneurons, and how intermediate-level interneurons help activate a command interneuron in a feed forward excitatory circuit. Specifically, I found that the intermediate interneuron AIB is a time-dependent accumulator of the ASH signals and is required for behavioral responses to slowly ramping ASH signals.

Thesis overview:

In Chapter 2, I investigate the encoding of stimuli in *C. elegans* sensory neurons. Focusing on the multimodal nociceptor ASH, I first show the complexity of ASH responses to long pulse and white-noise sequences of stimulation. Second, I show how non-nociceptive neurons can respond to ASH stimuli even though there has been no previous behavior defects ascribed to the selective loss of these neurons. Third, using ectopically expressed pheromone receptors, I show that ASH can generate calcium responses on different timescales to the same stimulus.

In Chapter 3, I use the ectopic ASH pheromone activation system to show the faithful transformations of sensory neuron calcium time course to the time course of avoidance behavior probabilities. Using selective hyperpolarization of interneurons, I then show how a simple circuit allows both deterministic and modulatable nociceptive behaviors.

Chapter 4 will suggest further experiments and analysis.

CHAPTER 2: *C. elegans* nociceptive neurons exhibit stimulus-specific activation dynamics to aversive stimuli

Summary

To understand how sensory neuron dynamics can instruct downstream circuits to generate behavior, neuron-specific temporal control of calcium dynamics in the sensory neuron must be achieved. Here, I characterize the calcium response dynamics of the polymodal nociceptor ASH to natural aversive stimuli. In addition to conventional long pulse presentations, I used a systems identification approach to quantify the rapid temporal component of ASH calcium responses. By presenting stimuli in a rapidly fluctuating "white noise" sequence, I derived linear temporal filters that describe ASH's ability to encode the history of encounter for each stimulus. ASH responses to naturally aversive stimuli differed by stimuli; glycerol and NaCl stimuli generated linear, history-dependent signals, but copper did not. Mutants in the ASH sensory G-protein cascade largely eliminated the neuron's ability to encode the history of encounter, while a voltage-gated calcium channel mutant altered the linear filter by eliminating the component for adaptation. I discovered that several additional classes of sensory neurons robustly generated calcium responses to classical ASH stimuli, despite previous reports showing their ablation had no behavioral consequence on stimulus avoidance. This discovery makes it difficult to attribute behavioral responses to ASH dynamics alone. To exert external control over ASH dynamics, I expressed the ascaroside C3 receptors SRG-34 and SRG-36 specifically in ASH. ASH:*srg-34* mediated fast peaking, fast adapting calcium signals, while ASH:*srg-36* mediated slow ramping, slow-adapting calcium signals in long pulse presentations. The linear temporal filter derived for ASH:*srg-36* calcium signals show an accumulation of stimulus history on the same scale as the linear temporal filters derived from glycerol and NaCl stimuli, while the linear temporal filter derived for ASH:*srg-34* calcium signals show a fast impulse response with little accumulation of stimulus history.

Introduction

The time course of sensory neuron activation can greatly affect behavioral outcomes. However, the mechanisms enabling this temporal dimension of neural processing have not been as well elucidated as those for primary signal detection. The complexity of neural activation to natural stimuli increases the challenges of dissecting temporal coding. In polymodal mammalian nociceptors, for example, single neuron fibers can respond to multiple stimulus modalities, and

multiple neuron fiber types can respond to the same stimulus modality. In a natural world where multiple stimuli are simultaneously present, the extraction of information after stimulus encoding occurs in multiple anatomic paths that interact in complex ways. Thus, how stimulus dynamics influence subsequent behavior may most easily be examined in a simple circuit. The *C. elegans* sensory neuron ASH is a polymodal nociceptor that directs avoidance through multiple intermediate interneurons. All the anatomical synapses in these circuits have been identified (White et al., 1986), making this system an ideal setting to investigate the temporal dimension of a neural circuit.

In order to study how sensory neuron dynamics are translated into behavior, two requirements should be met. First, to generate a clean signal from a single neuron, it must be possible to control the activation dynamics of that neuron cell-specifically. In *C. elegans*, genetic control of a defined neuron can be achieved with cell-selective transgenesis, providing an approach to influence activation dynamics. Second, the measurement of both the activation dynamics of the neuron and the respective behavior output must be at a resolution that is sensitive to the diversity of responses. In *C. elegans*, we have achieved the latter through microfluidic stimulus delivery systems that can deliver laminar, square-wave stimulus pulses of <200 ms (Chronis et al., 2007; Kato et al., 2014). This timescale compares favorably to the t_{on} and t_{off} of the GCaMP3 genetically-encoded fluorescent calcium indicator that is typically used for neuronal recording, suggesting that stimulus delivery will not limit accuracy (Hires et al., 2008; Tian et al., 2009). At the behavioral level, automatic tracking of animals in microfluidic environments allows stimulus-aligned histograms of behavior from 25 worms to be simultaneously resolved at 500 ms (Albrecht et al., 2011) and behaviors and calcium transients of individual animals to be simultaneously resolved at 100 ms (Larsch et al., 2013).

Reliable and tunable control of ASH activation proved a challenging, but soluble problem. In this chapter, I first describe the diversity of ASH calcium responses to natural, endogenously-sensed, stimuli. I show that mutations in specific molecules along known ASH signaling pathways reveal intrinsic temporal dynamics that are different from wild-type responses. I show that ASH calcium responses to different stimuli are similarly distinct, some showing different temporal dynamics on to different timescales of stimulation. I show that these ASH stimuli also activate other *C. elegans* sensory neurons in various combinations, making it difficult to map behaviors from natural stimuli specifically to ASH. I address these issues by ectopically expressing two chemoreceptors in ASH, *srg-34* and *srg-36*. Both of these receptors detect the ascaroside pheromone C3, but they respond with different dynamics. Because they

are expressed in the same neurons in a common genetic background, differences in behavioral responses to C3 in these transgenic animals can be directly ascribed to their signaling properties in a single neuron type. I show that these ectopic receptors signal through the known signal-transduction genes expressed in ASH to generate dynamically distinct calcium transients. The ectopic, cell-specific expression of *srg-34* and *srg-36* provides a tool to track the temporal dimension of neural signaling in *C. elegans* nociception.

ASH responds to aversive compounds with stimulus-specific calcium dynamics

ASH detects aversive mechanical and chemical stimuli including nose-touch, high-osmolarity solutions, detergents, bitter compounds like quinine, and heavy metals like copper (Hilliard et al., 2004). Previous qualitative calcium imaging experiments showed an intracellular calcium increase in ASH when the worm's nose comes in contact with these stimuli (Hilliard et al., 2005). Higher temporal-resolution imaging using laminar flow in a microfluidic chip revealed a calcium increase to the removal as well as the onset of high-osmolarity glycerol stimuli (Chronis et al., 2007).

To begin assessing the dynamic range of ASH for natural stimuli, I first evaluated the time-course of ASH calcium responses to different concentrations of glycerol. 10-second pulses of 1M glycerol with a 10-second inter-stimulus interval induced an immediate increase in ASH GCaMP3 fluorescence (ON response) that decreased in peak magnitude and slope to later pulses (Figure 2.1.a). A smaller, transient increase in fluorescence occurred upon removal of stimulus (OFF response, Figure 2.1.a). Reliable ON responses were observed at glycerol concentrations from 125 mM to 4 M above the 290 mM osmolarity of the baseline S basal solution, and OFF responses were observed from 250 mM to 4 M added glycerol (Figure 2.2, a-c). The ON response peaked at 1-2 M glycerol and then fell, while the OFF response continued to increase in magnitude to 4M glycerol, the highest concentration that could be delivered to the animals (Figure 2.1.c,d.).

a.

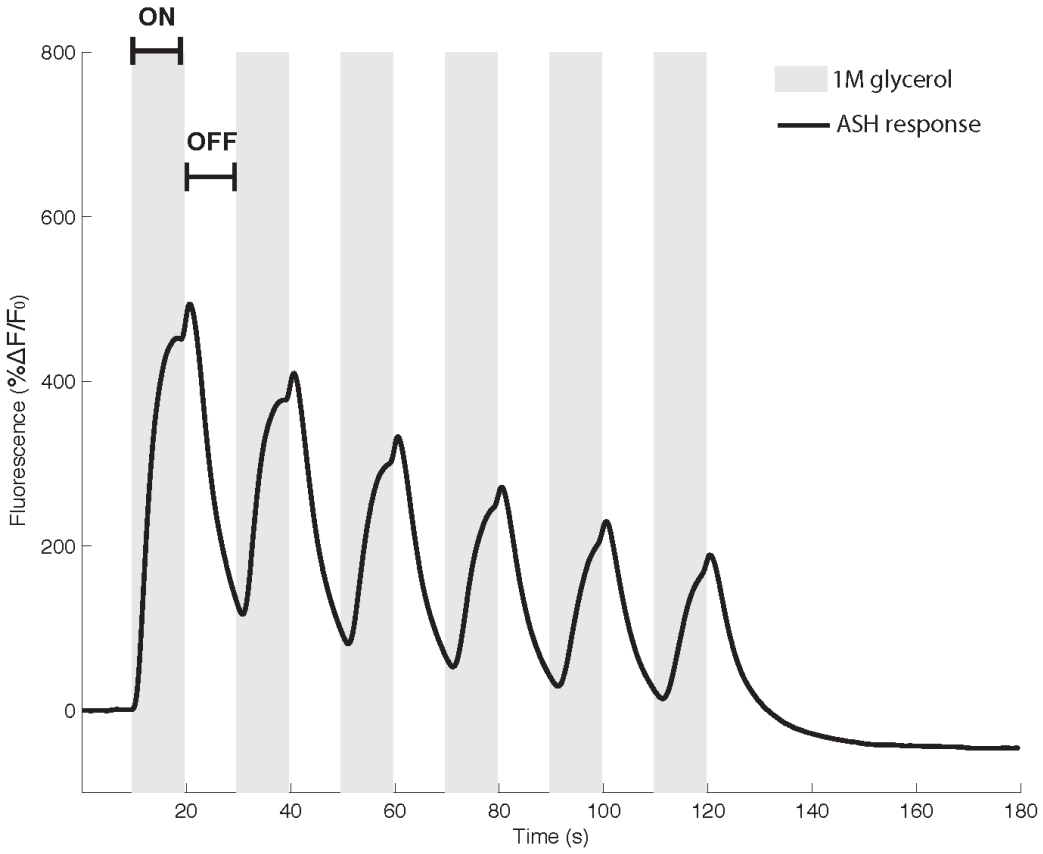

Figure 2.1. ASH responds to 10 s pulses of glycerol with complex calcium dynamics
a) Measured GCaMP3 fluorescence change (%$\Delta F/F_0$) in ASH cell body to 6 repeats of 10 s pulses ON and OFF pulses of 1 M glycerol (mean trace in black line, n=71; gray bars indicate stimulus presence).

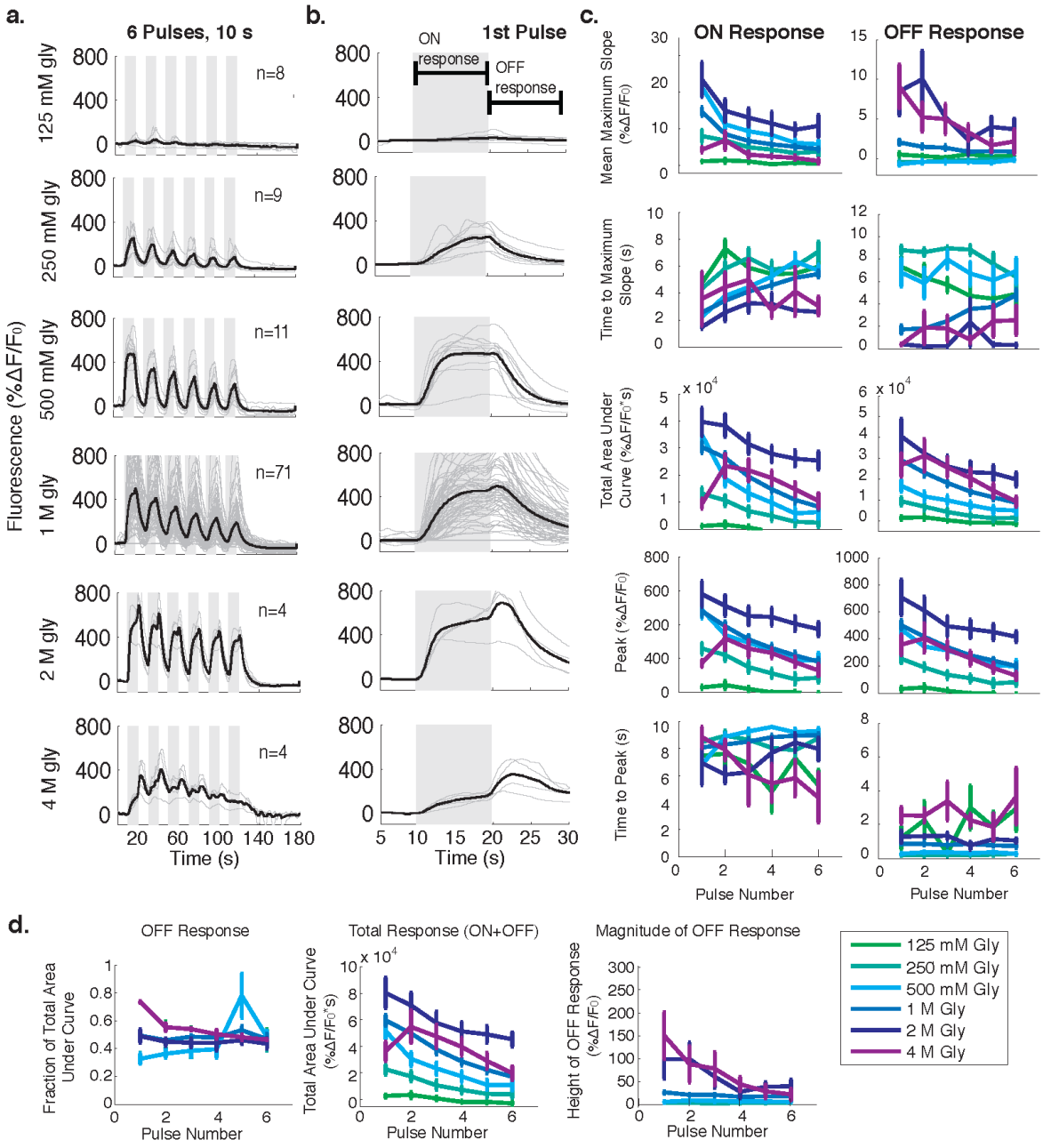

Figure 2.2. ASH responds to 10 s pulses of glycerol across a range of concentrations
a) Measured GCaMP3 fluorescence change (%ΔF/F0) in ASH cell body to 6 consecutive 10 s pulses of 125 mM to 4 M glycerol. **b)** Calcium response to first and last 10 s stimulations at shorter timescales. **c)** Maximum slope, time to maximum slope, integrated calcium response (by total area under curve), peak, and time to peak for each of six consecutive 10 sec pulses for each glycerol concentration. Center at mean, vertical bars = standard error of the mean. **d)** Percentage of response accounted for by OFF portions as the fraction of total area under the response curve. OFF responses increase in relative magnitude with increasing concentration.

Establishing a systems identification method to quantify the ASH temporal response

In order to assess the temporal response properties of ASH in more detail, I next asked whether ASH had reliable calcium responses to rapidly fluctuating stimuli. Measuring fluorescence dye changes in the stimulus channel of the microfluidic imaging chip, I showed that laminar flow of stimuli across the worm's nose can be accurately switched within 50 msec (Figure 2.3.a). GCaMP3 has rapid dynamics (344 ms $t_{1/2}$ decay time), making it a useable measure of subsecond calcium dynamics in the ASH neuron (Sun et al., 2013). Using a microfluidic chip, I characterized ASH calcium responses to 1 s flickers of 1M glycerol. Both 1 s flickers of 1M glycerol (Figure 2.3.d) and a single long pulse of 500 mM glycerol (Figure 2.3.c) resulted in a large transient rise in fluorescence (Figure 2.3.d, inset). Even after the large transient rise in calcium had stabilized, 1s flickers of 1M glycerol stimulus continued to direct regular calcium oscillations at 0.5 Hz in ASH, delayed by a >180° phase shift relative to each stimulus (Figure 2.2.a, inset). I found that while ASH exhibited an inflection change to each individual flicker presented at both 500 ms and 1 s intervals, it exhibited a steady, nearly uninterrupted fluorescence rise when presented with stimuli switched at 200 ms intervals (not shown). This suggests that ASH treats stimuli presented as fast as 500 ms as individual, separate stimuli, but either the neuron or GCaMP was close to its limit for tracking the stimulus at faster intervals, and could only respond as if being given a single long presentation.

While system identification is widely used in electrophysiological studies to capture quantitative insights, it has not been widely used to quantify neuronal calcium responses since calcium was considered a slow readout of neural responses (Clark et al., 2011). However, calcium dynamics are a good proxy for neural dynamics in *C. elegans* since, lacking sodium-based action potentials, their neurons have graded responses and use voltage-gated calcium channels to amplify neuronal inputs and regulate neurotransmitter release (Goodman et al., 1998; Liu et al., 2009). Thus, to precisely quantify the ASH temporal calcium response to a spectrally unbiased stimulus pattern, we employed a system identification approach. Full or zero concentration of stimulus was presented to ASH according to a pseudorandom m-sequence with a minimum pulse length of 200 ms and characterized by a 9 bit word length (Figure 2.3b). Two repeats of the same sequence were presented per trial, recorded at a frame rate of 50 Hz. As with faster flicker stimulus presentations, ASH still responded to the m-sequence stimuli with calcium fluctuations after the large initial transient had reached a steady-state (Figure 2.3.e). The overall shape of the response was stereotyped both within and across individuals (Figure

2.3.f), suggesting that a consistent temporal response is generated in ASH by exposure to 1M glycerol.

The calcium response of the neuron was aligned to stimulus concentrations using dye added to the stimulus stream, as ASH responses to 1M glycerol with and without dye in the stimulus stream were not found to be significantly different. Steady-state responses from the second repeat of the m-sequence were used to derive an input-output transformation between stimulus and neural response. The transformation required two sequential operations: first, the stimulus was passed through a linear filter that describes how the recent history of the stimulus contributes to the current value of an intermediate variable x at time t; second, a static non-linearity converts the x(t) from the first operation into an estimate of the measured fluorescence change (Figure 2.3.g; Appendix figure 2.1.a.). This analysis derived a positive-polarity, trial-averaged linear filter for ASH that peaks at 3.4 s and decays with a $t_{1/2}$ of 4.3 s (n=13, t_{peak}= 2.9-3.6 s, $t_{1/2}$ = 2.8-6.1 s) (Figure 2.3.h). Modeling this linear filter mathematically using a series of ordinary differential equations (ODE) showed that the filter was in fact biphasic, and switches to a negative-polarity response after a lag of 15 s (Appendix Figure 2.1.b-d., Figure 2.3.j-k). Deconstructing the biphasic filter into its separate positive and negative polarity components reveals two timescales of linear processing, a “fast” positive component responsible for the majority of the response and a “slow” negative component that caused adaptation over many seconds of stimulus presentation (Figure 2.3.k). Further analysis showed that the static nonlinearity was nearly identical to the nonlinearity of GCaMP3 with respect to calcium, suggesting that the ASH temporal response captured by the model is linear (Appendix Figure 2.1.f..; Kato et al., 2014). Consistent with the highly stereotyped shape observed in calcium responses in response to this 9-bit, 200 ms m-sequence of 1M glycerol, the response predicted by the trial-averaged linear filter could account for a high percentage of the variance (VAF of 64-84%) of each individual trial (Figure 2.3.m.,l.). Further, this linear filter was not specific to this particular m-sequence order since the same filter was derived from a second m-sequence using a different detailed structure (Figure 2.3.i.). Each of these two derived linear filters from the different m-sequence structures was able to predict the response for calcium responses generated by the other (Figure 2.3.1). These derived linear filters also predicted significant aspects of the 1 s flicker response (Figure 2.3.n.,o.). Further, the derived linear filter using fluorescence changes in the ASH axon was similar to that of the cell body, indicating that neurotransmitter release likely occurs on this same timescale (Figure 2.3.p.,q.). Therefore, ASH

exhibits a robust temporal filter to rapid fluctuations of 1M glycerol stimulus, showing that a history of encounter to this stimulus is salient to the neuron.

Figure 2.3. Using rapidly fluctuating stimuli to quantify the ASH temporal response (continued).
e) ASH response to a pseudorandom on/off pattern of 1 M glycerol (black: ASH response measured as ΔF/F0, red: presence of 1 M glycerol). Two repetitions of an m-sequence pulse of pulse length 200 ms, 9-bit sequence. Bracket indicate second repetition, shown for additional neurons in **f)**. ASH responses were reproducible within the same worm in sequential trials and across different worms (black traces): the first 100s included a strong calcium component that had adapted by the second half of the trial, though rapid fluctuations in calcium signals continue to be observed. The response to the second repeat (bracket) was used to generate an linear-nonlinear (LN) model of the ASH response (g-j). **g)** Schematic of the L-N model. $\kappa(\tau)$ describes a linear filter as a function of lag τ, and F(x) is an instantaneous function of the output from the linear filter. **h)** The inferred linear filter of ASH from individual input-output records (gray) and from trial-averaged input-output records (black). **i)** Response to two 9-bit, 200 ms m-sequences (sequence 1 and sequence 2) with different detailed structures were identical, with peaks at 3.4 s and decaying with a t1/2 of 4.3 s. **j)** Phenomenological filters for AWC and ASH neurons were modeled as a sum of three exponential functions generated by a system of three first-order linear ordinary differential equations (Appendix Figure 2.1). The model consists of input to an initial process A, that resproduces the response rise time, splitting into two parallel paths of opposite sign with fast and slow dynamics (F and S). The resulting biphasic sensory filter given by this model (black) closely matched the trial-averaged filters extracted from the data (gray). **k)** The A to F and A to S components decomposed from the ODE model filter from (j) shows the fast, positive polarity component (that accounts for most of the rapidly fluctuating signals) and the slow, negative polarity component (that accounts for the decreasing mean amplitude of the response over time) as separate processes. **l)** Performance (%VAF, percent variance accounted for) of simulated individual trial responses using from left to right: (1) full-parameter L-N models estimated from individual trials, (2) L-N model estimated from mean trial-averaged records, (3) ODE filter L-N model estimated from individual trials, and (4) ODE fitler L-N model estimated from mean trial-averaged records. Cross-validated (cross-val) performance of simulating individual trials responses from held-out data sets using ODE fitler are seen in bars 5-8 with (5) L-N model estimated from mean trial-averaged records, (6) trial-averaged L-N model applied to a cross validation set, (7) mean trial-averaged L-N model applied to a hold-out dataset driven by a second m-sequence stimulus, and (8) mean trial-averaged L-N model estimated from the second m-sequence set tested on trials of the first m-sequence. Bars = average performance, n=7 for cross-validation sets. **m)** Model responses generated by the LN model from trial-averaged input-output records (blue) or the ODE filter model (red) to the same m-sequence stimulus accounts for a high percentage of variance (VAF) of the actual measured response (black). **n)** Model responses generated by the LN-ODE model (green) to 1 s flickering stimuli (red) also capture a significant amount of measured calcium dynamics to 1 s flickers of 1 M glycerol (black) with detail of alignment in **o)**. **p)** Linear filters from M-sequences generated from the axonal GCaMP measurements (black) in ASH (with schematic of *C. elegans* neuron anatomy inset) are on similar timescales to linear filters generated by cell body responses (red) with enlargement of first 6 s in **(q)**.

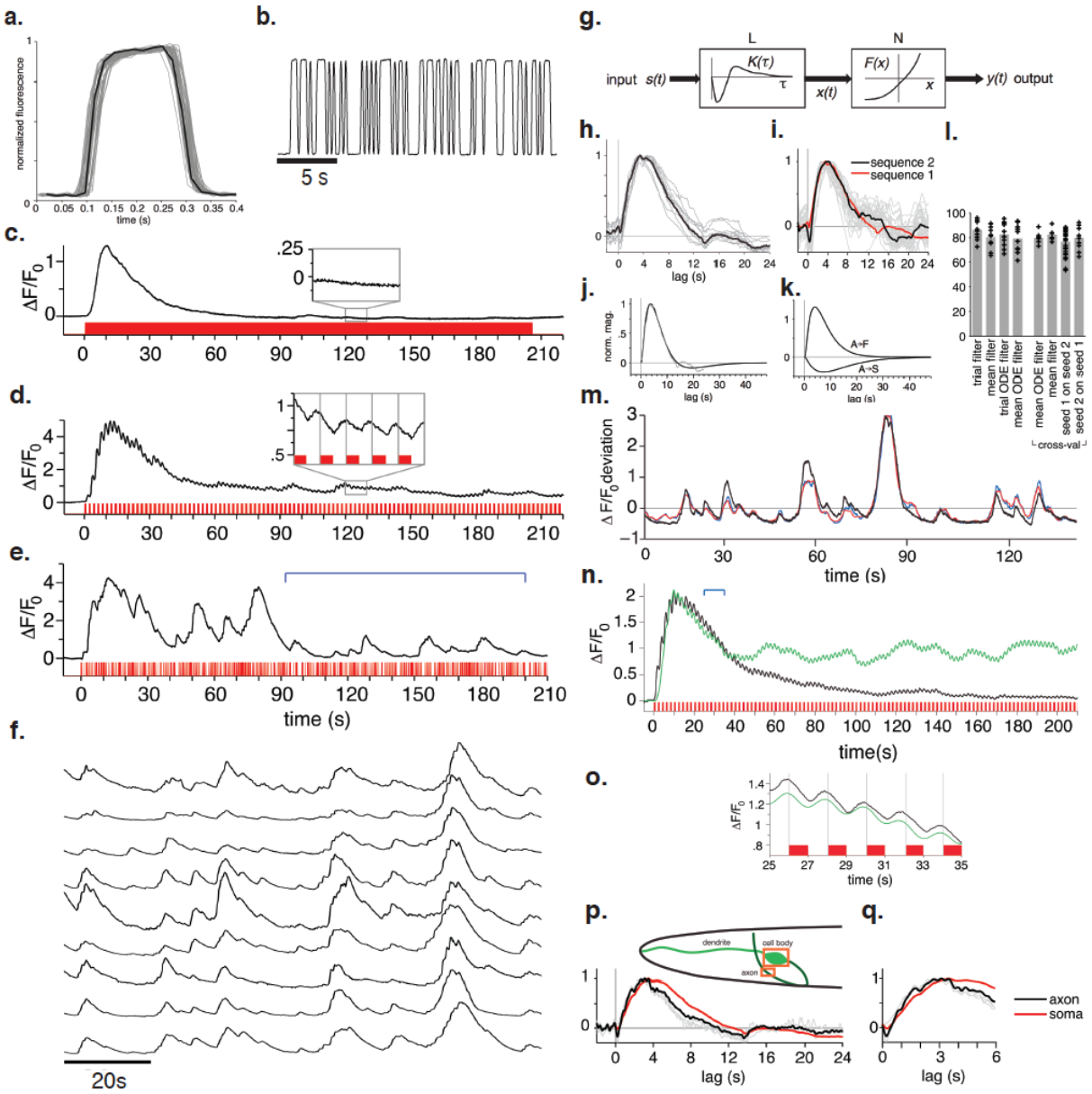

Figure 2.3. Using rapidly fluctuating stimuli to quantify the ASH temporal response.
a) Precise control of stimulus delivery by switching between two laminar flow streams in a microfluidic chip allowed completion of off-on and on-off transitions withint ~50 ms. Graph, superposition of 50 consecutive time segments of normalized dye intensity for 200 ms on/off square wave stimulus pattern, recorded at a frame rate of 50 Hz. Individual segments are shown in grey and mean intensity in black. **b)** A 25 s example trace of a 9 bit word-length, 200 ms m-sequence of 1 M glycerol, measured by fluorescent dye in the stimulus channel of a microfluidic imaging chip. The animal senses either 0 or full concentration onsets, with observed laminar flow persisting throughout the experiment. **c)** Large transient rises in calcium are observed in ASH to both a long single pulse of 1 M glycerol and **d)** 1 s flickers of 1 M glycerol (black: calcium response in cell body of ASH; red: presence of 1 M glycerol stimulus). 1 s flickers of 1 M glycerol elicit regular calcium oscillations after the initial large transient had stabilized. Inset: magnified views of 10 s intervals after the response reached steady state, presence of stimulus in red. Gray vertical lines divide inset graphs into 2 s epochs aligned to stimulus transitions.

ASH temporally tracks specific stimulus concentrations

To test whether ASH temporally tracks glycerol across multiple concentrations, I presented 125 mM, 250 mM, 500 mM, 2 M, and 4 M steps of glycerol to ASH using the same 9-bit, 200 ms m-sequence (Figure 2.4). Robust linear filters were derived from ASH responses to 500 mM or 1 M glycerol concentrations, and 250 mM or 2 M glycerol concentrations resulted in similar but less reliable responses (Figure 2.4.b.). All robust linear filters positively integrated signals experienced in the past 10 s, placing most weight on signals experienced ~3 s in the past (shown by the peak of the linear filter).

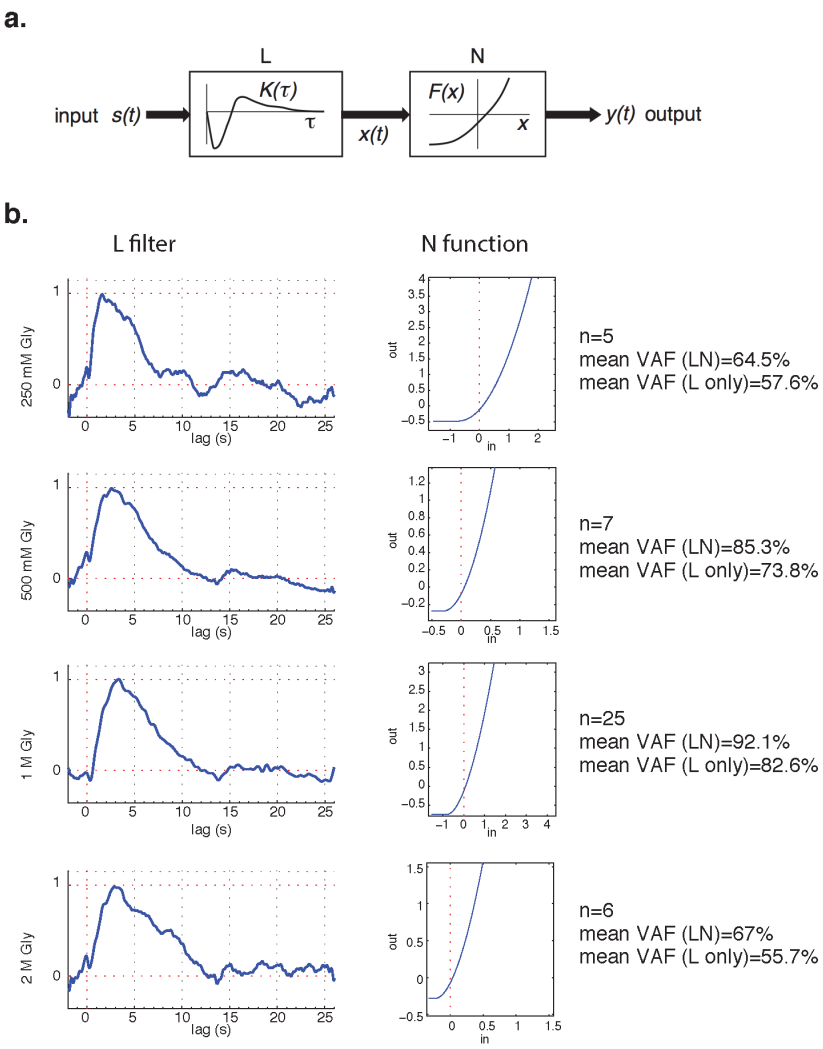

Figure 2.4. ASH temporally tracks specific concentrations of glycerol.
a) Schematic of the L-N model. **b)** Normalized linear (L) and nonlinear (N) filters derived by 9-bit, 200 ms m-sequences presentations of 250 mM, 500 mM, 1 M, and 2 M of glycerol with performance (% variance accounted for) of mean trial-averaged L-N models.

Stimulus-triggered correlations of ASH reveals nonlinear impulse OFF responses

The positive polarity of the linear filter does not fully explain the ASH calcium responses to 10 s pulses of 1 M glycerol, where a calcium increase was observed to both ON and OFF stimulus transitions. The asymmetry of the response to long glycerol pulses suggests that the OFF transient, if temporally linear, should contribute a negative polarity component to the beginning of the ASH filter. Since this was not observed, I reasoned that the 200 ms stimulus might interfere with this component, and used stimulus-triggered averaging (STA) on a slower, 2

s pulse length m-sequence to search for additional nonlinear dynamic responses to glycerol onset or offset. In this method, I separately aligned all measured calcium responses to the sequence of glycerol exposure by instantaneous “trigger” events of stimulus onset or offset, and averaged the subsequent population response in order to define separate ON and OFF temporal dynamics (Figure 2.5). Stimulus-triggered averaging using responses aligned to the onset of stimulus generated a filter similar to the linear filter from the L-N model, with a large increase in calcium that lasted around 10 s and peaked around 3 s. Stimulus-triggered averaging using responses aligned to the offset of stimulus revealed a biphasic response consisting of a transient increase of calcium followed by a large decrease in calcium. The large decrease in calcium was maximal at 3 s and lasted 10 s, indicating that it corresponds to the previously measured ASH filter. When inverted and superimposed, the ON and OFF stimulus-triggered ASH responses appear to be inverses of each other (symmetric), except for the initial 2 s transient of the OFF response (Figure 2.5). Control STAs done on 200 ms, 9-bit presentations of glycerol did not reveal this asymmetry between ON and OFF triggers (not shown). The impulse response of ASH to glycerol can therefore be divided into two parts of opposite polarities: a fast, nonlinear calcium increase to glycerol removal, which can be observed only by stimulus triggered averaging after long glycerol exposures, and a larger, linear calcium response to glycerol addition that is observed both in stimulus-triggered averages and in L-N analysis. Since the fast, nonlinear calcium increase to the removal of long glycerol pulses has a very small total area under the calcium curve compared to the slow, linear filter, it may be still be present during fast stimulus regimes, but masked by the slow linear filter.

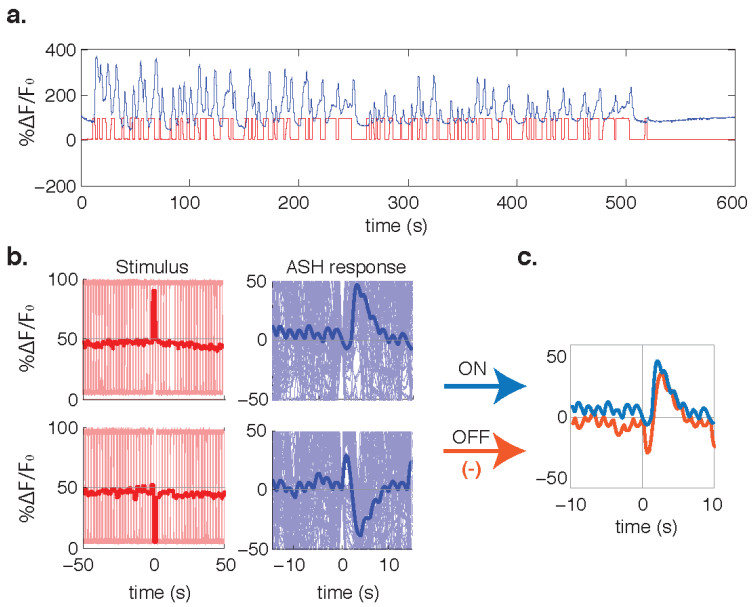

Figure 2.5. Stimulus triggered averages reveal nonlinear ASH impulse responses to longer stimulation with 1 M glycerol.
a) Representative ASH calcium response (%ΔF/F$_0$, in blue) with dye measuring presence of 1 M glycerol stimulus (red) given as a 7-bit, 2 s m-sequence. **b)** All ON (top) and OFF (bottom) events of stimulus presentation times are separately stacked, with t=0 as the point of switch. An average of responses centered at switch time t=0 were generated for fluorescent dye (stimulus proxy, in red) and GCaMP fluorescence (calcium proxy, in blue). **c)** When inverted and superimposed, stimulus-triggered averages of 2 s m-sequence reveals asymmetrical ON (blue) and OFF (orange) responses. The immediate OFF response is a feature seen for these and other long glycerol pulses, and is not captured by the linear temporal filter.

ASH responds to other aversive stimuli with heterogeneous dynamics

Since ASH has been shown to respond to diverse stimuli (Hilliard et al., 2005; Chatzigeorgiou et al., 2013; Aoki et al., 2011), I examined ASH calcium dynamics in response to 10 s pulses of 500 mM NaCl, 100 µM DHCA, 10 mM quinine, and 1-5 mM copper solutions (Figure 2.6.a. for NaCl, DHCA, quinine; Appendix Figure 2.5 and 2.6 for copper). Responses to 10 s pulse stimulation (measured as $\Delta F/F_0$) revealed a wide range of ASH response magnitudes and variable adaptation across stimulus pulses, as expressed in the peak height and initial slope of the 2nd through 6th pulse (Figure 2.6.b., Appendix Figure 2.5, 2.6.a.). Unlike high osmolar glycerol, high osmolar NaCl did not increase fluorescence to the removal of stimulus, indicating that the OFF response is not a signature of the all high osmolar modalities. DHCA and quinine elicited weak calcium signals that adapted quickly between stimuli (Figure 2.6). Copper elicited variable ASH responses to sequential pulses: while the first pulse was characterized with a positive calcium change to stimulus onset, the proportion of calcium change in response to stimulus onset and stimulus removal redistributed in subsequent copper pulses so that the

calcium response to the sixth pulse of copper was opposite in polarity to the calcium response to the first pulse of copper (Appendix Figure 2.5.a., Appendix Figure 2.6.a.).

White noise presentation of 9-bit, 200 ms m-sequences generated a linear filter for 500mM NaCl stimulus that is comparable to the glycerol filter in peak time and length, suggesting that ASH processes these two stimuli on similar timescales in rapidly fluctuating presentations, despite divergent features in longer pulses shown above (Figure 2.7.a., top panel). In other words, the temporal histories of both stimuli are similarly summed by ASH. When the presentation regime was slowed down to 2s (7-bit), a robust impulse response of negative polarity was seen in the linear filter analysis of the1 mM copper response sequence that peaked faster than the pulse length of the presentation, suggesting that while ASH can generate robust responses to copper, the neuron may not be summing the temporal history of this stimulus encounter (Figure 2.7.a., bottom panel). The copper linear filter more closely matches the ASH calcium response to the sixth 10 s copper pulse than the ASH calcium response to the first 10 s copper pulse (Appendix Figure 2.5.a., Appendix Figure 2.6.a.; see discussion for consequences of this result on the LN model). While DHCA and quinine were able to generate robust responses to 10 s pulse stimuli, no robust linear filter could be derived from ASH calcium responses from fast or slow white noise presentations of these stimuli even though some calcium changes were observed (not shown). This suggests that these substances may stimulate ASH in a less predictable, nonlinear manner. Thus, ASH is capable of different regimes of robust and non-robust responses, with a positive linear temporal filter that summates the history of encountering glycerol and NaCl stimuli, a negative linear filter that provides an instantaneous snapshot to copper encounter with little regard for stimulus history, and unpredictable nonlinear responses to DHCA and quinine.

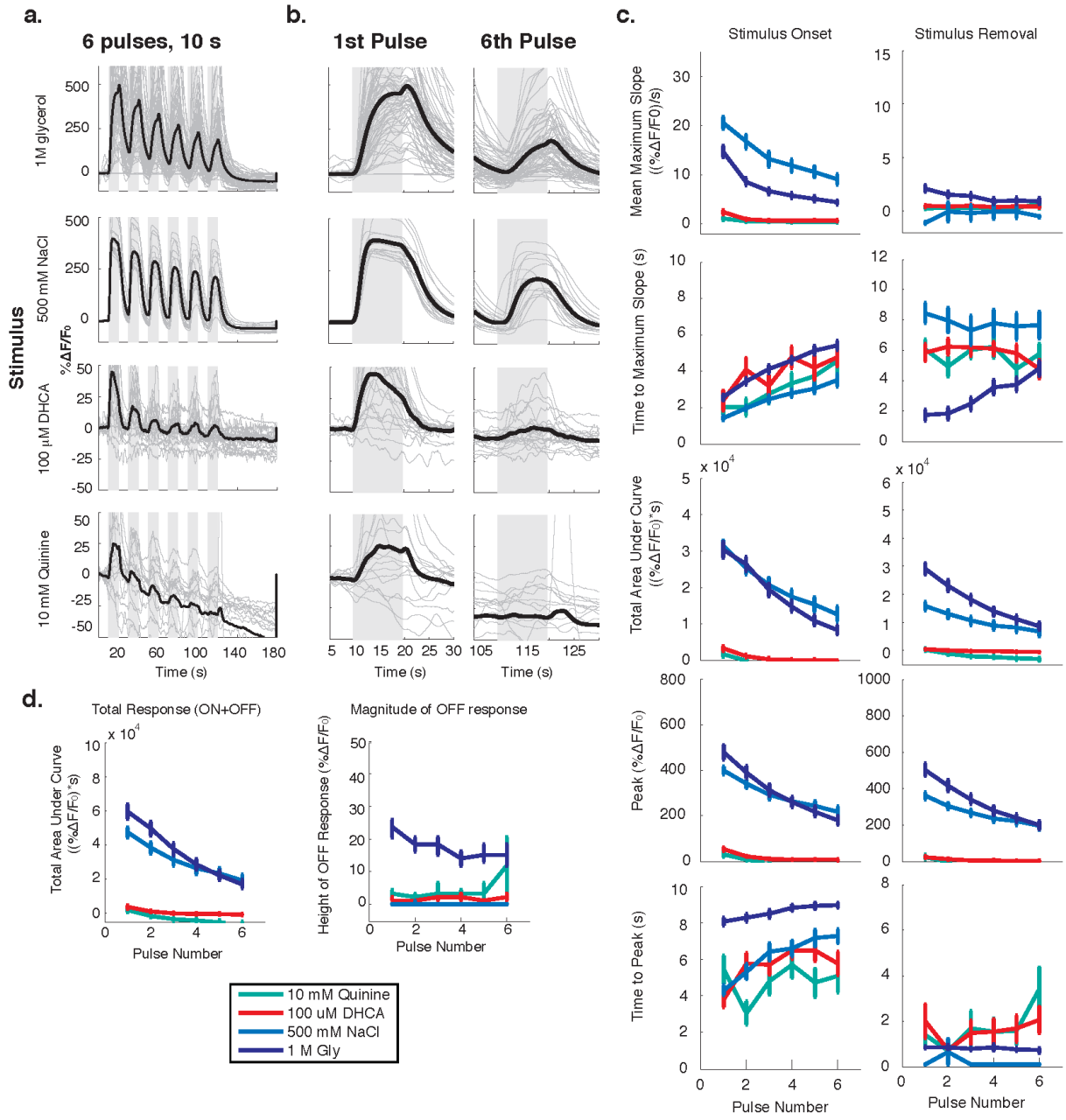

Figure 2.6. Heterogeneous ASH dynamics to other aversive stimuli

a) Measured GCaMP3 fluorescence change (mean trace in black, individual traces in light gray, %ΔF/F0) in ASH cell body to 6 repeats of 10 s ON and OFF pulses of 1M glycerol (n=71), 500 mM NaCl (n=17), 100 µM DHCA (n=21), and 10 mM quinine (n=16) (stimulus presence indicated by gray bars). **b)** Calcium response to first and last 10 s stimulations at expanded timescales. **c)** Maximum slope, time to maximum slope, integrated calcium response (by total area under curve), peak, and time to peak quantified for each of six consecutive 10 sec pulses for each glycerol concentration. Vertical bars = standard error of the mean. **d)** Heterogeneous total response (total integrated area under the calcium curve) and heterogeneous magnitude of the OFF response are observed in ASH to different aversive stimuli.

a.

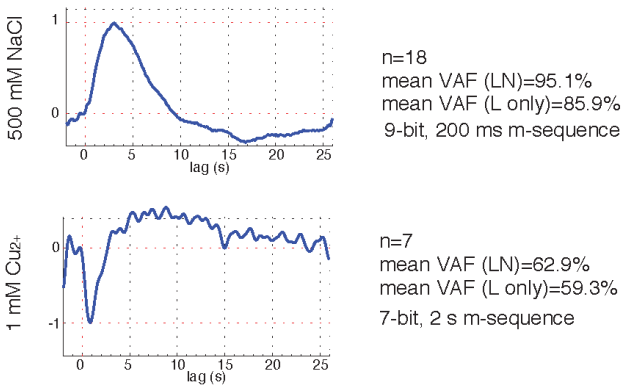

Figure 2.7. Linear-Nonlinear (L-N) models of ASH calcium responses to different aversive stimuli show different linear temporal filters in ASH.
a) ASH responses to 500 mM NaCl stimulation with a 9-bit word length, 200 ms m-sequence and ASH responses to 1 mM Cu2+ stimulation with 7-bit word length, 2 s m-sequence can be modeled with a robust linear filters using the LN model.

Signal transduction mutations in ASH can alter or eliminate the fast response to glycerol

To define the molecular basis of ASH calcium dynamics, I tested known ASH signal transduction mutants (Figure 2.8.a) to 10 s pulses (Figure 2.9.a, Figure 2.9.b) or m-sequences (Figure 2.10) of 1M glycerol. OSM-9 and OCR-2 are *C. elegans* channel proteins of the TRPV family, and the combination of these two channels is required for all known ASH responses (Colbert et al., 1997; Tobin et al., 2002; Kahn-Kirby et al., 2004; Hilliard et al., 2005). Indeed, *osm-9 ocr-2* double mutants were unable to generate responses to either long pulses or m-sequences of glycerol (Figure 2.9.a for long pulses, m-sequence not shown). The G_{α} subunit ODR-3 is required for normal ASH activation by 1M glycerol and other repellents (Hilliard et al., 2005). I observed a small residual response to glycerol pulses in *odr-3* mutants that was opposite in sign to the normal response –fluorescence increased, rather than decreased, upon glycerol addition (Figure 2.9.a.b). Stimulus offset was followed by a small response of opposite sign that was slower than the normal off response. Double mutants that lacked the two G_{α} proteins GPA-3 and ODR-3 lacked all responses to glycerol, but *gpa-3* single mutants had wild-type responses (Figure 2.9.a.b), suggesting that *gpa-3* normally plays only a small role in glycerol detection. These results implicate *osm-9*, *ocr-2*, *odr-3*, and to a lesser extent *gpa-3* in rapid ASH glycerol responses.

Other mutants yielded more subtle changes in calcium responses consistent with altered regulation of sensory dynamics. A subset will be highlighted in this section while a full ensemble

of responses can be found in Appendix Figure 2.11-2.13. The *rgs-3* mutant is defective for the Regulation of G-protein Signaling molecule, which resets the G-protein cascade by catalyzing the GDP to GTP on the G_{α} subuit in its active state (Ferkey et al., 2007). ASH neurons in *rgs-3* mutants had a greatly reduced ON response and an increased OFF response to 10 s pulses of 1M glycerol (Figure 2.9.a.b). These responses resembled the ASH responses to 4M glycerol in wild-type worms (Appendix Figure 2.2.a). Indeed, decreasing the concentration of glycerol presented to *rgs-3* mutants resulted in calcium traces comparable to the direction of wild-type traces at 1M (Appendix Figure 2.2), suggesting a shift in sensitivity. *grk-2* encodes a G-protein kinase that desensitizes signaling by phosphorylating G-protein coupled receptors; *grk-2* mutants showed diminished ON responses in the cell body (Figure 2.9.a.b) but were able to maintain significant ON and OFF responses in the axon, suggesting specific calcium signaling defects in the cell body (Appendix Figure 2.3). The adaptation protein arrestin internalizes GPCRs following GRK-2 phosphorylation. Surprisingly, *arr-1* mutants showed significant higher amplitude signals to 10 s pulses of 1 M glycerol, opposite to the *grk-2* phenotype (Figure 2.9.a.b). The *egl-19* voltage-gated calcium channel mutant facilitates calcium entry in response to voltage change (Figure 2.8.a). A reduction of function in *egl-19* resulted in an altered ON response to long pulses of 1M glycerol, in which the initial slope and adaptation across repeated pulses were both reduced (Figure 2.9.a.b).

Among the signal transduction mutants, *arr-1, gpa-3,* and *egl-19* mutants were able to track rapidly fluctuating stimuli with robust, temporally summating filters of positive polarity (Figure 2.10.a.). Among these robust linear filters, the *egl-19(n582)* loss of function mutants were remarkable in that they had a normal onset, but lacked the second slow phase of negative polarity from the LN-ODE model (Figure 2.10.b.). This result implicates voltage-activated calcium channels in rapid adaptation to aversive signals. Other than *gpa-3* and *arr-1*, the linear temporal filters derived from the G-protein cascade mutants did not generate positive polarity, linear filters to 1M glycerol m-sequences that emphasized encounter history. Instead, *grk-2* and *rgs-3* exhibited fast, negative inflections that troughed at <1 s, similar to the linear filter of the wild type ASH copper response (Figure 2.10.c.; see discussion). *odr-3* similarly exhibited a negative polarity fast filter, but which was only weakly predictive of the calcium response observed (VAF of linear filter =18.3%, Figure 2.10.c.). Thus, the ability to track the history of encountering rapidly fluctuating stimuli require normal regulation of the G-protein cascade in ASH. Indeed, cell-specific rescue of the ODR-3 G_{α} protein under the *sra-6* promoter was able to regenerate robust, wild-type response dynamics to 10 s pulses and rapidly fluctuating glycerol

stimuli (Figure 2.10.d). These results indicate that the positive, history-summating linear response of ASH is tied to the G-protein cascade whereas a fast response of negative polarity is less dependent on rapid G-protein signaling and can be uncovered with the destruction of the positive polarity filter in G-protein mutants. All linear and impulse responses, however, ultimately require the TRP channel for calcium signaling.

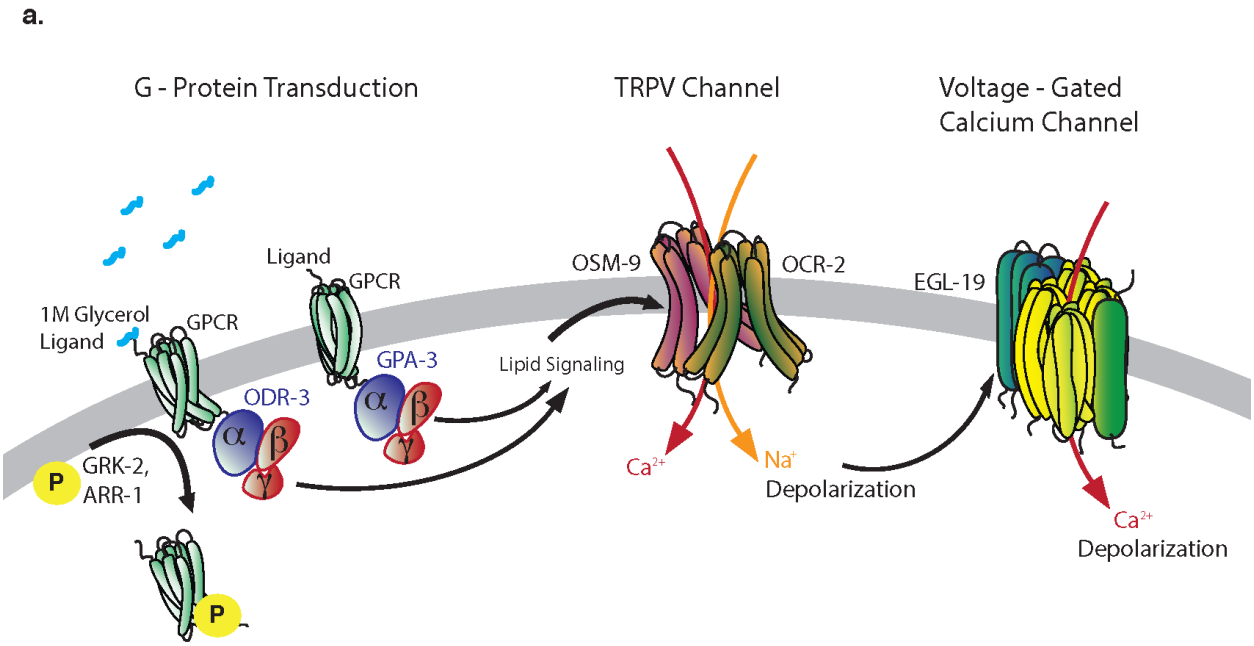

Figure 2.8. The known signal transduction cascade in ASH
a) The known signal transduction cascade (Kato *et al.*, 2014). The G-protein coupled receptors (GPCRs) responsible for sensation sit in the membrane of neural cilia. They can be desensitized and internalized by the G-protein Receptor Kinase (GRK-2) or arrestin (ARR-1) proteins, respectively. Stimulus binds GPCRs in ASH dendritic cilia and initiates a G-protein cascade with a conformation change of Gα (ODR-3 or GPA-3). The conformation change replaces the GDP bound to Gα with GTP, and GαGTP then dissociates from the GPCR and Gβ and Gγ subunits. The Gα subunit and Gβ/Gγ subunits bind to separate effectors and promote signal transduction until the GTP is hydrolyzed to GDP on the Gα subunit by a Regulator of G-protein Signaling enzyme (RGS-3). The reassembly of the heterotrimeric G-protein on the GPCR terminates signaling. Signal transduction downstream of an active G-protein involves intermediate lipid signaling and entry of Na+ and Ca+ via TRPV channels (OSM-9/OCR-2) to depolarize the neuron. Depolarization activates the voltage-gated calcium channel, EGL-19, which allows more calcium entry and further depolarization. Not shown, cytosolic calcium increase in the axon results in the release of neurotransmitters and neuropeptides at the nerve terminal.

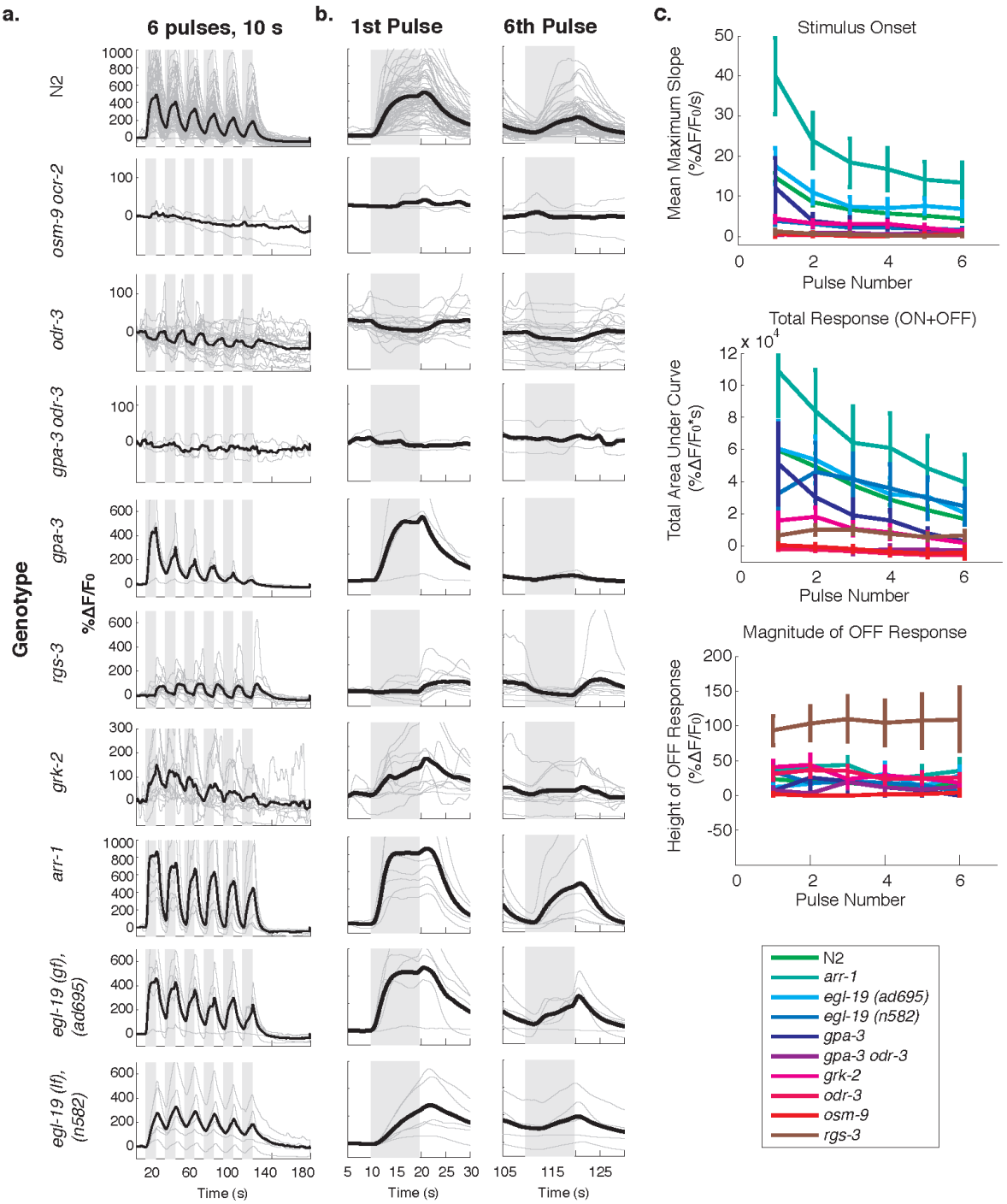

Figure 2.9. Signal transduction mutations in ASH can alter or eliminate sensory response
a) Measured GCaMP3 fluorescence change (mean trace in black, individual traces in light gray, %ΔF/F0 in ASH cell body to 6 repeats of 10 s ON and OFF 1M glycerol pulses (mean trace in black line; individual trials in light gray lines; gray bars indicate stimulus presence) in signal transduction mutants. (N2, n=71; *osm-9 ocr-2*, n=3; *odr-3*, n=21; *odr-3 gpa-3*, n=3; *gpa-3*, n=3; *rgs-3*, n=13; *grk-2*, n=11; *arr-1*, n=7; *egl-19(ad695)*, n=5; *egl-19(n582)*, n=5) **b)** Expanded response to first and last 10 s stimulus pulses. **c)** Maximum slope with glycerol onset, total response (integrated area under curve), and magnitude of OFF response quantified for each of six successive 10 sec 1 M glycerol pulses. Vertical bars = standard error of the mean.

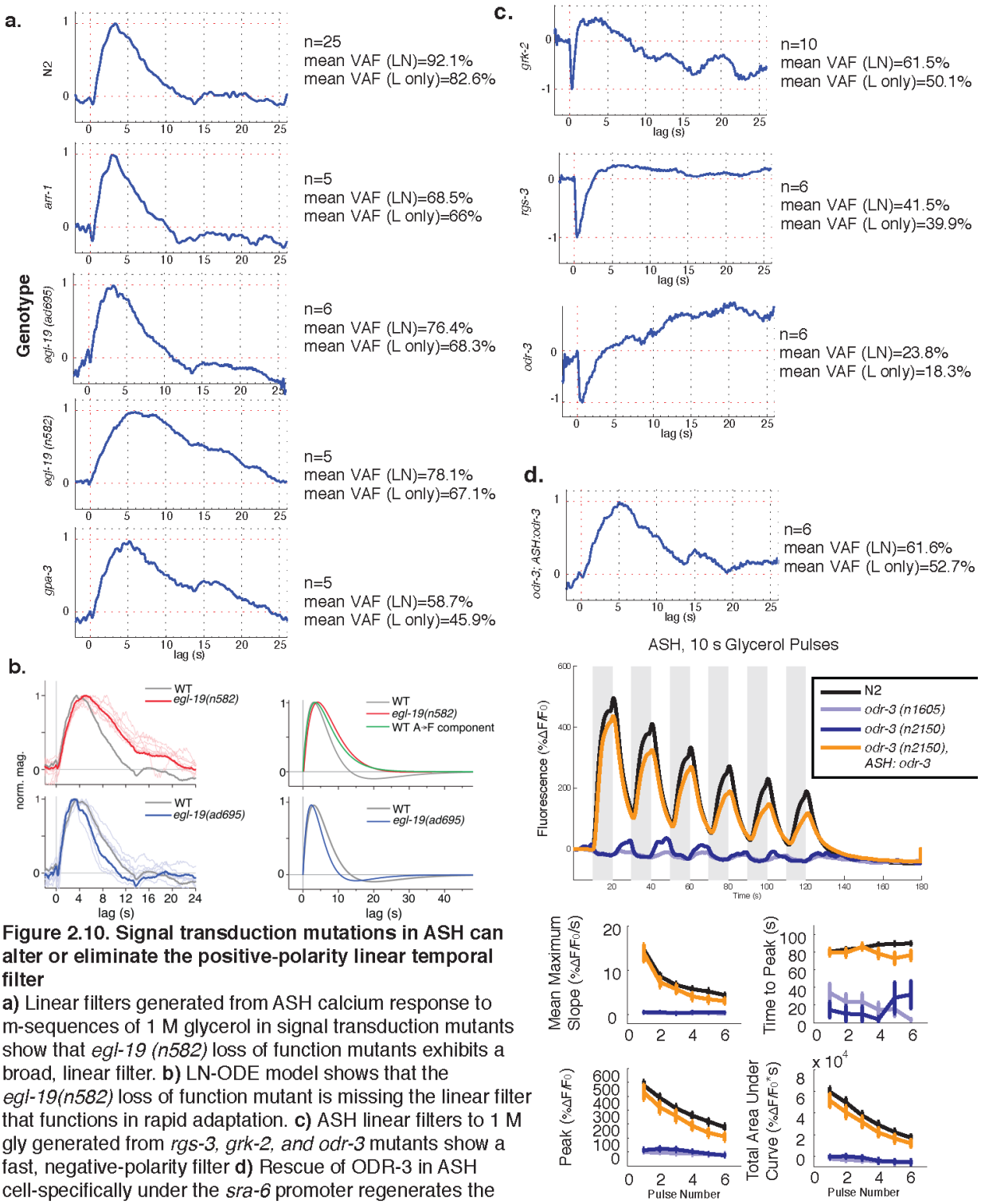

Figure 2.10. Signal transduction mutations in ASH can alter or eliminate the positive-polarity linear temporal filter

a) Linear filters generated from ASH calcium response to m-sequences of 1 M glycerol in signal transduction mutants show that *egl-19 (n582)* loss of function mutants exhibits a broad, linear filter. **b)** LN-ODE model shows that the *egl-19(n582)* loss of function mutant is missing the linear filter that functions in rapid adaptation. **c)** ASH linear filters to 1 M gly generated from *rgs-3, grk-2, and odr-3* mutants show a fast, negative-polarity filter **d)** Rescue of ODR-3 in ASH cell-specifically under the *sra-6* promoter regenerates the wild-type 10 s response to 1 M glycerol as well as the polarity and predictive value of the m-sequence generated linear filter (compare with c.); error bars = s.e.m..

Aversive stimuli activate other sensory neurons besides ASH

Canonical ASH stimuli are aversive and cause the worm to reverse upon an acute encounter (Colbert et al., 1997; Hilliard et al., 2002). Laser ablations of different sensory neurons showed that ASH is necessary for many avoidance responses (Kaplan and Horvitz, 1992). In agreement with this assignment, a *tax-2 tax-4* cGMP channel double mutant that lacks signals from about half of the sensory neurons, but spares ASH, has no effect on the avoidance of most aversive stimuli in low-resolution, binary behavioral assays (Hilliard et al., 2002). Natural, ASH-specific stimuli with different dynamics of activation could be the best tool to interrogate how the temporal dimension of neural activation instructs behavior. Fortuitously, however, I found that the ASI neuron, whose function requires the *tax-2 tax-4* channels and is not canonically required for aversive behaviors (Hilliard et al., 2002), responds to glycerol, quinine, and copper with Ca^{2+} transients that were opposite in sign to ASH responses (Figure 2.15.e.f.; 2.11.a.; Appendix Figure 2.6, 2.7). The response of ASI to 1M glycerol began 2 seconds after stimulus removal and was reduced in magnitude in the *unc-13* synaptic transmission mutant, suggesting that ASI is postsynaptic to another neuron that detects this repellent (Figure 2.11.a). I first asked if ASH was the upstream source of signals to ASI by examining the *osm-9* mutant, but found that ASI still responded, eliminating ASH as the upstream neuron (Appendix Figure 2.4.a). I next tested a *che-1* mutant that selectively disrupts the development of the ASE neurons (Figure 2.11.a). *che-1* mutants were nearly as severely defective in ASI responses as *unc-13* mutants, indicating that ASE, another *tax-2 tax-4* requiring neuron, is likely to be a source of synaptic input to ASI (Figure 2.11.d).

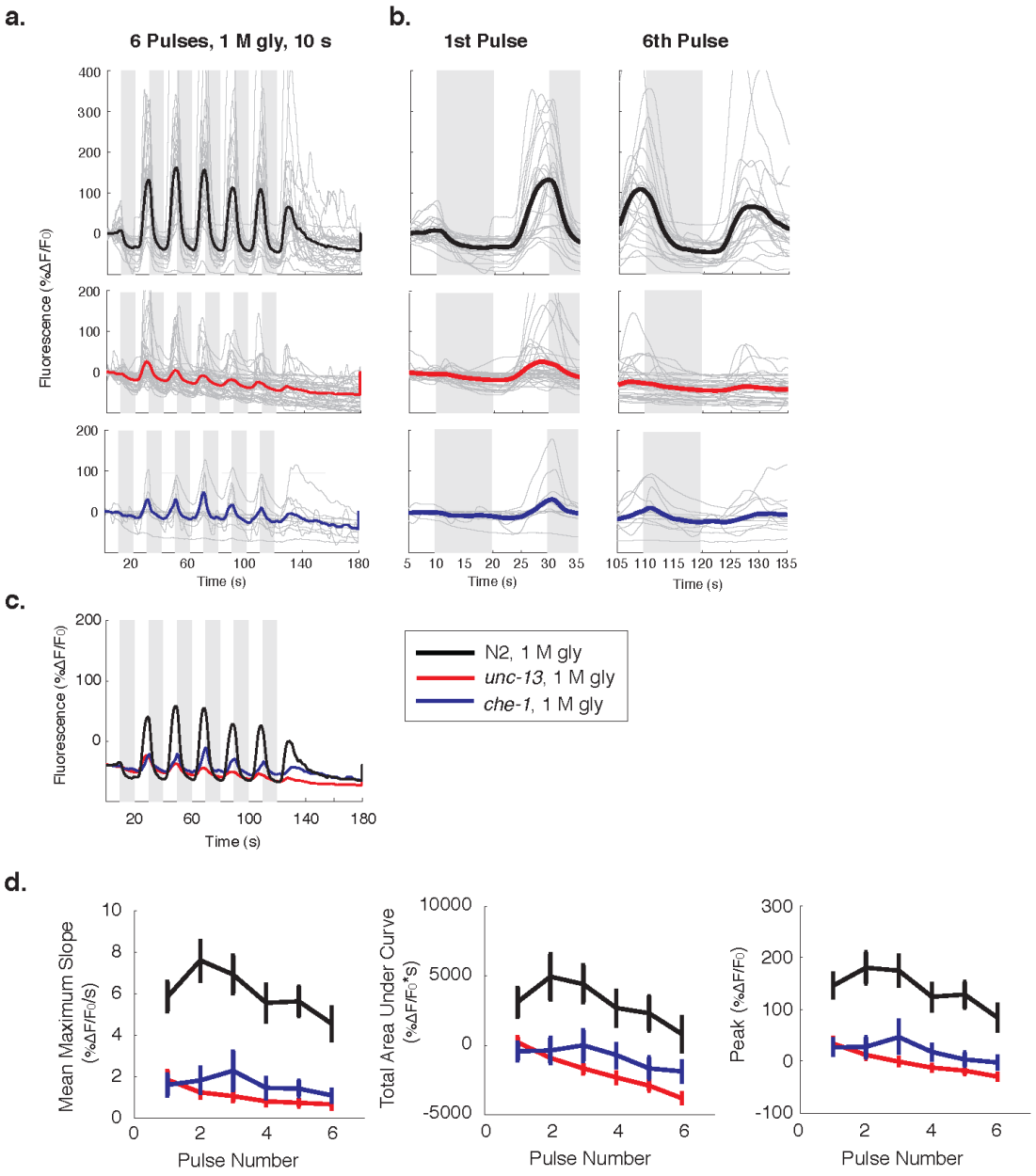

Figure 2.11. ASI response to 1 M glycerol depends on the *tax-2/tax-4* dependent ASE neurons
a) ASI shows robust calcium responses to 10 s presentations of 1 M glycerol. Stimulus onset results in calcium decrease while stimulus removal results in high amplitude calcium increase. The amplitude of the ASI calcium response decreases in *unc-13* (synaptic transmission mutant) and *che-1* (ASE neuron development mutant). Means in thick lines, individual traces in light gray. N2, n=25; unc-13, n=40; che-1, n=12. **b)** Calcium response to first and last 10 s stimulations at expanded time scales. **c)** Comparison of mean response in each genotype. **d)** Mean maximum slope, peak, and integrated response area are significantly diminished in *unc-13* and *che-1* ASI neurons compared to wild type responses across six consecutive 10 s pulses of 1 M glycerol.

The left and right ASE neurons respond to low concentrations of salts (0-100mM), and are functionally asymmetric. In calcium imaging response, ASEL is activated by salt increases and ASER by salt decreases (Suzuki et al., 2008; Ortiz et al., 2009). I found that ASEL and ASER are symmetric to response to 10 s pulses of 1M glycerol, with both neurons exhibiting calcium increases upon glycerol removal (Figure 2.12.a,b). Both ASE neurons responded to glycerol removal more quickly than ASI (Appendix Figure 2.13.e.), but the ASER response appeared to peak more quickly (Figure 2.12.a-c.). I tested their dynamic responses in greater detail by tracking 9-bit, 200ms white noise presentations of 1M glycerol (Figure 2.12.d.). These experiments revealed sharp but slightly different linear filters for ASER and ASEL. The ASER filter peaked at 0.5 s, where the ASEL filter peaked at 1 s, with corresponding delays to recovery to baseline (Figure 2.12.d).

To ask whether the temporal filter is intrinsic to ASE cell fates, I tested the *lsy-6* loss of function (lf) mutation that converts both ASE identities to ASER (Figure 2.12.a,b,c.). I found that the left ASE in *lsy-6(lf)* mutants responded to 10 s glycerol stimuli with a rapid response resembling normal ASER, suggesting that the cell fate mutation altered ASE dynamics. Other ASE cell fate mutants are also available. While the loss of function of LSY-6 results in the conversion of both ASE neurons to ASER, a gain of function transgene of *lsy-6* (*otIs204*) (gf) confers the ASEL identity to both ASE neurons. Two other worm strains, *otEx3830* and *otEx3822*, expresses the caspase executioner protein in ASER and ASEL respectively, and to specifically kill each neuron.

In order to test whether the ASE contribution to the ASI glycerol response originates from ASER, ASEL or both, I examined ASI calcium responses to 1M glycerol in the background of *lsy-6(lf)* (2ASER), *lsy-6(gf)* (2ASEL), *otEx3830* (ASER kill), and *otEx3822* (ASEL kill) strains. ASI responses to 1M glycerol were significantly diminished in all ASE developmental mutants (Figure 2.13.a-c). These results suggest that ASI requires both ASEL and ASER signals to generate a full glycerol response. The fact that both ASEL and ASER are required suggests that the different intrinsic dynamics seen between ASEL and ASER to 1M glycerol could serve a functional role in activating ASI. Alternatively or additionally, other aspects of ASEL and ASER cell fate, such as patterns of neuropeptide expression, could be important.

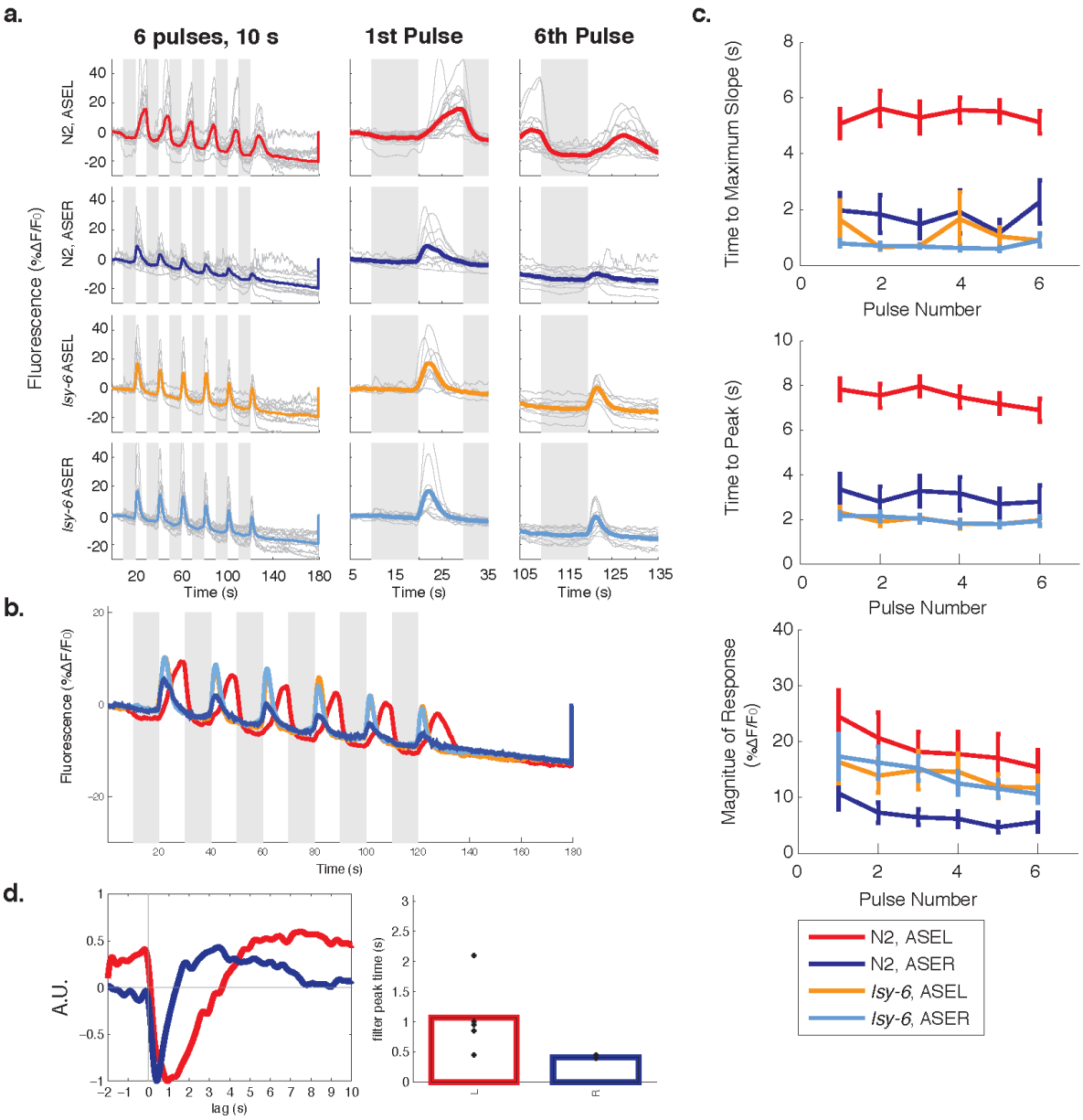

Figure 2.12. 1M glycerol elicits temporally asymmetric responses in ASEL and ASER neurons. **a)** ASEL and ASER calcium responses to 1 M glycerol have symmetric polarity but are temporally divergent. Loss of the *lsy-6* gene confers ASER identity onto ASEL and converts the ASEL temporal response to 1 M glycerol to the ASER-like response. Time to maximum slope and time to maximum peak of ASEL is divergent from that of ASER. Conversion of ASEL to an ASER-like identity in the *lsy-6* mutant converts these parameters in ASEL to ASER-like dynamics. The height of the response in both neurons converge in a *lsy-6* background. (means by pulse number, vertical lines = standard error of the mean). N2, ASEL, n=16; N2, ASER, n=12; *lsy-6* ASEL, n=9, *lsy-6*, ASER, n=13. **b)** Comparison of mean response between ASEL and ASER in N2 and lsy-6 genotypes. **c)** Quantification of time to maximum slope, time to maximum peak, and magnitude of response for each condition. **d)** Normalized linear filter derived from calcium responses in ASER (blue) and ASEL (red) to 9-bit, 200 ms m-sequence presentation of 1 M glycerol. Mean filter peak time (bars) and individual trial peak times (+) of linear filters.

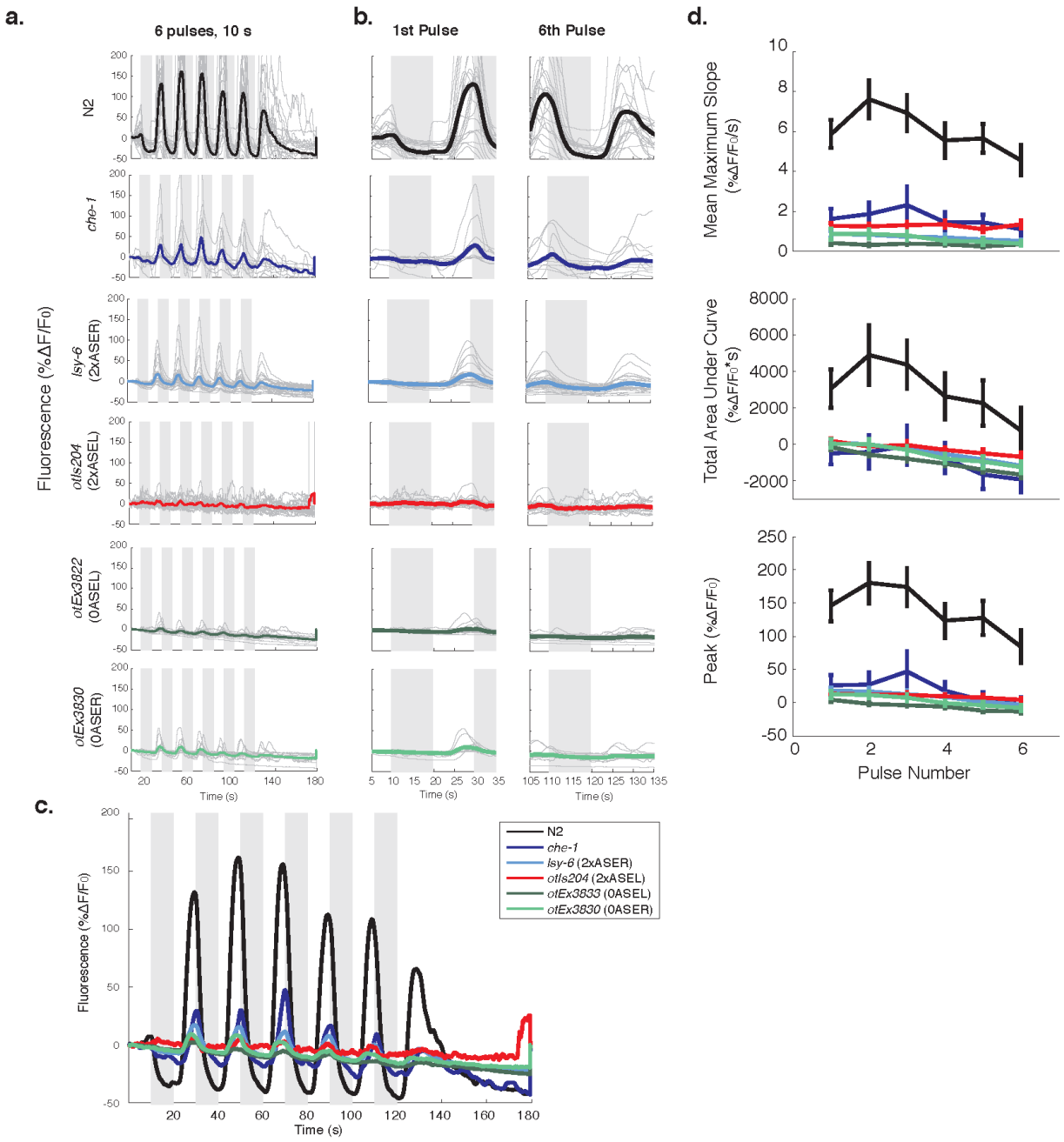

Figure 2.13. ASI response to 1 M glycerol depend on the temporally asymmetric responses of ASEL and ASER neurons.

a-c) ASI responses in ASE developmental mutant backgrounds. *che-1* is missing both ASE cell types; *lsy-6* loss of function results in 2 ASERs while *lsy-6* gain of function *(otIs204)* results in 2 ASELs; *otEx3822* contains 1 ASER but no ASEL while *otEx3830* contains 1 ASEL but no ASER. **a)** Measured GCaMP3 fluorescence change (mean trace in black, individual traces in light gray, %ΔF/F) in ASI cell body to 6 consecutive repeats of 10 s ON and OFF pulses of 1M glycerol (stimulus presence indicated by gray bars). N2, n=25; *che-1*, n=12; *lsy-6*, n=28; *otIs204*, n=18; *otEx3833*, n=16; *otEx3830*, n=12. **b)** Calcium response to first and last 10 s stimulations at expanded timescales. **c)** Superimposed means of ASI response in each mutant background. **d)** Mean maximum slope, peak, and integrated response area of ASI responses to 1 M glycerol are significantly diminished in all ASE developmental mutant backgrounds (means, vertical bars = standard error of the mean).

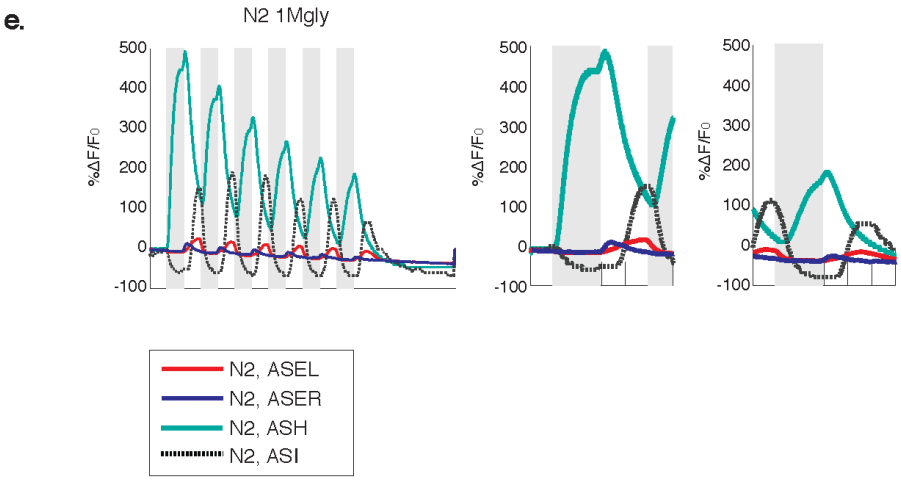

Figure 2.13. ASH, ASI, ASEL, and ASER show diverse responses to 1 M glycerol
e) Overlaid dynamics of calcium responses to 1 M glycerol in ASH, ASI, ASEL, and ASER.

ASI responds with robust linear filters to diverse aversive stimuli

While ASE and ASH neurons can track rapidly fluctuating stimuli with robust temporal filters, ASI did not exhibit reliable responses to m-sequences of 1 M glycerol presented at less than a 1.5 s minimal pulse length, making the extraction of its temporal response using the same white noise stimulus sequence as ASH noisy and imprecise (not shown). I therefore characterized stimulus-specific ASI responses using 10 s pulses and stimulus-triggered correlations of responses from 7-bit, 2 s pulse length m-sequences. To assess whether ASI glycerol responses were concentration specific, I presented 10 s pulses of 125 mM, 250 mM, 500 mM, 2 M, and 4 M concentrations of glycerol to the cell. ASI exhibited the same dynamic trends to each glycerol concentration: immediate inhibition to stimulus onset and delayed increase after stimulus offset (Figure 2.14.a). Within this concentration range, the highest calcium transients were seen to a concentration of 250 mM-2 M glycerol, similar to the preferred concentration range of ASH (Figure 2.14.a). 7-bit, 2 s presentations of glycerol in these concentrations showed robust, linear, biphasic history-summating filters that required about 10 s of “charging” with stimulus before the neuron began responding (not shown). The ASI temporal filter is best summarized in an LN-ODE model of temporal correlations extracted from 2 s m-sequences to 1 M glycerol: ASI initially showed a decreased fluorescence to glycerol onset that peaked at ~4 s, followed by an opposite increase of calcium above baseline that peaked ~15 s after initial stimulus onset; this biphasic response returned to baseline 20 s after the glycerol onset (Figure 2.14.c).

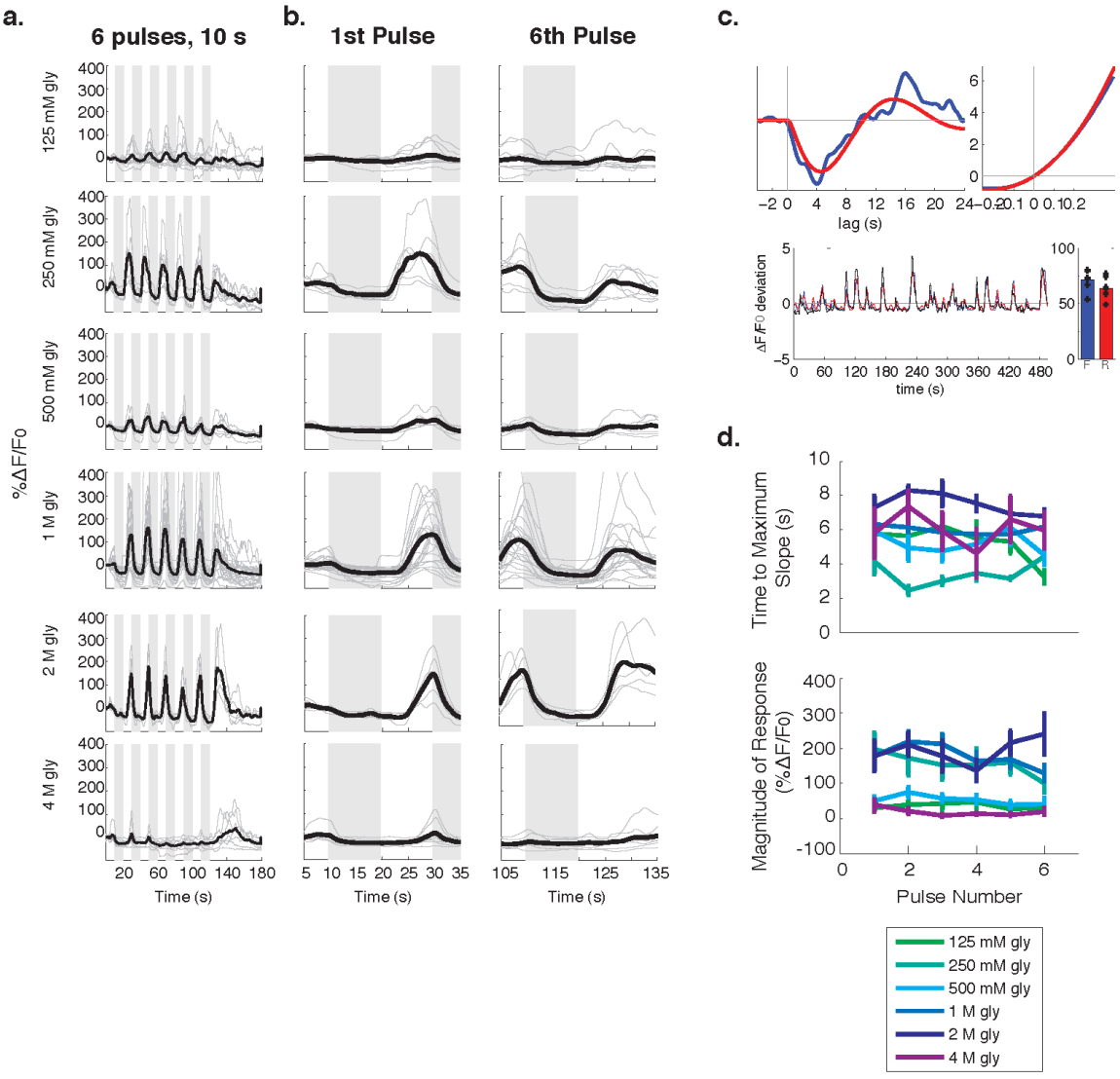

Figure 2.14. ASI responds robustly to glycerol across a range of concentrations.
a) ASI responds to 125 mM to 4 M glycerol in 10 s pulse series with significant calcium increases to glycerol removal. Measured GCaMP3 fluorescence change (mean trace in black, individual traces in light gray, %ΔF/F0) in ASI cell body to 6 repeats of 10 s ON and OFF pulses of 125 mM to 4 M glycerol concentrations (stimulus presence indicated by gray bars).125 mM gly, n=11; 250 mM gly, n=7; 500 mM gly, n=7; 1 M gly, n=25; 2 M gly, n=5; 4 M gly, n=7. **b)** Calcium response to first and last 10 s stimulations at shorter timescales. **c)** LN-ODE (red) and LN derived (blue) linear-nonlinear filters for ASI response to 1 M glycerol explains over 50% of ASI response to 7-bit, 2 s presentation of stimulus. **d)** Amplitude of ASI glycerol response to 10 s pulses of glycerol are highest in the 250 mM to 2 M range, with the maximum slope of response occurring >2 s after glycerol removal (means, vertical bars = standrad error of the mean).

The ASH stimuli copper and quinine also elicited ASI responses in 10 s pulses, though with different dynamics from glycerol (Figure 2.15.e.f, Appendix Figure 6.a.). 1 mM, 2 mM, and

10 mM quinine inhibited ASI in 10 s pulse presentations, and stimulus removal led to ASI activation (Figure 2.15.e.f., Appendix Figure 2.6, 2.7). These results demonstrate that, like ASH, ASI responds to diverse aversive stimuli.

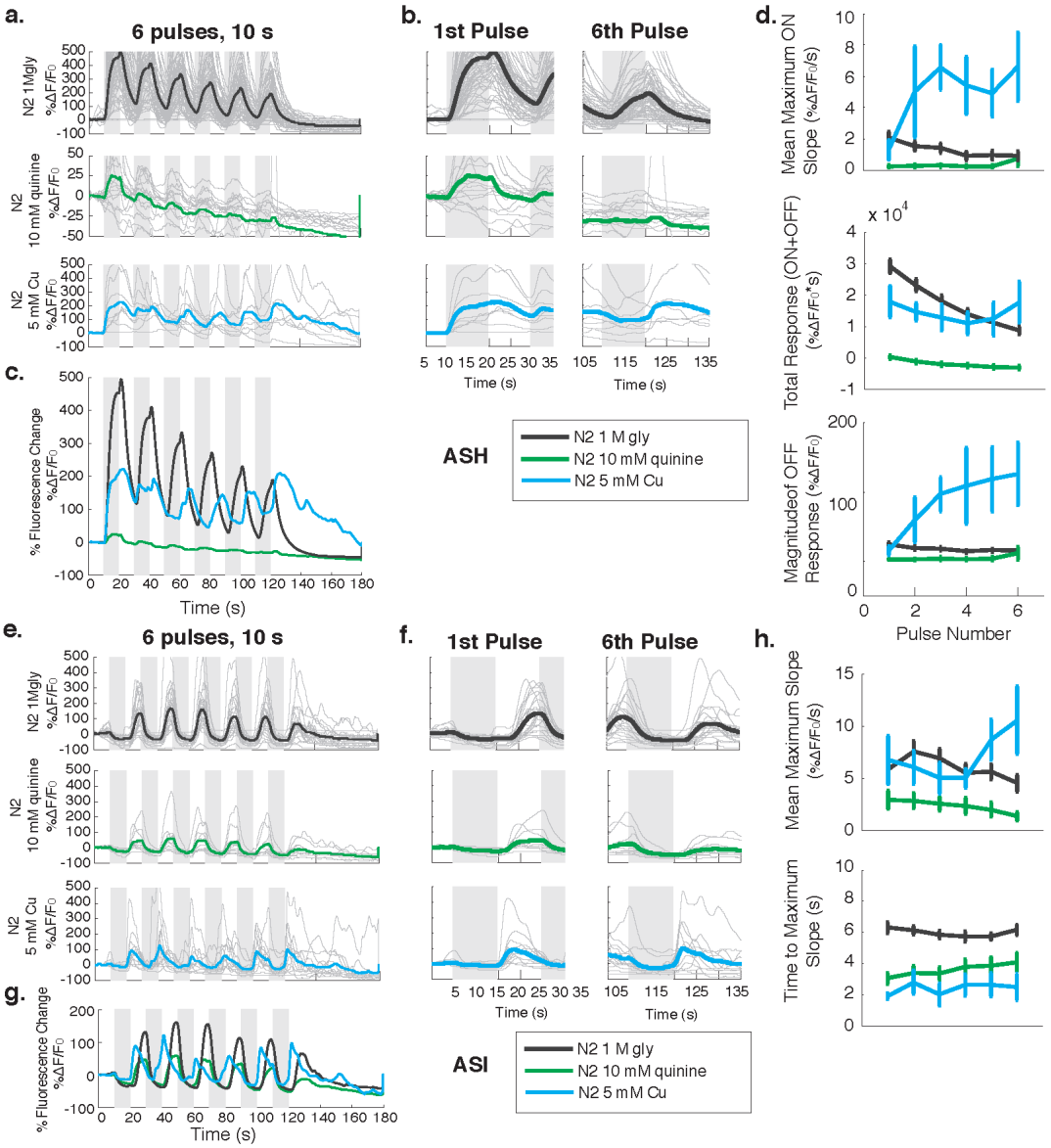

Figure 2.15. ASI responds robustly to aversive stimuli that are known to activate ASH.
a) Measured GCaMP3 fluorescence change (mean trace in black, individual traces in light gray, %ΔF/F0) in ASH cell body to 6 consecutive repeats of 10 s pulses of glycerol, copper, or quinine (stimulus presence indicated by gray bars). 1 M gly, n=71; 10 mM quinine, n=16; 5 mM Cu, n=8. **b)** ASH calcium response to first and last 10 s stimulations at expanded timescales. **c)** Superimposed means of ASH response to each stimulus **d)** Mean maximum ON slope, total response (integrated area), and magnitude of OFF response for each stimulus condition (means, vertical bars = standard error of the mean). **e)** Measured GCaMP3 fluorescence change (mean trace in black, individual traces in light gray, %ΔF/F0) in ASI cell body to 6 repeats of 10 s ON and OFF pulses of glycerol, copper, or quinine (stimulus presence indicated by gray bars). 1 M gly, n=25; 10 mM quinine, n=11; 5 mM Cu, n=13. **f)** ASI calcium response to first and last 10 s stimulations at expanded timescales. **g)** Superimposed means of ASI response to each stimulus **h)** Maximum slope and time to maximum slope varies by stimulus (means, vertical bars = standard error of the mean).

Natural ASH stimuli activate multiple neurons with different dynamics

In summary, the experiments described above show that while different stimuli activate ASH with different dynamics, they also activate other neurons in patterns that differ depending on the identity of the stimulus. This is further evidenced by the diversity of ASH and ASI responses to copper, quinine, and glycerol in the quinine-specific signal transduction mutant *qui-1* and the synaptic transmission mutant *unc-13* (Appendix Figure 8, 9). These results suggest that there are complex neuron-to-neuron interactions and within-neuron interactions to aversive stimuli. While these results offer intriguing insight into the diverse range of natural sensory responses, no comparison of stimulus-driven behavior across these natural aversive stimuli could generate a pure comparison of the effects of ASH dynamics on behavior.

Ectopic receptors can confer diverse dynamics to ASH with cell-specificity

To create an experimental system for isolating the effects of neuronal dynamics on behavior, I focused on heterologous expression of receptor proteins that are not endogenous to ASH. In initial experiments, I tested the capsaicin-sensitive TRPV1 channels, but found that stimulus delivery and responses were not reliable enough for the planned experiment. Channelrhodopsin (ChR2) expression in ASH has been shown to induce ASH calcium increases and ASH-related behaviors with blue light stimulation, but this was also suboptimal, because ASH has an endogenous blue light response that would confound both imaging and behavior experiments. Therefore, as an experimental system, I focused on the expression of *C. elegans* pheromone receptor proteins in ASH, knowing that wild-type ASH neurons did not have Ca^{2+} responses to ascaroside pheromones across a range of concentrations (McGrath et al., 2011).

Previous work had identified members of the *srg* family of G-protein coupled chemoreceptors as candidate receptors for a class of *C. elegans* pheromones called ascarosides. I confirmed the hypothesis that *srg* proteins are pheromone receptors by demonstrating that three different proteins, SRG-34, SRG-36, and SRG-37, could confer sensitivity to the ascaroside C3 on ASH when they are ectopically expressed under the *sra-6* promoter (McGrath et al., 2011) and Figure 2.16. SRG-34 and SRG-36 are endogenously expressed in ASI neurons, but no calcium responses to C3 were observed in ASI either endogenously or when *srg* genes were overexpressed with the *sra-6* promoter. It is possible that ASI lacks a signaling pathway for rapid calcium signaling downstream of pheromone receptors, and instead uses slower pathways that regulate gene expression for its main function, the

regulation of dauer larva formation. Thus, the expression of *srg* genes from the *sra-6* promoter confers calcium responses on ASH, and while it may increase expression of the same genes in ASI, does so consistently for all tested genes.

In characterizing the ectopic ASH responses mediated by these receptors, I found that both ASH:*srg-34* and ASH:*srg-36* responded to 30 s presentations of ascaroside C3 across a range in concentration (Figure 2.16.a). *srg-34* was about 100x more sensitive than *srg-36*, which detected only concentrations at or above 1 µM. However, the peak response for *srg-36* exceeded the peak response for *srg-34*, which saturated near 0.33 µM, whereas *srg-36* responses continued to rise up to 10 µM C3 (Figure 2.16). The magnitudes of the peak calcium responses driven by *srg-34* and *srg-36* were comparable to responses to the endogenous ASH stimulus, 500mM glycerol. At 1 µM C3, both *srg-34* and *srg-36* elicited robust ASH responses; however, these responses had different dynamics in both a 10 s and 30 s stimulus pulse. The *srg-34* response rose rapidly, peaked within 1 s, and then fell, whereas the *srg-36* responses rose continuously for the entire 10 s or 30 s and did not decay during the pulse (Figure 2.16.a., Figure 2.17.a.). Moreover, the *srg-34* response maintained a steeper initial slope than the *srg-36* response until the 10 µM concentration (Figure 2.16.a., quantified in b.). These dynamics were recapitulated in the linear filter derived from rapidly fluctuating presentations of 1 µM C3. The *srg-34* linear filter peaked at < 2 s and fell rapidly, whereas the *srg-36* linear filter resembled the linear filter derived from 1 M glycerol, peaking around 3 s and integrating over 12 s (Figure 2.20.a). Indeed, while both C3 responses can be described with linear filters, the long ASH:*srg-36* filter can account for much more stimulus history than the short ASH:*srg-34* filter.

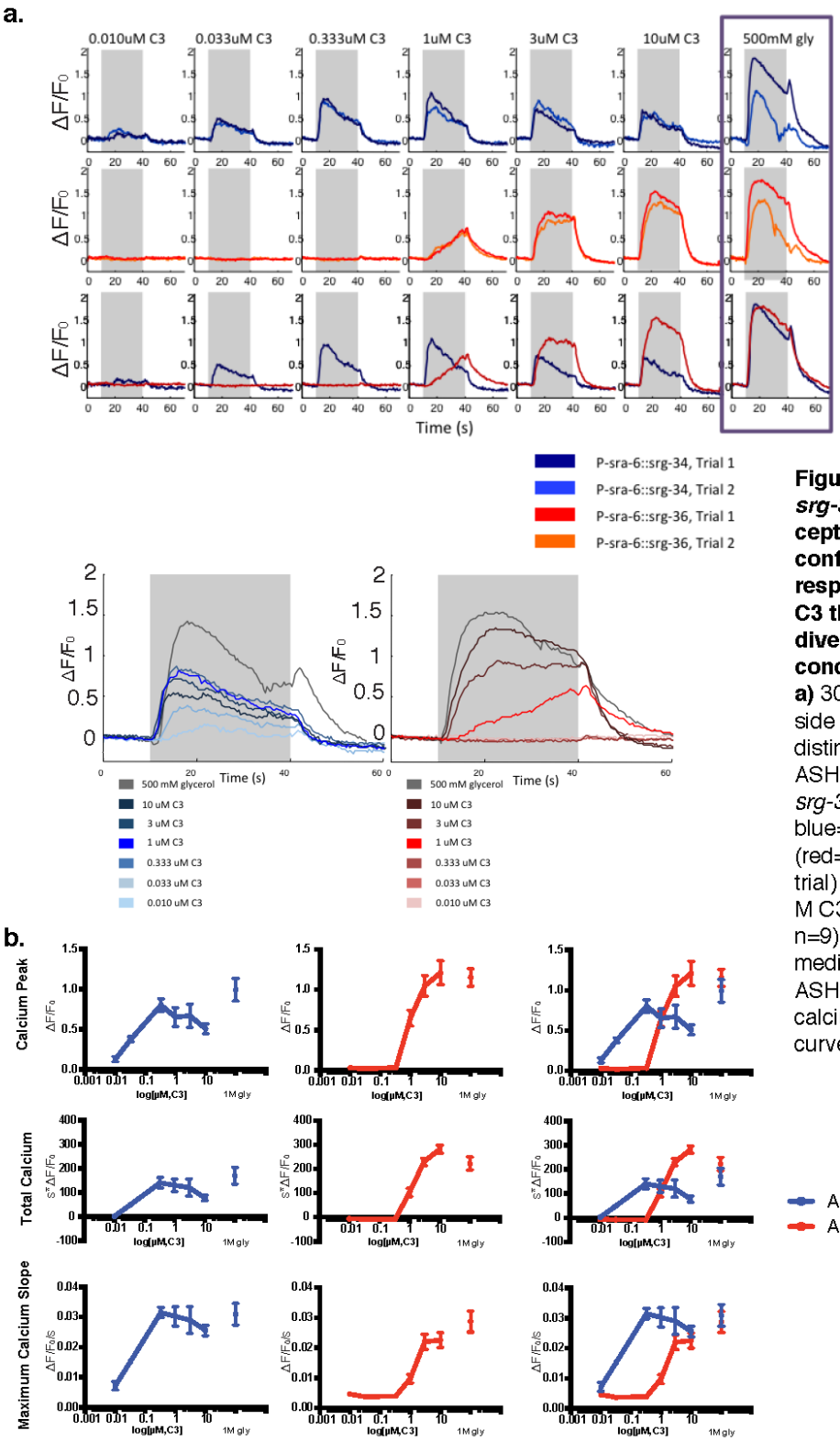

Figure 2.16. Expression of *srg-34* and *srg-36* chemoreceptors ectopically in ASH confers cell-specific calcium responses to the ascaroside C3 that are dynamically divergent across multiple concentrations.
a) 30 s pulses of the ascaroside C3 elicits temporally distinct calcium dynamics in ASH ectopically expressing *srg-34* (dark blue=1st trial, blue=2nd trial) or *srg-36* (red=1st trial, orange=2nd trial) from 0.01 μM C3 to 10 μM C3. (*srg-34*, n=7; *srg-36*, n=9) **b)** *srg-36* and *srg-34* mediated responses to C3 in ASH diverge in peak, total calcium (area under calcium curve), and maximum slope.

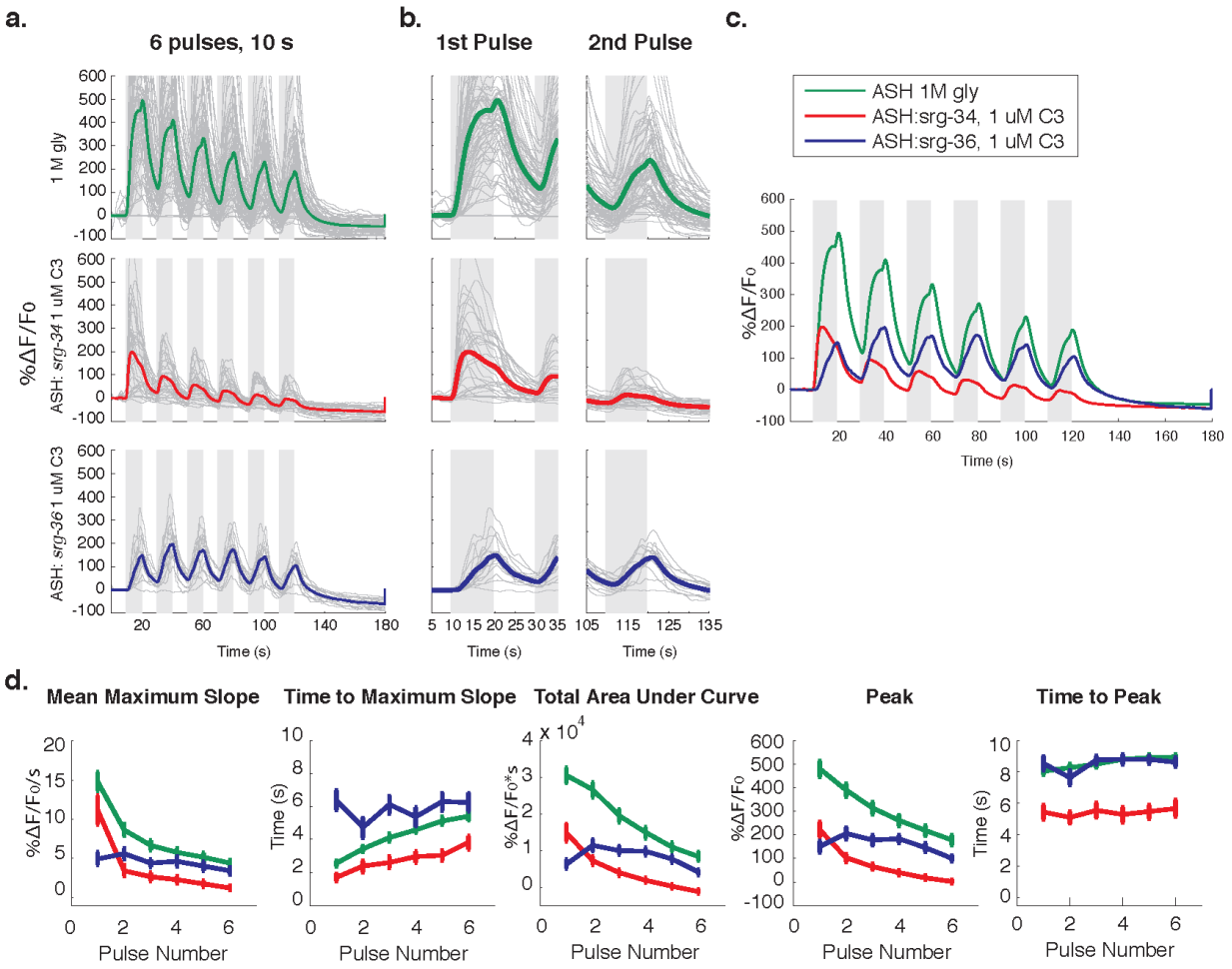

Figure 2.17. Expression of *srg-34* and *srg-36* chemoreceptors ectopically in ASH confers cell-specific calcium responses to 10 s pulses of the ascaroside C3.
a) 10 s pulses of the ascaroside C3 elicit temporally distinct calcium dynamics in ASH ectopically expressing *srg-34* (red) or *srg-36* (blue). Measured GCaMP3 fluorescence change (mean trace in color, individual traces in light gray, %ΔF/F) in ASH cell body to 6 consecutive 10 s ON and OFF pulses of 1 M gly or 1 µM C3 (stimulus presence indicated by gray bars). (N2, 1 M gly, n=71; ASH:srg-34, µM C3, n=32; ASH:srg-36, 1µM C3, n=15) **b)** Calcium response to first and last 10 s stimulations at expanded timescales. **c)** Superimposed means of ASH response from (a). **d)** *srg-36* and *srg-34* mediated responses to C3 in ASH diverge in maximum slope, time to maximum slope, and time to peak. Integrated response area and peak show different adaptation to *srg-36* and *srg-34* mediated responses across repeated 10 s stimulus presentation (means, vertical bars = standard error of the mean).

To assess whether the *srg-34* and *srg-36* calcium transients in ASH used the same signal transduction pathway as endogenously aversive stimuli, I looked their responses to 1 µM C3 in the G-protein cascade and TRP mutants. Consistent with native aversive stimuli, both *srg-34* and *srg-36* calcium transients were eliminated in the TRP mutants *osm-9* and *ocr-2* (not shown). Calcium transients elicited by *srg-34* and *srg-36* diverged in their dependence on the G-protein cascade. ASH neurons expressing *srg-34* or *srg-36* were still able to respond to 1 µM

C3 in *odr-3* mutants but the peak height of the *srg-36* response was lower than in wild-type worms, suggesting that *srg-36* requires the *odr-3* Gα mediated signaling cascade to generate a full response while *srg-34* does not (Figure 2.18). In the *gpa-3* background, *srg-34*-mediated calcium transients were slightly reduced compared to the wild type background and *srg-36*-mediated calcium transients were eliminated, suggesting that *srg-36* is more dependent on *gpa-3* to generate a response (Figure 2.18.a.,e.). In a double mutant background for both major Gα proteins of *odr-3* and *gpa-3*, all responses were eliminated or nearly so (Figure 2.18.a-e), indicating that these two G proteins cumulatively account for all responses to *srg-34* and *srg-36* in ASH.

Gain of function *odr-3* mutants and the *rgs-3* mutant actually significantly increased the total calcium response of *ASH:srg-34*, suggesting the existence of an inhibitory component to G-protein signaling (Figure 2.19). Therefore, similar to glycerol-mediated ASH calcium transients, the G-protein cascade is implicated in generating proper dynamics of ASH responses in response to activation of *srg-34* or *srg-36*. However, no simple matching of G proteins to temporal dynamics emerged from this analysis; instead, there appears to be a receptor-dependent requirement for different G proteins, and temporal dynamics appear to result from specific receptor-G protein interactions.

White noise stimulation by 1 µM C3 of ASH expressing either *srg-34* or *srg-36* was used to characterize their fast signaling dynamics (Figure 2.20). The *srg-36* generated linear filter resembled the time course of the endogenous 1 M gly and 500 mM NaCl linear filters (Figure 2.20), suggesting that this receptor mediates ASH responses that accumulate the history of stimulus encounters along a similar timescale. *srg-34* mediated ASH responses were fast adapting, and they could only be studied when the C3 pulse length within the m-sequence was increased from 200 ms to 2s. The m-sequence analysis yielded a consistent linear filter for *srg-34* that peaked around 1 s, although the adaptation caused the linear filter to overestimate the first half of the response while underestimating the second half of the response. The fact that the filter peaked more quickly than the stimulus pulse length used to generate it suggests that ASH responds to *srg-34* in an impulse scale, and accumulates very little information about the history of C3 encounters.

In summary, the dynamic differences between ASH responses elicited by ASH:*srg-34* and ASH:*srg-36* make these receptors candidates for interrogating how ASH-specific dynamic responses can interact with a neural circuit to direct behavior.

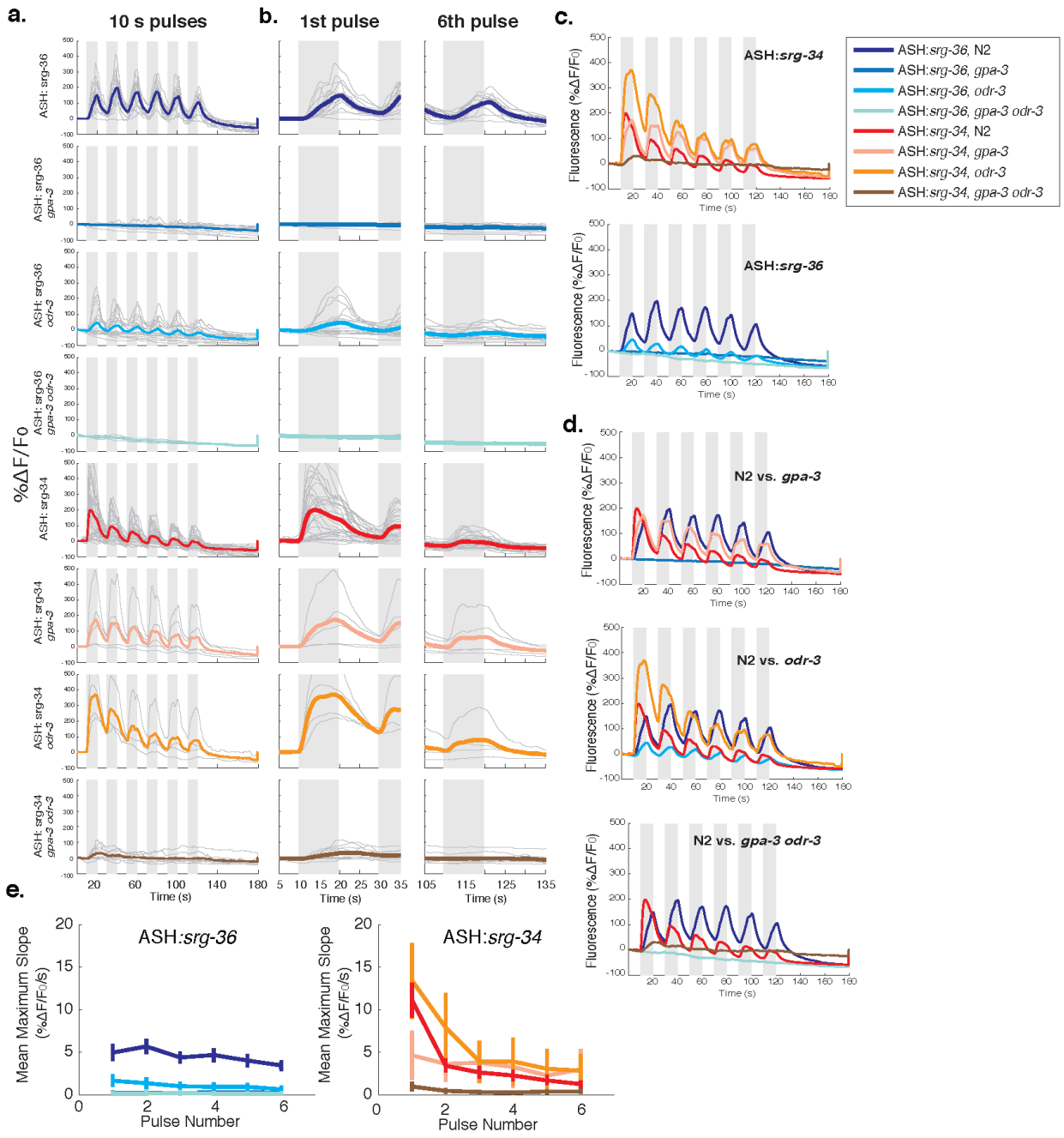

Figure 2.18. *srg-34* and *srg-36* chemoreceptors interact with endogenous ASH G proteins, in a receptor-specific fashion.

a) *srg-34* and *srg-36* mediated responses to 6 consecutive 10 s pulses of C3 differ in reliance on Gα subunits *gpa-3* and *odr-3*. Individual mutants are shown with mean response in color, individual trials in light gray (ASH:srg-36: N2, n=15; *gpa-3*, n=17, *odr-3*, n=18; *gpa-3 odr-3*, n=2. ASH:srg-34: N2, n=32; *gpa-3*, n=5; *odr-3*, n=4; *gpa-3 odr-3*, n=10). **b)** Calcium response to first and last 10 s stimulations at expanded timescales. **c)** Superimposed means of ASH response from (a) by srg. **d)** Superimposed means of ASH response from (a) by genotype showing difference in dependence on G-protein cascade mutants. **e)** G-protein cascade mutants differ their impact on the maximum slope of ASH calcium responses mediated by *srg-36* and *srg-34* to 1 µM C3 (means, vertical bars = standard error of the mean).

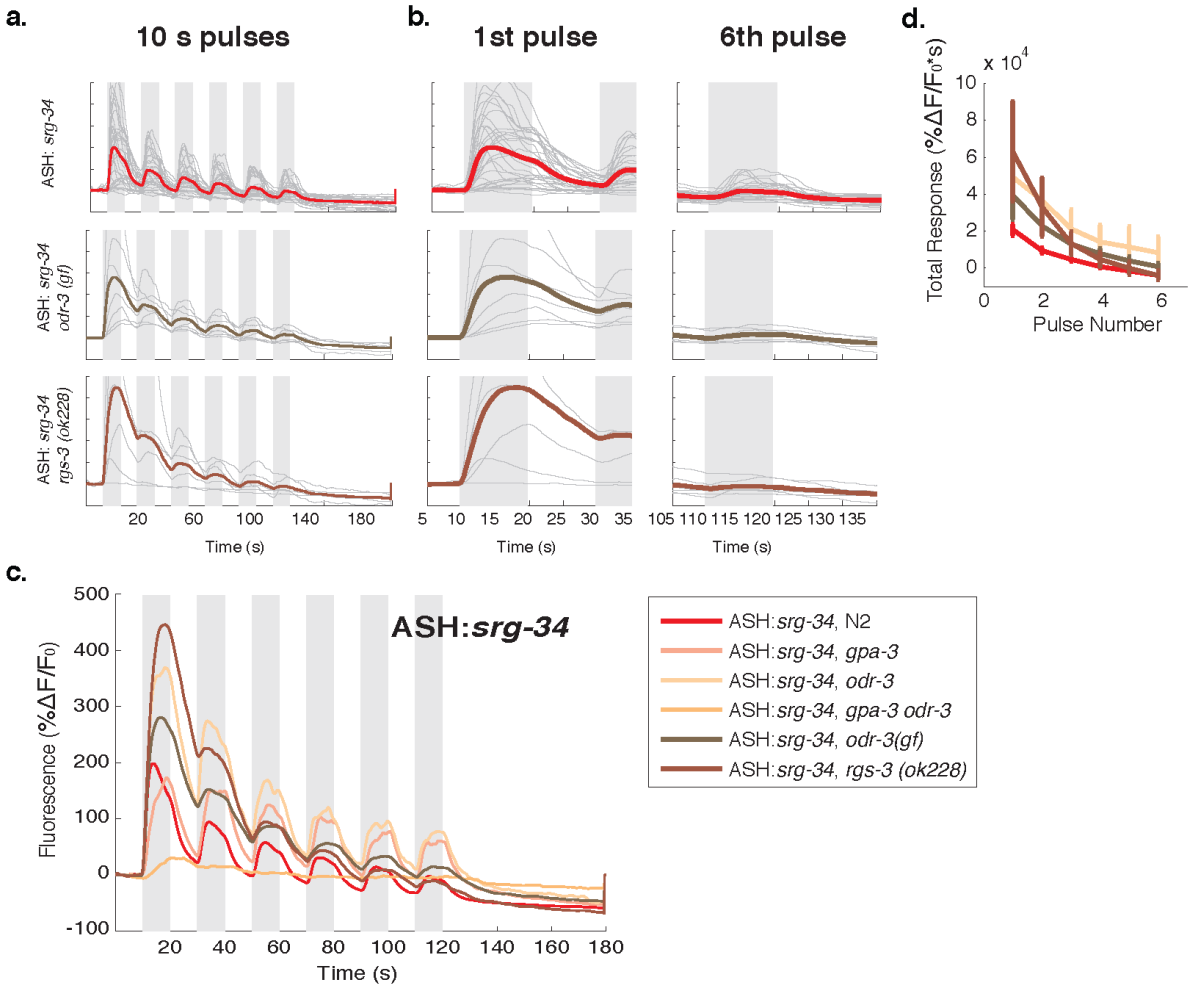

Figure 2.19. The *odr-3* and *rgs-3* mutants may increase the amplitude of srg-34 mediated responses to 1 µM C3.
a) *srg-34* mediated responses to 6 consecutive 10 s pulses of C3 are increased in the *odr-3(lf)*, *odr-3(gf)* and *rgs-3* mutant backgrounds, members of the G-protein cascade. Individual mutants are shown with mean response in color, individual trials in light gray (ASH:srg-34: N2, n=32; *odr-3(lf)*, n=4; *odr-3(gf)*, n=7; *rgs-3*, n=6). **b)** Calcium response to first and last 10 s stimulations at shorter times-cales. **c)** Superimposed means of ASH response from (a) and other mutants previously shown in Figure 2.18. **d)** *odr-3* and *rgs-3* mutants increase the total response (integrated area) of *srg-34* to 1 µ M C3 (means, vertical bars = standard error of the mean).

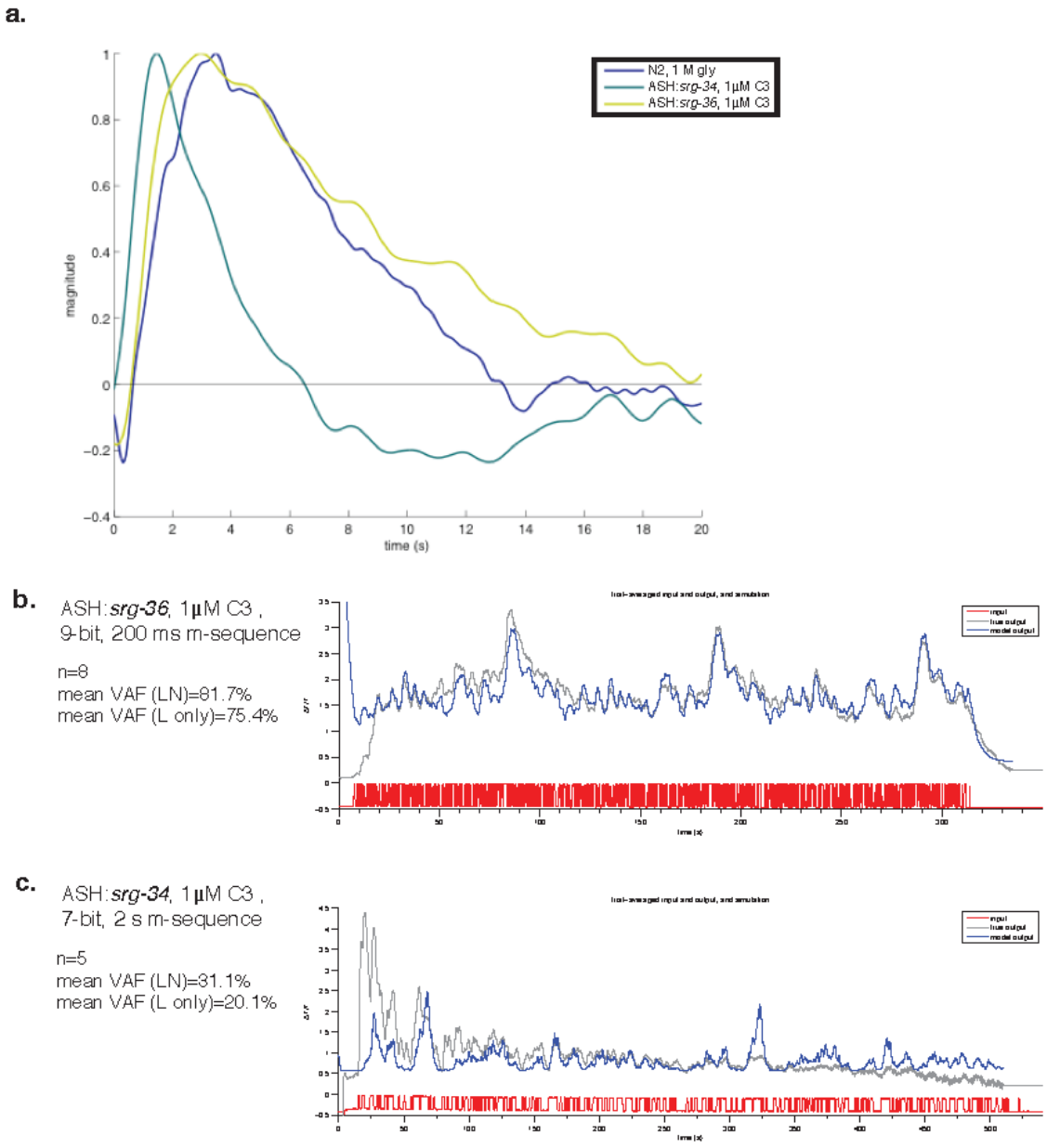

Figure 2.20. *srg-34* and *srg-36* elicit dynamically different linear temporal filters to m-sequence presentations of 1 µM C3

a) Linear filters derived from rapidly fluctuating pulses of 1 µM C3 (9-bit 200 ms for *srg-36*, 7-bit 2 s for *srg-34*) reveal that *srg-34* and *srg-36* induce temporally distinct calcium responses to C3. **b)** *srg-36* trial averaged m-sequence response (gray) is well-explained by the linear temporal filter (output of filter model in blue) while the **c)** *srg-34* trial averaged m-sequence response (gray) was less well-estimated by the derived temporal filter due to underestimation of the first 250 s and overestimation of the last 250 s, suggesting significant adaptation of overall calcium activity.

Intracellular calcium recapitulates cell voltage and stimulus-triggered depolarization

In *C. elegans*, genetically encoded calcium indicators are a standard proxy to measure neuronal activation. However, other than a few electrophysiological studies, the approximation between stimulus-elicited intracellular calcium entry and membrane voltage has not been verified. The complex dynamics of calcium responses in ASH to both natural and ectopic stimulation may either be induced by membrane voltage changes or be secondary to calcium regulation. To assess whether calcium dynamics match membrane voltage dynamics to ASH stimulation, I expressed the macCitrine genetically-encoded fluorescent indicator in ASH (Gong et al., 2014). The macCitrine indicator is FRET based and requires activation with all-trans retinal. Therefore, fluorescence measured in macCitrine-expressing neurons without retinal exposure serves as a control for true signals. When the neuronal membrane is depolarized by stimulus presentation, the fluorescence of macCitrine is quenched, opposite to the direction of calcium-mediated GCaMP fluorescence. macCitrine fluorescence in ASH neurons exposed to 10 s pulses of 1M glycerol showed both ON and OFF signals consistent with depolarization (Figure 2.21.a.). Similarly, *srg-34* and *srg-36* expression in ASH resulted in signals consistent with depolarization of the membrane in response to 1 µM C3 (Figure 2.21.a). These results suggest that the calcium signals observed here in ASH correlate with depolarization of the neuron.

The initial dynamics of the calcium responses elicited by each *srg* receptor were also reflected in the depolarization kinetics mediated with macCitrine. *srg-34* mediated depolarization was rapid and peaked within 1 s, whereas *srg-36* mediated depolarization ramped slowly and peaked at stimulus removal (Figure 2.21). No fluorescence change was observed in worms without all-trans retinal exposure (Figure 2.21.a.). These results demonstrate that ASH calcium activation dynamics are correlated with membrane voltage.

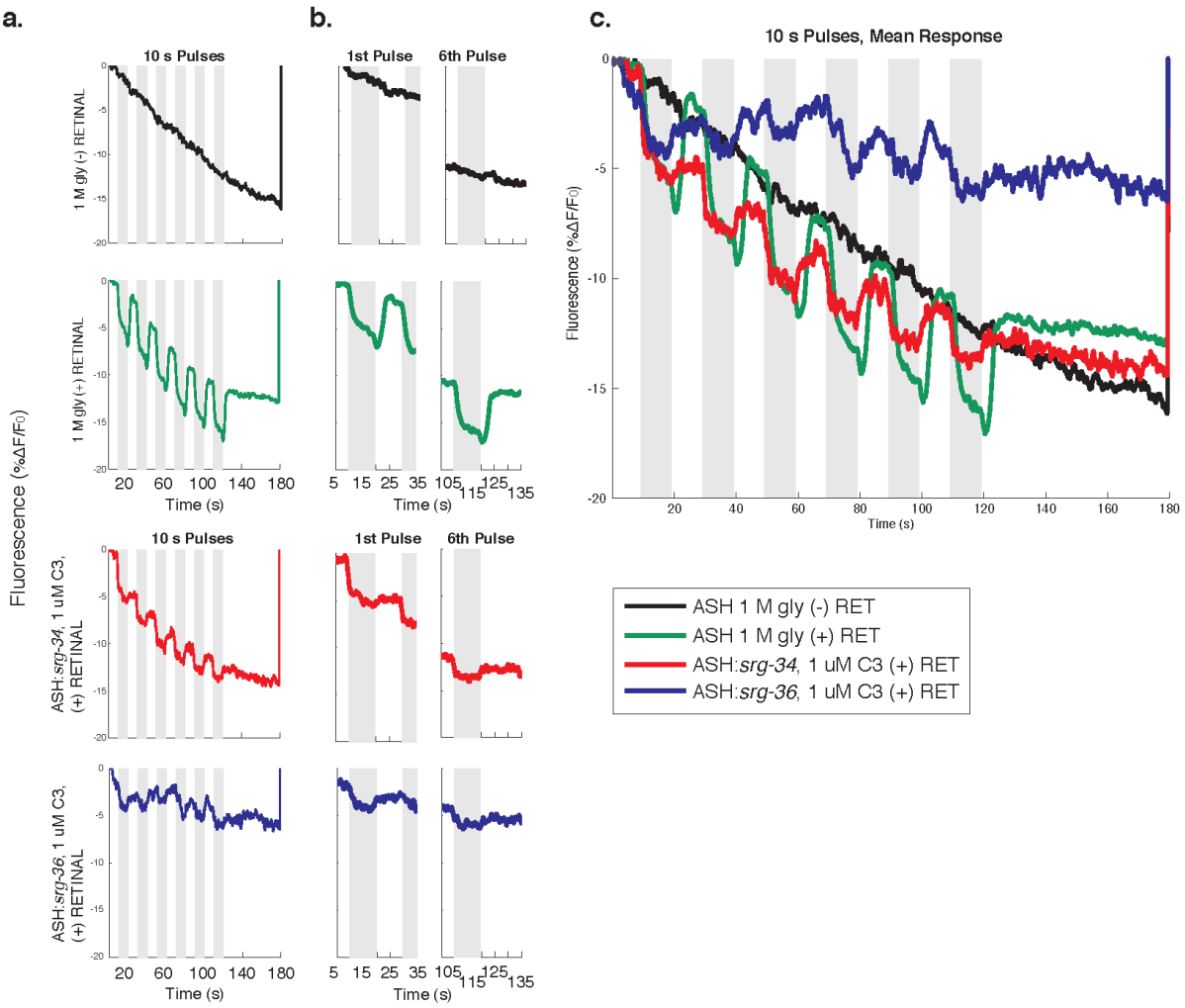

Figure 2.21. Stimulus-triggered depolarization of ASH.
a) macCitrine expressed in ASH under the *sra-6* promoter allows visualization of membrane voltage through fluorescence change. Fluorescence decreases with depolarization. Both the onset and removal of 1 M glycerol elicit fluorescence decreases in ASH:macCitrine, suggesting depolarization to both events. These responses require all-trans retinal. Fluorescence decreases in response to 1 µM C3 in ASH neurons expressing *srg-34* and *srg-36* are weaker. ASH response in six consecutive 10 s pulses of stimuli. **b)** Fluorescence changes to first and last pulse at shorter timescales. d) Comparison of mean response in each condition.

Discussion

Diversity of ASH responses

In order to probe how temporally different nociceptive cues instruct a small neural circuit to generate avoidance behavior, temporally divergent stimulation of a single, nociceptive neuron should be used. ASH, the classic polymodal nociceptor in *C. elegans*, is responsible for mediating avoidance behaviors to mechanical and chemical stimuli. Without ASH, responses to bitter compounds, heavy metals, nose touch, and high osmolarity stimuli are diminished. In published calcium imaging experiments, ASH was previously shown to exhibit positive-polarity calcium responses to these stimuli that were dependent on a subset of G-protein cascade molecules (Hilliard et al*.,* 2005; Ferkey et al*.,* 2007). In a temporally sensitive imaging assay in a microfluidic chip, a small positive polarity response was also observed to stimulus removal (Chronis et al*.,* 2007). Using 10 s pulses of stimuli as well as a rapid fluctuating white-noise stimulus presentation protocol, I found that ASH calcium responses showed far more diversity than previously demonstrated to different aversive stimuli and in different mutant backgrounds. Divergent responses to the same stimulus to stimulations at different timescales were also observed.

Specifically, linear filters generated from white-noise stimulation of ASH with 1 M glycerol revealed a dominant wild-type response to 1 M glycerol that shows positive polarity calcium increases to stimulus onset that peaked at 3 s and lasted around 10 s (Figure 2.4.; Kato et al., 2014). This linear filter thus accumulates the history of stimulus encounter by emphasizing events 3 s in the past and “remembering” 10 s of past encounters. Despite the fact that 10 s pulses of 500 mM NaCl stimulates different calcium dynamics from ASH as 10 s pulses of 1 M glycerol, the derived linear filter to both of these stimuli are essentially identical, suggesting that the ASH neuron, when generating a filter of stimulus history, attends to the same features in both stimuli.

An ordinary differential equation model of this linear filter predicts that this broad, positive temporal filter is biphasic and can be further broken down into a slightly shorter filter of positive polarity representing stimulus-triggered activation of ASH and a long, negative polarity filter representing adaptation. A loss of function mutation in the voltage-gated calcium channel, EGL-19, results in ablation of this latter component, showing in both ASH calcium traces (Figure 2.10.b.) and in behavior (not shown here; Kato et al., 2014) that the stimulus-evoked response lasts longer and does not adapt. This positive polarity ASH response filter is sensitive to disruption of the G-protein cascade –specifically, mutation of the ODR-3 G-alpha protein

obliterates this response filter to glycerol and the specific rescue of ODR-3 in ASH rescues the glycerol response both to rapidly fluctuating stimuli and to long 10 s pulses of stimuli.

One important limit of this work is that the ASH response to many repellents is not linear, and therefore violates assumptions of the LN model. A significant nonlinearity is that ASH responds positively both to addition and to removal of some repellents, including glycerol and copper. The LN model fuses these two elements, capturing the rapid off response in a small, initially negative component that peaks in the first ~1s, and the slower on response in the slower positive component of the filter that peaks around 6s. Mutation of some proteins in the G protein cascade, such as RGS-3 and GRK-2, emphasize the short, negative-polarity impulse response to 1 M glycerol that represents the off response. The off response is robust, but while its magnitude is affected by total stimulus exposure, its dynamics are not sensitive to short-term stimulus history. White-noise stimulation with glycerol generates ASH responses that are dominated by the positive polarity, stimulus-integrating filter, but white noise stimulation of ASH with copper are dominated by the negative polarity linear response filter, as are the GRK-2 and RGS-3 mutant responses.

Canonical ASH stimuli also stimulate non-nociceptive neurons

The nociceptive ASH is capable of exhibiting diverse temporal responses to different aversive stimuli. While it may be ideal to use these natural stimuli to investigate how ASH utilizes different temporal cues to instruct downstream interneurons, I found that these stimuli do not specifically activate ASH despite previous reports that ASH ablation significantly diminishes avoidance behaviors in response to encountering these stimuli. ASH, ASI, and ASE respond to 1 M glycerol on different timescales (Figure 2.12-2.13). ASEL and ASER responses to 1 M gly proved to be temporally asymmetric, with both neurons required to further stimulate ASI activity in response to 1 M glycerol. ASI also responds to two other “canonical” ASH stimuli, quinine and copper, without known behavioral consequence (Appendix Figures 2.6 and 2.7). With the sensory neuron ASE thus acting as an interneuron for glycerol stimulus to ASI and with both ASE and ASI neurons contributing to the same interneuron circuits as ASH, it would be difficult to assesss how the ASH nociceptor alone can instruct downstream interneurons to generate subsequent avoidance behaviors using temporally divergent cues.

Ectopic pheromone receptors allow cell-specific activation of the ASH nociceptor

We turned to the ectopic expression of the pheromone receptors *srg-34* and *srg-36* in ASH in order to better control cell-specific ASH calcium dynamics. Both of these receptors responded to the same concentration range of the ascaroside C3, but they responded with different dynamics. In long 10 s or 30 s stimulations, ASH neurons expressing *srg-34* showed a fast peaking, fast adapting calcium signal at most concentrations. ASH neurons expressing *srg-36* responded to C3 with a slow, ramping calcium signal that did not adapt throughout C3 exposure. Temporal differences were also evident in the response to white noise stimuli: the linear filter for *srg-36* peaked around 3s after stimulus presentation, whereas the linear filter for *srg-34* peaked in a second.

History accumulating linear filters vs. impulse linear filters

ASH linear temporal filters appear to fall into two timescales: a positive polarity filter that accumulates stimulus history for 10 s and most heavily emphasizes the past 3 s, and a short, fast, impulse stimulus that does not accumulate stimulus history. It is possible that these different filter timescales are salient to different members of the downstream interneuron circuit, or that they serve different roles in nociceptive signaling. Fast activating, fast adapting responses that do not measure the history of stimulus encounter may instruct a deterministic, reflexive circuit, for instance, in which not avoiding the stimulus could result in immediate damage. A slower signal that accumulates a long history of stimulus encounter may instead be salient for cues that require more temporal summation so that the stimulus can be ignored until it reaches a certain threshold. It is also possible that ASH tracks non-aversive aspects of certain signals in addition to its nociceptive duties.

CHAPTER 2: Appendix

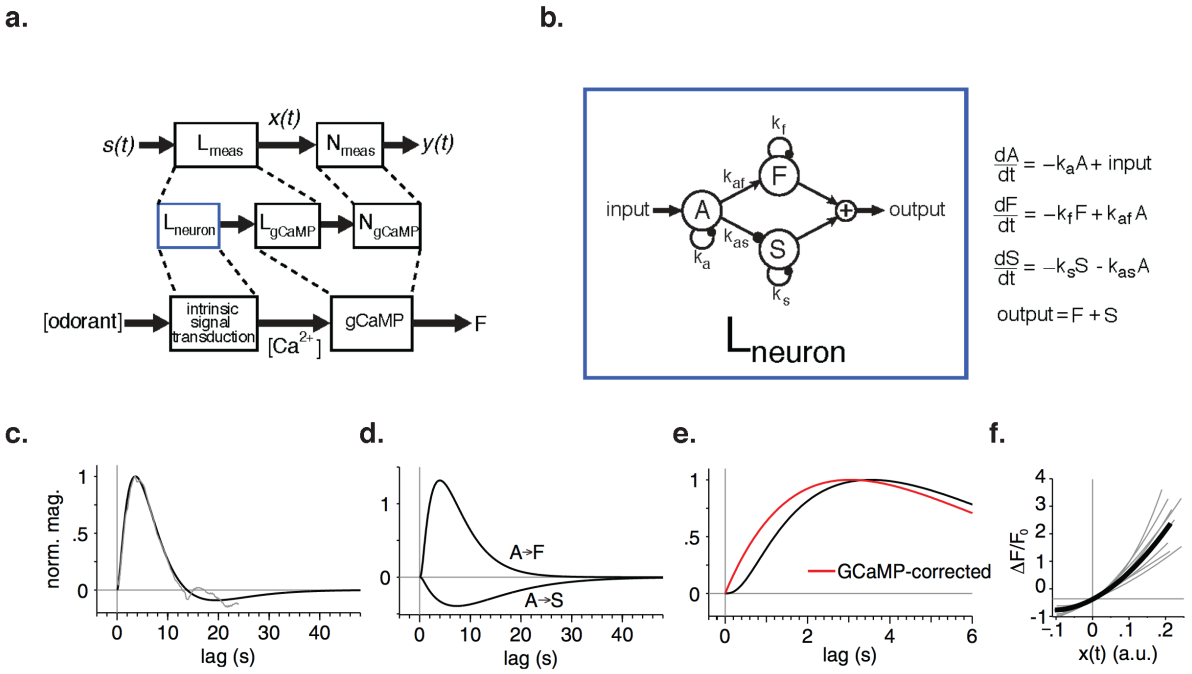

Appendix Figure 2.1. The Linear-Nonlinear (LN) and Linear-Nonlinear Ordinary Differential Equations (LN-ODE) model cascades (from Kato *et al.*, 2014).
a) Schematic of L-N model showing transformation of stimulus through the linear (L) and nonlinear (N) filters into the observed calcium signal. The measured linear filter (L_{meas}) is the combined linear filter from both the neuron and GCaMP linearity while the measured nonlinear filter (N_{meas}) is comprised from the GCaMP nonlinearity alone. **b)** A three-variable ODE model with optimized kinetic constants is able to recapitulate the linear filter of the neuron (L_{neuron}). **c)** The biphasic linear filter generated by the ODE model can be further decomposed into two filters of different timescales, **d)** a fast (A→F) filter of positive polarity and a slow (A→S) filter of negative polarity corresponding to the transformations between the input and outputs of variable F and S in (b). **e)** While not directly measureable, the intrinsic neural linear filter of ASH can be deconvolved from the measured linear filter by removing the theoretical dynamic effect of GCaMP3; this lends a model intrinsic linear filter of ASH neuron that peaks slightly faster than the measured response (red, "GCaMP corrected"). **f)** The nonlinear component of the LN model has a mean exponent of 1.8, near the Hill coefficient of 2.3 describing the cooperative dependence of GCaMP3 fluorescence intensity on calcium binding (Tian *et al.*, 2009); this suggests that the nonlinear component of the LN model is mostly due to the dynamics of GCaMP itself, and that the ASH temporal filter is near-linear.

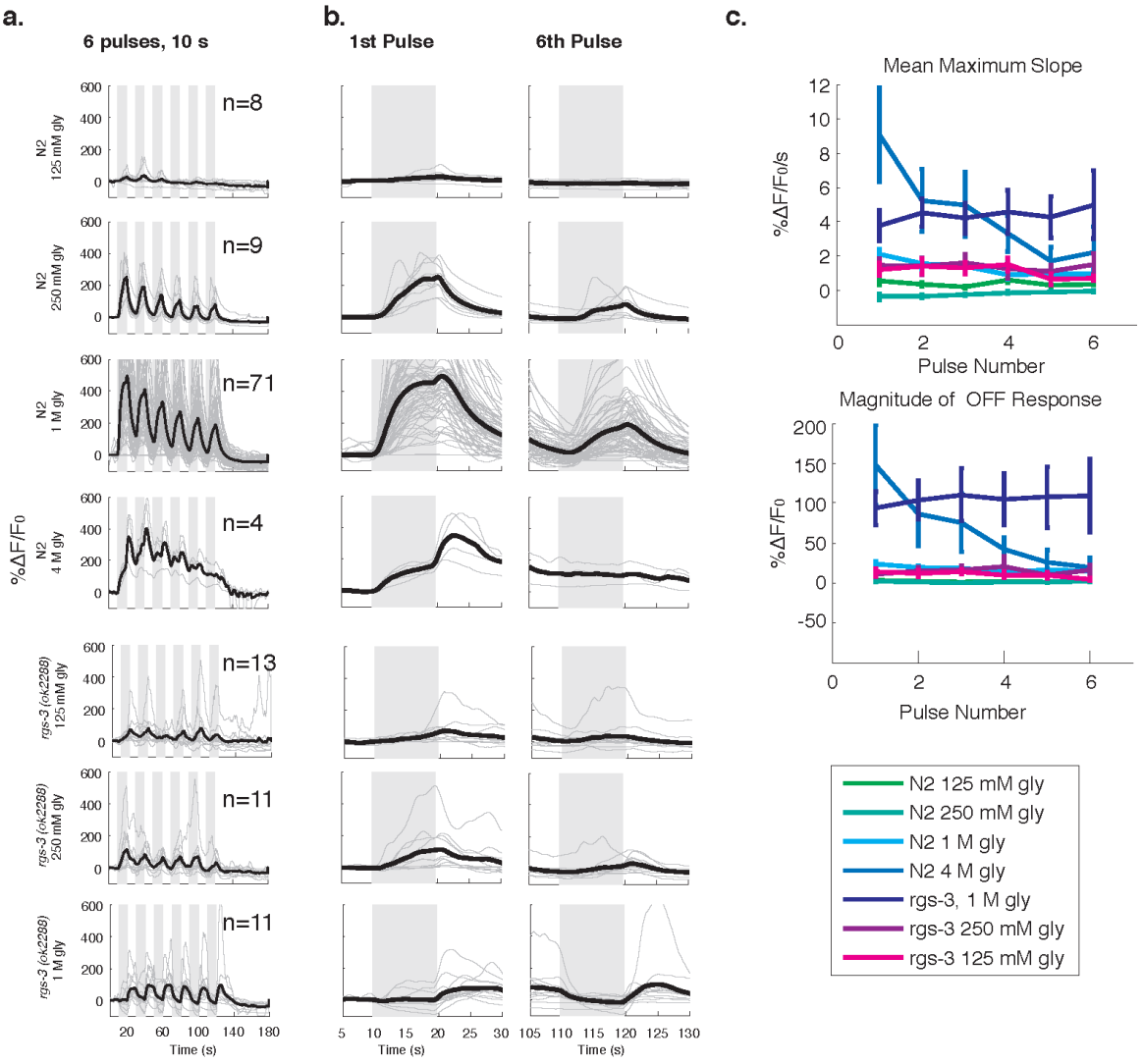

Appendix Figure 2.2. The regulator of G-protein cascade mutant *rgs-3* response to 1 M glycerol recapitulates some dynamics of wild-type response to higher concentration stimuli.
a) N2 response to 6 consecutive 10 s pulses of 125 mM, 250 mM, 1 M, and 4 M gly compared to the *rgs-3* mutant response to 125 mM, 250 mM, and 1 M gly. The nonlinear impulse response to glycerol removal dominates the highest concentration response in each genotype. **b)** Calcium responses to first and last 10 s stimulations at expanded timescales. **c)** Quantification of maximum slope and magnitude of OFF response for each condition for six consecutive pulses of stimuli. N2 response to 4 M glycerol and *rgs-3* response to 1 M glycerol exhibit similar high maximum slopes and height change to glycerol removal. (Centered at mean, vertical bars = standard error of the mean).

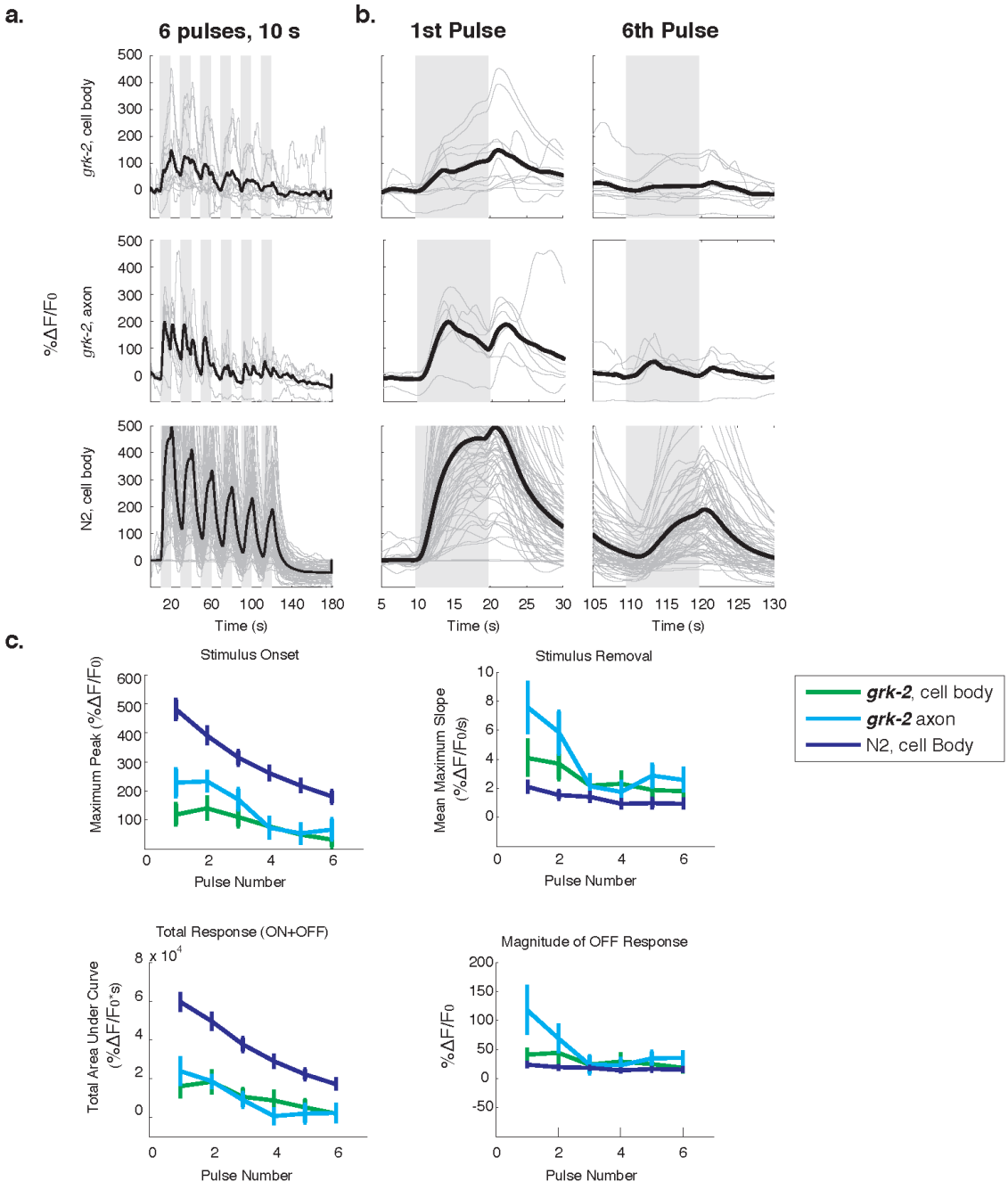

Appendix Figure 2.3. The GPCR kinase mutant *grk-2* has stronger axonal than cell body calcium responses.

a) Response to six consecutive 10 s pulses of 1 M glycerol in wild-type ASH cell body, *grk-2* cell body, and *grk-2* axons. **b)** Calcium responses to first and last 10 s stimulations at expanded timescales. **c)** Maximum peak of the ON response, maximum slope of the OFF response, Total response area, and the magnitude of the OFF response for N2, *grk-2* cell body, and *grk-2* axon (centered at mean, vertical bars = standard error of the mean).

a.

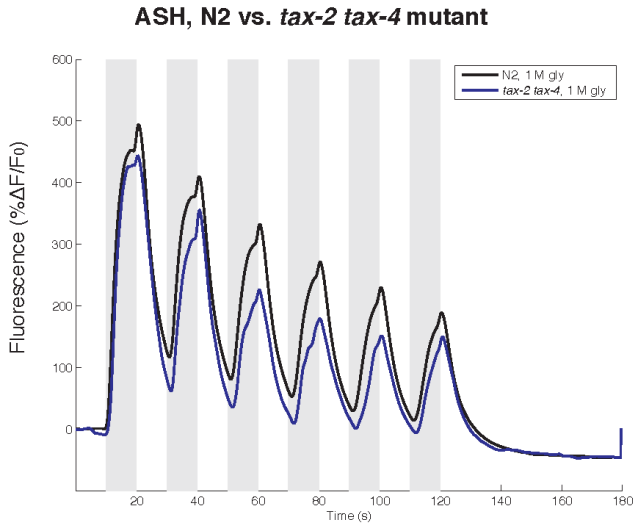

b.

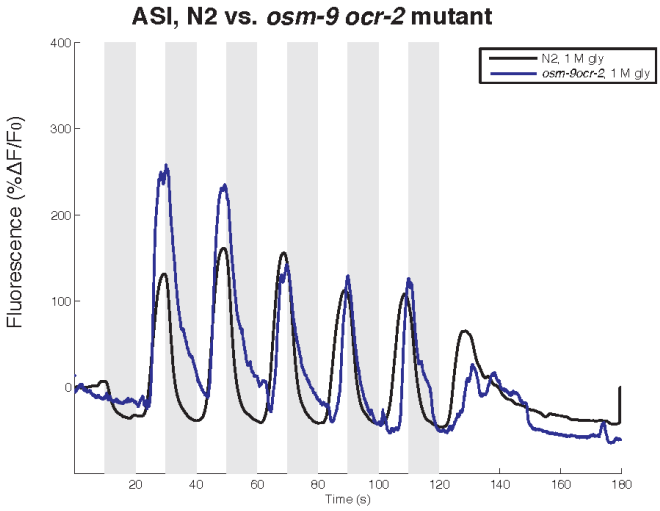

Appendix Figure 2.4. ASH responses do not depend on signaling from *tax-2 tax-4* requiring neurons. ASI responses do not depend on signaling from *osm-9 ocr-2* requiring neurons.
a) ASH responses to 10 s pulses of 1 M glycerol in both the wild-type and the *tax-2 tax-4* mutant that lacks functional ASI and ASE neurons. **b)** ASI responses to 10 s pulses of 1 M glycerol in wild-type and in the *osm-9 ocr-2* mutant that lacks functional ASH neurons.

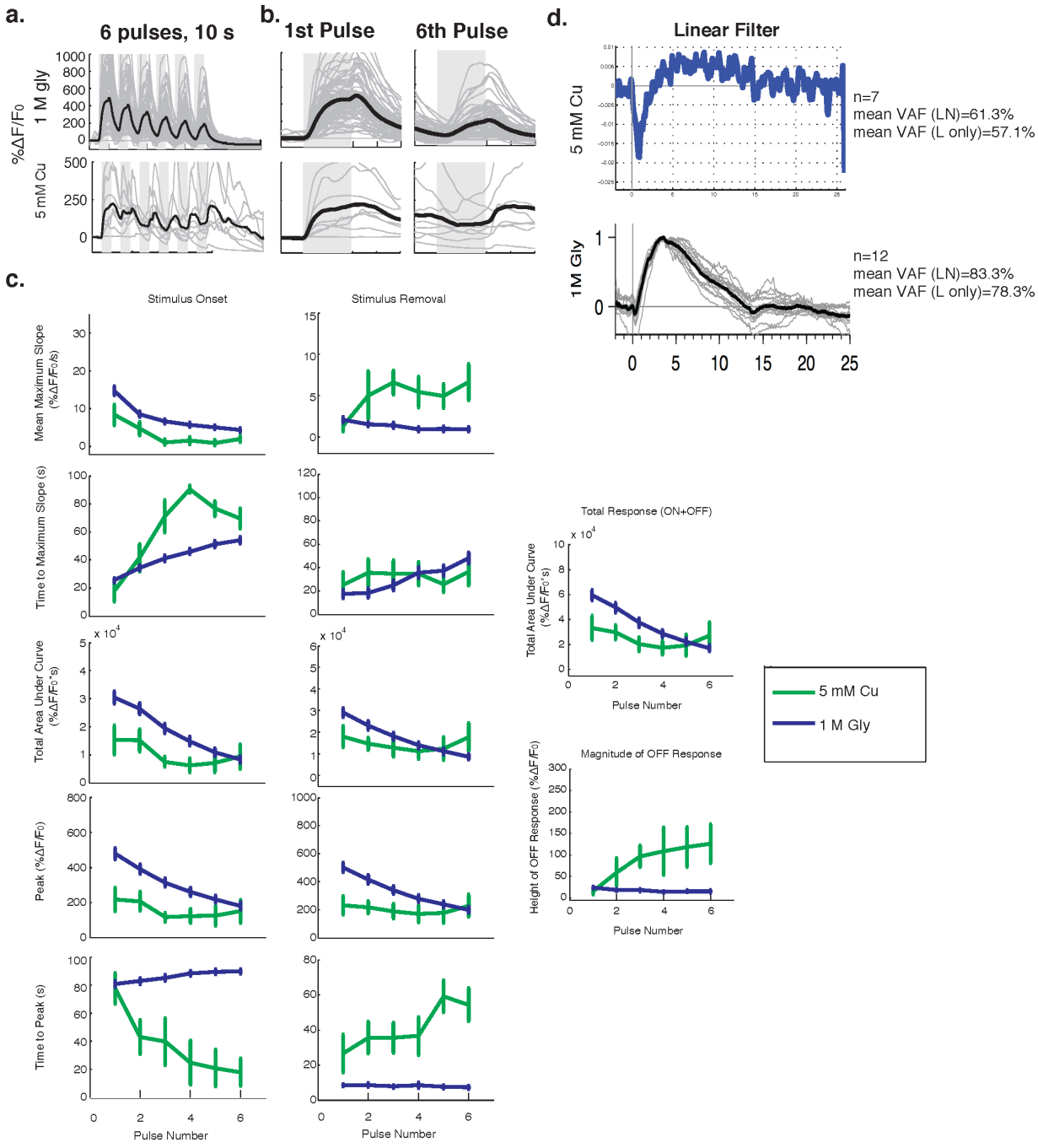

Appendix Figure 2.5. ASH responds to copper with different dynamics than glycerol.
a) ASH response to 6 consecutive 10 s pulses of 1 M glycerol or 5 mM copper (1M gly, n=71; 5 mM Cu, n=8) **b)** Calcium response to first and last 10 s stimulations at expanded timescales. **c)** Maximum slope, time to maximum slope, integrated calcium response (by total area under curve), peak, and time to peak quantified for each of 6 successive 10 sec pulses for each stimulus. Vertical bars = standard error of the mean. **d)** ASH temporal linear filters generated from copper (from 7-bit word length, 2 s m-sequence) and glycerol (from 9-bit word length 200 ms m-sequence) stimulus.

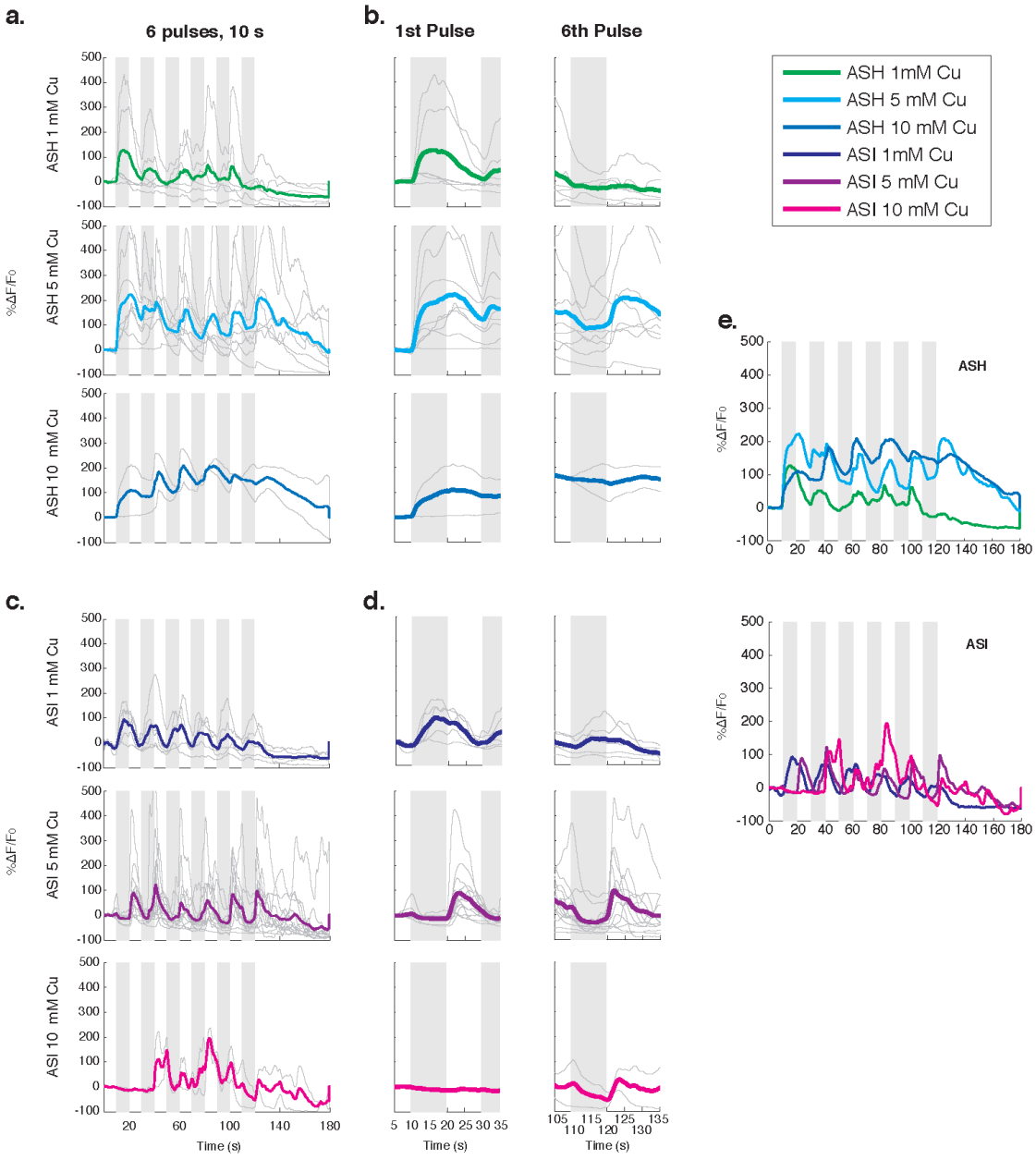

Appendix Figure 2.6. Wild type and mutant ASH and ASI neurons both respond to 1-10 mM copper.

a) ASH responses to 6 consecutive 10 s presentations of 1 mM (n=6), 5 mM (n=8), and 10 mM (n=2) Cu2+. **b) and d)** Calcium response to first and last 10 s stimulations at expanded timescales. **c)** ASI responses to 6 consecutive 10 s presentations of 1 mM (n=5), 5 mM (n=13), and 10 mM (n=2) Cu2+. Means in color, individual trials in light gray. **e)** Comparison of means of ASH and ASI response to copper concentrations.

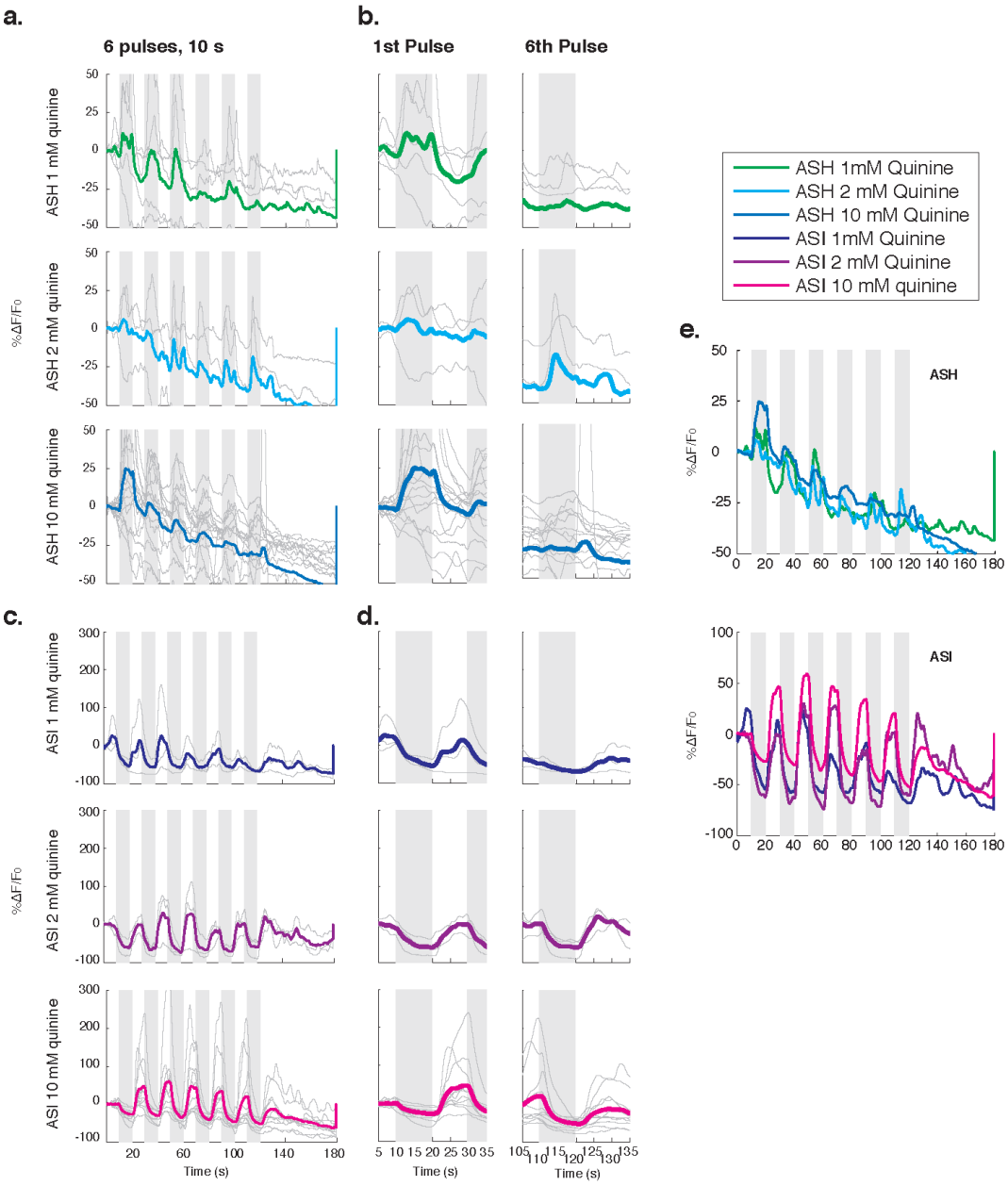

Appendix Figure 2.7. Wild type and mutant ASH and ASI neurons both respond to 1-10 mM quinine.

a) ASH responses to 6 consecutive10 s presentations of 1 mM (n=5), 2 mM (n=3), and 10 mM (n=16) quinine. **b) and d)** Calcium response to first and last 10 s stimulations at expanded timescales. **c)** ASI responses to 6 consecutive 10 s presentations of 1 mM (n=3), 2 mM (n=3), and 10 mM (n=11) quinine. Means in color, individual trials in light gray. **e)** Comparison of means of ASH and ASI response to quinine concentrations.

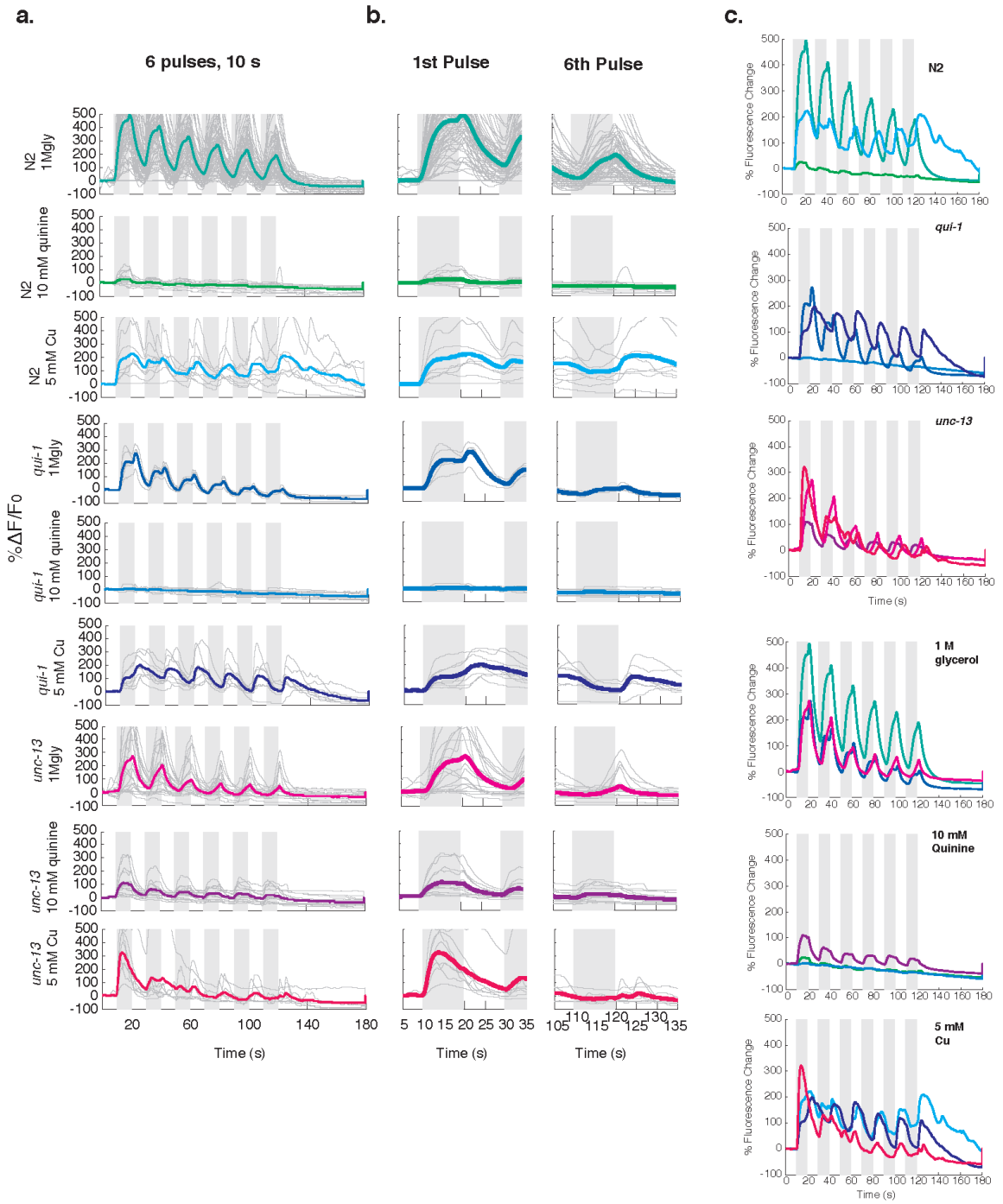

Appendix Figure 8. ASH responses to glycerol, copper, and quinine in *qui-1* and *unc-13* backgrounds.

a) N2, *qui-1*, and *unc-13* mutant ASH responses to 6 consecutive 10 s presentations of 1 M gly, 10 mM quinine and 5 mM Cu. N2: 1M gly, n=71; 10 mM quinine, n=16; 5 mM Cu, n=8. *qui-1*: 1M gly, n=6; 10 mM quinine, n=15; 5 mM Cu, n=8. *unc-13*: 1M gly, n=27; 10 mM quinine, n=15; 5 mM Cu, n=8. **b)** Calcium response to first and last 10 s stimulations at expanded timescales. Means in color, individual trials in light gray. **c)** Comparison of mutant and wild-type ASH responses to each stimulus.

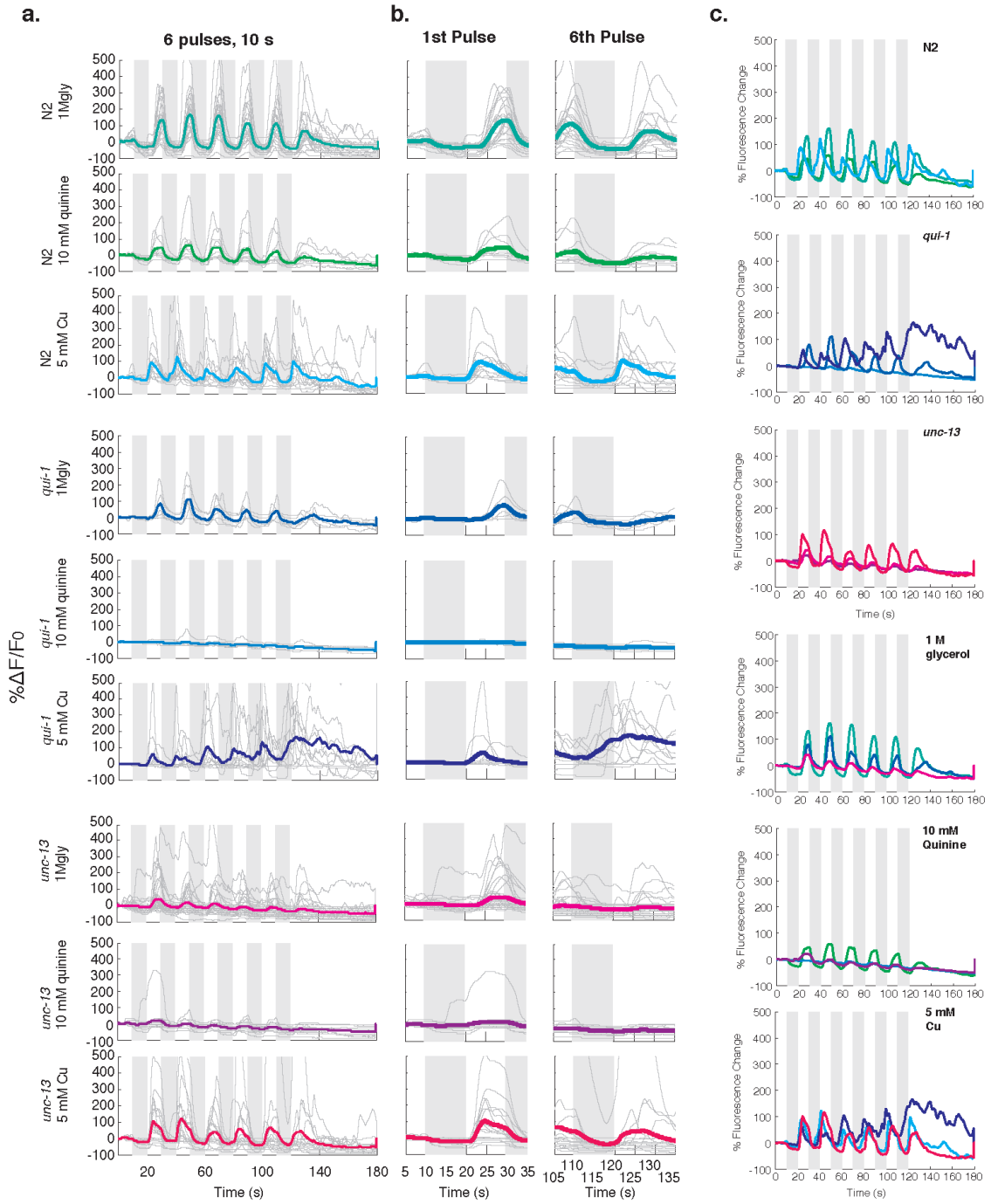

Appendix Figure 9. ASI responses to copper, quinine, and glycerol in *qui-1* and *unc-13* backgrounds

a) N2, *qui-1*, and *unc-13* mutant ASI responses to 6 consecutive 10 s presentations of 1 M gly, 10 mM quinine and 5 mM Cu. N2: 1M gly, n=25; 10 mM quinine, n=11; 5 mM Cu, n=13. *qui-1*: 1M gly, n=6; 10 mM quinine, n=11; 5 mM Cu, n=11. *unc-13*: 1M gly, n=46; 10 mM quinine, n=14; 5 mM Cu, n=18. **b)** Calcium response to first and last 10 s stimulations at expanded timescales. Means in color, individual trials in light gray. **c)** Comparison of mutant and wild-type ASI responses to each stimulus.

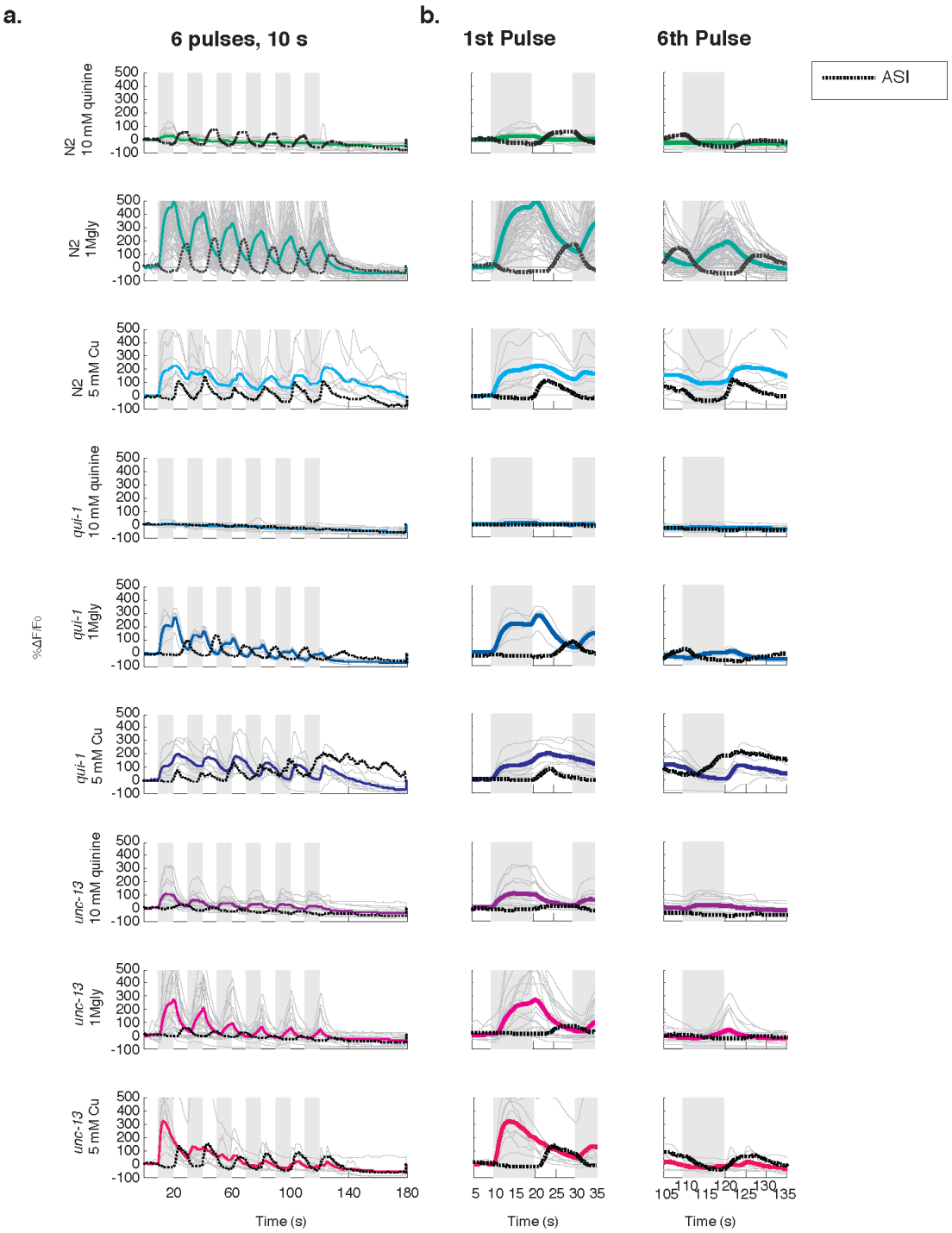

Appendix Figure 2.10. Wild type and mutant ASH and ASI neurons respond to multiple aversive stimuli with diverse dynamics.
a) Overlaid ASH (in color) and ASI (dotted line) mean responses in N2, *qui-1*, and *unc-13* mutants to 10 mM quinine, 5 mM Cu, and 1 M gly; response to 6 consecutive 10 s pulses of stimulus. **b)** Calcium response to first and last 10 s stimulations at expanded timescales.

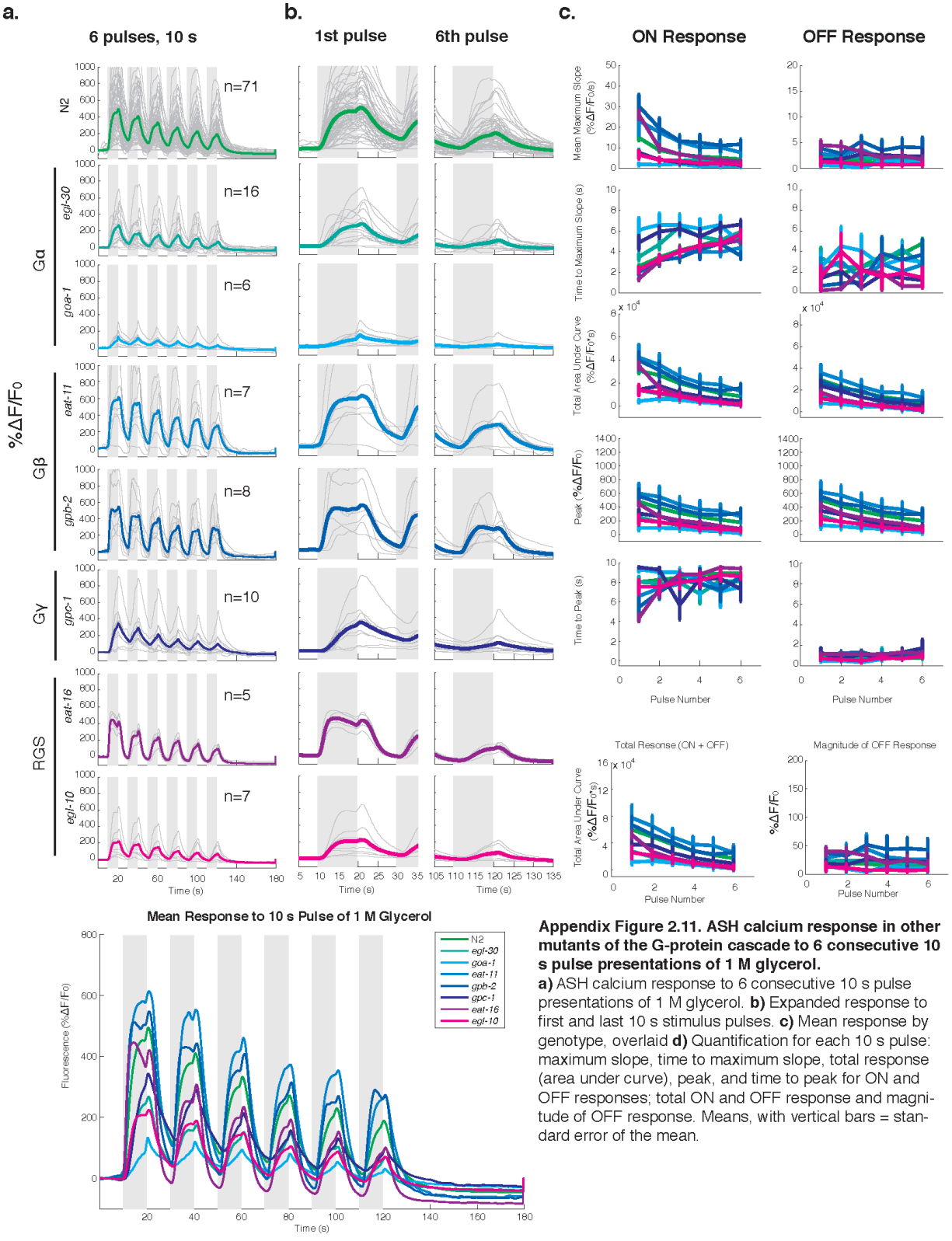

Appendix Figure 2.11. ASH calcium response in other mutants of the G-protein cascade to 6 consecutive 10 s pulse presentations of 1 M glycerol.
a) ASH calcium response to 6 consecutive 10 s pulse presentations of 1 M glycerol. **b)** Expanded response to first and last 10 s stimulus pulses. **c)** Mean response by genotype, overlaid **d)** Quantification for each 10 s pulse: maximum slope, time to maximum slope, total response (area under curve), peak, and time to peak for ON and OFF responses; total ON and OFF response and magnitude of OFF response. Means, with vertical bars = standard error of the mean.

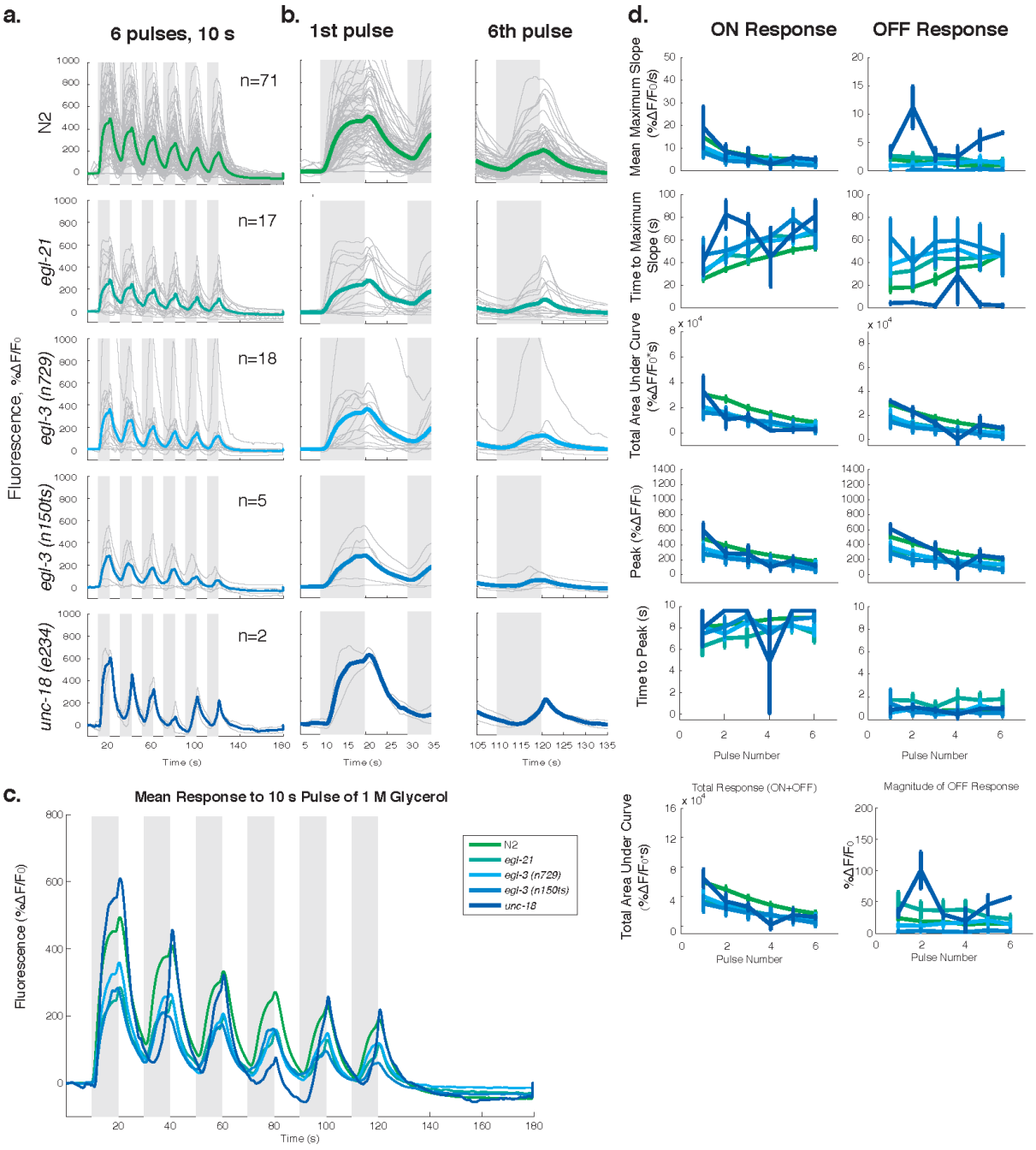

Appendix Figure 2.12. ASH calcium response in neurotransmitter release mutants to 6 consecutive 10 s pulse presentations of 1 M glycerol.

a) ASH calcium response to 6 consecutive 10 s pulse presentations of 1 M glycerol (*egl-21*, n=17; *egl-3 (n729)*, n=18; *egl-3 (n150ts)*, n=5; *unc-18 (e234)*, n=2), . **b)** Expanded response to first and last 10 s stimulus pulses. **c)** Mean response by genotype, overlaid **d)** Quantification for each 10 s pulse: maximum slope, time to maximum slope, total response (area under curve), peak, and time to peak for ON and OFF responses; total ON and OFF response and magnitude of OFF response. Means, with vertical bars = standard error of the mean.

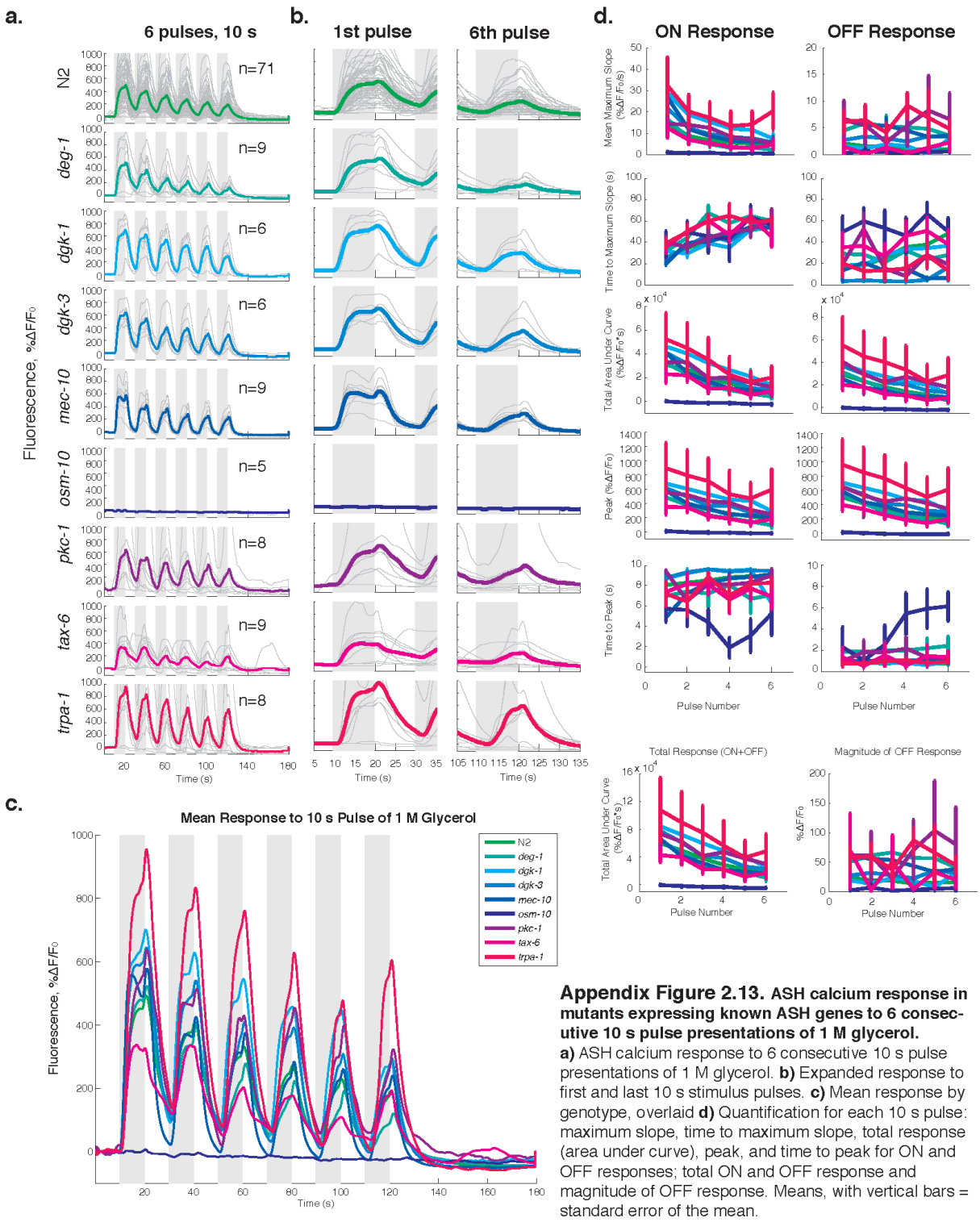

Appendix Figure 2.13. ASH calcium response in mutants expressing known ASH genes to 6 consecutive 10 s pulse presentations of 1 M glycerol. **a)** ASH calcium response to 6 consecutive 10 s pulse presentations of 1 M glycerol. **b)** Expanded response to first and last 10 s stimulus pulses. **c)** Mean response by genotype, overlaid **d)** Quantification for each 10 s pulse: maximum slope, time to maximum slope, total response (area under curve), peak, and time to peak for ON and OFF responses; total ON and OFF response and magnitude of OFF response. Means, with vertical bars = standard error of the mean.

Appendix Table 2.1. Types of linear and nonlinear calcium signals encountered in m-sequence stimulation.

Type of Linear Calcium Signal	Signature	Example	Notes
Symmetric linear with temporal summation	Linear filter convolves stimulus presented at diverse temporal regimes into accurate representation of neural response to that stimulus	WT ASH,1 M glycerol, after initial transient adapts	Ideal for L-N model, indicates neuron is tracking time history of stimulus presentation
Type of Nonlinear Calcium Signal	**Signature**	**Example**	**Notes**
Reliable Nonlinearity	**Stereotyped calcium responses to identical stimulus within and between individuals**		
Static nonlineaity	Applying nonlinear functionafter linear filter convolution further improves VAF	Static GCaMP3 nonlinearity for calcium binding	Simplest nonlinearity, captured by L-N model
Asymmetric nonlinearity			
-Asymmetric ON/OFF response	Different stimulus-triggered average responses generated by ON stimulus and OFF stimulus alignments; OFF impulse is inverse of ON impulse but with additional features	WT ASH, 1 M glycerol	Fast stimulation regimes potentially combines ON and OFF responses into single linear filter, dominated by the larger response.
-Impulse without temporal summation	One cycle of response must terminate before next cycle can begin (stimulus triggered average responses will shown that only ON or OFF filter exists, OFF filter is not inverse of ON filter)	(ADL/AWA, not shown)	Stimulation must be longer than entire response sequence in order to generate accurate linear filter; neuron is generating robust response but is free running other than onset of first stimulation
Transient gain nonlinearities			
-Initial baseline shift	Initial response to stimulus presentation results in baseline shift that adapts over time	WT ASH, 1 M glycerol	Begin VAF calculation after minimum initial exposure length. Partially resolved in ASH glycerol responses with slow negative polarity component of biphasic filter in LN-ODE model.
-Stochastic gain change	Stochastic shifts in gain throughout responses that differ in time of occurance within and between individuals	WT ASH, copper	Trial averaged VAF will be significantly higher than VAF of individual trials; SNR will be low.
Charge-requiring nonlinearity	Reliable response begins only after a minimum length of initial exposure	WT ASI, glycerol	Begin VAF calculation after minimum initial exposure length
Unreliable nonlinearity	Pure noise to repeated stimuli, signal to noise ratio (SNR) between traces < 2	300 uM DHCA, Quinine	Neural activation is not tied to continued stimulus onset or removal in any measureable way.

a.

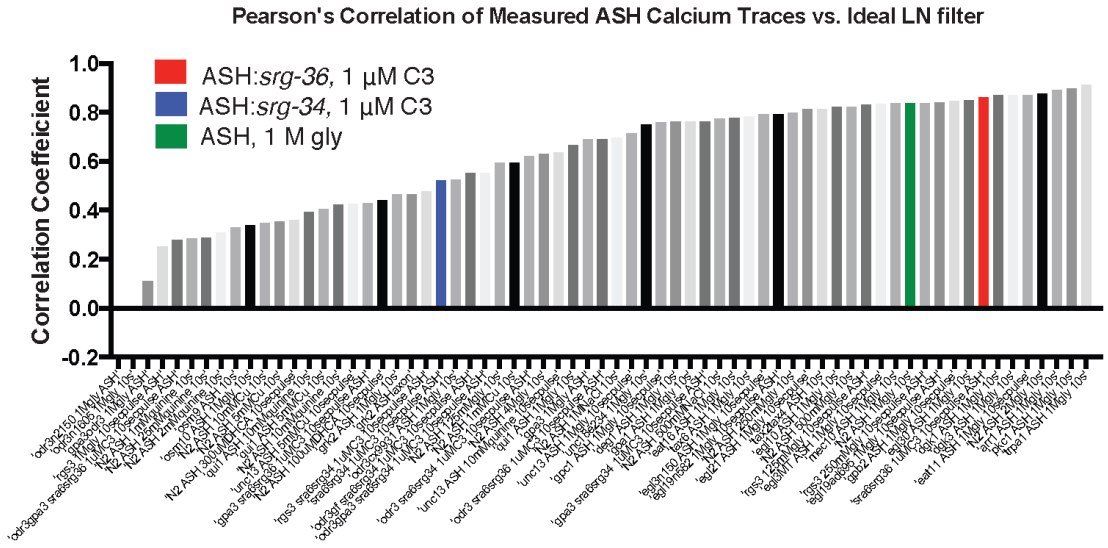

b.

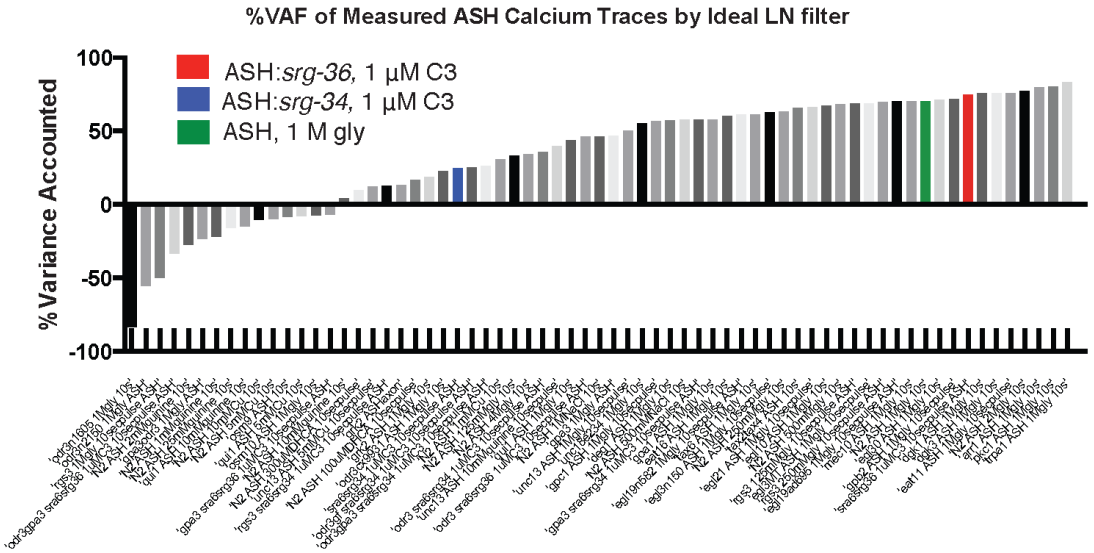

c.

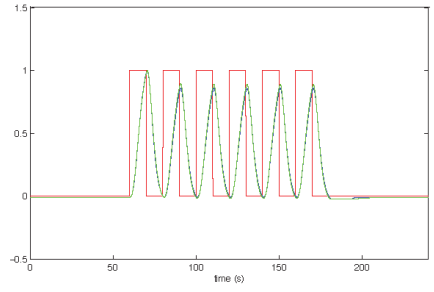

Appendix Figure 2.14. Closeness of fit between 10 s pulse responses from the ideal LN glycerol filter to measured ASH 10 s pulse responses in various conditions and genotypes
a) Pearson's correlation of measured mean ASH 10 s pulse responses to the ideal response shown in **c)**. The ASH:*srg-36,* 1 µM C3 response (red) is closer to the ideal LN filter generated response than the 1 M glycerol response (green). The mean ASH:*srg-34,* 1 µM C3 trace poorly resembles the ideal trace (blue). **b)** The ideal LN filter accounts for a significant amount of both ASH:*srg-36,* 1 µM C3 and 1 M glycerol responses, with slightly more variance accounted for in the ASH:*srg-36,* 1 µM C3 trace. The ideal LN filter explains only a small percent of variance for ASH:*srg-34,* 1 µM C3 traces.

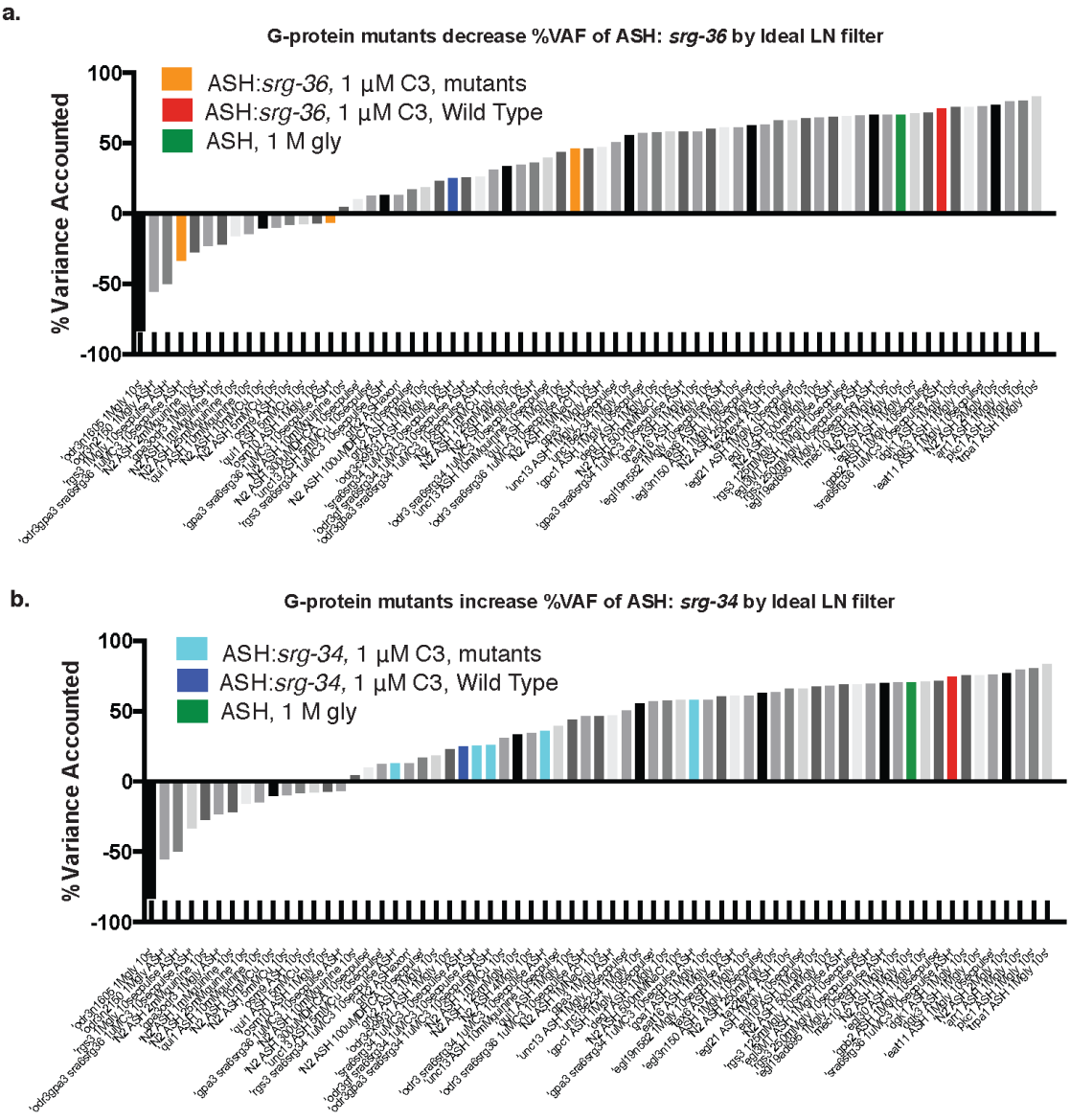

Appendix Figure 2.15. G-protein mutants decrease the %VAF of *srg-36* responses and increase the %VAF of *srg-34* responses by the ideal L filter

a) All G-protein mutants backgrounds with ASH:*srg-36,* 1 µM C3 (orange) showed a decrease in %VAF compared to the wild-type trace (red). From lowest %VAF to highest %VAF, orange bars are as follows: *odr-3 gpa-3, gpa-3, odr-3.* b) Most G-protein mutant backgrounds with ASH:*srg-34,* 1 µM C3 (light blue) showed an increase in % VAF compared to the wild-type trace (dark blue). From lowest %VAF to highest %VAF, light blue bars are as follows: *rgs-3, odr-3 gf, odr-3 gpa-3, odr-3 lf, gpa-3.* All srg-34 responses remain below the %VAF for glycerol and ASH:*srg-36,* 1 µM C3 responses.

CHAPTER 3: Temporal dynamics of nociception and avoidance behavior

Summary

The polymodal nociceptor ASH synapses directly onto the backward command interneuron AVA to evoke reversal behaviors. ASH can also indirectly stimulate AVA through the intermediate level interneuron AIB. I investigated whether different calcium dynamics evoked in ASH can differently access each of these pathways. Time-aligned behavior histograms to onset, presence, and removal of the ascaroside C3 showed that the probability of avoidance behaviors in populations expressing ASH:*srg-36* or ASH:*srg-34* reflected their respective calcium activation time course in ASH. However, this seemingly simple transformation from sensory neuron activity to behavior was differently dependent on AVA and AIB. The slow, ramping calcium signal of ASH:*srg-36* to 1 µM C3 did not stimulate avoidance behaviors when AIB was silenced, whereas ASH:*srg-34* triggered normal avoidance behaviors under this condition, For both receptors, silencing AVA led to a decrease in reversal behaviors, but a compensatory increase in other avoidance behaviors such as pausing. Calcium levels of AVA and AIB were measured in freely moving ASH:*srg-36* or ASH:*srg-34* worms stimulated by 1 µM C3. In ASH:*srg-34* worms, both neurons initiated calcium increases aligned with each other and aligned with the onset of stimulus. In ASH:*srg-36* worms, however, AIB initiated calcium increases prior to AVA activity. This result suggests that AIB may act as an accumulator of ASH signals that aids in the activation of AVA by slowly increasing aversive signals. A type-1 feed forward loop that uses AND logic in low ASH calcium slopes and OR logic in high ASH calcium slopes was able to model how AIB contributes to the ASH activation of AVA. Feedforward excitatory loops are a motif found in both mammalian and *C. elegans* neural circuits. My findings demonstrate that different temporal dynamics of activation in the same nociceptor neuron can instruct this circuit motif with behaviorally salient consequences.

Introduction

A primary purpose of the nervous system is to respond to salient sensory cues with survival-promoting behavior. Towards this goal, nociception systems throughout the animal kingdom promote avoidance of harmful substances. Indeed, certain nociception circuit motifs are conserved between *C. elegans* and mammals. In one such motif, a sensory neuron synapses onto an interneuron that synapses onto motor neurons that drive muscle contraction. In mammals, this motif occurs in the spinal cord, where the paraspinal Dorsal Root Ganglion

(DRG) sensory neurons that sense peripheral noxious stimuli terminate on spinal interneurons (Figure 1.1). The spinal interneurons activate motor neurons that control the body region from which the sensory signal originated. In *C. elegans*, polymodal noxious cues are sensed by the ASH sensory neurons, whose main postsynaptic output, the command interneuron AVA, activates motor neurons that promote backward movement (Figure 3.1, de Bono and Maricq, 2005). Some molecules are shared by these disparate avoidance circuits. The ASH neuron requires the *osm-9* and *ocr-2* TRPV channels for activation by noxious stimuli; these channels are *C. elegans* homologues of the mammalian capsaicin receptor TRPV1, which is expressed in subsets of DRG fibers (Julius, 2013). The endpoint of avoidance behavior is also congruous. In humans, the terminal behavior of this circuit is the withdrawal reflex, which can, for example drive contraction of muscle fibers to remove a hand from a hot stove before there is conscious awareness of the burn. Similarly, the headlong encounter of harmful stimuli during forward movement will cause the worm to suddenly stop, withdraw itself with a reversal, and swing its head to meet its tail (the omega turn). This stereotyped "pirouette" behavior ultimately results in forward movement opposite to the initial trajectory (Hilliard et al., 2002).

Previous work suggests that the *C. elegans* avoidance circuit is a hardwired, labeled line linked to activation of ASH. Wild-type *C. elegans* are insensitive to the red chili pepper compound capsaicin. However, ectopically expressing the mammalian capsaicin receptor, TRPV1, in ASH confers capsaicin sensitivity to *C. elegans* so that they execute stereotyped avoidance behavior upon capsaicin encounter (Tobin et al., 2002). This result suggests that activation of ASH is sufficient to generate a reversal behavior resembling a normal ASH-triggered reversal. While this inflexible response seems appropriate in the context of avoiding dangerous stimuli, other results suggest alternative regimes for ASH-directed behaviors. ASH synapses onto many "intermediate layer" interneurons in the nerve ring and is regulated by incoming synaptic connections, gap junctions, biogenic amines, and neuropeptides from other sensory neurons and interneurons before ultimately terminating onto command interneurons (Figure 3.1). In this "indirect" network, both "ascending" and "descending" connections are present, with interneuron classes and sensory neuron classes projecting back and forth in every combination. Sensory neurons in this network transmit responses to temperature, pheromones, volatile and soluble chemicals, mechanical cues, and food quality. The convergence of these inputs onto intermediate interneurons suggests that information entering the circuit is integrated, possibly to generate statistical probabilities of certain basal behaviors (Gray et al., 2005; de Bono et al., 2002).

Downstream of ASH, both direct and indirect synaptic pathways lead to AVA backward command interneurons (Figure 3.1). This organization suggests the possibility of parallel processing of ASH signals. In the shortest pathway, nociceptive cues can promote deterministic avoidance behavior directly by synapses from ASH to AVA. Simultaneously, nociceptive cues can provide indirect input to the command interneuron circuit through intermediate neural circuits that integrate nociceptive cues with other external and internal cues to generate more nuanced behavior incorporating ongoing environmental quality. The existence of parallel nociceptive pathways has been suggested in nose-touch avoidance, an ASH-triggered behavior, where a disinhibition circuit engaged by the intermediate layer interneuron RIM acts in parallel to a stimulatory circuit commanded by AVA to trigger reversals (Piggott et al., 2011). Moreover, there is evidence that ASH activation can be modulated by external and internal cues. The latency to reversal in ASH-dependent avoidance of weak octanol stimuli is either 3 s or 8 s, depending on food presence, serotonin levels, and adrenergic neurotransmitter secretion (Mills et al., 2007). This example of temporally-resolved avoidance behavior provides added information compared to a qualitative response ("to reverse or not to reverse").

Quantification of specific behaviors time-aligned to stimulus encounter can be used to evaluate elements of dynamic ASH-driven behaviors. Automated worm tracking of animals crawling in microfluidic devices enables an analysis of stimulus-aligned, population-scale behavioral time courses in response to attractive and repulsive stimuli (Albrecht and Bargmann, 2011). The behaviors observed in these devices are composed of at least four distinct states (forward, pause, reverse, and omega turn) (Albrecht and Bargmann, 2011). Behavioral tracking in microfluidic devices can be combined with calcium imaging of GCaMP-expressing sensory neurons or interneurons at a rate of 10 Hz (Larsch et al., 2013). These technological developments make it possible to correlate stimulus onset and removal with sensory neuron activity, interneuron activity, and subsequent behavior.

a.

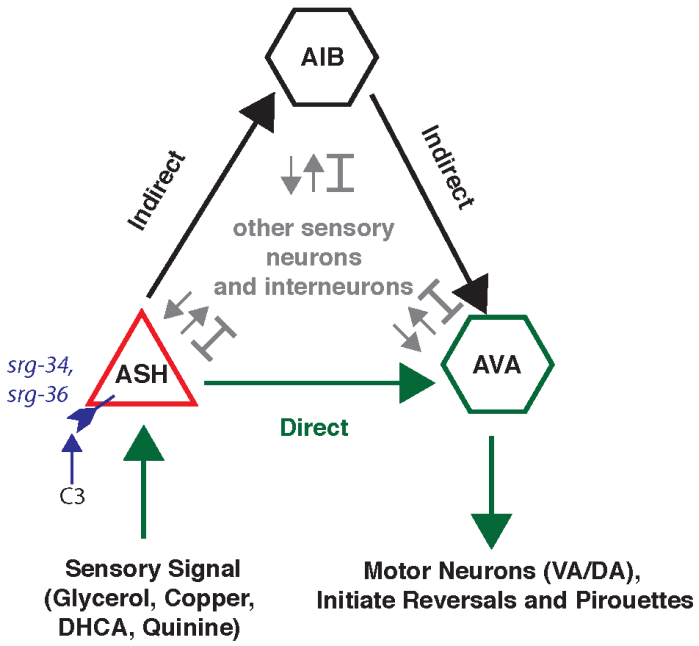

Figure 3.1. ASH can promote avoidance behavior in AVA directly or indirectly
a) Nociceptive signals activate ASH through various endogenous G protein coupled receptors. Ectopic expression of ASH:*srg-34* and ASH:*srg-36* conveys cell-specific ASH sensitivity to the ligand ascarocide C3. ASH can directly activate AVA synaptically to promote avoidance behaviors, or indirectly promote AVA activity through the intermediate interneuron AIB. Additional input regarding external and internal cues from other neurons can act on ASH, AIB, or AVA.

In the previous chapter, I demonstrated that the ectopic, cell-specific expression of ascaroside receptors *srg-34* and *srg-36* can generate receptor-specific calcium dynamics in ASH neurons. Do these ASH activation dynamics instruct different behavioral outcomes? What is their dependence on direct versus indirect anatomical circuits? Using microfluidic behavioral devices, calcium imaging, and selective neuronal silencing, I here investigate the role of ASH activation dynamics in direct and indirect nociception circuits. In this chapter, I show that expressing *srg-34* or *srg-36* chemoreceptors in ASH confers avoidance dynamics to the ascaroside C3 that are comparable to their respective ASH calcium dynamics. A population of worms expressing *srg-34* in ASH rapidly increases avoidance behaviors to stimulus onset and rapidly adapts prior to stimulus offset, while a population of worms expressing *srg-36* in ASH slowly increases avoidance behaviors during stimulus exposure and stops only after the stimulus is removed. The slow ramp of avoidance behaviors is seen in the *srg-36*-expressing population and in individual worms. Moreover, the correlation between calcium dynamics of the sensory neuron and the dynamics of C3 avoidance behavior is consistent over a 10-fold

concentration range of C3. Using chemically-induced cell-specific hyperpolarization, I show that fast *srg-34*-mediated ASH behavior dynamics require only AVA to generate correct motor patterns, but slow-ramping *srg-36*-mediated ASH behavior dynamics require the intermediate-layer interneuron AIB to generate avoidance. ASH calcium signals are therefore not faithfully transmitted to the command motor neuron in a single pathway; instead, the behavior generated by ASH activation is transmitted from the sensory neuron through direct and indirect pathways to the command interneurons.

Tracking avoidance behaviors in microfluidic devices

C. elegans animals crawling among the posts of a microfluidic device experience different spatial constraints compared to the same animals crawling in an agar plate (Figure 3.2.a). Upon entering the device, animals exhibit high reversal frequencies that decrease until a stable baseline is reached about 20 min after entry (Albrecht and Bargmann, 2011). Therefore, stimulus presentation and behavior tracking are typically started 20-25 min after worms enter the microfluidic device to bypass this initial adaptation to the microfluidic environment (Albrecht and Bargmann, 2011).

Recordings of behaviors from a population of 25-30 worms per arena were analyzed for behavior in response to noxious stimuli sensed by ASH, with behaviors time-aligned to stimulus presentation times. The velocity of near-laminar fluid flow across an arena is determined by the height difference between the source and the sink of fluid and accounted for in onset-offset stimulus aligned analysis (Figure 3.2.b). All worms in an arena were tracked and classified into 5 behavioral states -- forward motion, pause, reversal-alone, and the two components of a coupled reversal-omega series, pirouette reversal and pirouette forward (Figure 3.2.c). Forward moving worms were simultaneously tracked for locomotion speed (Figure 3.2.g; Albrecht et al., 2011; Ramot et al., 2008). In response to aversive stimuli, wild-type worms first pause, then either continue forward movement or follow the pause with a reversal. If, after the reversal, the worm continues moving forward in the same direction as before, the behavioral state is scored as a pure reversal. If the reversal is instead followed by an omega turn and the worm therefore heads forward in the opposite direction as before, the behavioral state is scored as a pirouette. This is similar to the behavioral sequence observed with drop tests of aversive stimulus on agar plates (Albrecht et al., 2011; Hilliard et al., 2002). Pausing, reversals, and pirouette behaviors

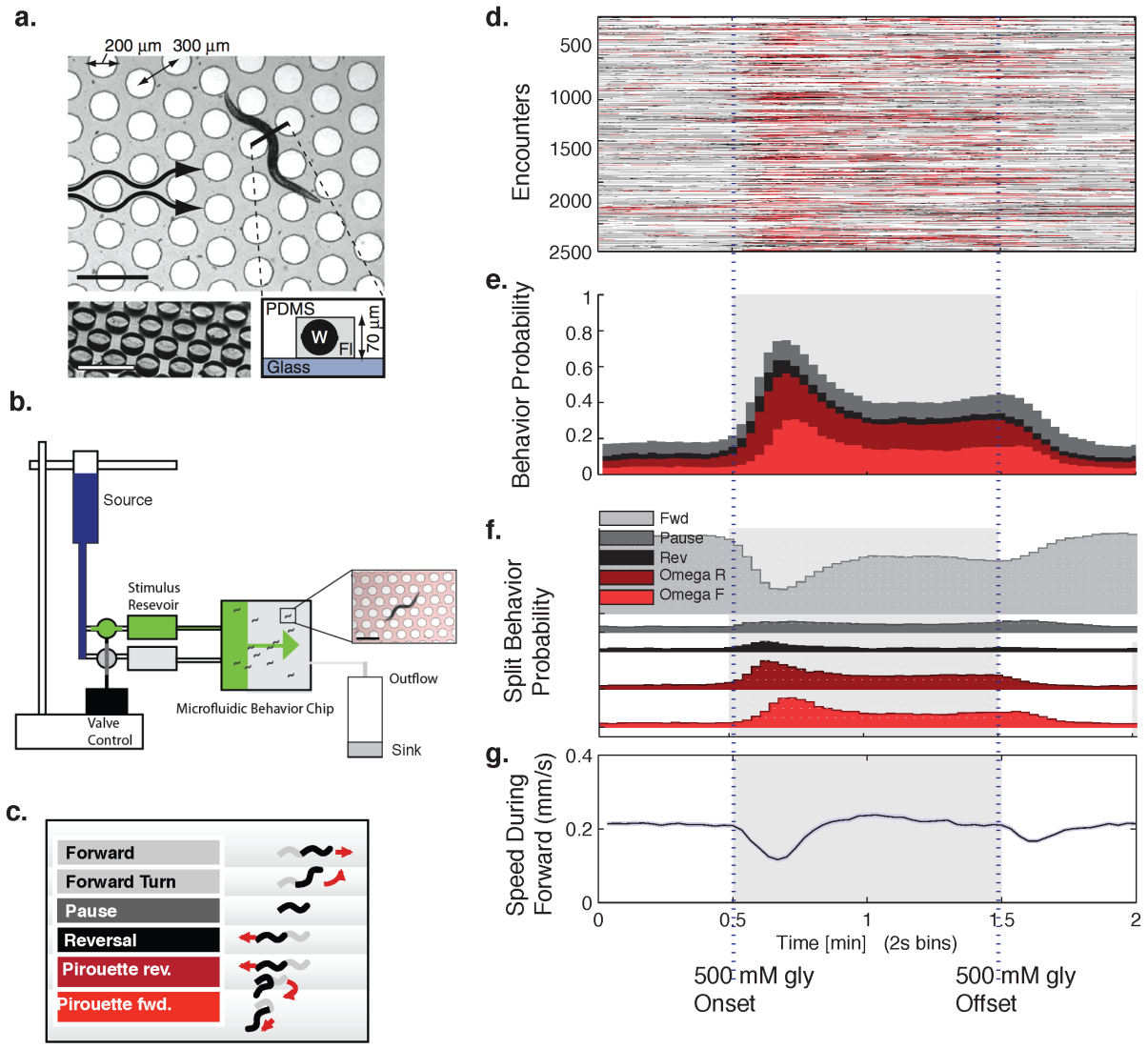

Figure 3.2. Laminar fluid flow in micro-environments allow precise time-alignment of stimulus-triggered avoidance behavior.
a) From Albrecht and Bargmann, 2011: precise dimensions of PDMS posts in microlfluidic chambers allow worms to crawl freely while stimulus is presented with laminar flow velocity determined by the height difference between a source and sink **b)**. **c)** Behavior key by color. After 20 minutes of adaptation to the new physical environment, worms predominantly perform forward behaviors (light gray) in microfluidic buffer. Upon onset of aversive stimuli, worms perform avoidance behavior sequences consisting of a pause and a backward movement that either ends with a new bout of forward locomotion (reversal) or is followed by an omega turn and results in forward motion along another trajectory (pirouette rev. and pirouette fwd). **d)** Raster plots of individual encounters to aversive stimuli within the same experiment. **e)** Summation of individual encounter rasters provides time-aligned histograms of behavior probabilities with presence of stimulus indicated in lightest gray. In this example, 2 s binned behavior probabilities are shown from 0-2 min, with 500 mM glycerol present from 0.5 min to 1.5 min. Number of worms n=100. Phasic and tonic avoidance behaviors can be resolved. Probability of total behavior is 1**. f)** Time-aligned histograms of behavior probability can be split into time courses of individual behaviors. **g)** The speed of the forward moving population is also tracked.

are considered avoidance behaviors, with forward motion considered the non-aversive state. Behavior raster plots of individually tracked worms at each time point were aligned by stimulus

encounter (Figure 3.2.d). Time-binned histograms of population behavior raster plots from each stimulation expressed the probability of each behavior among the population of tracked worms at any given time (Figure 3.2.e, f). The combined probability of all five behaviors is 1 at all times. Aligning behavior histograms with stimulus-onset and stimulus-offset times generated the population time course probability of each behavior in response to the phasic changes of stimulus onset and offset as well as to the tonic states of stimulus presence and absence (Figure 3.2.e,f). Behaviors were resolved as the total amount of avoidance behaviors at each time point (stacked, Figure 3.2.e) or as the split probability of each individual behavior (unstacked, Figure 3.2.f).

Population behavioral dynamics of *srg-34* and *srg-36* mediated C3 avoidance match their respective ASH calcium dynamics

My first experiment was to ask how receptor-mediated calcium dynamics in sensory neurons compared to the behavioral responses to the same stimulus. Since C3 is an endogenously-sensed chemical ascaroside pheromone, I first presented 1 µM C3 to a population of wild-type worms crawling in a microfluidic device with no ectopic receptor expression in ASH. Wild-type *C. elegans* exhibited an increase in avoidance behavior upon the removal, but not the onset, of the ascaroside C3 (Figure 3.3.a). This behavior suggests that wild-type animals find C3 attractive.

C3 sensitivity in a different assay, dauer larva formation, had previously been attributed to the *srbc-64* and *srbc-66* C3 receptors in the ASK neurons (Kim et al., 2009). To ask if the endogenous behavioral response was also ASK-dependent, we ablated the ASK neurons using cell-specific caspase expression. Upon ASK ablation, the “attractive” quality of 1 µM C3, as expressed by reversals upon its removal, was eliminated (Figure 3.3.b.). This result indicates that ASK is required for wild-type behavioral response to C3 at this concentration.

We next presented 1 µM C3 to transgenic animals expressing either *srg-34* or *srg-36* in ASH. In both cases, addition of 1 µM C3 elicited pauses, reversals, and pirouettes consistent with avoidance behavior, the opposite behavior to the wild-type response (Figure 3.1.c,e). In addition, the endogenous aversion to C3 removal was eliminated, suggesting that the ectopic receptors in ASH override endogenous ASK signaling, Expression of a caspase in ASK neurons of animals expressing ASH *srg-34* and *srg-36* transgenes preserved the avoidance behaviors observed with the transgene alone (Figure 3.3.d.f.). Because the ASH transgenes appeared to

take precedence over endogenous ASK signaling, I conducted remaining experiments in with-type animals with intact ASK neurons for the sake of convenience.

The ASH:*srg-34* and ASH:*srg-36* strains showed C3 avoidance with dynamics remarkably similar to dynamics of the ASH calcium response across a range of concentrations - 0.3 µM, 1 µM, and 3 µM C3 (Figure 3.4). When tracking the behavior in populations of 30 worms expressing *srg-34* in ASH, 1 µM C3 elicited avoidance behaviors that peaked with a latency of ~8 s after stimulus onset (Figure 3.4.k) but had adapted to 24% of peak height by the end of 30 s stimulation despite persistent C3 presence. *srg-34* induced ASH calcium time courses were similar across a ten-fold concentration range (Figure 2.18.a; Figure 3.4.a-c, blue traces), showing rapidly peaking, fast adapting ASH calcium signals (Figure 3.4. d-f). Similarly, matching *srg-36*-mediated ASH calcium responses, populations of worms expressing *srg-36* in ASH increased their avoidance behaviors gradually and maintained 44% of their peak response at the end of 30 s (Figure 3.4.h, n). Unlike *srg-34* mediated ASH calcium responses, *srg-36* mediated ASH calcium responses increased in a dose-dependent manner in this concentration range (Figure 2.18.a; Figure 3.4.a-c, red traces). 0.3 µM C3 elicited very little avoidance response above baseline (Figure 3.4.g, m), 1 µM C3 elicited a slow-ramping, slow adapting response, and stimulation with 3 µM C3 resulted in a higher initial slope in aversion increase that maintained 80% of peak aversion at the end of the 30 s stimulation (Figure 3.4.j.n.). Importantly, even at 3 µM C3, when the total aversion behavior mediated by *srg-36* during stimulus presence was comparable to that of *srg-34* mediated aversion behaviors (Figure 3.4.m), the initial slope of both the ASH calcium response and associated avoidance dynamics never exceeded the initial slopes elicited by *srg-34* at any C3 concentration (Figure 3.4.j).

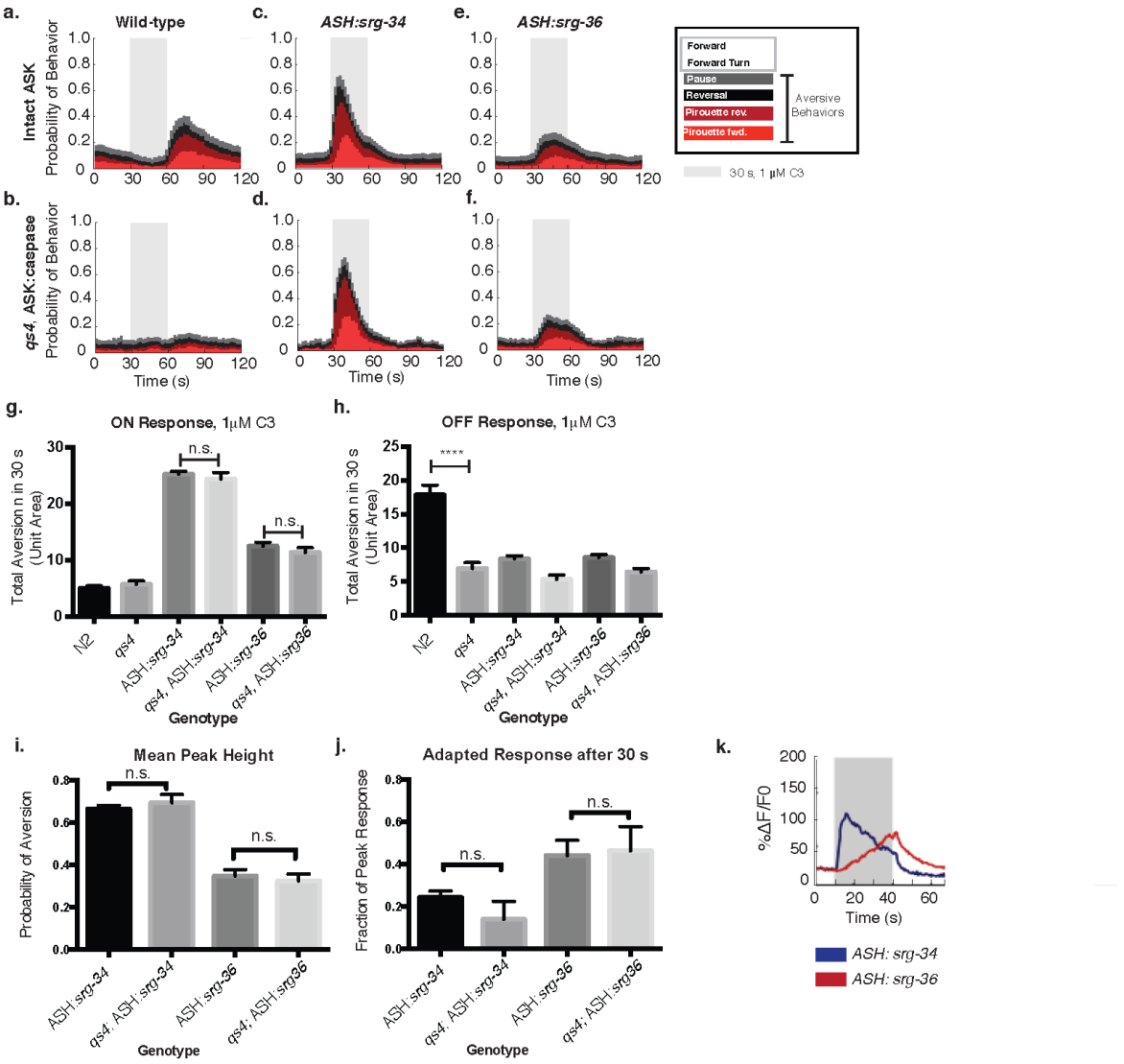

Figure 3.3. Population behavioral dynamics of ASH: *srg-34* and ASH: *srg-36* mediated C3 avoidance are not dependent on ASK neurons and match respective ASH calcium dynamics.

a) Wild type worms show increase of aversion behaviors (gray = pause, black = reverse, dark red = pirouette omega, red = forward pirouette turns; uncolored = forward state; total population behavior adds to 1.0 at any time point.) to removal of 1 µM C3 after 30 s exposure which is **b)** not present in caspase ablation (*qs4* strain) of C3-sensing ASK neurons. Avoidance responses to 1 µM C3 are elicited by ectopic *srg-34* receptors **(c,d)** or *srg-36* **(e,f)** receptors in ASH and the intact aversion response is supported, regardless of ASK ablation. **g)** ON responses of *srg-34* and *srg-36* elicited C3 avoidance behaviors are not significantly affected by *qs4*. **h)** While removal-elicited avoidance behaviors in wild-type worms are significantly reduced in the *qs4* background, OFF responses after ASH-mediated avoidance behaviors were comparable with or without intact ASK. **i)** Peaks of fast rising, fast adapting s*rg-34* mediated behavior to 1 µM C3 with and without ASK were not significantly different from each other. Peaks of slow rising, slow adapting *srg-36* mediated population behavior to 1 µM C3 with and without intact ASK were not significantly different from each other. **j)** Adaptation of total aversion behavior after 30 s stimulation with 1 µM C3 was not different between ASK intact and ablated animals for both ASH:*srg-34* mediated and ASH:*srg-36* mediated aversion. **k)** Behavior kinetics approximate the calcium response to 1 µM C3 measured in ASH expressing respective *srg* receptors. (Error bars = s.e.m., ****P<0.0001; n.s. P>0.05).

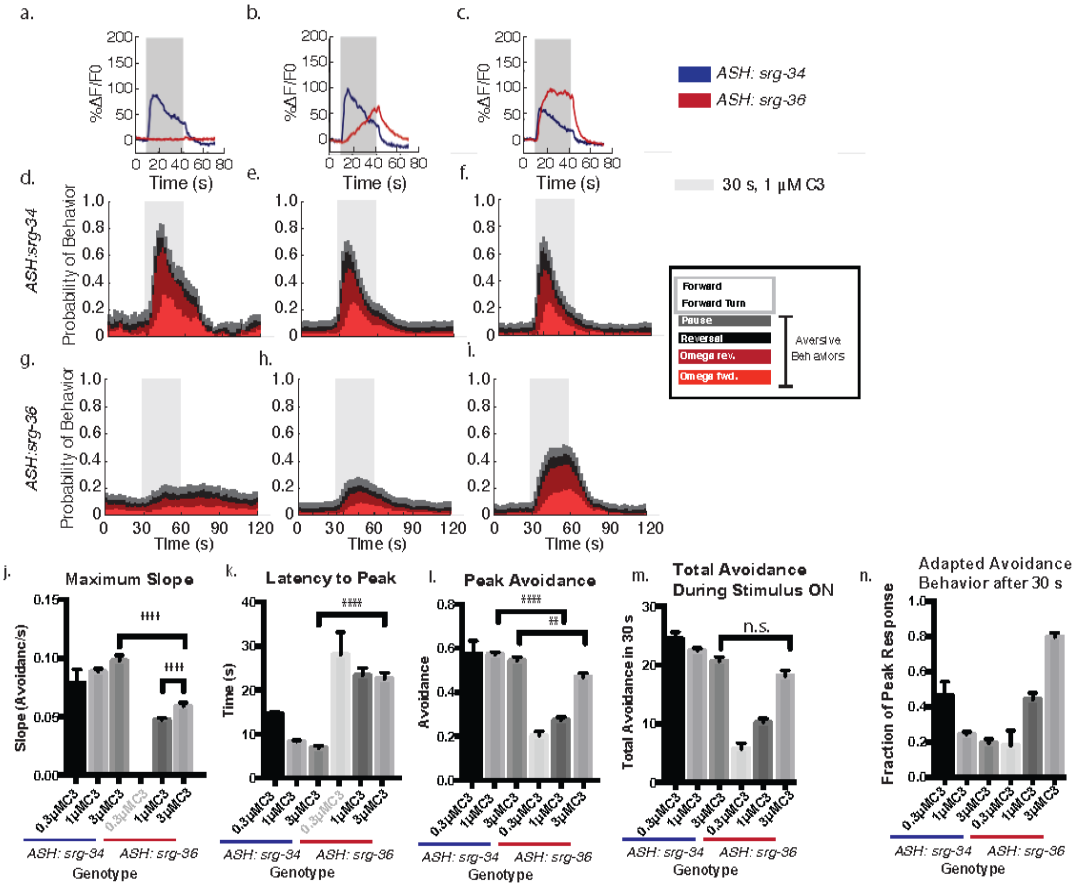

Figure 3.4. ASH calcium dynamics are mirrored in population behavior dynamics to ectopic *srg-34* and *srg-36* receptors.
a)-c) Calcium responses to 30 s stimulation by 0.3 µM, 1 µM, and 3 µM C3 in ASH neurons expressing *srg-34* (blue) or *srg-36* (red). *srg-34* popuation behavior probabilities in response to 0.3 µM (d), 1 µM (e), and 3 µM C3 (f) resemble respective ASH calcium traces. *srg-36* population avoidance probabilities also resemble ASH calcium traces to 0.3 µM (g), 1 µM (h), and 3 µM C3 (i). j)-n) quantification for *srg-34* and *srg-36* behavior dose response to C3.(****P<0.0001; **P<0.01; n.s. P>0.05).

Neural circuit dependence of *srg-34*- versus *srg-36*- directed nociception

To investigate how pertinent interneurons contribute to ASH-directed nociceptive behavior, I inactivated key interneurons prior to each experiment using a chemical genetic system. *C. elegans* do not have endogenous histamine receptors and exhibit no behavioral changes to histamine (Chase and Koelle, 2007; Alkema et al., 2005; Pokala et al., 2013). Expressing the *Drosophila* histamine-gated chloride channel (HisCl) in specific neurons using cell-selective promoters hyperpolarizes the neurons when histamine is present, allowing

reversible inactivation over a time scale of minutes in a dose-dependent manner (Pokala et al., 2013).

AVA, the backward command interneuron, strongly promotes reversals upon optogenetic activation, and is required for all known sustained reversal behaviors (Piggott et al., 2011; Gray et al., 2005; Chalfie et al., 1985). AIB is an intermediate layer interneuron that strongly modulates spontaneous reversal probability (Gray et al., 2005). AIB is both postsynaptic to ASH and presynaptic to AVA (White et al., 1986). Transgenes in which HisCl was expressed in AVA or AIB were used to silence these two neurons in strains expressing *srg-34* or *srg-36* in ASH, and these double transgenic strains were examined for effects of histamine-induced interneuron silencing on ASH-directed behavior.

AVA silenced populations exhibited significantly less reversals and pirouettes in response to 1 µM C3 than AVA intact populations in both the ASH:*srg-34* and the ASH:*srg-36* strains (Figure 3.5.a-d, middle column, Figure 3.5.e, black bars = reversals, red bars = pirouettes; Table 3.1.b). This was balanced by a significant increase in pause states observed across these C3 receptor-concentration conditions (Figure 3.5.e., gray bars; Table 3.1.b) so that the total avoidance behavior remained unchanged or increased across 30 s of ASH stimulation (Figure 3.5.e., white bars; Table 3.1.b). Reversal behavior appeared to be slowed, as there was an increase in both the time to peak and the fraction of behavior that remained at the end of 30 s (Figure 3.5.g-h; Table 3.1.b). Animals with silenced AVA neurons are known to generate omega turns in the absence of a prior reversal (Pokala et al., 2013), but the tracking software used here would not be able to recognize this behavior pattern; further analysis will be needed to examine the residual behaviors of AVA-silenced animals in more detail. For the purpose of this discussion, the main conclusion is that AVA is needed for avoidance behaviors that include reversals, but is not needed for avoidance behaviors mediated by pausing.

Worms with silenced AIB interneurons had a different set of behavioral changes to C3 (Figure 3.5.a-d, right column; Figure 3.3.f. Table 3.1.a.). AIB is known to have an important role in generating omega turns (Gray e al., 2005; Pokala et al., 2013), and indeed, AIB silencing resulted in significantly reduced pirouette state probabilities in ASH:*srg-34* worms in response to 30 s of either 1 µM C3 and 3 µM C3 (Figure 3.5.f., red bars 1-4; Table 3.1.a.). The increased probabilities of both pause (Figure 3.5.f., gray bars 1-4) and reversal (Figure 3.5.f., black bars 1-4) states in these conditions did not compensate for the pirouette reduction, so that the there was a 22% decrease in total avoidance behaviors to 1 µM C3 by worms expressing ASH:*srg-34* and a 35% decrease to 3 µM C3 (Figure 3.5.f., Table 3.1.a.; Student's T-test, *P<0.05). This

result suggests that ASH:*srg-34* worms without AIB activity show significantly increased forward state probability during C3 stimulation compared to the same population of worms with intact AIB. Despite these changes to total avoidance behavior, the dynamics of the ASH:*srg-34* induced population avoidance response were similar with and without intact AIB neurons. In response to 1 µM C3 or 3 µM C3, worms with and without intact AIB reached the peak of their avoidance probability at the same time (Figure 3.5.i, bars 1-4. Average time to peak for 1 µM C3: ASH:*srg-4*=6.3 s; AIB:HisCl ASH:*srg-34*=8.9 s; n.s. by Student's t-test, P>0.05. Average time to peak for 3 µM C3: ASH:*srg-34*=6.9 s; AIB:HisCl ASH:*srg-34*=7.1 s; n.s. by Student's t-test, P>0.05.). The adaptation for 30 s of stimulation was also comparable across all conditions (Figure 3.5.j, Fraction of peak response after 30s with 1 µM C3: ASH:*srg-34*=0.14; AIB:HisCl ASH:*srg-34*=0.24; n.s. by Student's t-test, P>0.05. Average time to peak for 3 µM C3: ASH:*srg-34*=0.19; AIB:HisCl ASH:*srg-34*=0.14; n.s. by Student's t-test, P>0.05).

After AIB silencing, ASH:*srg-36* mediated C3 avoidance exhibited changes in both behavior probability and dynamics. In the most striking result, 1 µM C3 ceased to elicit any avoidance in ASH:*srg-36* populations. This occurred due to a decrease in all aversion behaviors after AIB silencing, including pauses, reversals, and pirouettes (Figure 3.5.f., all colors, bars 5 and 6; Table 3.1.a.). Raising the concentration of stimulus to 3 µM C3 increased *srg-36* mediated aversion in intact worms so that the total aversion behavior during stimulus presence was comparable to the avoidance regime mediated by *srg-34* (Figure 3.5.f.; n.s., p>0.05 between 1 µM C3 avoidance by ASH:*srg-34* and 3 µM C3 avoidance by ASH:*srg-36*). This reflects the ASH calcium response, which shows significantly higher total calcium response over 30 s to 3 µM C3 stimulation of *srg-36* than *srg-34* (Figure 2.16.b.). However, while the initial slope of aversion behavior increased, it was still significantly lower than that mediated by *srg-34* (Figure 3.4.j.; ****P<0.0001), resembling the slope of their respective calcium measurements in ASH (Figure 2.16.b). Thus, raising the stimulus concentration to 3 µM C3 could help differentiate whether *initial slope* of ASH calcium activity and avoidance response or the *total* ASH calcium activity and avoidance response was relevant for maintaining C3 avoidance in the context of AIB silencing. In response to 3 µM C3, ASH:*srg-36* worms with hyperpolarized AIB interneurons expressed similar trends to ASH:*srg-34* worms: probabilities of pausing states and reversal states increased to partially compensate for decreased pirouette probability so that, though the total avoidance behavior decreased, some residual behavior was maintained. Interestingly, most of the residual avoidance behavior occurred early in the 30 s stimulation by 3 µM C3 so that the response adapted to 39% of the peak value in AIB silenced populations while

AIB-intact populations maintained 67% of its peak value at the end of 30 s (Figure 3.5.j, bar 7 and 8; ****P<0.0001; Table 3.1.a.). This hints that AIB may contribute to both the detection of slowly ramping signals and the maintenance of avoidance responses to prolonged calcium signals from ASH.

Figure 3.5. Fast *(srg-34)* **and slow** *(srg-36)* **ASH stimulation require different interneurons to promote avoidance behaviors.**
a)-d) Left column: Calcium imaging responses to 1 µM C3 **(a,c)** or 3 µM C3 **(b,d)** mediated by ASH:*srg-34* **(a,b)** or ASH:*srg-36* **(c,d)**. Row **a)** *srg-34* to 1 µM C3; Row **b)** *srg-34* to 3 µM C3; Row **c)** *srg-36* to 1 µM C3; and Row **d)** *srg-36* to 3 µM C3. **Second column**: Time-aligned histograms depicting population behavior responses with intact interneuron function, each panel shows on top: stacked behavior of all aversive responses (forward responses uncolored) with total behavior probability =1; and bottom: individual split behaviors of forward, **pause**, **reverse**, **pirouette forward**, and **pirouette reverse** state probabilities. Stimulus is present during gray vertical bar (30 s). **Third Column**: AVA:HisCl time-aligned behavior responses. **Fourth Column**: AIB:HisCl time-aligned behavior responses. **e)** Statistics of total probability for each behavior during 30 s stimulation by C3 in AVA:hiscl lines. Gray = pause probability, black = reverse probability, dark red = reverse pirouette probability, light red = forward pirouette probability, white = total aversion probability (pause+reverse+pirouettes). probabiltiy of foward states = (1 - total aversion probability). Stimulus tested, from left to right: Bar 1: 1 µM C3 , ASH:*srg-34*; Bar 2: 1 µM C3 , AVA:HisCl; ASH:*srg-34*; Bar 3: 3 µM C3 , ASH:*srg-34*; Bar 4: 3 µM C3 , AVA:HisCl; ASH:*srg-34*; Bar 5: 1 µM C3 , ASH:*srg-36;* Bar 6: 1 µM C3 , AVA:HisCl; ASH:*srg-36*; Bar 7: 3 µM C3 , ASH:*srg-36*; Bar 8: 3 µM C3 , AVA:HisCl; ASH:*srg-36*. ASH:*srg-34* mediated total aversion probability did not change with AVA silencing. ASH:srg-36 mediated total aversion increased with AVA silencing to 1 µM C3 but decreased to 3 µM C3. **f)** Statistics of total probability for each behavior during 30 s stimulation by C3 in AIB:hiscl lines. Stimulus tested, from left to right: Bar 1: 1 µM C3 , ASH:*srg-34*; Bar 2: 1 µM C3 , AIB:HisCl; ASH:*srg-34*; Bar 3: 3 µM C3 , ASH:*srg-34*; Bar 4: 3 µM C3 , AIB:HisCl; ASH:*srg-34*; Bar 5: 1 µM C3 , ASH:*srg-36*; Bar 6: 1 µM C3 , AIB:HisCl; ASH:*srg-36*; Bar 7: 3 µM C3 , ASH:*srg-36*; Bar 8: 3 µM C3 , AIB:HisCl; ASH:*srg-36*. Significant total aversion was seen in all AIB silenced lines, with ASH:srg-36 losing all aversion response to 1 µM C3. **g)** Latency to peak (s) after onset of 1 µM or 3 µM C3 in AVA intact or silenced populations. Peak latency increased in AVA silenced populations for every condition except the ASH:*srg-36* response to 1 µM C3. **h)** Adaptation of response: fraction of peak height remaining at the end of 30 s C3 stimulation for AVA intact or silenced populations. Less adaptation was observed when AVA was silenced. **i)** Latency to peak (s) after onset of 1 µM or 3 µM C3 in AIB intact or silenced populations. AIB silencing had no significant effect on peak latency. **j)** Adaptation of response: fraction of peak height remaining at the end of 30 s C3 stimulation for AIB intact or silenced populations. Silencing AIB had little effect on ASH:*srg-34* adaptation but significantly decreased the ability of ASH:*srg-36* to maintain activity to 3 µM C3.

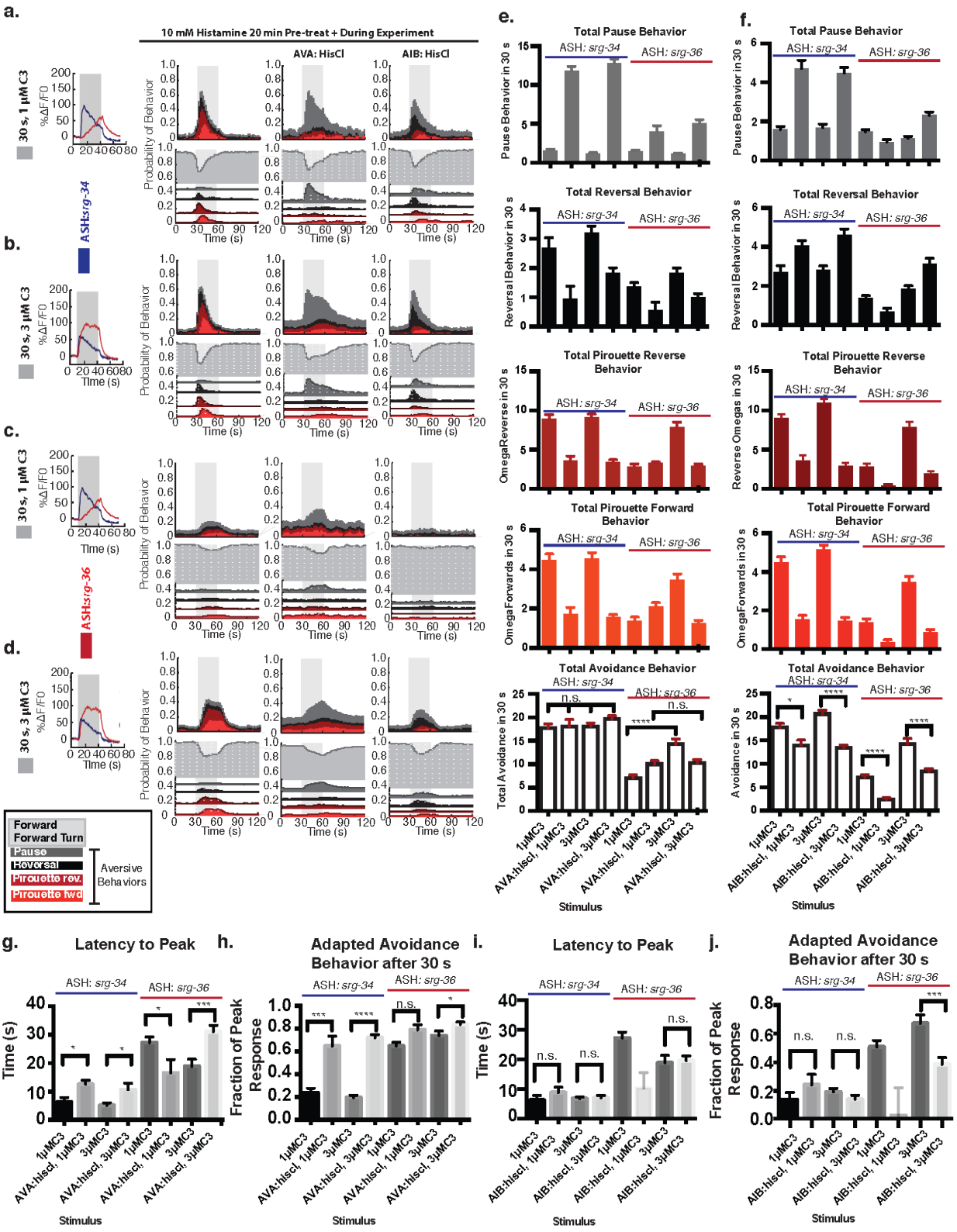
a.
b.
c.
d.
e.
f.
g.
h.
i.
j.
10 mM Histamine 20 min Pre-treat + During Experiment
AVA: HisCl
AIB: HisCl
30 s, 1 µM C3
30 s, 3 µM C3
%ΔF/F0
Probability of Behavior
Time (s)
ASH:srg-34
ASH:srg-36
Forward
Forward Turn
Pause
Reversal
Pirouette rev.
Pirouette fwd
Aversive Behaviors
Total Pause Behavior
Pause Behavior in 30 s
Total Reversal Behavior
Reversal Behavior in 30 s
Total Pirouette Reverse Behavior
OmegaReverse in 30 s
Reverse Omegas in 30 s
Total Pirouette Forward Behavior
OmegaForwards in 30 s
Total Avoidance Behavior
Total Avoidance in 30 s
Avoidance in 30 s
ASH: srg-34
ASH: srg-36
n.s.
1µMC3
3µMC3
AVA:hisCl, 1µMC3
AVA:hisCl, 3µMC3
AIB:hisCl, 1µMC3
AIB:hisCl, 3µMC3
Stimulus
Latency to Peak
Time (s)
Adapted Avoidance Behavior after 30 s
Fraction of Peak Response

a.

AIB:HisCl

		ASH Calcium Response			Behavior					
Receptor in ASH	[C3]	Calcium Slope	Calcium Peak	Total Calcium Response	Δpause	Δreverse	Δpirouette	Δtotal avoidance	Δtpeak	Δ%peak maintained
srg-34	0.5 nM	0	0	0	0	↓	↓	↓	0	0
srg-34	10 nM	0.0051	0.1285	1.912	↑	↑	↓	↓	↓	0
srg-36	1 µM	0.0093	0.6472	102.6	↓	↓	↓	↓	↓	↓
srg-34	33 nM	0.0192	0.3772	48.22	↑	↑	↓	↓	0	↑
srg-36	3 µM	0.0335	1.049	229.6	↑	↑	↓	↓	↓	↓
srg-34	3 µM	0.0383	0.6709	120.8	↑	↑	↓	↓	0	0
srg-34	1 µM	0.0407	0.6522	129.7	↑	↑	↓	↓	0	0

b.

AVA:HisCl

		ASH Calcium Response			Behavior					
Receptor in ASH	[C3]	Calcium Slope	Calcium Peak	Total Calcium Response	Δpause	Δreverse	Δpirouette	Δtotal avoidance	Δtpeak	Δ%peak maintained
srg-36	1 µM	0.0093	0.6472	102.6	↑	↓	↑	↑	↓	0
srg-36	3 µM	0.0335	1.049	229.6	↑	↓	↓	↓	↑	↑
srg-34	3 µM	0.0383	0.6709	120.8	↑	↓	↓	0	↑	↑
srg-34	1 µM	0.0407	0.6522	129.7	↑	↓	↓	0	↑	↑

>50%
<50%

Table 3.1. Summary of AIB and AVA silencing effects on trackable avoidance behavior during 30 s C3 stimulation of ASH.
a) Silencing AIB results in a general decrease of total avoidance, a decrease in the avoidance peak, and a decrease in the ability to maintain avoidance behaviors during stimulation (faster adaptation). While the amount of pausing and reversals increase in the absence of AIB, they are not able to compensate for the significant decrease of pirouettes in these populations. Dark blue boxes show scenarios with a <50% maintenance of intact behavior, suggesting that C3 receptor-concentration conditions with low initial calcium slope have higher dependence on AIB for total avoidance. **b)** Silencing AVA results in little change in total avoidance overall, though there is a possibility we are underestimating the amount of aversive behaviors conducted by these populations.

AIB is more important for maintaining avoidance at later time points

To distinguish whether the slope or total magnitude of the calcium response is more important for avoidance behaviors, I varied the concentrations of C3 presented to the ASH: *srg-34* strain. At C3 levels of 33 nM, calcium levels in ASH:*srg-34* rise with a significantly higher slope but a significantly lower peak and total calcium response than that observed in ASH:*srg-36* exposed to 1 µM C3. At still lower C3 levels of 10 nM, the ASH:*srg-34* calcium response has a lower slope as well as a lower peak and total calcium response than that observed in ASH:*srg-36* exposed to 1 µM C3 (Figure 3.6.f.). At 0.5 nM C3, GCaMP3 did not give a detectable calcium response in ASH:*srg-34*.

An initial sharp increase of ASH:*srg-34* mediated avoidance behaviors was observed at all concentrations tested, even at 0.5 nM C3 when ASH calcium changes were not detected (Figure 3.6.d.). Though the peak of magnitude of avoidance behavior diminished at lower C3 concentrations, the peak it remained sharply aligned to stimulus onset. This suggests that ASH can drive avoidance at a stimulus level below the detection threshold of our GCaMP3 calcium indicator when activated by *srg-34.*

I next compared ASH:*srg-34* low-concentration behavior responses to ASH:*srg-36* 1 µM C3 behavior responses in AIB intact and silenced populations (Figure 3.6.d.). At 33 nM C3, avoidance was largely maintained in AIB silenced populations of ASH:*srg-34* expressing worms (Figure 3.6.d.). However, there was a significant decrease in behavior after 10 s of stimulation in AIB silenced worms when the C3 concentration was lowered to 10 nM (Figure 3.6.d.). A regression of behavior against the initial slope of measured ASH calcium activity suggested a stronger requirement for AIB in cases where the initial calcium slope was low for both *srg-34* and *srg-36* (Figure 3.6.e). This effect was greatest for the later time points in the behavioral response (Figure 3.6.e). No correlation was observed between the AIB requirement and the peak calcium height or total calcium amount measured in ASH. The greater requirement for AIB at later time points suggests that AIB has a role in maintaining behavior over time (Figure 3.6.e.).

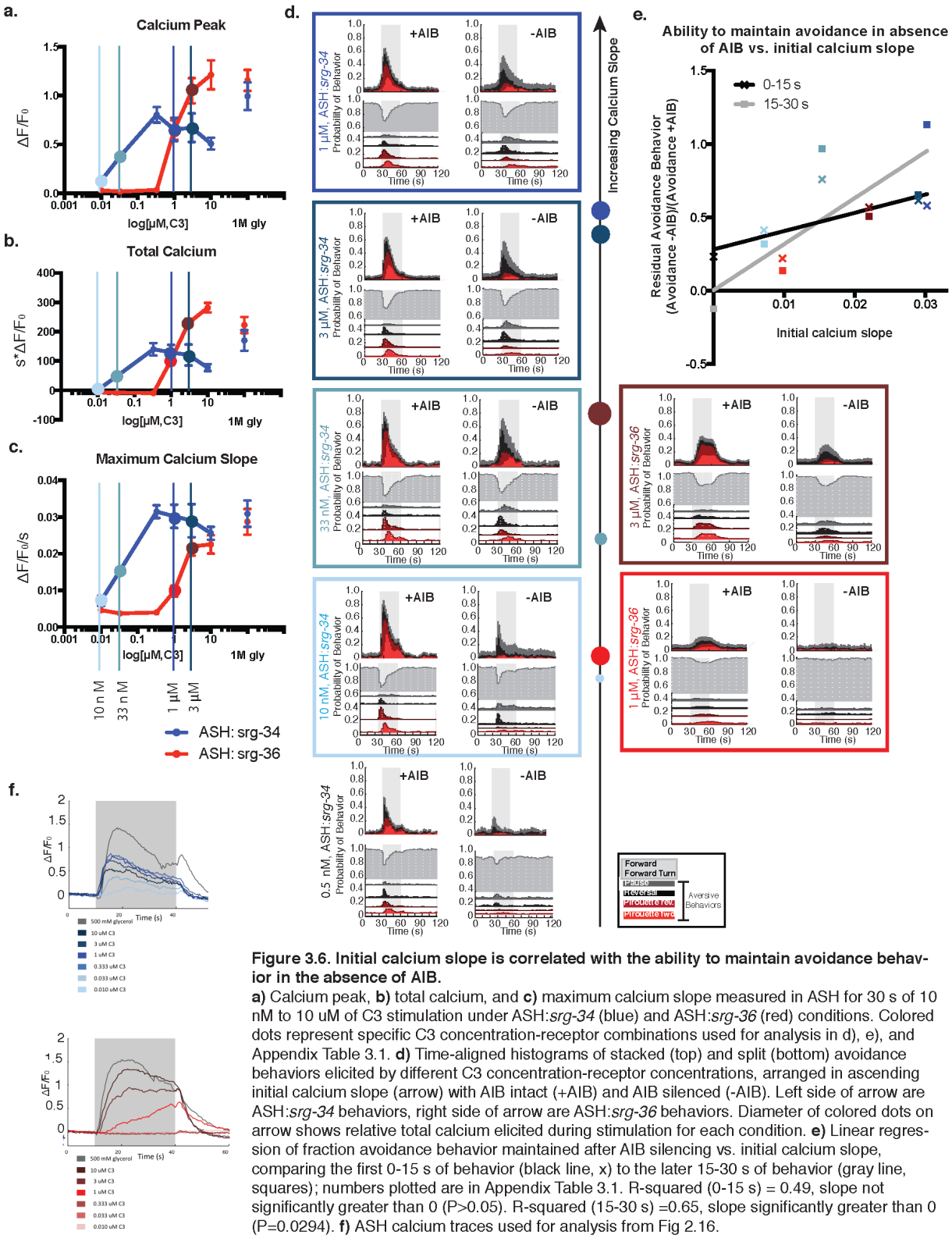

Figure 3.6. Initial calcium slope is correlated with the ability to maintain avoidance behavior in the absence of AIB.

a) Calcium peak, **b)** total calcium, and **c)** maximum calcium slope measured in ASH for 30 s of 10 nM to 10 uM of C3 stimulation under ASH:*srg-34* (blue) and ASH:*srg-36* (red) conditions. Colored dots represent specific C3 concentration-receptor combinations used for analysis in d), e), and Appendix Table 3.1. **d)** Time-aligned histograms of stacked (top) and split (bottom) avoidance behaviors elicited by different C3 concentration-receptor concentrations, arranged in ascending initial calcium slope (arrow) with AIB intact (+AIB) and AIB silenced (-AIB). Left side of arrow are ASH:*srg-34* behaviors, right side of arrow are ASH:*srg-36* behaviors. Diameter of colored dots on arrow shows relative total calcium elicited during stimulation for each condition. **e)** Linear regression of fraction avoidance behavior maintained after AIB silencing vs. initial calcium slope, comparing the first 0-15 s of behavior (black line, x) to the later 15-30 s of behavior (gray line, squares); numbers plotted are in Appendix Table 3.1. R-squared (0-15 s) = 0.49, slope not significantly greater than 0 (P>0.05). R-squared (15-30 s) =0.65, slope significantly greater than 0 (P=0.0294). **f)** ASH calcium traces used for analysis from Fig 2.16.

Fast and slow ASH calcium dynamics differently access AVA and AIB interneurons in freely moving worms

The results described above suggests that AIB is required for generating avoidance behavior to low, ramping signals from ASH as well as for maintenance of avoidance behavior over longer times of tonic ASH signaling. Since AVA activity alone could not compensate for the lack of AIB, my data also suggest that different features of ASH responses instruct different downstream interneurons. To see how AIB and AVA respond to ASH activation, I first attempted calcium imaging of these neurons in the trapped microfluidic device to 1 µM C3 with ASH:*srg-34* or ASH:*srg-36*. Unfortunately, AVA and AIB neurons have a high level of spontaneous activity and relatively little stimulus-induced activity in our standard microfluidic device (not shown). This suggests that the aversive environment of the trapped chip may provide an unfavorable environment to investigate interneuron responses to aversive stimuli.

Therefore, to observe the activity of this circuit for ASH-mediated behaviors, I performed simultaneous GCaMP imaging and behavioral tracking of freely-moving worms responding to C3 in a microfluidic device (Larsch et al., 2013). I measured calcium changes in AVA or AIB in single worms with ASH:*srg-34*, with ASH:*srg-36*, or with no ectopic transgene expression, in response to a temporal pulse of 1 µM C3. Acquiring images of the freely-moving worm at 10 Hz allowed consistent automated tracking of GCaMP-indicated neural activity with less than 10% of frames requiring additional manual tracking (Sagi Levy). Behavior segmentation was generated by hand for each video. While forward movement, pauses, reversals and pirouettes were tracked, only pirouette events were used for initial analysis. 30 total pulses of 1 µM C3 were presented for 30 s to each worm. Three types of time-course analyses were conducted: 1. Stimulus-aligned behavior time course, 2. Stimulus-aligned AVA or AIB neural activity, and 3. Neural activation aligned by initiation of pirouette behavior. These three parameters allowed us to visualize how interneuron activity relates to stimulation and to behavior.

The analyses were conducted as follows. 1. To generate a stimulus-triggered time course of pirouette probabilities, raw, stimulus-aligned behavior raster plots depicting pirouette events were generated for each worm to each pulse, with the onset of each stimulus at t=0 (Figure 3.7.a,b,c, right column). The mean probability of conducting a pirouette behavior was generated for each time point using these raster plots, resulting in a time course of pirouette behavior probability in response to stimulus for each worm (Figure 3.7.a.,b.,c. left column). 2. To generate a stimulus-triggered time course of AVA or AIB fluorescence levels, the percent fluorescence change ($\Delta F/F_0$) measured in the freely moving worms was time-aligned with the

onset of C3 stimulus at t=0 for all 30 C3 presentations for each worm. The average fluorescence of the neuron across all 30 C3 presentations was calculated per worm in each frame to generate a time course of neural activity for that worm (Figure 3.7.d, left and middle columns). The time course of average neural fluorescence was normalized from 0 to 1 for each worm and averaged together to generate a population time course of neural activation for worms expressing ASH:*srg-34* or worms without ectopic receptor expression (Figure 3.7.d. right column). Due to the variability of interneuron responses seen in AVA neurons in the ASH:*srg-36* background, only individual averages for each worm are shown for ASH:*srg-36* interneuron activity data (Figure 3.7.e.). 3) AVA or AIB fluorescence levels measured in the freely moving worms were time-aligned to every initiation of a pirouette behavior at t=0 for each worm. The average neural fluorescence level was calculated per worm and normalized between 0 and 1 (Figure 3.7.f., left and middle columns). Further averaging the time course of neural activity from all worms generated a population time course of neural activity (Figure 3.7.f., right column) that shows the average activity of the AVA and AIB neurons before and during pirouette initiation.

I first examined whether individual time courses of avoidance behavior to 1 µM C3 reflected the population time course of avoidance behaviors seen in the previously described large microfluidic arenas. When presented with 1 µM C3, worms expressing ASH:*srg-34* increased reversals significantly, a behavior that aligned with odor onset (Figure 3.7.a.). Indeed, raster plots for each worm shows that every worm began a pirouette within 10 s of stimulus onset in >90% of trials (Figure 3.7.a., second column). This suggests that the ASH:*srg-34* mediated behavior is fairly deterministic. Further, this was observed both in worms expressing AVA:GCaMP5 and AIB:GCaMP3, suggesting that the calcium indicator itself is not interfering with the initial stimulus dynamics. Similarly, wild-type worms that do not express an ectopic C3 receptor in ASH responded with a robust decrease in pirouette probability at stimulus onset and an increase of pirouette probability at stimulus removal (Figure 3.7.c.), resembling the ASK-intact population wild-type responses in Figure 3.1.

All three AIB:GCaMP3, ASH:*srg-36* expressing worms responded to C3 with a slow ramping increase of pirouette probability over the course of 30 s (Figure 3.7.b., red dot). The peak probability of pirouette activity was lower in magnitude compared to ASH:*srg-34* responses (0.79 vs. 0.45, ***P<0.001), and the latency to peak was 16.0 s compared to the 7.0 s measured in ASH:*srg-34* responses (**P<0.01). A lower peak of avoidance probability and an increase of the time to peak activity compared to ASH:*srg-34* responses were also characteristics of

ASH:*srg-36* mediated behaviors to 1 µM C3 in the population experiments described in Figures 3.3-3.5.

On the contrary, pirouette probability dynamics in response to 1 µM C3 were variable in AVA:GCaMP5 worms expressing ASH:*srg-36* (Figure 3.7.b., black dot). Out of the three worms tested, two worms showed a ramping increase of pirouette probability during C3 stimulation, while a third resembled wild-type worms with a decrease in pirouette probability to stimulus onset and an increase in pirouette probability to stimulus removal. Further experiments will be required to determine whether this is an effect of the indicator strain, a rare occurrence in all strains, or something else; in any case, these three worms were not averaged for analysis.

When neural activity was time-aligned to C3 onset, AVA and AIB GCaMP fluorescence rose immediately at stimulus onset in ASH:*srg-34* expressing worms (Figure 3.7.d. upper row). This was reflected in individual averages of neural activity in each worm, as well as in the population average (Figure 3.7.d, top row). Thus for *srg-34,* ASH activity, sensory input, and avoidance behaviors were well-correlated.

Switching to the slower *srg-36* response, the variability observed in ASH:*srg-36* mediated behaviors was reflected in the interneuron activity averages for each individual (Figure 3.7.e.). The average response of AIB activity in individual worms was consistent, (Figure 3.7.e, red traces, left and middle column), and was matched to the pirouette probability of the respective worms over the 30 s time course (Figure 3.7.e., right column, red dot). At a single animal level, it was evident that neuronal activity correlated more closely with the behavioral response than with the sensory input. AVA interneuron activity over the 30 s time course aligned with the respective pirouette probability in each individual (Figure 3.7.e., right column, black dot), but the AVA activity time course across the three worms was as variable as the behavior time course shown in Figure 3.7.b. (Figure 3.7.e., left and middle column, black traces).

In wild-type worms that showed consistent decreased pirouettes to C3 onset and increased pirouettes to C3 removal, AVA and AIB both showed an immediate rise to C3 removal in individual and population fluorescence averages (Figure 3.7.d., bottom row). In this case, AVA and AIB appear to correlate with reversals, and anticorrelate with the presence of C3.

These results suggest that the AIB and AVA neurons correlate more closely with behavioral state than with sensory input. Since neural activity and behaviors appear correlated in all conditions, we used behavior-aligned interneuron activity to better assess how the time course of interneuron activity predict behaviors mediated in each receptor condition (Figure

3.7.f). AVA, the backward command neuron, began to rise in fluorescence around 5 s before all pirouette initiations in ASH:*srg-34* (Figure 3.7.f. top row, black trace), ASH:*srg-36* (Figure 3.7.f., middle row, black trace), and wild-type (Figure 3.7.f., bottom row, black trace) C3-evoked behaviors. However, while ASH:*srg-34* and wild-type mediated C3 responses showed identical rise times between AVA and AIB, there was a clear lag of ~3 s in AVA rise after AIB rise in ASH:*srg-36* mediated activity. This lag was consistent in all individual worms (Figure 3.7.f., middle row) as well as in the population average (Figure 3.7.f, right row). Thus, in ASH:*srg-36* worms, while AVA was still correlated with the initiation of pirouette behaviors, AIB appeared to start rising in activity before AVA, possibly aiding ASH to activate AVA.

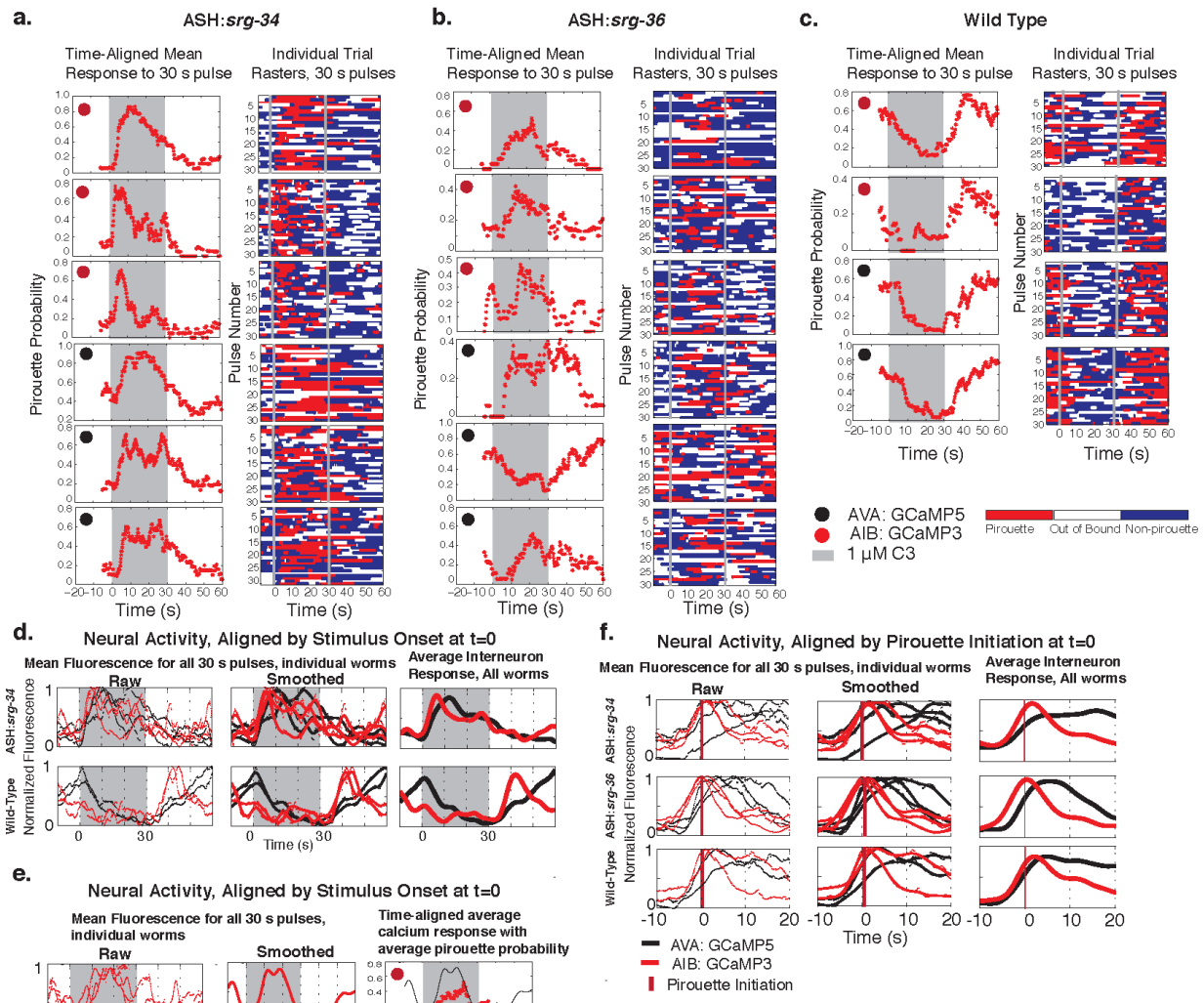

Figure 3.7. Simultaneous interneuron imaging and behavior tracking reveal that fast and slow ASH signals differently access AVA and AIB interneurons. **a)-c) Left panels:** Time course of ASH:*srg-34* **(a)**, ASH:*srg-36* **(b)** and wild-type **(c)** behavior in response to 30 s stimulation by 1 µM C3, expressed by the mean probability of pirouette behavior. Gray bar indicates presence of stimulus, with onset at t=0. Each red trace represents average behavior in a single worm stimulated with 30 pulses of 30 s 1 µM C3. 3 worms of ASH:*srg-34*; AIB:GCaMP3 (**a**), red dots), ASH:*srg-34*; AVA:GCaMP5 (**a**), black dots), ASH:*srg-36*;AIB:GCaMP3 (**b**), red dots), and ASH:*srg-36*;AVA:GCaMP5 (**b**), black dots) and 2 worms of Wild-type; AIB:GCaMP3 (**c**) red dots) and Wild-Type; AVA:G-CaMP5 (**c**) black dots) were tested. **Right panels**: 30 individual raster plots per worm depicting trial response to 1 µM C3 (stimulus is present between gray lines). dark blue = non-pirouette behavior, dark red = pirouette behavior, white = untrackable worms/ worms out of bounds of arena. **d)** Measured normalized GCaMP fluorescence in response to 1 µM C3 stimulus onset at t=0 and lasting 30 s (gray bar). Red traces = AIB, black traces = AVA. Time course of average fluorescence for individual worms are depicted for each trackable frame as raw data points (left panels), smoothed response curves (middle panels), and the average of AVA or AIB fluorescence for all worms (right panels) are depicted. Top row = AVA and AIB responses for ASH:*srg-34*; Bottom row = AVA and AIB responses for wild type worms. **e)** Individual mean of AVA and AIB responses for ASH:*srg-36* (AVA traces too variable to average). Alignment of calcium response to probability of aversive behavior in the same worm show similar trends. **f)** Measured normalized GCaMP fluorescence aligned by initiation of pirouette activity at t=0 (vertical red line). Red traces = AIB, black traces = AVA. Time course of average fluorescence for individual worms are depicted for each trackable frame as raw data points (left panels), smoothed response curves (middle panels), and the average of AVA or AIB fluorescence for all worms (right panels) are depicted. Top row = AVA and AIB responses for ASH:*srg-34*; Middle row = AVA and AIB responses for ASH:*srg-36*; Bottom row = AVA and AIB responses for wild type worms. Behavior initiated after AVA rise initiation in all scenarios, but AIB began to rise earlier than AVA in ASH:*srg-36* mediated behavior.

Discussion

ASH:*srg-34* and ASH:*srg-36* promote behavioral dynamics to 1 µM C3 and 3 µM C3 that are similar to the calcium transients observed in ASH to these stimuli-receptor combinations. ASH can influence behavior by synapsing directly onto the backward command interneuron AVA to generate reversals and pirouettes. ASH can also promote behavior indirectly by synapsing onto the intermediate neuron AIB, which in turn synapses onto AVA. By silencing each neuron in turn using the chemical genetics reagent HisCl, I have investigated how the direct and indirect pathways differently contribute to nociceptive behavior that is specifically instructed by ASH. AVA, the backward command interneuron, promotes reversals, but animals unable to reverse to ASH:*srg-34* or ASH:*srg-36* mediated C3 avoidance due to hyperpolarization of AVA are still able to maintain their total avoidance response through pausing. AIB, previously suggested to play a role in promoting omega turns (Gray et al., 2005), cannot do so efficiently when hyperpolarized, and these worms therefore continue reversing or moving back into forward states instead of completing pirouettes. Thus, silencing AVA and AIB had different motor consequences. Since a significant increase in pausing was found in AVA silenced populations and a significant increase in both pausing and reversals was found in AIB silenced populations, it appears that hyperpolarizing an interneuron results in a redistribution of wild type behaviors among achievable avoidance behaviors. However, while this redistribution was enough to compensate in AVA silenced worms so that the total behavior observed was unchanged, silencing AIB resulted instead in significantly decreased total avoidance behaviors across all conditions tested.

While both ASH:*srg-34* and ASH:*srg-36* worms with silenced AVA neurons were able to produce avoidance behaviors to 1 µM C3 and 3 µM C3, worms with silenced AIB neurons had altered sensory-to-motor processing. The slow, ramping ASH:*srg-36* response to 1 µM C3 depended on AIB completely to produce any avoidance behaviors at 1 µM C3 –no compensatory increase in pausing or reversals were observed. Increasing the stimulation to 3 µM C3 rescued some avoidance behaviors in ASH:*srg-36,* but they adapted during the 30 s stimulation, in contrast to the response in worms with intact AIB interneurons (Figure 3.5.f). In worms with intact interneurons, the ASH:*srg-36* response to 3 µM C3 had comparable total avoidance to that of ASH:*srg-34* during stimulation, but had lower initial response slopes in both behavior and ASH calcium signals. AIB may thus accumulate signals over time for slow responses, and transduce accumulated ASH signals to AVA to enhance motor output. AIB is not required to generate avoidance to fast ASH responses, as seen across all ASH:*srg-34* mediated

responses and in the residual fast peaking, fast adapting response observed in response to ASH:*srg-36* at 3 µM C3.

Interneuron imaging in freely moving worms contributes additional evidence that AIB can act as a signal accumulator (Figure 3.7). In both individual trial averages and population trial averages, AIB:GCaMP3 and AVA:GCaMP5 start to increase fluorescence activity in the ASH:*srg-34* worms simultaneously at C3 onset, ~5 s before the initiation of pirouette behavior (Figure 3.6). However, in *srg-36*-mediated ASH responses, while AVA calcium activity begins to increase on average about ~5 s before the initiation of pirouette behavior, AIB calcium activity begins to increase about 3 s before AVA (Figure 3.6.f.). This delay may be the signature of AIB accumulating weak ASH input over time before generating enough evidence to instruct AVA to initiate avoidance behavior.

Modeling AIB contribution as a coherent type-1 feed forward loop with slope-determined AND or OR logic

The temporal delay described above is characteristic of a coherent type-1 feed forward loop (FFL1) with AND logic (Alon, 2007; Figure 3.8.f.). Originally described as the most common circuit motif in transcriptional networks, it was also suggested to be a common neural circuit motif in the *C. elegans* wiring diagram, based on its anatomy (Alon, 2007). Based on this model, the simple ASH, AIB, and AVA avoidance circuit consists of ASH directly activating AVA, or indirectly activating AVA by activating AIB. The circuit is coherent since all “edges” consists of positive relationships so that both the direct and indirect pathways result in the same end behavior (avoidance). In an AND logic FFL1, both ASH AND AIB activity are required to activate AVA, which in turn instructs avoidance; thus, if a temporal delay exists between ASH activation and the activation of AIB by ASH, AVA will not become active until this delay is over. ASH:*srg-36* mediated, 1 µM C3 stimulated interneuron activity exhibited a ~3 s delay between AIB and AVA calcium responses when aligned to pirouette behavior initiation. Thus, AIB began increasing activity around 3 s before AVA initiated activity in this scenario. Since this behavior was completely AIB dependent, with no residual avoidance in AIB silenced populations, this C3 receptor-concentration condition appears to operate entirely through a FFL1 with AND logic.

However, AIB is not required to generate avoidance behaviors in ASH:*srg-34*, 1 µM C3 or ASH:*srg-36*, 3 µM C3 receptor-concentration conditions. This was reinforced by the result of AVA and AIB imaging in freely moving worms under the ASH:*srg-34*, 1 µM C3 condition, in which AVA and AIB activations were aligned to both the onset of stimulus and to each other.

This suggests that ASH was able to activate AVA without additional AIB input. If ASH can instantaneously activate AIB, the AND logic circuit essentially becomes an OR logic circuit. Modeling the simple ASH, AIB, AVA circuit as a type 1 FFL1 circuit with OR logic (Figure 3.8.i), ASH alone can activate AVA to initiate avoidance behaviors (conversely, AIB alone may be enough to activate AVA signals without ASH). However, an opposite temporal delay occurs when a signal ends in an OR logic circuit –both neurons must stop signaling before the output behavior can terminate (Alon, 2007), i.e. if either ASH or AIB remain active, AVA can continue to generate avoidance behaviors. Interestingly, a decrease in the ability to maintain avoidance behaviors at later time points was observed across many C3 receptor-concentration conditions (Figure 3.6.e.), suggesting that AIB may delay the termination of avoidance behaviors in scenarios where it may not be required to initiate avoidance behavior.

To investigate these possibilities, I generated a rudimentary model to use ASH calcium responses to explain characteristics of avoidance behavior dynamics in various C3 receptor-concentration conditions with and without AIB silencing (Figure 3.8). I first used experimentally generated behavior time courses from AIB intact (Figure 3.8.a.) and AIB silenced (Figure 3.8.b.) populations to derive the "residual" behavior after AIB silencing (Figure 3.8.c.). Using experimentally generated ASH calcium traces (Figure 3.8.d.), I calculated the derivative of each trace (Figure 3.8.e.) since the slope of the ASH response was shown to be important for AIB dependence from prior analysis (Figure 3.6). Setting a slope of 0.01 $\Delta F/F_0$ as the cut off between a type-1 FFL with AND (slope <0.01 $\Delta F/F_0$) or OR (slope >0.01 $\Delta F/F_0$) logic, I conducted the following models of AIB input, assuming that AIB is an accumulator of ASH activity. In type-1 FFL1 AND logic circuit models (Figure 3.8.f.), I integrated the entire ASH slope function since input from AIB is required for AVA activation (Figure 3.8.g.). In type-1 FFL1 OR logic circuit models (Figure 3.8.i.), I integrated the ASH slope function only after the slope peaked (Figure 3.8.j.) so that ASH is initially allowed to activate AVA without AIB input as it is itself sharply activated by C3. Subtracting the model AIB contribution (Figure 3.8.g and Figure 3.8.j.) from each respective experimentally derived intact avoidance behavior in Figure 3.8.a. generates models of avoidance behavior time courses after AIB silencing (Figure 3.8.h.).

Results from this slope-determined AND or OR logic type-1 FFL model (Figure 3.8.h.) recapitulates many features observed in changes to the behavioral time course after experimental AIB silencing (Figure 3.8.b.). First, because the shape of the ASH:*srg-36*, 1 µM C3 behavior response (Figure 3.8.a.) was so similar to its respective ASH activation dynamics (Figure 3.8.d.), in the AND logic circuit AIB silencing eliminated the entire avoidance response

(Figure 3.8.h.), in agreement with experimental data (Figure 3.8.b.). Since the ASH:*srg-34*, 10 nM C3 response (Figure 3.8, 1st column) had a large initial avoidance response to stimulus onset (Figure 3.8.a.), subtracting the integrated slow calcium slope function only eliminated the later avoidance behaviors, leaving a residual sharp increase of avoidance behavior at stimulus onset (Figure 3.8.h.) that resembles the experimental data in AIB silenced populations (Figure 3.8.b.). Because the slope of neural activity is negative (Figure 3.8.e.) for a significant portion of the ASH:*srg-34*, 1 µM C3 and ASH:*srg-34*, 3 µM C3 conditions (right two columns), subtracting the integration of the calcium slope after the peak of calcium slope results in the most subtraction near the peak of behavior, with more intact behavior towards the end of stimulation (Figure 3.8.h); this was also characteristic of the experimental data for these conditions (Figure 3.8.b). The model for ASH:*srg-34*, 33 nM C3 was least predictive of the measured result (Figure 3.8, third column). The behaviors in this data set were noisy, however, and repeating the experiment might add clarity (Figure 3.8.a-b). It is possible that other interneurons can add additional nodes to this model that are currently unaccounted for.

There are clearly aspects of behavior that are not explained by this model. First, we do not account for the original behavior in AIB intact worms. For instance, the sharp initial peak of ASH:*srg-34* mediated responses persist even when no ASH calcium signals can be observed (0.5 nM C3), and do not reflect the observed low-slope calcium signals at a low (10 nM) C3 concentration (Figure 3.6.d.). These may be explained by voltage changes that do not require calcium amplification or by calcium signals that are high enough to activate downstream interneurons of ASH but are too low to be detected by the GCaMP3 fluorescent calcium indicator. In any case, the low calcium slope measured to ASH:*srg-34*, 10 nM C3 was able to trigger immediate, non-AIB dependent avoidance behaviors while a slightly higher calcium slope with much higher calcium peak and total evoked calcium in ASH (ASH:*srg-36*, 1 µM C3) was only able to trigger ramping behavior increases that were entirely AIB dependent. This suggests that ASH:*srg-34* and ASH:*srg-36* mediated behaviors result from different ASH activation regimes. They also interact with different G proteins (Figure 2.18 and Figure 2.19). Whether the resulting behavior difference occurs through access to different calcium stores, different neurotransmitter pools, or different signaling cascades remains to be elucidated.

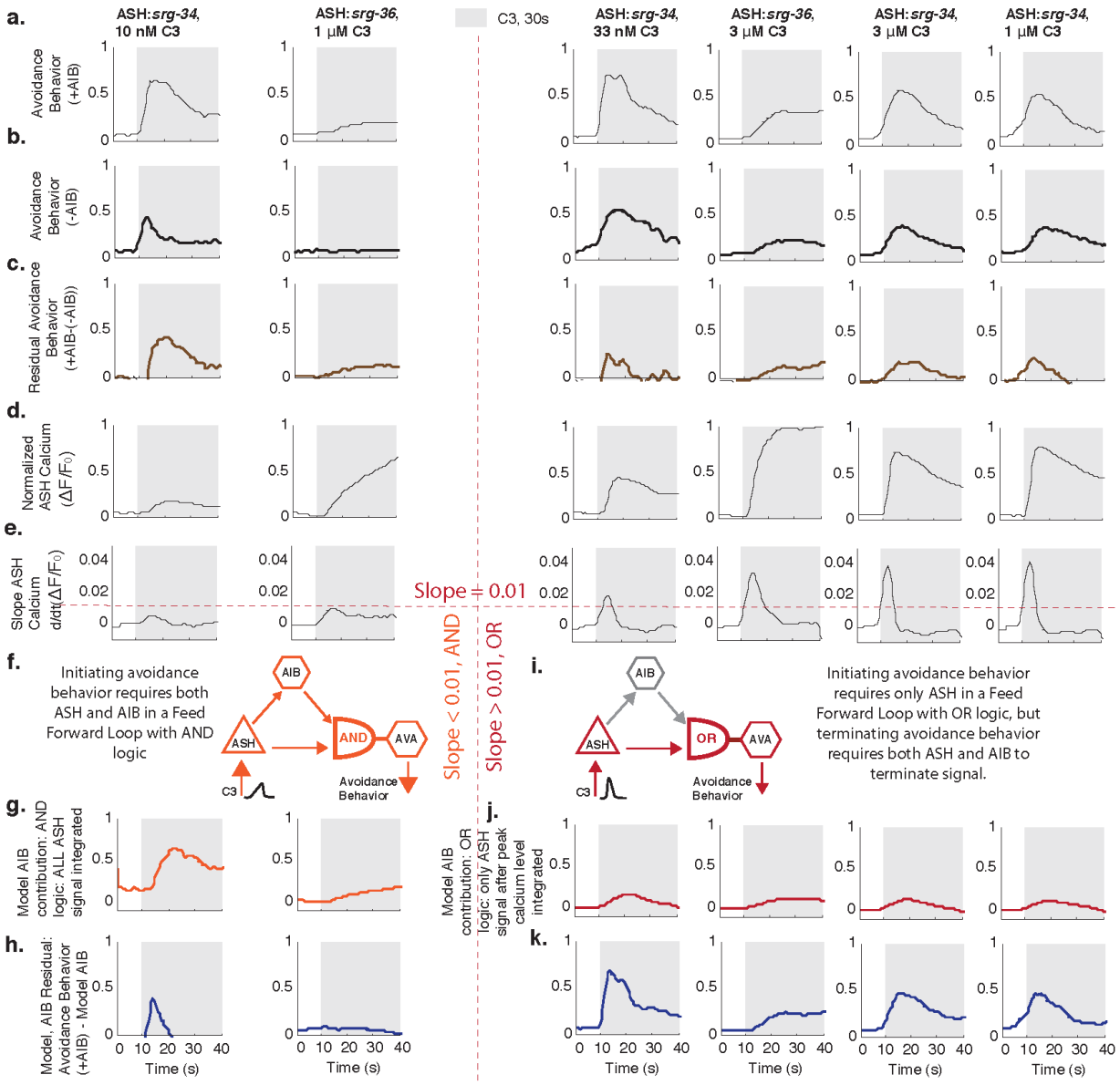

Figure 3.8. Contribution of AIB integration of ASH signaling in avoidance circuit can be modeled using a coherent type-1 feed forward loop with slope-determined AND or OR logic (Alon, 2007)

a) Time-aligned sums of avoidance (pause, reverse, and omega) behaviors in response to 30 s stimulation to each C3 receptor-concentration condition in AIB-intact populations. **b)** Time-aligned sums of avoidance behaviors in response to 30 s stimulation to each C3 receptor-concentration condition in AIB-silenced populations (residual behavior). **c)** Subtraction of b) from a); the measured AIB-dependent behavior. **d)** Measured ASH calcium traces in response to 30 s stimulation to each C3 receptor-concentration condition, normalized to maximum height (peak of ASH:*srg-36*, 3 uM condition). **e)** Slope of measured ASH calcium traces for each condition derived from d). **f)** Coherent type-1 feed forward loop with AND logic (orange) models the simple ASH avoidance circuit with maximum measured ASH calcium slope <0.01 ΔF/F0/s. Both ASH and AIB must be coactive in order for AVA to initiate avoidance behavior; all of ASH calcium signal slopes are integrated by AIB to generate model AIB contribution in **g)**. **h)** Model of residual behavior is calculated by subtracting Model AIB contribution in (g) from AIB intact behavior in a). **i)** Coherent type-1 feed forward loop with OR logic (red) models the simple ASH avoidnace circuit with maximum measured ASH calcium slope >0.01 ΔF/F0/s. Only ASH signals are required to activate AVA to initiate avoidance behaviors; however, since both ASH and AIB must be OFF to terminate behavior, ASH calcium signal slope is integrated by AIB only after the peak is reached to generate the model of AIB contribution in **j). k)** Model of residual behavior is calculated by subtracting Model AIB contribution in (j) from AIB intact behavior in a). Traces in g) and j) were normalized by integrating slopes derived from calcium traces normalized to the maximum of the respective behavior in a). Compare g)/j) to c) (brown) and h)/k) to b) (black).

Consequences of a modulatable feed forward excitatory circuit in nociception

In response to 1 µM C3, ASH:*srg-34* and ASH:*srg-36* appear to induce two different classes of ASH activity, which respectively instruct different classes of aversion behavior with different neural circuit dependences. ASH:*srg-34* has a fast ASH calcium rise and fast adaptation, it instructs correspondingly fast behavior dynamics and does not require AIB to drive avoidance behaviors. This cluster of results suggests that direct chemical synapses from ASH to AVA are enough to drive aversion in the context of fast, strong sensory inputs. ASH:*srg-36* has a slower ASH calcium response, no adaptation, and accordingly slower behavioral dynamics. The timing of aversive behavior after stimulus onset is more variable than the timing of ASH:*srg-34* responses. AIB is critical for ASH:*srg-36* to elicit behavior, and animals in which AIB is hyperpolarized behave as if they do not sense 1 µM C3.

The existence of two classes of ASH responses has previously been suggested based on differences in requirements for downstream glutamate receptors (Hart et al., 1995, Maricq et al., 1995). Further evidence is provided by the modulatable timing of response initiation to low octanol concentrations, which show that worms reliably move from a rapid to a slow avoidance regime based on external and internal modulating factors (Chao et al., 2004; Harris et al., 2009; Wragg et al., 2007). Since AIB is an intermediate-level interneuron with many other sensory and interneuron inputs, its position could allows signal integration across many internally and externally generated stimuli. It may act as a coincidence detector, allowing many nociceptive signals to summate so that an environment of many weakly aversive stimuli can bring AIB, and thus AVA, into an active state. Conversely, it may allow weakly nociceptive signals in ASH to compete with internal and external attractive signals that converge on AIB.

A simple circuit that can measure slow and fast changes in the environment, integrate them with other external and internal cues, and accumulate information over time is well-suited to signal nociceptive cues. It allows nociceptive cues to act in a deterministic manner when survival is immediately challenged, but also allows the circuit to “decide” whether weaker nociceptive cues outweigh the attractive cues in the environment. This flexible circuit thus has many survival benefits but can be disrupted. If the nociceptive tone, for instance, is disturbed through genetic mutations or injury, weaker nociceptive cues may be perceived to be deterministic or stronger cues to be ignorable, resulting in imprecise behaviors.

CHAPTER 3: Appendix

Appendix Table 3.1. Initial calcium slope and fraction of avoidance behavior maintained after AIB silencing for each C3 receptor-concentration (30 s total stimulation).

Receptor, [C3]	Initial Slope (Calcium)	Residual Avoidance Behavior (Total Behavior -AIB)/(Total Behavior +AIB)		
		0-15 s	**15-30 s**	**0-30 s**
ASH:*srg-34*, 0.0005 µM	0.0000	0.232	-0.123	0.144
ASH:*srg-34*, 0.010 µM	0.0051	0.412	0.317	0.377
ASH:*srg-36*, 1.000 µM	0.0093	0.220	0.136	0.162
ASH:*srg-34*, 0.033 µM	0.0192	0.759	0.968	0.824
ASH:*srg-36*, 3.000 µM	0.0335	0.569	0.506	0.528
ASH:*srg-34*, 3.000 µM	0.0383	0.616	0.652	0.627
ASH:*srg-34*, 1.000 µM	0.0407	0.580	1.131	0.721

CHAPTER 4: Discussion and Future Directions

My thesis work focused on how the temporal dynamics of nociceptor activation instructs downstream interneurons to initiate avoidance behavior.

In Chapter 2, I describe two main types of calcium dynamics observed in ASH in response to naturally aversive stimuli, either measured with long stimulus pulses or derived as linear temporal filters from imaging responses to white noise stimuli. Temporal filters to glycerol and NaCl were slowly ramping, summing stimulus history for the past 10 s while most highly weighing the previous 3 s of exposure. Temporal filters to copper peaked within the first two seconds of stimulation before sharply returning to baseline. I showed that the *srg-34* and *srg-36* receptors both respond to 1 µM C3, but with different calcium dynamics. *srg-36* is slowly ramping, generating a linear filter to m-sequence presentations of stimulus that is comparable to the slow, broad filter found in endogenous ASH glycerol responses, while *srg-34* was fast peaking and fast adapting in response to both long stimulus pulses and in its m-sequence derived linear filter.

In Chapter 3, I described the relationship between neural signaling and avoidance behaviors. I discovered that ASH:*srg-36* behavioral responses to 1 µM C3 depend on the intermediate level interneuron AIB, which may accumulate such signals before activating AVA in an indirect pathway for avoidance behavior. ASH:*srg-34* did not require temporal summation by AIB and could still generate avoidance behaviors in response to nociceptive stimuli even when AIB was silenced. This suggests that *srg-34* can drive AVA directly from ASH. How different ASH calcium signals can be perceived by different downstream interneurons remains to be elucidated; I suggest some possibilities below

On the sensory neuron side, ASH:*srg-36* and ASH:*srg-34* may access different calcium sources within ASH to generate their respective calcium signals. Calcium-induced calcium release using either the inositol tris-phophate receptor or the ryanodine receptor has been implicated in mediating ASH-driven aversive responses to 1-octanol (Zahratka et al., 2014). Using calcium imaging, this study showed a change in calcium dynamics with a loss of function mutation in either of these regulators of intracellular calcium stores. This study also found that voltage changes to neuromodulatory cues such as serotonin may not necessarily change voltage amplitude and calcium amplitude in the same direction. Thus, there are some calcium-independent aspects of avoidance behavior that can be mediated by ASH. At the extremely low

C3 concentration of 10 nM, *srg-34* was still able to mediate a fast and high peak of avoidance behavior despite a low slope and low peak in calcium (Figure 3.4), but the later maintenance of avoidance behavior was significantly diminished. It is possible that the SRG-34 receptor may intrinsically be less dependent on calcium amplification of voltage signals to generate behavior than SRG-36. Looking at changes to *srg-34* and *srg-36* mediated ASH responses in the *egl-19* voltage-gated calcium channel, *unc-68* (ryanodine receptor), and *itr-1* (inositol triphosphate receptor) mutant backgrounds may help to elucidate whether SRG-34 and SRG-36 are accessing different intracellular calcium stores to generate their respective calcium dynamics. Since adding serotonin increased the nociceptive tone in ASH for 1-octanol responses, it is also possible to add serotonin into my calcium imaging or behavior experiments to see how SRG-34 and SRG-36 responses are modulated.

The ability of *ASH:srg-34* and *ASH:srg-36* to differently engage AVA and AIB could result from these receptors triggering release of different neurotransmitter or neuropeptide pools within ASH. To investigate this, *eat-4* vesicle glutamate transporter mutants, *egl-3* proprotein convertase mutants or *egl-21* carboxypeptidase mutants (both involved in neuropeptide processing) can be assessed to see if signaling from either receptor is more glutamate or neuropeptide dependent. On the interneuron side, different glutamate receptor or neuropeptide receptor mutants could be checked for changes in behavioral dynamics to C3 avoidance.

AVA is not the only command interneuron in the *C.elegans* circuit to which ASH has access; AIB is not the only intermediate layer interneuron that could affect ASH behaviors. Investigating the role of other interneurons postsynaptic of ASH by silencing them with the HisCl system could add additional nodes to our simple circuit. The forward command interneuron, AVB, for instance, is postsynaptic to AVA, AIB, and ASH and may contribute to the circuit by either reinforcing the AVA response by terminating its own activation in the presence of deterministic signals or pull against AVA activity if attractive stimuli are also present in conjunction with a weaker signal from ASH.

While I have demonstrated the ability of ASH to instruct downstream interneurons differentially through different calcium dynamics, I have done so with ectopic receptors. This is because the endogenous response to natural stimuli in ASH is complex and because these stimuli are not specific to ASH. However, in the *tax-4 tax-2* genetic background, both ASE and ASI are silenced while leaving ASH signals intact. It could be interesting to see if ASH behavior responses to endogenous stimuli are more predictable in this background under AIB intact or

silenced conditions. Similarly, I would like to use my Type 1 FFL model to see which aspects of the ASH endogenous behaviors can be predicted and which can not be explained by this model.

Feed forward excitatory loops like our simple circuit in *C. elegans* have their counterparts in the mammalian nociception system. Specifically, Aδ and C fiber synapse onto both the ascending projection cells in lamina I of the spinal cord dorsal horn as well as to the intermediate layer vertical cell spinal cord interneurons in lamina II of the dorsal horn. Vertical cells then in turn synapse positively onto the same projection cells (Braz et al., 2014). This feed forward excitatory motif generates a “back-up” excitatory drive for nociceptive signals that result in significant loss of pain perception in mammals without this system. This is not the only example of feed forward excitation in the complex mammalian pain circuit, suggesting that this motif is not only critical for accurate pain perception, it may also be a major point of error in chronic pain states.

METHODS

Nematode Growth

Strains were grown and maintained under standard conditions at 22-23 °C on nematode growth medium (NGM) 2% agar plates as described in Brenner (1974). All animals used for hehavioral assays were grown on plates seeded with dense *E. coli* OP50 lawns.

Molecular Biology and Transgenes

Extrachromosomal transgenes

The gene of interest was cloned into a pSM vector (S. McCarroll, PhD thesis) expressing a cell-selective promoter. Transgenes were made by injection of DNA plasmid clones into the gonads of young adult hermaphrodites together with a fluorescent coinjection marker (Mello and Fire, 1995). To control for variation between transgenes, between two and five independent lines from each injection were characterized.

Microfluidic Device Design and Fabrication

Monolayer microfluidic devices were devised using soft lithography (Albrecht et al., 2011). Silicon mold masters were fabricated by using conventional photolithographic techniques to pattern a 70-µM layer of SUB 2050 photoresist (Microchem) on 4-inch wafers (Silicon uest). Photomasks were printed at 5080 dpi (Pageworks). We cast ~5-mm-thick polydimethylsiloxane (PDMS) devices (Sylgard 184 A and B, 1:10 by weight; Dow Corning) and cored inlet and outlet holes with a 1-mm (for metal posts) or 1.5-mm dermal punch (for Hamilton Valve tubing) (Accuderm). Devices were cleaned in ethanol after fabrication to remove residual PDMS monomers, rinsed in water, and baked at least 30 min at 55 °C to evaporate residual ethanol. Devices were reversibly sealed against a hydrophobic 25x50 mm glass slide, prepared by exposure to (tridecafluoro-1,1,2,2-tetrahydrooctyl)-1-trichlorosilane (United Chemical Technologies) vapor for 1 h under vacuum. A support glass slide with diamond-coated bit-drilled inlet and outlet holes was placed on the PDMS device on the non-featured side and clamped with a stage adapter (P-2; Warner Instruments) modified with longer screws and rubber washers to even clamping pressure.

Odor pulses were delivered by using a microfluidic device designed with a shifting-flow strategy that prevents pressure or flow rate discontinuities detectable by the animal (Chronis et al., 2007). One of two stimulus streams was directed into the arena by using a computer-

controlled three-way valve (Lee company) that switched the flow position of a “control” fluid stream while the other stimulus stream bypassed the arena directly to the outflow. Arenas were composed of either one square arena or two arenas of half that area, modified from the one-arena device by adding a second animal loading port and a physical barrier parallel to fluid flow (Larsch et al., 2013). The two-arena device allowed direct comparison of two populations. Chemical switch timing was comparable to both arenas in this design.

Trapped chip imaging

Experimental design and data acquisition

Young adult worms were trapped in a custom-designed microfluidic device made of the transparent polymer PDMS, where their noses were exposed to liquid streams under laminar flow (Chronis et al., 2007). Switching between odor streams was accomplished via two alternative laminar side-streams to minimize changes in fluid pressure with odor delivery. Movement artifacts were reduced using a cholinergic antagonist, 1mM tetramisole, in the worm-loading channel. Tetramisole had no apparent effect on chemosensory responses in the neurons tested. Wide-field microscopy was used to monitor fluorescence from the cell of interest as six sequential 10-s pulses or an m-sequence of stimulus was presented to the worm’s nose. Fluorescein (1:250,000 dilution) was added to the stimulus stream to measure accurate switching between stimulus and buffer in each trial. Stimulus presentations were automated using ValveBank (AutoMate Scientific) and LabJack interfaces to control a solenoid valve (LFAA1201610H, The Lee Company) with a pre-generated sequence. Switch time limitations were initially evaluated using 100 ms, 200 ms, 500 ms, 1 s, and 2 s flicker presentations ofr 5 minutes per trial to worms expressing GCaMP3 in ASH under the sra-6 promoter. Protocols using S basal buffer as background and either 1 M glycerol (with fluorescein) or S Basal buffer (with fluorescein) as the stimulus were used at each timescale to compare ASH calcium activity with stimulus onset. Measurement of fluorescein dye in the liquid stream near the worm’s nose showed reliable square waves of dye fluorescence at 200 ms switch times. Thus, the m-sequence pulse length was limited to a minimum of 200ms because of the mechanical limit of the microfluidic switch, assessed by tracking fluorescein. Insignificant changes in ASH calcium signals were observed when the flickering stimulus switched between S basal and S basal with 1:250,000 dilution of fluorescein, allowing the use of fluorescein dye as a surrogate for odor concentration. Subsequent control experiments indicated that ASH calcium signals were insensitive to fluorescein inclusion with odor. For m-sequence stimulation, the dye fluorescence

in each frame was used as a surrogate for odor concentration for modeling. Fluorescence signals were analyzed after a newly developed bleach-correction algorithm with gain correction (Kato et al., 2014). The ASH neuron expressing GCaMP3, specifically, had a near-fusion response to 200 ms flow, indicating that the cell or sensor was close to its limit for tracking the stimulus. Pseudorandom sequences were 2x repeats of 9-bit word length m-sequence, ie. an m-sequence length of 2^9-1=511 pulses.

Metamorph and a Coolsnap HQ (Photometrics) camera were used to capture stacks of TIFF images at 10 frames s^{-1} during the odor presentation sequence. Custom Metamorph or ImageJ programs were used to identify the region of interest encompassing the cell body in all frames (Saul Kato). The background intensity and the average fluorescence intensity of the cell in each frame were determined by running a journal script based on either a “track objects” feature thresholding algorithm (Metamorph) or by tracking the brightest 100 pixels in the TIFF stack within a bounding region and subtracting the average intensity of a 16 pixel background region adjacent to a corner of the bounding box. (ImageJ). A Matlab (7.0R14, MathWorks) script generated cell-response plots using log files generated by Metamorph or ImageJ. The average fluorescence of the region of interest was generated by subtracting the recorded value fro the average intensity of the background region of a similar area. The average fluorescence in a 3-s window (t=1-4s) was set as F_0. For figures, the percentage change in fluorescence intensity for the region of interest ($\Delta F/F_0$) relative to F_0 was plotted individually for each trial. A second Matlab script was used to plot the average of all trials with standard errors for each time point.

Data analysis and statistics

Dynamical model estimation for GCaMP3 response dynamics, including bleach correction and model performance evaluation were generated in collaboration with Saul Kato as described in Kato et al. (2014) to construct the LN model.

Multi-worm tetramisole imaging (as described in Larsch et al.***, 2013)***

Stimulus preparation

Pheromone dilutions in S-basal buffer were prepared fresh on the day of the experiment from 10mM stock of C3 synthesized ascaroside (Rebecca Butcher) dissolved in DMF.

Equipment and Experimental set-up

Experiments were conducted on an automated microscope on a Zeiss AxioObserver.At inverted body with Zeiss Fluar objective lenses (5x/0.25 N.A.) and a Hamamatsu ORCA-Flash4.0 camera mounted with a 1.0x Zeiss adapter. A custom-built digital timing circuit synchronized image capture with illumination pulses of adjustable duration and delay from a Lumencor SOLA-LE solid-state lamp. Metamorph 7.7.6 software controlled both image streaming (10 frames per s for 1 hr) and stimulus delivery via digital signals (from National Instruments NI-DAQmx to an Automate Valvebank 8 II actuator and Lee solenoid valves) and via serial commands to a Hamilton MVP eight-way distribution valve. Custom journal scripts selected from various preprogrammed reocroding parameter (exposure, binning, stream length, trial interval) and stimulation parameters (stimulation valve timing and odor selection valves). Fully automated experiments (tested up to 1 hr) required no further user intervention after a session had been initiated.

Two-arena devices were used for multi-worm tetramisole-paralyzed imaging in order to compare neural calcium responses between different genotypes or extra-chronosomal array expression. Microfluidic arenas were assembled and degassed through a vacuum dessicator for at least 20 minutes before loading S-basal buffer through the outlet port. Any air bubbles were absorbed into the PDMS within 30 s of fluid input. We connected tubing from the Lee solenoid-controlled switch buffer, stimulus, and control reservoirs to the arena and initiated gravity-directed flow. All buffers and stimuli contained 1mM (-)tetramisole hydrochloride (Sigma) to paralyze muscles and prevent motion artifacts during imaging. 10-14 worms were injected into each arena via syringe attached to loading tubing. Animals were allowed to paralyze for 1 hour while buffer flow continuously washed the animals and removed any residual bacteria.

Cleaning the apparatus after image acquisition required flushing arenas with water and soaked them in ethanol for 24 hours to remove any residual stimulus. Water was used to rinse off ethanol before drying PDMS with an air-stream and baked at 55 °C for at least 30 min. After this cleaning procedure, buffer-to-buffer controls showed no response, and devices could be reused.

Data analysis and statistics

Movies were analyzed for neural fluorescence using a set of custom ImageJ macros and MATLAB scripts. Typically, 80-90% of animals in the device could be tracked. The normalized calcium response ($\Delta F/F_0$) for each animal was calculated using by dividing background-corrected integrated neural fluorescence F(t) by baseline fluorescence F_0 (mean for the first 5s).

Normalized traces were averaged across repeated trials for each animal. Population-average responses were used to calculate the mean and variance of individual animal responses. Statistical comparisons were made by ANOVA using Bonferroni correction for multiple comparisons. Data were presented from repeated trials as indicated per experiment.

Neuronal calcium response dynamics were quantified as the peak fluorescence, peak delay time, initial slope, and the area under the response curve for total response time was determined for each animal and trial from normalized fluorescence traces smoothed with a 0.3 s window. Peak fluorescence was calculated as maximum fluorescence during the stimulus pulse (stim) minus maximum fluorescence during the 2-s (20 frames) period before stimulation (prestim): $\max(\Delta F/F_0)_{stim}$-$\max(\Delta F/F_0)_{prestim}$. Peak delay time was calculated as the time after stimulus onset when peak fluorescence occurred. Initial slope was calculated as the slope immediately following the inflection point. The area under the curve was calculated by integrating the height of fluorescence for every time point during stimulus presentation.

Variance across repeated trials and across trials was calculated by using the MATLAB "var" function on peak calcium fluorescence per neural trace. Dose-response curves were fit using the MATTLAB curve-fitting toolbox and function "cfit" to a four-parameter sigmoidal curve defined by $F'=F'_{min}+(F'_{max}-F'_{min})/[1+(EC_{50}/C)^{\beta}]$ where $F'= \Delta F/F_0$ for each trace and C is the odor concentration. EC_{50} represents the odor concentration eliciting a 50% maximal peak response and the parameter β represents the dynamic range of the response.

Free-moving imaging (as described in Larsch et al.***, 2013)***

Stimulus Preparation, Equipment, and Experimental Setup

Equipment and experimental set-up were conducted as with Multi-worm tetramisole imaging with specific exceptions. First, single-arena devices were used to increase the area of exploration and a single worm was loaded to facilitate tracking. Buffers and stimuli contained no tetramisole. The worm was allowed to explore the device for 20 minutes (about 30 minutes after food removal when local search behavior had subsided) before image acquisition and stimulus presentation begins.

Data analysis and statistics conducted in collaboration with Sagi Levy.

Neural fluorescence and the fluorescence of a nearby "control" background region on the worm body were tracked for each frame using a custom MATLAB script (Sagi Levy). X-Y positions of the neuron and the "control" region were also recorded for each frame. Normalized

fluorescence was calculated by subtracting neural fluorescence by “control” fluorescence for each frame. Behavior was separately hand-tracked using a custom ImageJ ethogram GUI into forward, pause, reverse, forward omega, backward omega, and untrackable states.

Stimulus-aligned correlations were calculated for the initiating and termination of the following events to each other: stimulus presentation, omega behaviors, and changes in neural fluorescence.

Multi-arena chip behavior

Young adult worms were removed from food and washed, and ~25 animals were injected into each of four arenas of a custom-designed PDMS microfluidic device (Albrecht and Bargmann 2011; Kato et al., 2014). Each arena contained a structured micropost array optimized for crawling locomotion, barriers to prevent animal escape, and inlet channels to deliver temporal pulses of stimulus. After 30 min of acclimation to the PDMS environment in continuously flowing S-basal buffer, animals were exposed to a sequence of 10 s pulses, 30 s pulses, and 1 min pulses controlled by automated three-way switch valves (Lee Corporation) actuated by computer using a LabJack U3-hV digital controller, a Valvebank 8 II actuator (Automate), and custom MATLAB scripts. In each experiment, pulses of stimuli were given with 31 minutes, with 2 min of buffer both before and after the sequence. The entire sequence was repeated four times. At least two separate experiments on two separate days were done for every condition and genotype. Animals were recorded at 2 fps and analyzed using automated tracking software. Behaviors were segmented into forward locomotion, pauses, reversals, and omega turns, and animals in the forward locomotion state were also analyzed for speed, binned by 2s intervals. A stimulus-aligned ethogram of instantaneous behavioral state was assembled for each trial and averaged for each condition and genotype.

Strains

<u>ASH wild type calcium imaging lines</u>

CX10979 *kyEx2865* [*Psra-6::GCaMP3, Pofm-1::GFP*]

CX15304 *kyIs602* [*Psra-6::GCaMP3, Pofm-1::GFP*], outcrossed 12X to N2

<u>ASH mutant calcium imaging lines</u>

CX12739 *osm-9 (ky10) IV; ocr-2 (ak47) IV; kyEx2865* [*Psra-6::GCaMP3, Pofm-1::GFP*]

CX12740 *unc-13 (e51) I; KyEx2865* [*Psra-6::GCaMP3, Pofm-1::GFP*]

CX12741 *unc-18 (e234) X; KyEx2865* [*Psra-6::GCaMP3, Pofm-1::GFP*]

CX12608 *egl-3 (n150ts) V; KyEx2865* [*Psra-6::GCaMP3, Pofm-1::GFP*]

CX12855 *osm-10 (n1602) III; KyEx2865* [*Psra-6::GCaMP3, Pofm-1::GFP*]

CX12860 *egl-21 (n611) IV; KyEx2865* [*Psra-6::GCaMP3, Pofm-1::GFP*]

CX12861 *egl-3 (n729) V; KyEx2865* [*Psra-6::GCaMP3, Pofm-1::GFP*]

CX13030 *tax-2 (p691) I; tax-4 (p678) III; KyEx2865* [*Psra-6::GCaMP3, Pofm-1::GFP*]

CX13128 *egl-19 (ad695) IV; KyEx2865* [*Psra-6::GCaMP3, Pofm-1::GFP*]

CX13129 *egl-19 (n582) IV; KyEx2865* [*Psra-6::GCaMP3, Pofm-1::GFP*]

CX13131 *gpa-3 (pk35) V; KyEx2865* [*Psra-6::GCaMP3, Pofm-1::GFP*]

CX13132 *gpa-3 (pk35) V; odr-3 (n1605) V; KyEx2865* [*Psra-6::GCaMP3, Pofm-1::GFP*]

CX13133 *odr-3 (n2150) V; KyEx2865* [*Psra-6::GCaMP3, Pofm-1::GFP*]

CX13134 *rgs-3 (ok2288) II; KyEx2865* [*Psra-6::GCaMP3, Pofm-1::GFP*]

CX13287 *odr-3 (ky879) V; KyEx2865* [*Psra-6::GCaMP3, Pofm-1::GFP*]

CX13289 *odr-3 (n1605) V; KyEx2865* [*Psra-6::GCaMP3, Pofm-1::GFP*]

CX13292 *tax-6 (p675) IV; KyEx2865* [*Psra-6::GCaMP3, Pofm-1::GFP*]

CX13525 *arr-1 (ok401) X; KyEx2865* [*Psra-6::GCaMP3, Pofm-1::GFP*]

CX13526 *dgk-1 (nu199) X; KyEx2865* [*Psra-6::GCaMP3, Pofm-1::GFP*]

CX13527 *dgk-3 (gk110) III; KyEx2865* [*Psra-6::GCaMP3, Pofm-1::GFP*]

CX13528 *eat-11 (ad541) I; KyEx2865* [*Psra-6::GCaMP3, Pofm-1::GFP*]

CX13529 *gpc-1 (pk298); KyEx2865* [*Psra-6::GCaMP3, Pofm-1::GFP*]

CX13530 *grk-2 (rt97) III; KyEx2865* [*Psra-6::GCaMP3, Pofm-1::GFP*]

CX13531 *pkc-1 (ok563) V; KyEx2865* [*Psra-6::GCaMP3, Pofm-1::GFP*]

CX13532 *trpa-1 (ok999) IV; KyEx2865* [*Psra-6::GCaMP3, Pofm-1::GFP*]

CX13533 *gpb-2 (pk751) I; KyEx2865* [*Psra-6::GCaMP3, Pofm-1::GFP*]

CX13619 *eat-16 (sa609) I; KyEx2865* [*Psra-6::GCaMP3, Pofm-1::GFP*]

CX13620 *deg-1 (u38ts) X; KyEx2865* [*Psra-6::GCaMP3, Pofm-1::GFP*]

CX13621 *mec-10 (e1515) X; KyEx2865* [*Psra-6::GCaMP3, Pofm-1::GFP*]

CX13622 *egl-10 (n1068) V; KyEx2865* [*Psra-6::GCaMP3, Pofm-1::GFP*]

CX13623 *egl-30 (n686sd) I; KyEx2865* [*Psra-6::GCaMP3, Pofm-1::GFP*]

CX13648 *goa-1 (n363) I; KyEx2865* [*Psra-6::GCaMP3, Pofm-1::GFP*]

CX13781 *qui-1 (ok3571) IV; KyEx2865* [*Psra-6::GCaMP3, Pofm-1::GFP*]

ASI calcium imaging lines

CX13047 *kyEx3743* [*Pstr-3::GCaMP3, Pofm-1::GFP*]

CX13617 *unc-13 (e51) I; kyEx3743* [*Pstr-3::GCaMP3, Pofm-1::GFP*]

CX13782 *qui-1 (ok3571) IV; kyEx3743* [*Pstr-3::GCaMP3, Pofm-1::GFP*]

CX14120 *che-1 (p680) I; kyEx3743* [*Pstr-3::GCaMP3, Pofm-1::GFP*]

CX14971 *lsy-6 (ot71) V; kyEx3743* [*Pstr-3::GCaMP3, Pofm-1::GFP*]

CX14941 *ntIs1* [*Pgcy-5::GFP*]; *otEx3830* [*Pceh-36::CZ-caspase3(p17); Pgcy-5::caspase3(p12)-NZ; Pmyo-3::mCherry*]; *kyEx3743* [*Pstr-3::GCaMP3, Pofm-1::GFP*]

CX14935 *otIs204* [*Pceh-36::lsy-6*]; *kyEx3743* [*Pstr-3::GCaMP3, Pofm-1::GFP*]

CX14991 *otIs4* [*Pgcy-7::GFP*]; *otEx3822* [*Pceh-36::CZ-caspase3(p17); Pgcy-7::caspase3(p12)-NZ; Pmyo-3::mCherry*]; *kyEx3743* [*Pstr-3::GCaMP3, Pofm-1::GFP*]

Voltage imaging lines

CX15967 *kyEx5413* [*Psra-6::mac::mCitrine; Pofm-1::mCherry*]

CX16115 *kyEx5222* [*Psra-6::srg-36, Pmyo-2::mCherry*]; *kyEx5413* [*Psra-6::mac::mCitrine; Pofm-1::mCherry*]

CX16128 *kyEx5220* [*Psra-6::srg-34, Pmyo-2::mCherry*]; *kyEx5413* [*Psra-6::mac::mCitrine; Pofm-1::mCherry*]

ASE calcium imaging lines

CX14571 *kyEx4732* [*Pflp-6::GCaMP3; Pofm-1::GFP*]

CX14957 *lsy-6 (ot71) V; kyEx4732* [*Pflp-6::GCaMP3; Pofm-1::GFP*]

Interneuron HisCl lines

CX14845 *kyEx4863* [*Prig-3::HisCl1:sl2mCherry*]

CX15457 *kyIs620* [*Pinx-1::HisCl1::sl2GFP; Pmyo-3:mCherry*]

Interneuron calcium imaging lines

CX13440 *kyEx4018* [*Pinx-1::GCaMP3; Punc-122::dsRed*]

CX15380 *kyEx5170* [*Prig-3::GCaMP5*]

ASH:*srg-34* strains

CX15317 *kyEx5029* [*Psra-6::srg-34, Pofm-1::dsred*]

CX15319 *qrIs2* [*Psra-9::caspase*]; *kyEx5029* [*Psra-6::srg-34, Pofm-1::dsred*]

CX15303 *kyIs602* [*Psra-6::GCaMP3, Pofm-1::GFP*], *kyEx5029* [*Psra-6::srg-34, Pofm-1::dsred*]

CX14336 *gpa-3 (pk35) V; odr-3 (n1605) V; KyEx2865* [*Psra-6::GCaMP3, Pofm-1::GFP*]; KyEx4174 [*Psra-6::srg-34, Pofm-1::RFP*]

CX14338 *odr-3 (n1605) V; KyEx2865* [*Psra-6::GCaMP3, Pofm-1::GFP*]; KyEx4174 [*Psra-6::srg-34, Pofm-1::RFP*]

CX14337 *rgs-3 (ok2288) II; KyEx2865* [*Psra-6::GCaMP3, Pofm-1::GFP*]; KyEx4174 [*Psra-6::srg-34, Pofm-1::RFP*]

CX15696 *egl-19 (n582) IV; kyEx5220* [*Psra-6::srg-34, Pmyo-2::mCherry*]; *kyIs602* [*Psra-6::GCaMP3, Pofm-1::GFP*]

CX15701 *egl-19 (ad695) IV; kyEx5220* [*Psra-6::srg-34, Pmyo-2::mCherry*]; *kyIs602* [*Psra-6::GCaMP3, Pofm-1::GFP*]

CX15721 *gpa-3 (pk35)V; odr-3 (n1605) V; kyEx5220* [*Psra-6::srg-34, Pmyo-2::mCherry*]; *kyIs602* [*Psra-6::GCaMP3, Pofm-1::GFP*]

CX15462 *kyEx5220* [*Psra-6::srg-34, Pmyo-2::mCherry*]; *kyIs620* [*Pinx-1::HisCl1::sl2GFP; Pmyo-3:mCherry*]

CX15733 *osm-9 (ky10) IV; kyEx5220* [*Psra-6::srg-34, Pmyo-2::mCherry*]; *kyIs602* [*Psra-6::GCaMP3, Pofm-1::GFP*]

CX15546 *kyEx5220* [*Psra-6::srg-34, Pmyo-2::mCherry*]; *kyEx4863* [*Prig-3::HisCl1:sl2mCherry*]

CX15533 *kyEx5220* [*Psra-6::srg-34, Pmyo-2::mCherry*]

CX15536 *kyEx5220* [*Psra-6::srg-34, Pmyo-2::mCherry*]; *kyIs602* [*Psra-6::GCaMP3, Pofm-1::GFP*]

CX15704 *kyEx5220* [*Psra-6::srg-34, Pmyo-2::mCherry*]; *kyEx4018* [*Pinx-1::GCaMP3; Punc-122::dsRed*]

CX15712 *kyEx5220* [*Psra-6::srg-34, Pmyo-2::mCherry*]; *kyEx5170* [*Prig-3::GCaMP5*]

ASH:*srg-36* strains

CX15302 *kyEx5032* [*Psra-6::srg-36, Pofm-1::dsred*], *KyIs602* [*Psra-6::GCaMP3, Pofm-1::GFP*]

CX15318 *kyEx5032* [*Psra-6::srg-36, Pofm-1::dsred*]

CX15320 *kyEx5032* [*Psra-6::srg-36, Pofm-1::dsred*]; *qrIs2* [*Psra-9::caspase*]

CX14328 *gpa-3 (pk35) V; odr-3 (n1605) V; KyEx2865* [*Psra-6::GCaMP3, Pofm-1::GFP*]; KyEx4171 [*Psra-6::srg-36, Pofm-1::RFP*]

CX14330 *odr-3 (n1605) V; KyEx2865* [*Psra-6::GCaMP3, Pofm-1::GFP*]; KyEx4171 [*Psra-6::srg-36, Pofm-1::RFP*]

CX14329 *rgs-3 (ok2288) II; KyEx2865* [*Psra-6::GCaMP3, Pofm-1::GFP*]; KyEx4171 [*Psra-6::srg-36, Pofm-1::RFP*]

CX15464 *kyEx5222* [*Psra-6::srg-36, Pmyo-2::mCherry*]; *kyIs620* [*Pinx-1::HisCl1::sl2GFP; Pmyo-3:mCherry*]

CX15529 *kyEx5222* [*Psra-6::srg-36, Pmyo-2::mCherry*]

CX15544 *kyEx5222* [*Psra-6::srg-36, Pmyo-2::mCherry*]; *kyIs602* [*Psra-6::GCaMP3, Pofm-1::GFP*]

CX15554 *kyEx5222* [*Psra-6::srg-36, Pmyo-2::mCherry*]; *kyEx4863* [*Prig-3::HisCl1:sl2mCherry*]

CX15706 *kyEx5222* [*Psra-6::srg-36, Pmyo-2::mCherry*]; *kyEx4018* [*Pinx-1::GCaMP3; Punc-122::dsRed*]

CX15691 *osm-9 (ky10) IV; kyEx5222* [*Psra-6::srg-36, Pmyo-2::mCherry*]; *kyIs602* [*Psra-6::GCaMP3, Pofm-1::GFP*]

CX15700 *egl-19 (n582) IV; kyEx5222* [*Psra-6::srg-36, Pmyo-2::mCherry*]; *kyIs602* [*Psra-6::GCaMP3, Pofm-1::GFP*]

CX15741 *egl-19 (ad695) IV; kyEx5222* [*Psra-6::srg-36, Pmyo-2::mCherry*]; *kyIs602* [*Psra-6::GCaMP3, Pofm-1::GFP*]

CX16472 *gpa-3 (pk35) V; kyEx5222* [*Psra-6::srg-36, Pmyo-2::mCherry*]; *kyIs602* [*Psra-6::GCaMP3, Pofm-1::GFP*]

REFERENCES

Akopian, A.N. et al., 1999. The tetrodotoxin-resistant sodium channel SNS has a specialized function in pain pathways. *Nat Neurosci.* **2**(6):541-548.

Albrecht, D.R., and Bargmann, C.I. (2011). High-content behavioral analysis of *Caenorhabditis elegans* in precise spatiotemporal chemical environments. *Nat Methods* **8**(7), 599-605.

Alkema, M.J., Hunter-Ensor, M., Ringstad, N, Horvitz, H.R. 2005. Tyramine functions independently of octopamine in the *Caenorhabditis elegans* nervous system. *Neuron* **46**(2):247-260.

Alon, U. 2007. An Introduction to Systems Biology: Design Principles of Biological Circuits. (London: Chapman & Hall), pp. 120-130.

Amir, R., Devor, M. 2003. Electrical excitability of the soma of sensory neurons is required for spike invasion of the soma, but not for through-conduction. *Biophys J.* **84**(4):2181-2191.

Aoki, R., Yagami, T., Sasakura, H., Ogura, K., Kajihara, Y., Ibi, M., Miyamae, T., Nakamura, F., Asakura, T., Kanai, Y., Misu, Y., Iino, Y., Ezcurra, M., Schafer, W.R., Mori, I., Goshima, Y. 2011. A seven-transmembrane receptor that mediates avoidance response to dihydrocaffeic acid, a water-soluble repellent in *Caenorhabditis elegans. J Neurosci* **31**(46):16603-16610.

Awatramani, G.B., Slaughter, M.M. 2000. Origin of transient and sustained responses in ganglion cells of the retina. *J Neurosci.* **20**(18):7087-7095.

Babes, A. 2009. Ion channels involved in cold detection in mammals: TRP and non-TRP mechanisms. *Biophysical Rev.* **1**(4):193-200.

Babes, A., Zorzon, D., Reid, G. 2004. Two populations of cold-sensitive neurons in the rat dorsal root ganglia and their modulation by nerve growth factor. *Eur J. Neurosci.* **20**(9):2276-2282.

Bargmann, C.I. (2006) Chemosensation in *C. elegans* (October 25, 2006). WormBook, ed. The C. elegans Research Community, WormBook, doi/10.1895/wormbook.1.123.1, http://www.wormbook.org.

Bargmann, C.I., Hartwieg, E., Horvitz, H.R. (1993). Odorant-selective genes and neurons mediate olfaction in *C. elegans*. *Cell* **74**(3), 515-527.

Basbaum, A.I., Bautista, D.M., Scherrer, G., and Julius, D. (2009). Cellular and molecular mechanism of pain. *Cell* **139**, 267-284.

Basbaum, A.I., Jessell, T. (2000). The perception of pain. In Principles of Neuroscience, E.R. Kandel, J. Schwartz, and T. Jessell, eds. (New York: Appleton and Lange), pp. 472-491.

Bautista, D.M., et al. 2007. The menthol receptor TRPM8 is the principal detector of environmental cold. *Nature* **448**:204-208.

Bautista, D.M., Jordt, S.E., Nikai, T., Tsuruda, P.R., Read, A.J., Poblete, J., Yomoah, E.N., Basbaum, A.I., and Julius, D. 2006. TRPA1 mediates the inflammatory actions of environmental irritants and proalgesic agents. *Cell* **124**: 1269-1282.

Bautista, D.M., Lumpkin, E.A. 2011. Probing mammalian touch transduction. *J. Gen. Phys.* **138**(3):291-301.

Bishop, G. H. 1933. Fiber groups in the optic nerves. *Am. J. Physiol.* **106**, 460–470.

Braz, J., Solorzano, C., Wang, X., Basbaum, A.I. 2014. Transmitting pain and itch messages: a contemporary view of the spinal cord circuits that generate gate control. *Neuron* **82**(3):522-536.

Brenner, S. 1974. The genetics of *Caenorhabditis elegans*. *Genetics* **77**:71-94.

Burkhardt, D.A., Fahey, P.K., Sikora, M.A. 2008. Retinal bipolar cells: temporal filtering of signals from cone photoreceptors. Visual Neuroscience **24**:765-774.

Busch, K.E., Laurent, P., Soltesz, Z., Murphy, R.J., Faivre, O., Hedwig, B., Thomas, M., Smith, H.L., de Bono, M. 2012. Tonic signaling from O2 sensors sets neural circuit activity and behavioral state. *Nat Neurosci.* **15**(4), 581-591.

Butcher, R.A., Ragains, J.R., Kim, E., Clardy, J. 2008. A potent dauer pheromone component in Caenorhabditis elegans that acts synergistically with other components. *Proc. Natl. Acad. Sci. USA* **105:**14288-14292.

Chalfie, M., Sulston, J.E., White, J.G., Southgate, E., Thomson, J.N., and Brenner, S. (1985). The neural circuit for touch sensitivity in *Caenorhabditis elegans. J Neurosci.* **5**, 956-964.

Campell, J.N., LaMotte, R.H. 1983. Latency to detection of first pain. *Brain Res.* **266**(2):203-208.

Cang, C.L., Zhang, H., Zhang, Y.Q., Zhao, Z.Q. 2009. PKCε-dependent potentiation of TTX-resistant $Na_v1.8$ current by neurokinin-1 receptor activation in rat dorsal root ganglion neurons. *Molecular Pain* **5**:33.

Cao, Y.Q. 2006. Voltage-gated calcium channels and pain. *Pain* **126**:5-9.

Cao, Y., Pahlberg, J., Sarria, I., Kamasawa, N., Sampath, A.P., Martemyanov, K.A. 2012. Regulators of G protein signaling RGS7 and RGS11 determine the onset of the light response in ON bipolar neurons. *Proc. Natl. Acad. Sci. USA* **209**(20):7905-7910.

Carr, R.W., Pianova, S., McKenny, D.D., Brock, J.A. 2009. Action potential initiation in the peripheral terminals of cold-sensitive neurons innervating the guinea-pig cornea. *J Physiol.* **587**(6):1249-1264.

Caterina, M.J., et al. 2000. Imparied nociception and pain sensation in mice lacking the capsaicin receptor. *Science* **288**:306-313.

Chao, M.Y., Komatsu, H., Fukuto, H.S., Dionne, J.M., Hart, A.C. 2004. Feeding status and serotonin rapidly and reversibly modulate a *Caenorhabditis elegans* chemosensory circuit. *Proc. Natl. Acad. Sci. USA* **101**:15512-15517.

Chase, D.L. and Koelle, M.R. Biogenic amine neurotransmitters in *C. elegans* (February 20, 2007), *WormBook*, ed. The *C. elegans* Research Community, WormBook, doi/10.1895/wormbook.1.132.1, http://www.wormbook.org.

Chatzigeorgiou, M. and Schafer, W.R. 2011. Lateral facilitation between primary mechanosensory neurons controls nose touch perception in *C. elegans*. *Neuron* **70**: 299-309.

Chronis, N., Zimmer, M., Bargmann, C.I. (2007) Microfluidics for in vivo imaging of neuronal and behavioral activity in *Caenorhabditis elegans*. *Nature Methods* **4**(9): 727-731.

Clark, D.A., Bursztyn, L., Horowitz, M.A., Schnitzer, M.J., and Clandinin, T.R. 2011. Defining the computational structure of the motion detector in *Drosophila*. *Neuron* **70**:1165–1177.

Colbert, H.A., Smith, T.L., and Bargmann, C.I. (1997). OSM-9, a novel protein with structural similarity to channels, is required for olfaction, mechanosensation, and olfactory adaptation in *Caenorhabditis elegans*. *J. Neurosci.* **17**(21): 8259-8269.

Colburn, R.W., Lubin, M.L., Stone, D.J., Wang, Y., Lawrence, D., D'Andrea, M.R., Brandt, M.R., Liu, Y., Flores, C.M., and Qin, N. 2007. Attenuated cold sensitivity in TRPM8 null nice. *Neuron* **54**: 379-386.

Coste, B., Mathur, J., Schmidt, M., Earley, T.J., Ranade, S., Petrus, M.J., Dubin, A.E., Patapoutian, A. 2010. *Piezo1* and *Piezo2* are essential components of distinct mechanically activated cation channels. *Science.* **330**: 55-60.

Cox, J.J., et al. 2006. An SCN9A channelopathy causes congenital inability to experience pain. *Nature* **444**:894-898.

Craig, A.D., Bushnell, M.C. 1994. The thermal grill illusion: unmasking the burn of cold pain. *Science* **265**:252-255.

Culotti, J.G., Russell, R.L. 1978. Osmotic avoidance defective mutants of the nematode *Caenorhabditis elegans. Genetics*. **90**(2):243-256.

Davies, A., Hendrich, J., Van Minh, A.T., Wratten, J., Douglas, L., and Dolphin, A.C. 2007. Functional biology of the alpha(2)delta subunits of voltage-gated calcium channels. *Trends Pharmacol. Sci.* **28**: 220–228.

Davis, J.B., et al. 2000. Vanilloid receptor-1 is essential for inflammatory thermal hyperalgesia. *Nature* **405**:188-187.

Davis, K.D., Pope, G.E. 2002. Noxious cold evokes multiple sensations with distinct time courses. *Pain* **98**(1-2):179-185.

Dayan, P., Abbott, L.F. 2001. Theoretical Neuroscience: Computational and Mathematical Modeling of Neural Systems. (Cambridge:The MIT Press).

De Bono, M., Maricq, A.V. 2005. Neuronal substrates of complex behaviors in *C. elegans. Ann. Rev. Neuro.* **28**:451-501.

De Bono, M., Tobin, D.M., Davis, M.W., Avery, L., Bargmann, C.I. 2002. Social feeding in *Caenorhabditis elegans* is induced by neurons that detect aversive stimuli. *Nature* **419**(6910):899-903.

DeVries, S.H. 2000. Bipolar cells use kainite and AMPA receptors to filter visual information into separate channels. *Neuron* **28**:847-856.

de Vries, B., Stam, A.H., Kirkpatrick, M. et al. 2009. Familial hemiplegic migraine is associated with febrile seizures in an FHM2 family with a novel de novo ATP1A2 mutation. *Epilepsia* **50**(11):2503-4.

Dhaka, A., Murray, A.N., Mathur, J., Earley, T.J., Petrus, M.J., Patapoutian, A. 2007. TRPM8 is required for cold sensation in mice. *Neuron* **54**(3):371-378.

Dib-Hajj, S.D., Yang, Y., Waxman, S.G. 2008. Genetics and molecular pathophysiology of Na(v)1.7-related pain syndromes. *Adv. Genet.* **63**:85-110.

Donnelly, J.L., Clark, C.M., Leifer, A.M., Pirri, J.K., Haburcak, M., Francis, M.M., Samuel, A.D.T., Alkema, M.J. 2013. Monoaminergic orchestration of motor programs in a complex *C. elegans* behavior. *PLoS Biology* **11**(4): e1001529.

Dubin, A.E., Patapoutian, A. 2010. Nociceptors: the sensors of the pain pathway. *J. Clin. Inv*. **120**(11): 3760-3772.

Estacion, M., Dib-Hajj, S.D., Benke, P.J., Te Morsche, R.H., Eastman, E.M., Macala, L.J., Drenth, J.P., Waxman, S.G. 2008. Nav1.7 gain-of-function mutations as a continuum: A1632E displays physiological changes associated with erythromelagia and paroxysmal extreme pain disorder mutations and produces symptoms of both disorders. *J. Neurosci.* **28**:11079-11088.

Ezak, M.J., Ferkey, D.M. 2010. The *C. elegans* D2-like dopamine receptor DOP-3 decreases behavioral sensitivity to the olfactory stimulus 1-octanol. *PLoS One* **5**(3):e9487.

Ezak, M.J., Hong, E., Chaparro-Garcia, A., Ferkey, D.M. 2010. *Caenorhabditis elegans* TRPV channels function in a modality-specific pathway to regulate response to aberrant sensory signaling. *Genetics* **185**(1):233-244.

Ferkey, D.M., Hyde, R., Haspel, G., Dionne, H.M., Hess, H.A., Suzuki, H., Schafer, W.R., Koelle M.R., Hart, A.C. 2007. *C. elegans* G protein regulator RGS-3 controls sensitivity to sensory stimuli. *Neuron* **53**(1):39-52.

Fertleman, C.R., Baker, M.D., Parker, K.A., Moffatt, S., Elmslie, F.V., Abrahamsen, B., Ostman, J., Klugbauer, N., Wood, J.N., Gardiner, R.M. et al. 2006. SCN9A mutations in paroxysmal

extreme pain disorder: allelic variants underlie distinct channel defects and phenotypes. *Neuron* **52**:767-774.

Fukuto, H.S., Ferkey, D.M., Apicella, A.J., Lans, H., Sharmeen, T., Chen, W., Lefkowitz, R.J., Jansen, G., Schafer, W.R., Hart, A.C. 2004. G protein-coupled receptor kinase function is essential for chemosensation in *C. elegans*. *Neuron* **42**(4):581-593.

Gasser, H. S. & Erlanger, J. (1929). Role of fiber size in establishment of nerve block by pressure or cocaine. *Amer. J. Physiol.* **88**: 581-591.

Geffen, M.N., Broome, B.M., Laurent, G., and Meister, M. (2009). Neural encoding of rapidly fluctuating odors. *Neuron* **61**, 570-586.

Geffeney, S.L., Cueva, J.G., Glauser, D.A., Doll, J.C., Lee, T.H., Montoya, M., Karania, S., Garakani, A.M., Pruitt, B.L., Goodman, M.B. 2011. DEG-ENaC but not TRP channels are the major mechanolelectrical transduction channels in a *C. elegans* nociceptor. *Neuron* **71**(5):845-857.

Goodman, M.B., Hall, D.H., Avery, L., Lockery, S.R. 1998. Active currents regulate sensitivity and dynamic range in *C. elegans* neurons. **20**(4):763-772.

Gong, Y., Wagner, M.J., Zhong, L.J., Schnitzer, M.J. 2014. Imaging neural spiking in brain tissue using FRET-opsin protein voltage sensors. *Nature Communications* **5**:3674. ncomms4674.

Goodman, M.B. Mechanosensation (January 06, 2006), *WormBook*, ed. The *C. elegans* Research Community, WormBook, doi/10.1895/wormbook.1.62.1, http://www.wormbook.org.

Gray, J.M., Hill, J.J., and Bargmann, C.I. 2005. A circuit for navigation in *Caenorhabditis elegans. Proc. Natl. Acad. Sci. USA* **102**(9), 3184-3191.

Hapiak, V., Summers, P., Ortega, A., Law, W.J., Stein, A., Komuniecki, R. 2013. Neuropeptides amplify and focus the monoaminergic inhibition of nociception in *Caenorhabditis elegans. J Neurosci.* **33**(35):14107-14116.

Harris, G.P., Hapiak, V.M., Wragg, R.T., Miller, S.B., Hughes, L.J., Hobson, R.J., Steven, R., Bamber, B., Komuniecki, R.W. 2009. Three distinct amine receptors operating at different levels within the locomotory circuit are each essential for the serotonergic modulation of chemosensation in *Caenorhabditis elegans. J. Neurosci.* **29**(5):1446-1456.

Harris, G., Korchnak, A., Summers, P., Hapiak, V., Law, W.J., Stein, A.M., Komuniecki, P., Komuniecki, R. 2011. Dissecting the serotonergic food signal stimulating sensory-mediated aversive behavior in *C. elegans*. *PLoS One* **6**(7):e21897.

Harris, G., Mills, H., Wragg, R., Hapiak, V., Castelletto, M., Korchnak, A., Komuniecki, R.W. 2010. The monoaminergic modulation of sensory-mediated aversive responses in *Caenorhabditis elegans* requires glutamatergic/peptidergic cotransmission. *J Neurosci.* **30**(23):7889-7899.

Hart, A.C., Kass, J., Shapiro, J.E., Kaplan, J.M. 1999. Distinct signaling pathways mediate touch and osmosensory responses in a polymodal sensory neuron. *J. Neurosci* **19**(6): 1952-1958.

Heitz, R.P., Schall, J.D. 2012. Neural mechanisms of speed-accuracy tradeoff. *Neuron* **76**(3):616-628.
Heinricher, M.M. Tavares, I., Leith, J.L., Lumb, B.M. 2009. Descending control of nociception: specificity, recruitment and plasticity. *Brain Res. Rev.* **60**(1):214-225.

Hellman, K.M., Mason, P. 2012. Opioids disrupt pro-nociceptive modulation mediated by raphe magnus*. J. Neurosci.* **32**(40):13668-13678.

Hilliard, M.A., Apicella, A.J., Kerr, R., Suzuki, H., Bazzicalupo, P., and Schafer, W.R. (2005). *In vivo* imaging of *C. elegans* ASH neurons: cellular response and adaptation to chemical repellents. *EMBO J.* **24**(1),63-72.

Hilliard, M.A., Bargmann, C.I., and Bazzicalupo, P. (2002). *C. elegans* responds to chemical repellents by integrating sensory inputs from the head and the tail. *Curr Biol.* **12**, 730-734.

Hilliard, M.A., Bergamasco, C., Arbucci, S., Plasterk, R.H., Bazzicalupo, P. 2004. Worms taste bitter: ASH neurons, QUI-1, GPA-3, and ODR-3 mediate quinine avoidance in *Caenorhabditis elegans. EMBO J.* **23**(5):1101-1111.

Hires, S.A., Tian, L., Looger, L.L. 2008. Reporting neural activity with genetically encoded calcium indicators. *Brain Cell Biol.* **36**(1-4):69-86.

Julius, D. 2013. TRP channels and pain. *Annu. Rev. Cell Dev. Biol.* **29**:355-84.

Kahn-Kirby, A.H., Dantzker, J.L.M., Apicella, A.J., Schafer, W.R., Browse, J., Bargmann, C.I., and Watts, J.L. (2004). Specific polyunsaturated fatty acids drive TRPV-dependent sensory signaling in-vivo. *Cell* **119**, 889-900.

Kaplan, J.M., and Horvitz, H.R. (1992). A dual mechanosensory and chemosensory neuron in *Caenorhabditis elegans. PNAS* **90**, 2227-2231.

Kass, J., Jacob, T.C., Kim, P., Kaplan, J.M. 2001. The EGL-3 proprotein convertase regulates mechanosensory responses of *Caenorhabditis elegans. J Neurosci.* **21**(23):9265-9272.

Kato, S., Xu, Y., Cho, C.E., Abbott, L.F., and Bargmann, C.I. (2014) Temporal responses of *C. elegans* chemosensory neurons are preserved in behavioral dynamics. *Neuron* **81**, 1-13.

Kim, A.J., Lazar, A.A., Slutskiy, Y.B. 2011. System identification of Drosophila olfactory sensory neurons. *J Comput Neurosci*. **30**:143-161.

Kim, K., Sato, K., Shibuya, M., Zeiger, D.M., Butcher, R.A., Ragains, J.R., Clardy, J., Touhara, K., Sengupta, P. 2009. Two chemoreceptors mediate developmental effects of dauer pheromone in *C. elegans. Science* **326**(5955):994-998.

Kobayashi, K., Yamanaka, H., Fukuoka, T., Dai, Y., Obata, K., Noguchi, K. 2008. P2Y12 receptor upregulation in activated microglia is a gateway of p38 signaling and neuropathic pain. *J. Neurosci.* **28**: 2892-2902.

Koda, H., Mizumura, K. 2002. Sensitization to mechanical stimulation by inflammatory mediators, by second messengers possibly mediating these sensitizing effects, and by mild burn in canine visceral nociceptors in vitro. *J Neurophysiol* **87**:2043-2051.

Kung, C. 2005. A possible unifying principle for mechanosensation. *Nature* **436**:647-654.

Kwan, K.Y., et al. 2006. TRPA1 contributes to cold, mechanical, and chemical nociception but is not essential for hair-cell transduction. *Neuron* **50**(2):277-289.

Lans, H., Jansen, G. 2007. Multiple sensory G proteins in the olfactory, gustatory and nociceptive neurons modulate longevity in *Caenorhabditis elegans*. *Dev Biol*. **303**(2):474-482.

Larsch, J., Ventimiglia, D., Bargmann, C.I., and Albrecht, D.R. 2013. High-throughput imaging of neuronal activity in *Caenorhabditis elegans. Proc. Natl. Acad. Sci. USA,* E4266-E4273.

Latremoliere, A., Woolf, C.J. 2009. Central sensitization: a generator of pain hypersensitivity by central neural plasticity. *J Pain* **10**(9):895-926.

Leipe, D.D., Koonin, E.V., Aravind, L. 2004. STAND, a class of P-loop NTPases including animal and plant regulators of programmed cell death: multiple, complex domain architectures, unusual phyletic patterns, and evolution by horizontal gene transfer. *J Mol Biol.* **343**(1): 1-28.

Lin Q, Li D, Xu X, Zou X, Fang L. 2007. Roles of TRPV1 and neuropeptidergic receptors in dorsal root reflex-mediated neurogenic inflammation induced by intradermal injection of capsaicin. *Mol Pain* **3**:30.

Liu, C.N., Michaelis, M., Amir, R., Devor, M. 2000. Spinal nerve injury enhances subthreshold membrane potential oscillations in DRG neurons: relation to neuropathic pain. *J Neurophys* **84**:205-215.

Liu, J., Ward, A., Gao, J. et al. 2010. C. elegans phototransduction requires a G protein-dependent cGMP pathway and a taste receptor homolog. *J. Neurosci.* **13**:715-722.

Liu, Q., Hollopeter, G., and Jorgensen, E.M. 2009. Graded synaptic transmis- sion at the *Caenorhabditis elegans* neuromuscular junction. *Proc. Natl. Acad. Sci. USA* **106**(10823–10828).

Lumpkin, E.A., Caterina, M.J. 2007. Mechanisms of sensory transduction in the skin. *Nature* **445**:858-865.

Luo, Z.D., Chaplan, S.R., Higuera, E.S., Sorkin, L.S., Stauderman, K.A., Williams, M.E., and Yaksh, T.L. 2001. Upregulation of dorsal root ganglion (alpha)2(delta) calcium channel subunit and its correlation with allodynia in spinal nerve-injured rats. *J. Neurosci.* **21**: 1868–1875.

Macosko, E.Z., Pokala, N., Feinberg, E.H., Chalassani, S.H., Butcher, R.A., Clardy, J., and Bargmann, C.I. 2009. A hub-and-spoke circuit drives pheromone attraction and social behavior in *C. elegans*. *Nature* **458**: 1171-1175.

Malan, T.P., Mata, H.P., Porreca, F. 2002. Spinal GABA(A) and GABA(B) receptor pharmacology in a rat model of neuropathic pain. *Anesthesiology* **96**:1161-1167.

Mandadi, S., et al. 2009. TRPV3 in keratinocytes transmits temperature information to sensory neurons via ATP. *Pflugers Arch.* **468**(6):1093-1102.

Maricq, A.V., Peckol, E., Driscoll, M., and Bargmann, C.I. (1995). Mechanosensory signaling in *C. elegans* mediated by the GLR-1 glutamate receptor. *Nature* **378**, 78-81.

Maslund, R.H. (2012). The neuronal organization of the retina. *Neuron* **76**, 266-280.

McGrath, P.T., Xu, Y., Ailion, M., Garrison, J.L., Butcher, R.A., and Bargmann, C.I. (2011) Parallel evolution of domesticated *Caenorhabditis* species targets pheromone receptor genes. *Nature* **477**, 321-325.

McMaon, S.B., Bennett, D.L.H., and Bevan, S. 2008. Inflammatory mediators and modulators of pain. In Wall and Melzack's textbook of Pain (Philadephia:Elsevier), S.B. McMahon and M. Koltzenburg, eds., pp.49-72.

Mellem, J.E., Brockie, P.J., Zheng, Y., Madsen, D.M., Maricq, A.V. 2002. Decoding of polymodal sensory stimuli by postsynaptic glutamate receptors in *C. elegans. Neuron* **36**(5):933-44.
Mello, C. and Fire, A. 1995. DNA transformation. *Methods Cell Biol.* **48**:451-482.

Melzack, R., Wall., P.D. 1965. Pain mechanisms: a new theory. *Science* **150**:971-979.

Mense, S., et al. 2008. Anatomy of nociceptors. In: Bushnell, M.C., Smith, D.V., Beauchamp, G.K., Firestei, S.J. eds. The senses: a comprehensive reference. (New York, New York, USA: Academic Press) pp.11-41.

Messinger, R.B., Naik, A.K., Jagodic, M.M., Nelson, M.T., Lee, W.Y., Chloe, W.J., Orestes, P., Latham, J.R., Todorovic, S.M., Jevtovic-Todorovic, V. 2009. In vivo silencing of the Ca(V)3.2 T-type calcium channels in sensory neurons alleviates hyperalgesia in rats with stretozocin-induced diabetic neuropathy. *Pain* **145**:184-195.

Meyer, R.A., Ringkamp, M., Campbell, J.N., Raja, S.N. (2008). Peripheral mechanisms of cutaneous nociception. In Wall and Melzack's Textbook of Pain, S.B. McMahon and M. Koltzenburg, eds. (Philadelphia: Elsevier), pp.3-34.

Mills, H., Wragg, R., Hapiak, V., Castelletto, M., Zahratka, J., Harris, G., Summers, P., Korchnak, A., Law, W., Bamber, B., Komuniecki, R. 2012. Monoamines and neuropeptides interact to inhibit aversive behavior in *Caenorhabditis elegans*. *EMBO J.* **31**(3):667-678.

Miraucourt, L.S., Dallel, R., Voisin, D.L. 2007. Glycine inhibitory dysfunction turns touch into pain through PKCgamma interneurons. *PLoS ONE* e1116.

Morgans, C.W., Zhang, J., Jeffrey, B.G., Nelson, S.M., Burke, N.S., Duvoisin, R.M., Brown, R.L. 2009. TRPM1 is required for depolarizing light response in retinal ON-bipolar cells. *Proc. Natl. Acad. Sci. USA* **106**(45):19174-19178.

Murayama, T., and Maruyama I.N. 2013. Decision making in *C. elegans* chemotaxis to alkaline pH. *Communicative and Integrative Biology* **6**(6): e26633-1-e26633-3.

Nagel, K.I., and Wilson, R.I. (2010). Biophysical mechanisms underlying olfactory receptor neuron dynamics. *Nature Neuroscience* **14**(2), 208-216.

Nassar, M.A., Levato, A., Stirling, L.C., Wood, J.N. 2005. Neuropathic pain develops normally in mice lacking both Nav1.7 and Nav1.8. *Mol. Pain* 1:24.

Ortiz, C.O., Faumont, S., Takayama, J., Ahmed, H.K., Goldsmith, A.D., Pocock, R., McCormick, K.E., Kunimoto, H., Iino, Y., Lockery, S., Hobert, O. 2009. Lateralized gustatory behavior *C. elegans* is controlled by specific receptor-type guanylyl cyclases. **19**(12):996-1004.

Patapoutian, A., Tate, S., Woolf, C.J. 2009. Transient receptor potential channels: targeting pain at the source. *Nat Rev Drug Discov.* **8**(1):55-68.

Piggott, B.J., Liu, J., Feng, Z., Wescott, S.A., Xu, X.Z.S. (2011). The neural circuits and synaptic mechanisms underlying motor initiation in *C. elegans*. *Cell* **147**(4), 922-933.

Pokala, N., Liu, Q., Gordus, A., and Bargmann, C.I. (2014). Inducible and titratable silencing of *Caenorhabditis elegans* neurons in vivo with histamine-gated chloride channels. *Proc. Natl. Acad. Sci. USA* Doi:10.1073/pnas.1400615111.

Rabinowitch, I., Chatzigeorgiou, M., Schafer, W.R. 2013. A gap junction circuit enhances processing of coincident mechanosensory inputs. *Current Biology* **23**: 963-967.

Ramot, D., Johnson, B.E., Berry, T.L., Carnell, L., Goodman, M.B. 2008. The parallel worm tracker: a platform for measuring average speed and drug-induced paralysis in nematodes. *PLoS ONE*, **3**:e2208.

Rauck, R.L., Wallace, M.S., Burton, A.W., Kapural, L., and North, J.M. 2009. Intrathecal ziconotide for neuropathic pain: a review. *Pain Pract.* **9**: 327–337.

Reynolds DV. 1969. Surgery in the rat during electrical analgesia induced by focal brain stimulation. *Science* **164**:444–445.

Richardson JD, Vasko MR. 2002. Cellular mechanisms of neurogenic inflammation. *J Pharmacol Exp Ther*. **302**(3):839–845.

Rinberg, D., Koulakov, A., Gelperin, A. (2006) Spped-accuracy tradeoff in olfaction. *Neuron* **51**(3):351-358.

Ringkamp, M., Peng, Y.B., Wu, G., Hartke, T.V., Campbell, J.N., Meyer, R.A. 2001. Capsaicin responses in heat-sensitive and heat-insensitive A-fiber nociceptors. *J Neurosci.* **21**(12):4460-4468.

Rush, A.M., Cummins, T.R., Waxman, S.G. 2007. Multiple sodium channels and their roles in electrogenesis within dorsal root ganglion neurons. *J Physiol.* **579**(1)1-14.

Ritner, H.L., Machelska, H., and Stein, C. (2009). Immune system pain and analgesia. In Science of Pain (Oxford: Academic Press), A.I. Basbaum and M. Bushnell, eds., pp. 407–427.

Roayaie, K., Crump, J.G., Sagasti, A., Bargmann, C.I. 1998. The G-alpha protein ODR-3 mediates olfactory and nociceptive function and controls cilium morphogenesis in *C. elegans* olfactory neurons. *Neuron*, **20**(1):55-67.

Sambongi, Y., Nagae, T., Liu, Y., Yoshimizu, T., Takeda, K., Wada, Y., Futai, M. 1999. Sensing of cadmium and copper ions by externally exposed ADL, ASE, and ASH neurons elicits avoidance response in *Caenorhabditis elegans. Neuroreport* **10**(4):753-757.

Schafer, W.R. Neurophysiological methods in *C. elegans*: an introduction (June 2, 2006), *WormBook*, ed. The *C. elegans* Research Community, WormBook, doi/10.1895/wormbook.1.111.1, http://www.wormbook.org.

Schmidt, R., Schmelz, M., Forster, C., Ringkamp, M., Torebjork, E., Handwerker, H. (1995) Novel classes of responsive and unresponsive C nociceptors in human skin. *J. Neurosci.* **15**:333-341.

Shen, Y., Heimel, J.A., Kamermans, M., Peachey, N.S., Gregg, R.G., Nawy, S. 2009. A transient receptor potential-like channel mediates synaptic transmission in rod bipolar cells. *J Neurosci.* **29**(19):6088-6093.

Solinski, J.H., Zierler, S., Gudermann, T., Breit, A. 2012. Human sensory neuron-specific Mas-related G protein-coupled receptors –X1 sensitize and directly activate transient receptor potential cation channel V1 via distinct signaling pathways. *J. Biol. Chem.* **287**:40956-40971.

Su, C.Y., Martelli, C., Emonet, T., Carlson, J.R. 2011. Temporal coding of odor mixtures in an olfactory receptor neuron. *PNAS* **108**(12):5075-5080.

Sun, X.R., Badura, A., Pacheco, D.A., Lynch, L.A., Schneider, E.R., Taylor, M.P., Hogue, I.B., Enquist, L.W., Murthy, M., and Wang, S.S.-H. 2013. Fast GCaMPs for improved tracking of neuronal activity. *Nat. Commun.* **4:** 2170.

Suzuki, H., Thiele, T.R., Faumont, S., Ezcurra, M., Lockery, S.R., Schafer, W.R. 2008. Functional asymmetry in *Caenorhabditis elegans* taste neurons and its computational role in chemotaxis. *Nature* **454**(7200):114-117.

Tian, L., Hires, S.A., Mao, T., Huber, D., Chiappe, M.E., Chalasani, S.H., Petreanu, L., Akerboom, J., McKinney, S.A., Schreiter, E.R., Bargmann, C.I., Jayaraman, V., Svoboda, K., Looger, L.L. 2009. Imaging neural activity in worms, flies, and mice with improved GCaMP calcium indicators. *Nat Methods* **6**(12):875-881.

Tobin, D.M., Bargmann, C.I. 2004. Invertebrate nociception: Behaviors, neurons, and molecules. *Journal of Neurobiology* **61**:161-174.

Tobin, D.M., Madsen, D.M., Kahn-Kirby, A., Peckol, E.L., Moulder, G., Barstead, R., Maricq, A.V., and Bargmann, C.I. (2002) Combinatorial expression of TRPV channel proteins defines their sensory functions and subcellular localization in *C. elegans* neurons. *Neuron* **35**, 307-318.

Treede, R.D., Meyer, R.A., Raja, S.N., Campbell, J.N. 1995. Evidence for two different heat transduction mechanisms in nociceptive primary afferents innervating monkey skin. *J Physiol.* **483**(3):747-758.

Troemel, E.R., Chou, J.H., Dwyer, N.D., Colbert, H.A., Bargmann, C.I. 1995. Divergent seven transmembrane receptors are candidate chemosensory receptors in *C. elegans. Cell* **83**(2):207-218.

Veldhuijzen, D.S., Kenemans, J.L., van Wijck, A.J.M., Olivier, B., Kalkman, C.J., Volkerts, E.R. 2006. Processing capacity in chronic pain patients: A visual event-related potentials study. *Pain* **121**(1-2): 60-68.

Wang, S., Dai, Y., Fukuoka, T., Yamanaka, H., Kobayashi, K., Obata, K., Cui, X., Tominaga, M., Noguchi, K. 2008. Phospholipase C and protein kinase A mediate bradykinin sensitization of TRPA1: a molecular mechanism of inflammatory pain. *Brain* **131**(5):1241-1251.

Way, J.C. and Chalfie, M. 1989. The *mec-3* gene of *Caenorhabditis elegans* requires its own product for maintained expression and is expressed in three neuronal cell types. *Genes Dev.* **3:** 1823-1833.

Westwick, D.T., and Kearney, R.E. 2003. Identification of Nonlinear Physiological Systems. (Hoboken: Wiley & Sons).

White, J., Southgate, E., Thomson, J., Brenner, S. 1986. The structure of the nervous system of the nematode *Caenorhabditis elegans*. *Phil. Trans. R Soc. Lond. (Biol)* **314**: 1-340.

Woolf, C.J., Ma, Q. 2007. Nociceptors –noxious stimulus detectors. *Neuron* **55**(3):353-364.

Wragg, R.T., Hapiak, V., Miller, S.B., Harris, G.P., Gray, J., Komuniecki, P.R., Komuniecki, R.W. 2007. Tyramine and octopamine independently inhibit serotonic-stimulated aversive behaviors in *Caenorhabditis elegans* through two novel amine receptors. *J. Neurosci* **27**: 13402-13412.

Yang, Y., Wang, Y., Li, S., Xu, Z., Li, H., Ma, L., Fan, J., Bu, D., Liu, B., Fan, Z. et al., 2004. Mutations in SCN9A, encoding a sodium channel alpha subunit, in patients with primary erythermalgia *J Med Genet*. **41**:171-174.

Zahratka, J.A., Williams, P.D.E., Summers, P.J., Komuniecki, R.W., Bamber, B.A. 2014. Serotonin differentially modulates stimulus-dependent Ca++ influx and depolarization in a *C. elegans* nociceptive neuron. (submitted)

Zamponi, G.W., Lewis, R.J., Todorovic, S.M., Arneric, S.P., and Snutch, T.P. 2009. Role of voltage-gated calcium channels in ascending pain pathways. *Brain Res. Rev*. **60**:84-89.

Zheng, Y., Brockie, P.J., Mellem, J.E., Madsen, D.M., Maricq, A.V. 1999. Neuronal control of locomotion in *C. elegans* is modified by a dominant mutation in the GLR-1 ionotropic glutamate receptor. *Neuron* **24**: 347-361.

Zimmermann, K., Leffler, A., Fischer, M.., Messlinger, K., Nau, C., Reeh, P.W. 2005. The TRPV1/2/3 activator 2-aminoethoxydiphenyl borate sensitizes native nociceptive neurons to heat in wildtype but not TRPV1 deficient mice. *Neuroscience* **135**(4):1277-84.